Structural studies of cell surface signalling molecules for neuronal guidance and connectivity

Nikolaos Mitakidis

A thesis submitted in partial fulfilment of the requirements for the degree of *Doctor of Philosophy* at the University of Oxford



Trinity College

Department of Biochemistry

Division of Structural Biology

University of Oxford

Trinity Term 2013

Structural studies of cell surface signalling molecules for neuronal guidance and connectivity

Nikolaos Mitakidis

A thesis submitted in partial fulfilment of the requirements for the degree of *Doctor of Philosophy*
Trinity College, Department of Biochemistry, Division of Structural Biology
University of Oxford, Trinity Term 2013

Abstract

Signal transduction is critical during the lifetime of a neuron as it navigates to reach its targets, forms functional synaptic connections and adjusts the molecular architecture of these connections in an activity-dependent manner. Understanding the molecular organisation of components required for neuronal signalling will provide novel biological insight and can contribute to the design of therapeutics for neurodevelopmental and neurodegenerative disorders.

The focus of the thesis is on determining mechanistic molecular details of a number of distinct cell surface systems implicated in neuronal signalling. Crystallographic studies on the cell surface complex between Eph receptor A4 and ephrinA5 contributed to understanding how the modes of higher order arrangements of receptors involved in guidance affect signal transduction across the membrane. A set of structural and biophysical studies addressed the proteoglycan regulation of RPTPσ-TrkC *trans*-synaptic interaction and contributed to deciphering the principles of the switch from axonal growth to synapse establishment and formation. A crystallographic and biochemical analysis of the neuronal C1q-like family, enabled mapping their interactions with potential synaptic partners, and guided functional studies aimed at elucidating their roles in the maintenance of synaptic integrity. Preliminary work on the neuronal Sigma-1 receptor chaperone laid the foundations for the structural determination of this receptor.

The structural work presented in this thesis strives to propose functional hypotheses. Some of these have been tested in collaboration with other laboratories, in cellular assays, and animal model experiments are currently ongoing to provide functional validation within a physiological context.

Acknowledgements

Firstly, I would like to cordially thank my supervisors Prof. Yvonne Jones and Dr. Radu Aricescu for their continuous support, guidance and encouragement during the course of my doctoral studies. It was a real privilege to be mentored by them while working at the Division of Structural Biology. I am deeply grateful to both of them for giving me the opportunity to undertake research in such a unique environment.

I would like to additionally thank my collaborators in the laboratories of Prof. Michisuke Yuzaki (Keio University, Japan), Dr. Terunaga Nakagawa (University of California, San Diego), Prof. Ann Marie Craig (University of British Columbia, Canada) and Prof. Rüdiger Klein (Max-Planck Institute for Neurobiology, Germany) for their input and assistance in various aspects in my projects. I must thank to Prof. Chris O'Callaghan (Nuffield Department of Clinical Medicine) and Dr David Staunton (Department of Biochemistry) for access to surface plasmon resonance equipment.

I would like to thank the members of the Division of Structural Biology for providing such a happy environment to work in. I am particularly grateful to Ms. Amber Clayton, Dr. Charlotte Coles, Dr. Jonathan Elegheert, Dr. Jordan Clay, Ms. Margaret Jones, Dr. Paul Miller, Ms. Aletheia Lee, Dr. Ross Robinson, Dr. Yuguang Zhao, Dr. Luke Yates, Dr. Geoff Sutton, Dr. Tomas Malinauskas, and Mr. Thomas Brantzos for their practical assistance, advice and discussions at all times. I am also grateful towards the staff at Diamond Light Source, Oxfordshire, UK, and the European Synchrotron Radiation Facility, Grenoble, France, for giving me the opportunity to collect X-ray diffraction data. I thank the Wellcome Trust for the generous funding, as well as Trinity College and the University of Oxford for their pastoral care.

Finally, I would like to thank my parents, my sister Rafaela, and Fay for their love, support and encouragement throughout my DPhil.

Table of Contents

Abstract 1

Acknowledgements 2

Table of Contents 3

Chapter 1 – General Introduction

1.1 Neuronal guidance 9

1.2 The synapse 16

1.3 Aim of this thesis 23

Chapter 2- Materials & Methods

2.1 Molecular Biology 26

2.1.1 Expression vectors and complementary DNA 26

2.1.2 Construct design and Polymerase Chain reaction 27

2.1.3 Restriction digests, ligations and transformations 29

2.2 Protein Expression and Purification 31

2.2.1 Protein expression in mammalian systems 31

2.2.1.1 Cell lines 31

2.2.1.2 Small scale expression 32

2.2.1.3 Large scale expression 33

2.2.2 Detergent screening for solubilisation of membrane-embedded proteins 34

2.2.3 Large-scale solubilisation of membrane-embedded proteins 36

2.2.4 Protein purification 37

2.2.4.1 Sample Preparation 37

2.2.4.2 Immobilised-Metal Affinity Chromatography 37

2.2.4.3 Antibody Affinity Chromatography 38

2.2.4.4 Analytical Size Exclusion Chromatography 39

2.3 Crystallisation 39

2.3.1 Crystallisation screens 39

2.3.2 Optimisation of crystallisation hits 41

2.3.3 Reductive lysine-methylation 42

2.4 X-ray data collection 43

2.4.1 Cryo-protection crystal preparation and mounting 43

2.4.2 Data collection 43

2.5 Structure solution 44

2.5.1 Data processing 44

2.5.2 Structure determination & Refinement 45

2.5.3 Structure validation & analysis 47

2.6 Surface Plasmon Resonance (SPR) 48

2.6.1 Sample preparation & SPR binding assays 48

2.6.2 Data analysis 50

2.7 Multi-Angle Laser Light Scattering (MALLS) 50

2.8 Fluorescence Microscopy 51

2.9 CPM Thermostability Assay 51

Chapter 3 - Preliminary structural studies of neuronal Sigma-1 receptor

3.1 Summary 54

3.2 Introduction 55

3.2.1 Intracellular signalling activity by non-opioid sigma-1 receptor 55

3.2.2 Sigma-1 receptor pharmacology 57

3.2.3 Functional implications of cholesterol binding in sigma-1 receptor signalling 59

3.2.4 Structural features of Sigma-1 receptor 60

3.3 Aims 61

3.4 Expression and screening for optimal membrane extraction 62

3.5 Purification of full-length sigma-1 receptor 66

3.6 Stability optimisation of Sigma-1 receptor detergent micelle 69

3.7 Future perspectives 72

Chapter 4 - Structural studies of the EphA4/ephrinA5 signalling complex

4.1 Summary 75

4.2 Introduction 76

4.2.1 Signalling by Eph receptors 76

4.3 Aims 84

4.4 Expression and purification of EphA4 and EphrinA5 85

4.4.1 Expression of EphA4 and EphrinA5 85

4.4.2 Purification of native EphA4 and EphrinA5 86

4.4.3 Purification of lysine-methylated EphA4 and EphrinA5 88

4.5 Crystal optimization of existing hits and crystallographic analysis of EphA4/EphrinA5 complex 89

4.6 Comparison of EphA4/EphA2 ectodomain structures and implications for EphrinA5-mediated signalling 94

4.7 Discussion and future perspectives 97

Chapter 5 - Proteoglycan regulation of RPTP-TrkC mediated synaptogenesis

5.1 Summary 99

5.2 Introduction 100

5.2.1 Protein Tyrosine Phosphorylation and signalling 100

5.2.2 Regulation of Protein Tyrosine Phosphatases 105

5.2.3 An overview of the receptor Protein tyrosine phosphatase subfamily 108

5.2.3.1 RPTP domain organisation and classification 108

5.2.3.2 Type IIa RPTP knock-out studies 110

5.2.3.3 Type IIa RPTP ligands 111

5.2.3.4 Type IIa RPTP involvement in synapse formation 112

5.2.4 Proteoglycan regulation of axon guidance 114

5.2.5 Proteoglycan mediation of synapse formation 115

5.2.6 An overview of neurotrophin signalling 118

5.3 Aims 122

5.4 Expression and purification of RPTPσ and TrkC proteins 123

5.4.1 Small scale expression of RPTPσ and TrkC proteins 123

5.4.2 Large scale expression of RPTPσ and TrkC proteins 124

5.4.3 Purification of RPTPσ and TrkC proteins 125

5.5 Structure determination of cRPTPσ-cTrkC complex 127

5.6 Biophysical characterisation of hRPTPσ-mTrkC interaction, and competition with proteoglycans 132

5.6.1 Minimal unit of hRPTPσ required for interaction of mTrkC 132

5.6.2 Biophysical analysis of structure-based mutants targeting the hRPTPσ-mTrkC interfaces 134

5.6.3 mTrkC competes with heparan sulfate for hRPTPσ binding 139

5.7 Conclusions and future perspectives 140

Chapter 6 - Structural investigations of C1q-like proteins and characterisation of their synaptic interactions

6.1 Summary 143

6.2 Introduction 144

6.2.1 The action of Complement C1q in the nervous system 144

6.2.2 An overview of the C1q family 145

6.2.3 An overview of C1q-like proteins 150

6.2.4 In search of C1q-like synaptic partners: The case of BAI proteins 153

6.3 Aims 155

6.4 Expression and Purification of C1ql, BAI3, iGluK2 proteins 156

6.4.1 Expression of C1ql, BAI3, iGluK2 proteins 156

6.4.2 Purification of individual C1ql, BAI3, iGluK2 proteins 157

6.5 Structure determination of C1ql1 and C1ql3 c1q domains 161

6.6 Molecular dissection of C1ql/BAI-3 interaction 170

6.6.1 Mapping C1ql3/BAI3 interaction with deletion constructs 170

6.6.2 Structure-based mutagenesis of C1ql proteins and effect on BAI-3 binding 179

6.7 Molecular dissection of C1ql/GluK-2 interaction 183

6.8 Molecular dissection of C1ql/βNeurexin1 interaction 185

6.9 Attempts to crystallise C1ql/BAI3 and C1ql/GluK2 complexes 187

6.10 Conclusions and future perspectives 187

Chapter 7 – List of references 189

Appendices

Appendix A **Expression Vectors** 223

Appendix B **Constructs** 227

Appendix C **List of Formulae** 238

Appendix D **Abbreviations** 241

Appendix E **Publication** 245

Chapter 1

General Introduction

Chapter 1

General Introduction

1.1 Neuronal guidance

Axons extend over long distances to reach their targets during nervous system development. Ramon y Cajal first commented on the tendency of axons to grow in certain directions, and suggested that such oriented movements should be driven by cues: “If one admits that neuroblasts are endowed with chemotactic properties, then one might also imagine that they are capable of ameboid movements, initiated by factors secreted from epithelial, neural, or mesodermal elements. As a result, their processes may be oriented in the direction of chemical gradients, and thus guided to the secreting cells” (Cajal RY., 1890). In 1963, Sperry demonstrated that growing retinal axons could respond to attractive or repulsive guidance cues, in order to reach their targets in the frog tectum (Sperry RW., 1963). Axon guidance has since been shown to be a mechanistically complex and tightly regulated process, in order to ensure that neuronal connectivity is correctly established (Lowery LA., and Van Vactor D., 2009).

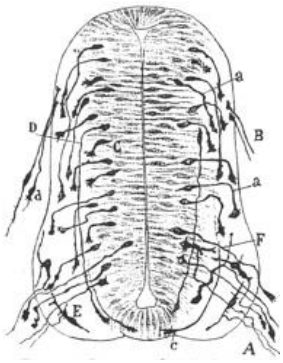


Figure 1.1: Ramon y Cajal’s first published image of growth cones in a spinal cord from a chick embryo (Cajal RY., 1890)

The axonal growth cone, which was originally described by Cajal as a "concentration of protoplasm of conical form, endowed with amoeboid movements" (Figure 1.1) (Cajal RY., 1890), possesses dynamic filopodia structures which scout the local territory the axon is moving into (Figure 1.2). Filopodia protrude from the base of the growth cone face, due to their protein core which consists of F-actin bundles, supported by an F-actin network spread over the base of the growth cone intracellularly. The F-actin network is directly connected to the bundled microtubules, which remain enclosed within the C domain regions in the axon shaft, leading the propagation of movement from the growth cone to the rest of the axon (Figure 1.2).

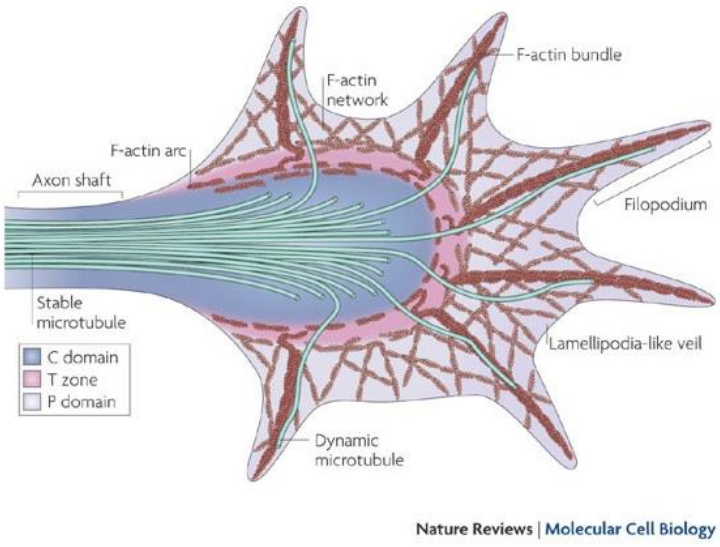


Figure 1.2: The structure of the growth cone is fundamental to its function. The leading edge consists of dynamic, finger-like filopodia that explore the road ahead, separated by sheets of membrane between the filopodia called lamellipodia-like veils (see the figure). The peripheral (P) domain contains long, bundled actin filaments (F-actin bundles), which form the filopodia, as well as mesh-like branched F-actin networks, which give structure to lamellipodia-like veils. Additionally, individual dynamic 'pioneer' microtubules (MTs) explore this region, usually along F-actin bundles. The central (C) domain encloses stable, bundled MTs that enter the growth cone from the axon shaft, in addition to numerous organelles, vesicles and central actin bundles. Finally, the transition (T) zone sits at the interface between the P and C domains, where actomyosin contractile structures (termed actin arcs) lie perpendicular to F-actin bundles and form a hemicircumferential ring. The dynamics of these cytoskeletal components determine growth cone shape and movement on its journey during development (Figure and caption adopted from Lowery LA., and Van Vactor D., 2009).

The axon outgrows in four distinct stages. When the growth cone meets an attractive cue (stage 1, substrate encounter), its filopodia will initially extend forward (stage 2, protrusion), leading to a re-arrangement of its cytoskeletal components (stage 3, engorgement), which will eventually facilitate the extension of the axon in the new direction (stage 4, consolidation). However, when the growth meets a repulsive cue, the signal is propagated to the F-actin network which will break down and the filopodia retract without any outgrowth for the axon (reviewed in Lowery LA., and Van Vactor D., 2009). Cell surface receptors of the growth cone interact with a range of molecules, expressed from neighbouring cells, or present in concentration gradients of secreted nature, or in the extracellular matrix (Chilton JK., 2005). Such recognition events trigger intracellular signalling outcomes that modulate axonal pathfinding, via regulation of the cytoskeleton, as described above. Within this context, canonical cell surface protein-protein interactions (Figure 1.3) have been demonstrated to exhibit attractive or repulsive effects.

Semaphorins are a large evolutionary conserved family of both secreted and cell-surface attached guidance cues, bearing a characteristic ~420 amino acid “Sema” domain at the N-terminus (Yazdani U and Terman JR., 2006). The first member to identified was a protein necessary for pathfinding of sensory axons during grasshopper limb development (Kolodkin Al., et al., 1992). The first vertebrate semaphorin to be characterised was Sema3A, originally named as “Collapsin”, when it was demonstrated that it can mediate axonal repellence *in vitro* (Luo Y., *et al.*, 1993). Their growth inhibitory role has been since established in vertebrates and invertebrates *in vivo* (Tran TS., *et al.*, 2007). Semaphorins have been shown to exhibit their effects via multimeric receptor interactions, involving a

member of the plexin family, with a particular bivalent architecture necessary for the promotion of signal transduction (Fujisawa H. 2003, Janssen B., *et al.*, 2010). The activation of plexin receptor leads to signalling events that facilitate the collapse of local cytoskeletal components and eventually the growth cone (Zhou Y., 2008). It has been also shown that co-receptors such as the neuropilins mediate selective semaphorin/plexin activation of downstream signalling events (Janssen B., *et al.*, 2012).

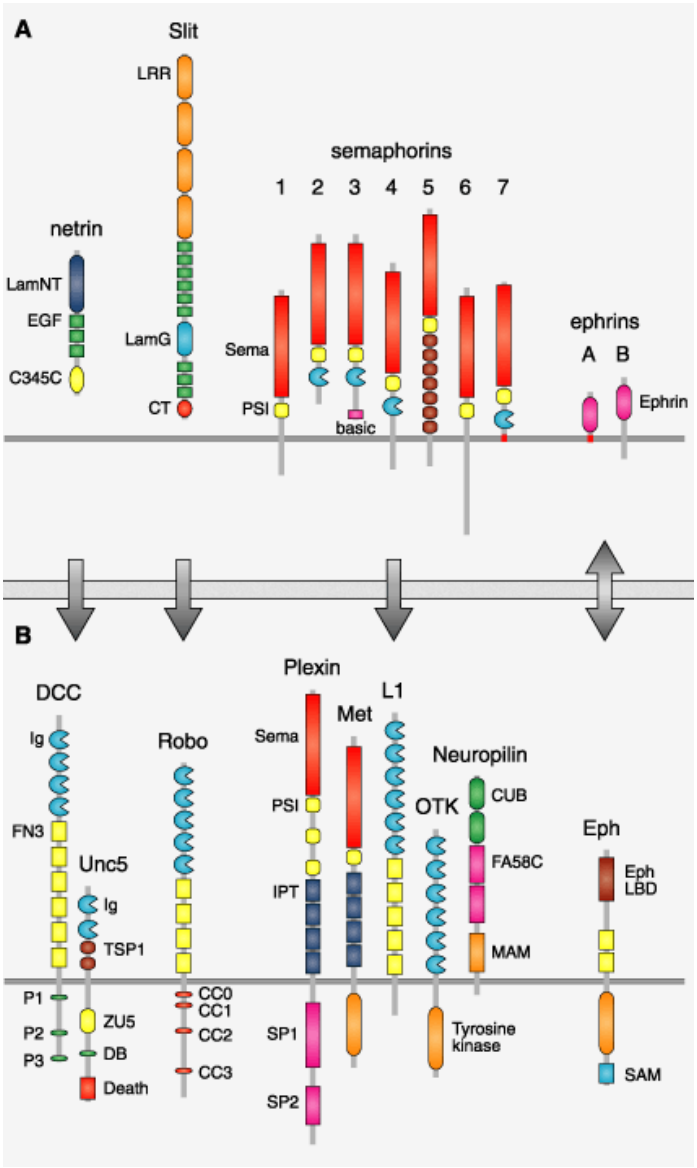


Figure 1.3: Conserved families of cell surface guidance molecules (**A**) and their receptors (**B**). Domain names are from SMART (http://smart.embl-heidelberg.de). P1 to P3, DB (DCC-binding), CC0 to CC3, and SP1 and SP2 indicate conserved regions in the cytoplasmic domains of DCC, UNC-5, Robo, and Plexin receptors, respectively (Image and caption adopted from Dickson BJ., 2002).

Slits are secreted molecules that have been demonstrated to be involved in midline axonal repulsion in both *Drosophila* and vertbrates (Kidd T., *et al.*, 1999, Brose K., *et al.*, 1999, Li HS., *et al.*, 1999). Robo cell surface receptors, which are members of the immunoglobulin superfamily, have been shown to bind Slits for exertion of their chemorepulsive guidance effects as well as for dendritic and axonal branching (Ma L. and Tessier-Lavigne M., 2007). Structural analyses of Slit/Robo interactions have demonstrated that heparin binding stabilises the Slit-Robo interaction (Hussain SA., *et al.*, 2006, Morlot C., *et al.*, 2007).

Ephrins are another family involved in axonal guidance via their specialised Eph receptors (reviewed in Klein R., 2004). They are capable of mediating either attractive or repellent axonal effects and have also been implicated in short-range guidance, pruning of axonal trajectories, as well as synaptogenesis in the Central Nervous System (Flanagan JG. And Vanderhaeghen P., 1998, Shen K. and Cowan CW., 2010). A focused overview of Eph/eprhin signalling is given in chapter 4 of this thesis.

Netrins are grouped in a small and tightly conserved family of laminin-related proteins that were initially identified to guide migrations on the ectoderm of *C.elegans* (Ishii N., *et al.*, 1992, Wadsworth WG., et al., 1996). The nematode UNC-6 homolog in vertabrates, namely Netrin-1, was demonstrated to be essential for chemoattractant spinal commissural axon guidance *in vitro* (Serafini T., *et al.*, 1994) and *in vivo* (Serafini T., *et al.*, 1996). The attractant effects of netrin heave been established to be mediated by *Deleted in Colorectal Cancer* (DCC) cell surface receptor in vertebrates (Keino-Masu K., *et al.*, 1996), which is defined by the presence of four immunoglobulin domains and six fibronectin type III repeats at the extracellular side. DCC homologs UNC-40 in *C.elegans*

(Chan SSY., *et al.*, 1996) and frazzled in *Drosophila* (Kolodziej PA., *et al.*, 1996), have also been shown to respond to netrin family members within the context of motor axon guidance. More recently, Down Syndrome Cell Adhesion Molecule (DSCAM) receptors have been shown to be expressed in commissural axons, bind netrin-1 and collaborate with DCC for axon turning reponses (Ly A., et al., 2008). However, netrins have been shown to exert repulsive responses as well, through their interaction with another receptor family, Unc5, which bears two immunoglobulin domains and two thrombospondin repeats on their extracellular portion (Keleman K. and Dickson BJ., 2001).

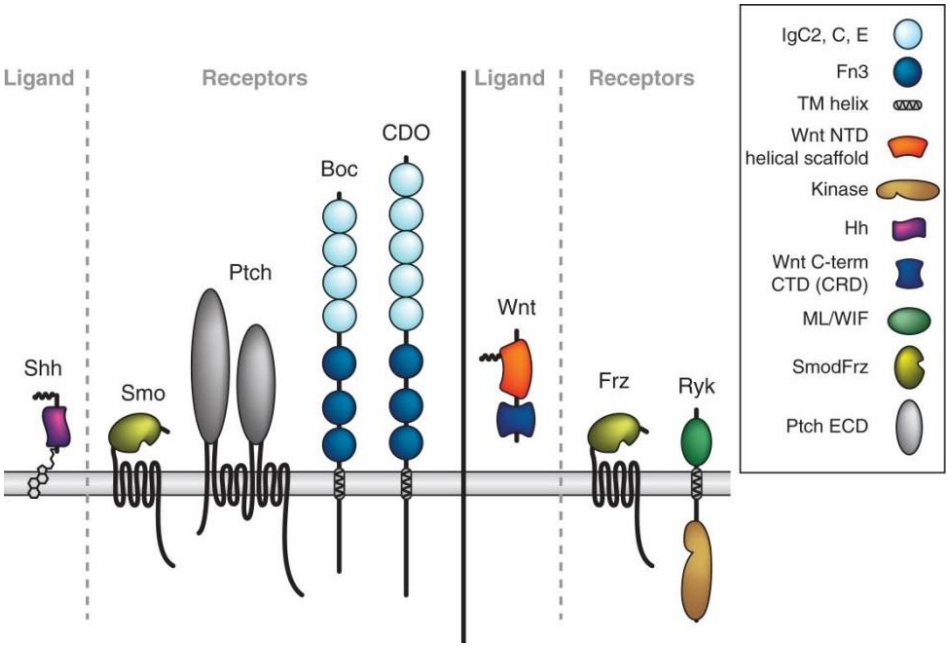


Figure 1.4: Morphogens involved in neuronal guidance and their receptors. A schematic showing Shh and its receptors (Smo, Ptch, Boc, and CDO), and Wnts and their receptors (Frz and Ryk), all of which serve guidance functions. The key defines distinct molecular domains found in these proteins (Image and caption adopted from Kolodkin A. and Tessier-Lavigne M., 2011).

Morphogens have been increasingly been implicated in axonal guidance within the last decade. Wnt5 interacts with Derailed, a homolog of Ryk receptor kinase, in Drosophila

and mutagenesis analysis showed that this interaction is critical for the axonal repulsion from the posterior commissure (Yoshikawa S., *et al.*, 2003). Vertebrate Wnts have been shown to maintain an anterior-posterior balance along the longitudinal axis of the Central Nervous System, by attracting –via the Frizzled receptor- ascending somatosensory projections from the spinal cord to the brain (Lyuksyutova AI., *et al.*, 2003), and via the Ryk receptor repelling corticospinal tract axons towards the opposite direction (Liu Y., *et al.*, 2005). The vertebrate Sonic hedgehog (Shh) has been demonstrated to repel Retinal Ganglion Cell axons, which express Patched receptor, growing towards the diencephalic ventral midline during embryogenesis (Trousse F., *et al.*, 2001). On the contrary, Shh was shown to act as an attractant of commissural axonal growth to the midline (Charron F., *et al.*, 2003). In either case, Boc and CDO proteins act as receptors for Shh (Okada A., et al., 2006, Fabre PJ., *et al.*, 2010), while it was shown *in vivo* that Shh controls contralateral projections of Retinal Ganglion Cells via the Smoothened receptor (Sanchez-Camacho C. and Bovolenta P., 2008).

A number of genetic disorders have been proposed to occur due to defects in axon guidance machinery setting a clinical imperative for the elucidation of the underlying molecular mechanisms. Disorders that have been described include corpus callosum agenesis, horizontal gaze palsy with progressive scoliosis, albinism, Duane retraction syndrome, pontine tegmental cap dysplasia, congenital fibrosis of the extraocular muscles type 1, Kallmann syndrome, L1 syndrome and Joubert syndrome (reviewed in Engle EC., 2010).

1.2 The synapse

In neural development axons extend and navigate towards their target regions, where they aim to establish functional connections with other neurons or cells. These functional connections were first observed with silver stain in the late 19th century (Figure 1.5), and named by Sir Charles Sherrington as “synapses”, a greek term derived from the words “συν-“ which means “together”, and “-απτειν” which means “to clasp”.

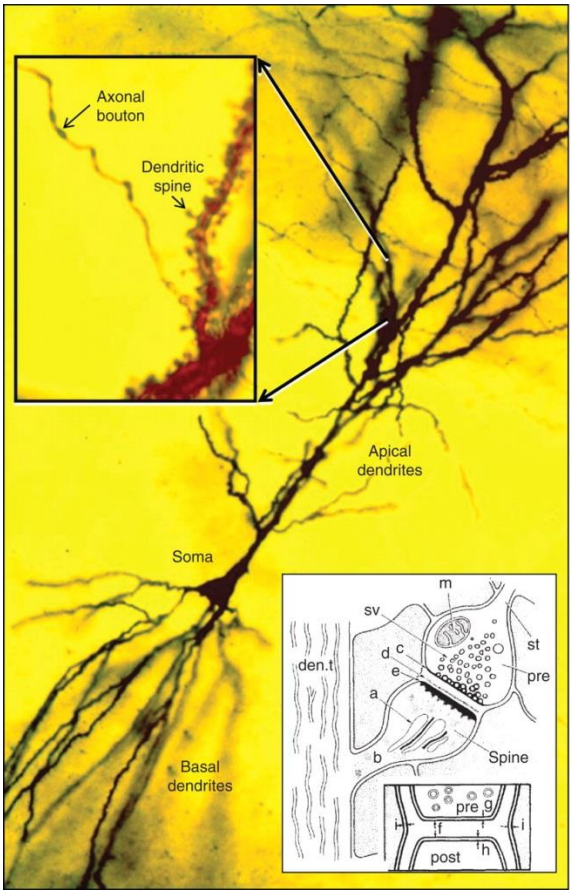


Figure 1.5: Golgi-impregnated pyramidal cell in hippocampal area CA1, showing the soma and apical and basal dendrites. (inset, *left*) Higher magnification shows an axon passing by dendritic spines protruding from the apical dendritic shaft. (inset, *right*) A drawing from the earliest EMs of dendritic spines: (a) spine apparatus; (b) spine neck; (c) presynaptic membrane; (den.t.) dendritic microtubules; (d) dense material in synaptic cleft; (e) postsynaptic membrane; (f) synaptic cleft; (g,h,i) plasma membranes of pre-, post-, and neighboring processes; (m) mitochondrion; (pre) presynaptic axons; (st) “stalk” of axon; (sv) synaptic vesicles (Figure and caption adopted from Harris KM. and Weinber RJ., 2012).

Early electron microscopy studies in mid-20th century contributed to the efforts of deciphering the structural principles mediating synaptic function, by exhibiting the morphological distinction between the two main groups of synapses: assymetric (or as demonstrated later excitatory glutamatergic) and symmetric (or as demonstrated later inhibitory) (Gray EG., 1959, Cline H., 2005). The mature human brain reaches levels of extraordinary complexity when one considers that the approximately 20 billion neurons establish synapses with more than 10000 other targets each (Sheng M., *et al.*, 2012), leading to the physical and convoluted expression of a range of cognitive and behavioural outputs such as consciousness, emotions, memory and motor coordination. Neural activity as well as its tight regulation is at the centrefold of the physical manifestation of the mind, mediated by the physiology of the building units of the nervous system, the neurons, according to the neuron doctrine (Finger S., 2001). The interaction of the nervous systems with the environment and the bombardment of sensory stimuli at all times, is translated at the cellular and the molecular level, enabling neural activity to modify and mature its established synaptic circuit in response (Katz LC. And Shatz CJ., 1996, Cohen S. and Greenberg ME., 2008). So instead of a static, hardwired computational unit, the nervous system is viewed as a highly plastic set of specifically interconnected building blocks that responds to external stimuli and adjusts the parameters of its synaptic connectivity (Shepherd JD., and Huganir RL., 2007). Cellular mechanisms that confer synaptic plasticity in an neural activity-dependent manner, have been proposed (reviewed in Malenka RC. And Bear MF., 2004). Long-term potentiation (LTP) is described as a persistent increase of the evoked post-synaptic response due to the activity-driven amplification of synaptic signalling (Bliss TVP. and Lomo T., 1973, Bliss TVP. and Gadner-dewin AR., 1973). A number of LTP types have been described since the

early observation of the phenomenon in the 1960s, according to synaptic localisation and the time of induction during development (Malenka RC. And Bear MF., 2004), however the most extensively studied is the *N*-methyl-d-aspartate (NMDA) receptor-dependent LTP in the CA1 region of the hippocampus (Figure 1.6) (Bliss TVP. and Collingridge GL., 1993). It has been demonstrated that NMDA receptors materialise the coincidence-detection principles, originally proposed by Hebb (Hebb DO., 1949) requiring both ligand binding and depolarisation of the post-synaptic membrane (Bliss TVP. and Collingridge GL., 1993). A magnesium ion bound on NMDA receptors, ensures that they remain closed unless depolarisation by α-amino-3-hydroxy-5-methyl-4-isoxazole-propionic acid (AMPA) receptors has taken place (Collingridge GL., *et al.*, 1983, Bliss TVP. and Collingridge GL., 1993). When the pre-synaptic signals are strong and NMDA channels open, an influx of calcium ions promotes the activation of a range of signalling cascades involving mediators such as the calcium/calmodulin-dependent protein kinase II (CaMKII), the cAMP-dependent protein kinase (PKA), the protein kinase C (PKC), the mitogen-activated protein kinase (MAPK), the phosphatidylinositol-3 (PI3) kinase and the Src kinase (Malenka RC. And Bear MF., 2004). As as result, AMPA function is regulated by direct phosphorylation (Benke TA., *et al.*, 1998, Malenka RC. and Nicoll RA., *et al.*, 1999, Lee HK., *et al.*, 2003) while their trafficking to the surface is adjusted in order for the LTP to be maintained (Shepherd JD. and Huganir RL., 2007). Further structural effects of LTP involve changes in gene expression, via the cAMP response element-binding protein (CREB), that facilitate the enhanced potency of the particular synapse (Malenka RC. And Bear MF., 2004) as well as trigger morphological changes such as spine enlargement (Kasai H., *et al.*, 2010) and spine density increase (Toni N., *et al.*, 1999).

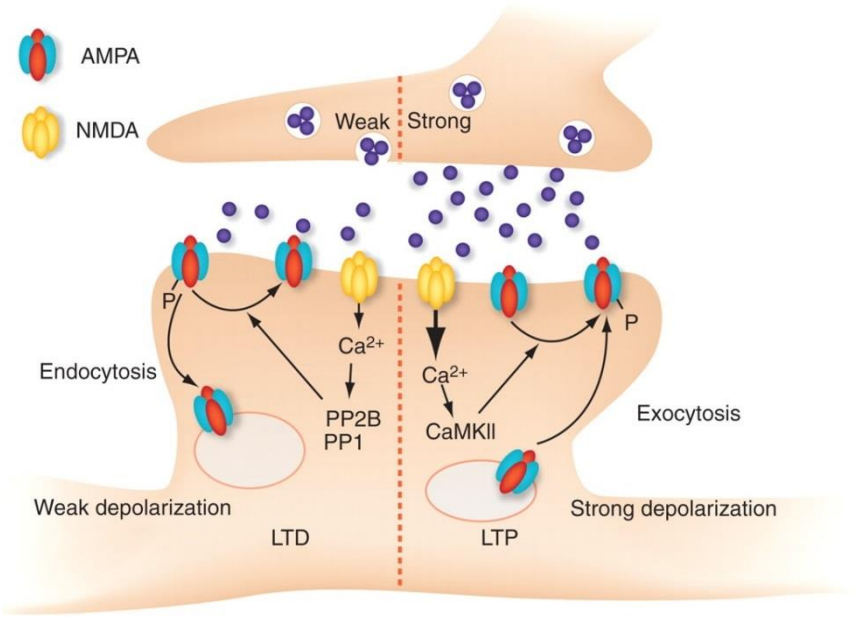


Figure 1.6: Postsynaptic expression mechanisms of LTP and LTD. Weak activity of the presynaptic neuron leads to modest depolarization and calcium influx through NMDA receptors. This preferentially activates phosphatases that dephosphorylate AMPA receptors, thus promoting receptor endocytosis. Strong activity paired with strong depolarization triggers LTP in part via CaMKII, receptor phosphorylation, and exocytosis (Image and camption adopted from Luscher C. and Malenka RC., 2012).

Conversely, long-term depression (LTD) is described as a dampening effect on the evoked post-synaptic response when the pre-synaptic inputs are consistently below a certain threshold, achieved experimentally by low frequency stimulation (Dudek SM. and Bear MF., 1992). It has been demonstrated that NMDA receptor activation is required for certain kinds of LTD responses (Mulkey RM. and Malenka RC., 1992), mediating an increase in post-synaptic calcium concentration. Similar LTD induction modes have been demonstrated to apply to neocortical synapses (Kirkwood A., *et al.*, 1993). NMDA-independent LTD types have also been described involving metabotropic glutamate receptors (mGluR) as in the case of mGluR-dependent LTD occurring at the parallel fiber to Purkinje cell synapses at the cerebellum (Ito M., 1989, Ito M., 2002), or as in the case of endocannabinoid-mediated LTD in the nucleus accumbens (Robbe D., *et al.*, 2002). For NMDA-dependent LTD, since calcium influx represents a shared characteristic with LTP induction, the magnitude and the temporal pattern of calcium influx activation is critical

for LTD (over LTP) induction (Mulkey RM. and Malenka RC., 1992). LTD involves the activation of serine-threonine protein phosphatase cascades such as the calcium/calmodulin-dependent protein phosphatase calcineurin and protein phosphatase 1 (PP1) (Lisman J., 1989, Mulkey RM., *et al.*, 1993, Mulkey RM., *et al.*, 1994) which in turn have an effect on AMPA receptor phosphorylation state and internalisation (Carroll RC., et al., 2001). More recently, it has been proposed that additional levels of control over AMPA receptor trafficking, namely the lysosomal/proteasome mediated degradation, implicate apoptotic mechanisms regulated by mitochondrial caspase-3 (Li Z., *et al.*, 2010).

The central molecules involved in the facilitation of synaptic plasticity and function are the ionotropic glutamate receptors (iGluR), such as the AMPA and the NMDA receptors mentioned above. They are classified as members of a superfamily of ligand-gated ion channels, and they bind almost universally glutamate as an endogenous substrate, a process critical for their activation (Dingledine R., *et al.*, 1999, Traynelis SF., *et al.*, 2010). The superfamily is divided into four sub-families, according to specialised agonist binding (Dingledine R., *et al.*, 1999). The α-amino-3-hydroxy-5-methyl-4-isoxazole-propionic acid (AMPA) receptor subfamily is composed of GluA1-4 (Boulter J., *et al.*, 1990, Honore T., *et al.*, 1982). GluK1-5 constitute the Kainate subfamily (Hollman M., *et al.*, 1989, Simon RJ., *et al.*, 1976). The *N*-methyl-d-aspartate (NMDA) subfamily is formed by GluN1, GluN2A-D and GluN3A-B subunits (Kumar KN., *et al.*, 1991). The Delta-iGluR subfamily is composed of GluD1-2 (Lomeli H., *et al.*, 1993). Following transcription of these initial genes, RNA editing as well as alternative splicing give rise to a diverse range of presumably functionally distinct isoforms (Dingledine R., *et al.*, 1999, Traynelis SF., *et al.*, 2010). Their architecture is modular and includes an extracellular portion comprised of an amino-

terminal domain (ATD) followed by an extracellular ligand-binding core (LBC). They also possess a multi-pass transmembrane domain (TMD) and an intracellular C-terminal domain (CTD) (Traynelis SF., *et al.*, 2010). Crystallographic analyses showed that they adopt tetrameric assemblies at the cell surface, and have been very informative with regards to ion channel activation, desensitization and allosteric modulation (Sobolevsky AI., et al., 2009, Clayton A., *et al.*, 2009) (Figure 1.7).

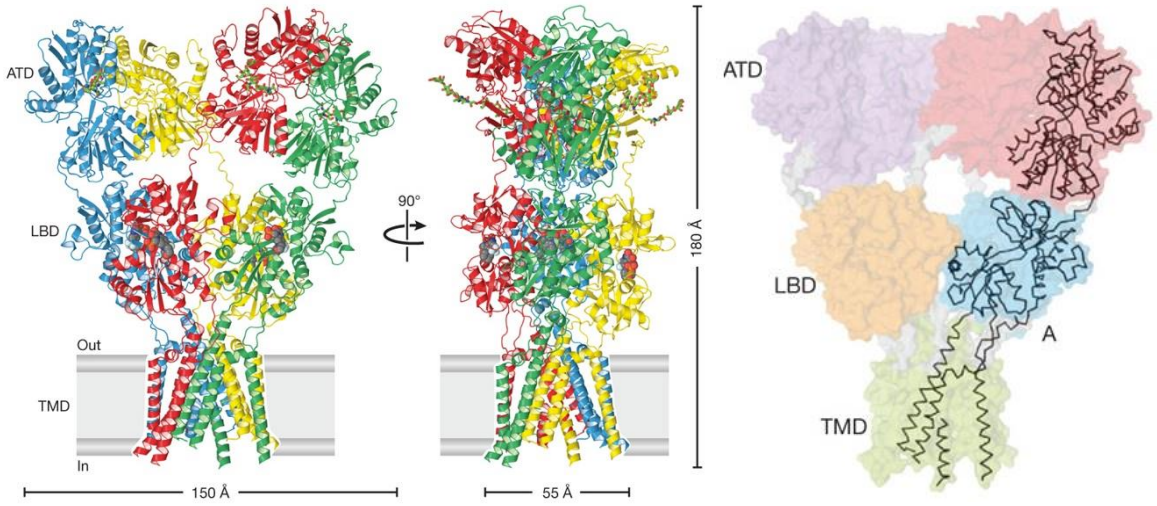


Figure 1.7: Crystal structure of GluA2 receptor (Sobolevsky AI., *et al.*, 2009). In the left a view of the 'broad' face of the receptor is depicted, perpendicular to the overall two-fold axis of molecular symmetry. Each subunit is in a different colour. In the middle a view of the 'narrow' face of the receptor is depicted. In both views competitive antagonist molecules lodged within each the LBD clamshell are shown in space-filling representation. In the right, α-Carbon trace of one of the four subunits is shown overlaid on partially transparent solvent-accessible surface of the entire receptor (images and captions partially adopted from Sobolevsky AI., *et al.*, 2009).

iGluR do not exert their functions in isolation. An intricate network of protein-protein interactions with auxiliary proteins and postsynaptic proteins is critical for their function and trafficking (reviewed in Yan D. and Tomita S., 2011, Sumioka A., 2013). Neuronal pentraxins NP1 and NARP (O'Brien RJ., *et al.*, 1999, Sia GM., *et al.*, 2007) as well as N-cadherin (Saglietti L., *et al.*, 2007) have been shown to bind directly AMPA receptor. Ephrin receptor EphB, acting in coordination with ephrinBs has been proposed to bind

the NR1-containing ATD of the NMDA receptor (Dalva MB., *et al.*, 2000, Grunwald IC., *et al.*, 2001, Takasu MA., *et al.*, 2002). The modulation of heteromerisation of kainate receptors has been demonstrated to be mediated by Neto1 (Copits BA. and Swanson GT., 2012, Fisher JL. and Mott DD., 2013). Neuroligin-1 has been demonstrated to associate with GluN1 containing NMDA receptors (Budreck EC., *et al.*, 2013). GluD2 has been established to participate in trans-synaptic organisation complexes involving Neurexin-1 and Cerebellin-1 (Matsuda K., *et al.*, 2010, Uemura T., *et al.*, 2010).

The neuron doctrine proposed that that synapse acts as a barrier that may or may not permit transmission (Finger S., 2001). It becomes increasingly obvious that a highly regulated and so far obscure network of protein-protein interactions between ligand-regulated receptors, cell surface receptors, secreted factors, adhesion molecules and proteoglycans facilitate control, integrity, specificity and continuity of communication between the pre-synaptic cell to the post-synaptic neuron (Dalva MB., et al., 2007, Shen K. and Scheiffele P., 2010). Our knowledge is amazingly limited with regards to architecture of these higher-order supra-molecular interactions, even though cryo-electron microscopy and cryo-electron tomography developments provide new experimental tools to address this question (Zuber B., *et al.*, 2005, Lucic V., *et al.*, 2005). Grasping the functional consequences of these peri-synaptic higher-order arrangements, in normal and disease states, will become increasingly relevant in the pursuit of novel therapeutics.

A large number of synaptic proteins have been so far isolated, while relevant mutations enriched in cognitive, affective and motor phenotypes have been demonstrated to be critical for more than a hundred neurological conditions (Bayes A., et al., 2011).

Expanding our understanding on the genetics and proteomics of the organisation of these proteins into multimeric complexes will provide a detailed classification system for brain conditions, with regards to their molecular pathogenesis (Grant S., 2012). Synaptic protein components are increasingly demonstrated to participate in complex neurological pathologies such as autism spectrum disorders (ASDs), Altzheimer's disease, various other dementia types as well as schizophrenia (Selkoe DJ., 2002, Sudhof TC., 2008, Clare R., et al., 2010, Penzes P., *et al.*, 2011). In addition, there are a number of autoimmune pathologies where "self" synaptic proteins are being targeted by autoantibodies, providing future opportunities for targeted therapies (Rogers SW., *et al.*, 1994, Vincent A., et al., 2011, Lancaster E., *et al.*, 2011).

1.3 Aim of this thesis

This thesis aims to contribute towards our understanding of the molecular organisation of selected components required for signal transduction events during the lifetime of a neuron as it navigates to reach its targets, forms functional synaptic connections and adjusts the molecular anatomy of these connections in an activity-dependent way. Chapters 3-6 contain biochemical, biophysical and structural studies of distinct systems that participate in specialised signalling mechanisms, as described in the individual introductory fields. In chapter 4, studies on the cell surface complex between Eph receptor A4 and ephrinA5 aim to contribute to understanding on how the modes of higher order arrangements of receptors involved in guidance affect cellular response across the membrane. In chapter 5, a set of studies addressing the proteoglycan regulation of RPTPσ-TrkC *trans*-synaptic interaction aims to contribute to deciphering the

principles of the switch from axonal growth to synapse establishment and formation. In chapter 6, members of the neuronal C1q-like family are studied, with regards to their interactions with potential synaptic partners, and ultimately their roles in the maintenance of synaptic integrity. Chapter 3 is on the enigmatic neuronal Sigma-1 receptor chaperone, which upon cellular stress participates in the modulation of a number of synaptic cell surface and neurotransmitter receptors.

The focus of the thesis is on determining the mechanistic molecular details of the systems in question, in order to propose functional hypotheses. Some of these have been tested in collaboration with other laboratories which approach the same systems from behavioural perspectives.

Chapter 2

Materials and Methods

Chapter 2

Materials and Methods

2.1 Molecular Biology

2.1.1 Expression vectors and complementary DNA

cDNA encoding wild-type full length human sigma non-opioid intracellular receptor 1 was purchased from Mammalian Gene Collection [MGC Project Team, 2004], through its European distributor, SourceBioscience (IMAGE 3529352). cDNA encoding *Mus musculus* proteins C1q-like 1 (Genbank AF095155), C1q-like 2 (Genbank AK144471), C1q-like 3 (Genbank AB044560), Brain-specific angiogenesis receptor 3 (Genbank AY168406) as well as *Rattus norvegicus* ionotropic glutamate receptor (of the kainate subfamily) K2 (ENA Z11715) were kindly provided by Prof. Michisuke Yuzaki (Keio University, Japan).

For expression in mammalian expression systems, a number of different vectors derived from a common pLEXm backbone (Aricescu AR., *et al.*, 2006) were used. Inserts were directionally cloned using mainly restriction sites recognised by AgeI and KpnI, unless otherwise indicated in Appendix B, in the shared multiple cloning site of the pLEXm vector variations in order to create constructs with a kozak sequence and a N-terminal secretion signal at the 5' end. While pHLSec bears a hexahistidine tag at the C-terminus, pHLAvitag3 has a biotin ligase (BirA) recognition site. pHLSec-mVenus fused the insert of interest after KpnI site to a 3C protease cleavage site, a Yellow Fluorescent Protein variant called mVenus (Genbank DQ092360, residues 1-239) and a C-terminal hexahistidine tag. EcoRI enzyme was used instead of AgeI, in the cases where the vector

derived N-terminal secretion signal sequence was to be replaced by the native secretion signal sequence of the protein of interest. For the requirements of this thesis the pLEXm backbone was further modified to give rise to new variations termed as pHL-1D4 and pHL-SBP-1D4. pHL-1D4 vector lacked the N-terminal signal sequence as well as the hexahistidine tag on the C-terminus and the insert was cloned with EcoRI and KpnI restriction enzymes. The hexahistidine tag, present in pHLSec, was replaced by a highly specific antibody epitope: -T-E-T-S-Q-V-A-P-A- (or GAGACCAGCCAGGTGGCCCCTGCA) recognized by Rhodopsin 1D4 antibody (purchased by Flintbox, University of British Columbia). In the case pHL-SBP-1D4 vector the N-terminal signal sequence was substituted with the Streptavidin Binding Peptide (SBP), MDEKTTGWRGGHVVEGLAGELEQLRARLEHHPQGQREP, followed by a Tobacco Etch Virus (TEV) protease recognition site, ENLYFQ|G, at the N-terminus. All vector variations implemented in this thesis are provided in Appendix A.

2.1.2 Construct design and Polymerase Chain reaction

All constructs used in this thesis were designed with information collected by a number of sources: domain boundaries identified in UniprotKB protein sequence database, existing structural data entries in PDB for homologous targets, HHPRED homology detections and structure predictions (Soding J., *et al.*, 2005), disorder predictions from RONN (Yang ZR., *et al*., 2005), theoretical estimates of N-linked glycosylation sites (NetNGlyc 1.0 server) (Gupta R. and Brunak S., 2002) and theoretical secretion signal sequence recognition (SignalP 4.0 server) (Petersen T., et al., 2011). A full list of

constructs used in this thesis, together with corresponding primers used during the PCR amplification step and vectors used during ligation step, is available in Appendix B.

Polymerase Chain reaction (PCR) (Saiki R., *et al.*, 1988) was implemented to amplify a certain DNA segment encoding the target protein. PRC primers were designed using the online bioinformatics tools included in the Java Molecular Biology Directory (www.bioinformatics.org/JaMBW/) and purchased by MWG Operon. Primer would prefereable have T_m values around 60°C and a GC content of around 60%. Relevant restriction sites were introduced during primer design so to enable directional cloning and construct generation. All restriction sites used are highlighted in the full construct list in Appendix B. Usual 50 µl PCR reaction mixes contained: template DNA (1 ng/ µl), forward primer (0.2 pmol/ µl), reverse primer (0.2 pmol/ µl), 0.4 mM excess dNTPs, 1x *Pyrobest*™ buffer (Takara Co.) and 0.1 units of an optimised high-fidelity, thermostable *Pyrobest*™ polymerase (Takara Co.) which is in possession of 3'-5' exonuclease activity. PCR cycles were performed as described below:

1. 96°C for 1 min to fully melt and denature template DNA
2. 94 °C for 50 sec to denature template DNA into single DNA strands
3. 58 °C for 50 sec for primer annealing onto single DNA strands
4. 72 °C for 1-4 min for polymerisation time, according to the length of the target DNA product
5. Repetition of steps 2-4 for 30 times
6. 72 °C for 10 min to ensure that the last polymerisation step has been completed

Site directed mutagenesis was performed with a generic joining PCR approach. For each target mutant, a pair of internal partially overlapping primers, containing altered base pairs coding for the mutation of interest, was designed. During a first PCR round, N-terminal and C-terminal end regions of the mutation would be amplified by using the original forward primer in pair with the internal reverse primer, and the internal forward primer with the original reverse one. The PCR products were then gel purified using the QIAquick gel extraction kit (Qiagen). Equimolar amounts of the two PCR products would be merged as template in another PCR round during the first three cycles of which no primers would be present. That enabled the elongation of the joined/partially overlapped template before adding the original primers for the subsequent amplification of the mutated target DNA segment. The outcomes of PCR reactions were always evaluated by subsequent agarose gel electrophoresis and the PCR products were subsequently purified with the QIAquick PCR Purification kit (Qiagen).

2.1.3 Restriction digests, ligations and transformations

PCR products, after purification, and corresponding vectors were subjected to restriction digests for approximately 2 hours with appropriate restriction endonucleases (New England BioLabs), as highlighted in Appendix B. The correct restriction reaction outcomes were then evaluated by agarose gel electrophoresis, the appropriate bands were excised from the gel with a scalpel and DNA of interest was purified with the Qiaquick gel extraction kit (Qiagen). Ligation reactions were set up using Quick Ligation Kit (New England Biolabs) to final volumes of 20 µl for 10 min at room temperature. The reaction mixtures contained vector and DNA insert of interest to 1:3 ratios. 1.5 µl of ligation

reaction mixtures were added to 50 µl of Library Efficiency DH5a Competent Cells (Invitrogen) and the transformation mixture was incubated on ice for 30 min, prior to a heat shock step at 42 ^{o}C for 45 sec. After a short 2 min incubation on ice, 70 µl of SOC medium (Invitrogen) was added to the cells and they were incubated at 37 ^{o}C for 1 h shaking at 200 rpm. Cells suspensions were then spread on LB-Agar plates prepared to contain 100 µg/ml ampicillin and incubated overnight at 37 ^{o}C. Three colonies were picked under sterile conditions for each construct and were inoculated in 4ml LB cultures in presence of 100 µg/ml ampicillin. The cultures were incubated at 37 ^{o}C overnight shaking at 200 rpm. QIAprep Spin Miniprep Kin (Qiagen) was used to extract and purify plasmid DNA containing constructs of interest. After a digestion test with appropriate restriction enzymes and agarose gel evaluation of construct sizes, clones that contained inserts of expected sizes were sequenced (Source Bioscience). Sequencing primers for constructs presented in this thesis were the following (written 5' to 3'): pHLsec_fwd GCTGGTTGTTGTGCTGTCTCATC, pHLsec_rev CACCAGCCACCACCTTCTGATAG, and pHLsec_Venus_rev GCCCTGGAACAGCACCTCCAG.

2.2 Protein Expression and Purification

2.2.1 Protein expression in mammalian systems

2.2.1.1 Cell lines

Human Embryonic Kidney cell lines, HEK293T or N-acetylglucosaminyltransferase I negative 293S GnTI (HEK293S) cells (Reeves PJ. *et al.*, 2002), were the preferred mammalian system for protein production of proteins presented in this thesis. COS7 monkey fibroblast cells were used for FRET/FLIM experiments (see section 2.9). Cells were maintained in 175 cm^2 flasks (Corning) at 37 ^{o}C in Dulbecco's Modified Eagle's Medium (DMEM high glucose, Sigma), supplemented with 1% v/v Non-essential amino-acids (Gibco), 1% v/v L-glutamine (Gibco) and 10% foetal calf serum (FCS, Sigma) in humidified incubators providing 5% CO_2 (Aricescu AR., *et al.*, 2006). Since most of the protein targets of this thesis were heavily glycosylated, the selection of cell line was instrumental for the sugar trimming during the protein purification process (see section 2.2.3). N-linked glycosylation is an inherent cause of heterogeneity in a protein sample which has to be treated to increase crystal contact formation probability and successful production of well-ordered protein crystals (Chang VT., *et al.*, 2007). To address this issue certain steps were required at the expression stage. When using HEK293T cells to produce protein for crystallisation purposes, 5µM kifunensine (Toronto Research chemicals), a small molecule that stalls the glycosylation process at the $Man_9GlcNAc_2$ stage by inhibiting α-Mannosidase I (Elbein AD., *et al.*, 1990), was added immediately after transfection. In the case of HEK293S cells, no action was required because they have been originally designed to lack GnTI enzyme thus stalling the N-glycan post-translational modification process at an homogenous state of $Man_5GlcNAc_2$ (Reeves PJ. *et al.*, 2002). In

both cases the resulting protein product was subsequently sensitive to Endoglycosidase F1 (EndoF1) treatment resulting to single N-acetylglucosamine residues.

2.2.1.2 Small scale expression

1.5-3x10^5 cells were seeded in 6-well plates (9.5 cm^2, 16.8ml well volume, Corning CellBIND) in DMEM supplemented with 10% FCS and cultured to approximately 90-95% confluence. During transfection, media in each well was exchanged into 1.5 ml of DMEM containing 2% FCS. A mix of two 250 µl serum-free media solutions was prepared to contain 4 µg of plasmid DNA of interest and 8 µl of Lipofectamin 2000 (Invitrogen). The mix was vortexed lightly and incubated for 20 min at room temperature, before being added to each well. 72 hours after transfection the cells and media were collected and prepared for expression analysis by Western Blot.

Collected cell media were subjected to centrifugation (20 min at 5000 rpm on table top Centrifuge 5425, Eppendorf) to remove cell debris and cells were re-suspended in 1ml of PBS. 20 µl aliquots were mixed with 20 µl loading buffer and boiled in 100^oC for 10 min. 8 µl per sample was used for loading sodium dodecyl sulphate polyacrylamide gels (NuPAGE Bis-Tris Precast Gels, Invitrogen) and size-depended separation of proteins took place with electrophoresis (SDS-PAGE). A mix of 0.5 µl of Benchmark hexa-histidine tagged 10 µl of Benchmark pre-stained protein ladders (Invitrogen) was also loaded on every gel, to serve as indications of efficient transfer and as a set of molecular weight indicators based on which the molecular of target protein could be estimated by comparison. After electrophoresis, the proteins in the gel were transferred, by wet

transfer, to activated nitrocellulose membrane (Amersham Hybond ECL Nitrocellulose Membrane, GE Healthcare) for 1 hour at 30V at room temperature using NuPAGE transfer buffer (Invitrogen) and a XCell II Blot module (Invitrogen). The membrane was blocked in 5% milk in 1x PBS, 0.01% Tween20 for 2 min, before probing with a monoclonal mouse PentaHis primary antibody (1:1000, Qiagen) for 30 min at room temperature. The membrane was then probed with a goat anti-mouse peroxidase-coupled secondary antibody (1:2000, Sigma-Aldrich). The membrane was then thoroughly washed with 1x PBS, 0.01% Tween20 (6 washes of 150ml for 10 min at room temperature), before performing the peroxidase reaction for 1 min (Amersham ECL Advance Western Blotting Detection Kit, GE Healthcare) and film development (Hyperfilm ECL, GE Healthcare).

2.2.1.3 Large scale expression

Cell cultures from 175 cm^2 flasks were seeded into expanded surface polystyrene roller bottles (850 cm^2, 2520 ml volume, CELLMASTER, Greiner Bio-One) in presence of 230 ml of DMEM supplemented with 10% FCS, until they reached approximate 90% confluency (3-4 days).

During transfection, media in each bottle was exchanged into 230 ml of DMEM containing 2% FCS. A mix of two 50 ml serum-free media solutions was prepared to contain chloroform- extracted 0.5 mg of plasmid DNA of interest (previously purified with Endotoxin-Free Plasmid Giga Kit, Qiagen) and a 1:2 ratio of polyethylenimine (PEI) per roller bottle (Aricescu AR., *et al.*, 2006). The mix was added to the bottle after 10 min

incubation at room temperature. Roller bottles were then incubated 5-12 days at 37 ^{o}C, in incubators providing 5% CO_2.

In the case of secreted soluble target proteins, cell media was harvested by centrifugation at 5000g for 30 min, on Avanti J-30 centrifuges (Beckman Coulter Inc.) using JLA-8.1000 rotors. The media were then filtrated with Steritop filter units (Millipore) and stored at 4 ^{o}C.

In the case of membrane embedded target protein, cells and media were separated, by centrifugation at 5000 g for 30 min, on Avanti J-30 centrifuges (Beckman Coulter Inc.) using JLA-8.1000 rotors. Cells were collected and washed in 1x PBS before being flash-frozen in liquid N_2 and stored to -80 ^{o}C until further use. Excreted vesicles consisting of the target membrane protein were collected by centrifugation of harvested media at 9500 rpm, 4 ^{o}C using Allegra X-22R centrifuges and C0650 conical rotors (Beckman Coulter Inc.).

2.2.2 Detergent screening for solubilisation of membrane-embedded proteins

A critical step in the purification and subsequent structural analysis of target proteins embedded in membrane (see chapter 4) is their solubilisation. Extracting membrane proteins from membranes involves identifying the appropriate solubilisation mixture of potential detergents, lipids and/or other molecular agents which increases the optimal extraction efficiency and stability of the resulting protein-containing aqueous solution suitable for purification and further *in vitro* analysis (Mus-Veteaux I., 2009). The evaluation of solubilisation can be an iterative and high-throughput process, until the

optimal conditions for an efficient re-constitution of the membrane protein into detergent/lipidic micelles are determined. HEK293T cells, transfected with a mono-Venus fusion of sigma1 receptor, were harvested and various detergents were tested for extraction directly from cell pellets (Table 2.1). Solubilisation took place while incubating the solution for 1h at 4^{o}C on a rotor. Supernatant containing the solubilized material was separated after spinning for 30 min at 55000 rpm (4^{o}C) in an Ultima TL Ultracentrifuge with a TLA-100.2 fixed angle rotor (Beckman Coulter Inc.). Supernatants occurring after solubilisation with different detergents were subjected to Fluorescent Size Exclusion Chromatography (FSEC) on a High Pressure Liquid Chromatography (HPLC) setup (Kawate T. and Gouaux E., 2006) using a Prominence Ultra-Fast Liquid Chromatograph (Shimadzu Corp.). Solubilisation efficiency was additionally monitored by Western blotting. After rigorous testing, the solubilisation buffer for Sigma-1 receptor produced in HEK293 cells, was optimised to include 50 mM Hepes pH 7.5, 500 mM NaCl, 0.2% w/v Cholesteryl Hemisuccinate (re-suspended in 2% w/v n-Octyl-β-D-Glucopyranoside), 1 mM haloperidol (re-suspended in 1% v/v DMSO), a protease inhibitors' cocktail (Sigma Aldrich) and 2% w/v n-Octyl-β-D-Glucopyranoside (Affymetrix).

Name	Molecular Weight	CMC mM (%)	Aggregation Number	Company
Lysofos-choline 12	351.5	1.5 (0.047%)	50-60	Anatrace (Affymetrix)
Dodecyldimethylamineoxide (LDAO)	229.41	1 (0.023%)	76	Anatrace (Affymetrix)
N-dodecyl-b-d-maltoside (DDM)	510.6	0.17 (0.0087%)	78-149	Anatrace (Affymetrix)
N-decyl-b-d-maltoside (DM)	482.6	1.8 (0.087%)	69	Anatrace (Affymetrix)
N-nonyl-b-d-glucoside	306.4	6.5 (0.2%)	-	Anatrace (Affymetrix)
Tetraethylene glycol monooctyl ether (C8E4)	306.45	8 (0.25%)	82	Anatrace (Affymetrix)
Pentaethylene glycol monodecyl ether (C10E5)	378.55	0.81 (0.031%)	73	Anatrace (Affymetrix)
Cymal-4	494.5	2.4 (0.12%)	66	Anatrace (Affymetrix)
N-octyl-b-d-glucoside (b-OG)	292.4	18 (0.53%)	27-78	Anatrace (Affymetrix)
CHAPS	614.9	8 (0.49%)	10	Anatrace (Affymetrix)
Triton X-100	647	0.23 (0.015%)	-	Anatrace (Affymetrix)
Tween 20	1228	0.059 (0.0072%)	-	Anatrace (Affymetrix)
Sodium dodecyl sulfate (SDS)	288.38	2.6 (0.075%)	62-101	Anatrace (Affymetrix)
Digitonin	1229.3	0.087	60-70	Sigma Aldrich

Table 2.1: List of detergents implemented in solubilisation trials

2.2.3 Large-scale solubilisation of membrane-embedded proteins

After identifying the appropriate conditions for solubilisation in high-throughput FSEC experiments, large-scale trials were performed. Harvested cells as well as excreted vesicles fractions from 12 Roller Bottle expression preparations were thawed from -80 ^{o}C (see section 2.2.1.3), re-suspended and gently homogenised using glass homogenisers in 50 mM Hepes pH 7.5, 500 mM NaCl, protease inhibitors (Sigma Aldrich). Cells were disrupted at 30.000 psi using a Cell Disruptor (Constant Systems). The resulting solution containing disrupted cells was supplemented with 0.2% w/v Cholesteryl Hemisuccinate (re-suspended in 2% w/v n-Octyl-β-D-Glucopyranoside), 1 mM haloperidol (re-suspended

in 1% v/v DMSO) and 2% w/v n-Octyl-β-D-Glucopyranoside (Affymetrix). Solubilisation took place while incubating the solution for 1h at 4°C on a rotor. Supernatant containing the solubilized material was separated after spinning for 1.5 hours at 28.000 rpm (4°C) in an Optima L-90K Ultracentrifuge with a SW28 swinging bucket rotor (Beckman Coulter Inc.).

2.2.4 Protein purification

2.2.4.1 Sample preparation

Collected and filtered media containing recombinant proteins (see section 2.2.1.3) were subjected to buffer exchange prior purification. A QuixStand™ Benchtop system (Watson Marlow, GE Healthcare) was utilised and the final buffer was 20 mM Hepes pH 7.5, 300 mM NaCl.

2.2.4.2 Immobilised-Metal Affinity Chromatography

Pre-packed HisTrap (GE Healthcare) columns were pre-equilibrated in 20 mM Hepes pH 7.5, 300 mM NaCl, 5 mM Imidazol before being used for loading buffer exchanged conditioned media. A peristaltic pump was used for loading at a flow rate of 4-5 ml/min, at room temperature. An AKTA FPLC system (GE Healthcare) was used for analytical elution after HisTrap loading. The two pumps of the FPLC system were pre-equilibrated with the following buffers: 20 mM Hepes pH 7.5, 300 mM NaCl, 5 mM Imidazol for pump A and 20 mM Hepes pH 7.5, 300 mM NaCl, 500 mM Imidazol for pump B. The loaded HisTrap column was washed with 40 ml of 20 mM Hepes pH 7.5, 300 mM NaCl, 5 mM

Imidazol. Most of media impurities were then removed by application of an 5-50 mM imidazol gradient over the course of 50 ml from the HisTrap column. An additional imidazol gradient 50-500 mM Imidazol enabled the determination of appropriate imidazole concentration required to eventually elute the protein of interest. Protein fractions were analysed by SDS-PAGE. In the case of RPTPσ/TrkC proteins (see Chapter 6), the buffer components 20 mM Hepes pH 7.5, 300 mM NaCl, that were stated in this section, were replaced by component 1X Phosphate Buffered Saline (PBS).

2.2.4.3 Antibody Affinity Chromatography

In the case of Sigma-1 receptor purification, 1D4-affinity resin was generated by covalently attaching pure 1D4 antibody to CNBr-activated Sepharose beads [GE Healthcare]. The volume ratio for the binding was 30 ml of solubilisation supernatant (see section 2.2.3) versus 2 ml of 1D4 bead volume. Binding took place while incubating the mix solution for 3-4h at 4^{o}C on a rotor. Beads were then washed with 2x10 column volumes. Protein was eluted in fractions with 500 µM 1D4 peptide [AnaSpec, Inc.] after 45 min rotor incubation per fraction. The eluted protein was concentrated and loaded on a Superdex S200 HR10/30 gel filtration column (GE Healthcare). The protein purity was monitored during purification procedures, by SDS-PAGE and Western blotting using 1D4, as well as antiHis primary antibodies (Sigma Aldrich).

2.2.4.4 Analytical Size Exclusion Chromatography

Fractions containing the target protein of interest were concentrated, using appropriate molecular weight cut-off centrifugal filters. When applicable, N-glycans attached on proteins of interest where treated with EndoF1 (Grueninger L., *et al.*, 1996, Aricescu AR., *et al.*, 2006), for 2-12 hours at room temperature. Typically 5 µl of enzyme from a stock of 2.5 mg/ml in 10 mM Tris pH 7.5, 200 mM NaCl, 20% glycerol, would be added to 100 µl of protein solution. Samples were then injected onto a Superdex S200 HR10/30 (or HiLoad HR16/60) or a Superose 6 10/300 GL gel filtration column (GE Healthcare), previously equilibrated in 10 mM Hepes pH 7.5, 150 mM NaCl, 2 mM $CaCl_2$, 2 mM $MgCl_2$ or (in the case of Sigma-1 receptor) 50 mM Hepes pH 7.5, 250 mM NaCl, 30 µM Haloperidol, 0.01% w/V CHS, 1% w/v N-octyl-b-d-glucoside. Protein fractions were analysed by SDS-PAGE and selected fraction were recovered and concentrated for subsequent use. Final samples after purification were targeted to be of at least 95% purity.

2.3 Crystallisation

2.3.1 Crystallisation screens

Crystallisation trials were prepared in a high-throughput fashion using Cartesian Technologies robots (Walter TS., *et al.*, 2006). Sitting drop vapour diffusion crystallisation setups (Rupp B., 2010) were performed in 96-well Greiner plates, placing 100 nl protein solution plus 100 nl reservoir solution against 90 µl of each potential crystallisation condition in the reservoir. Plates were sealed, deposited in TAP Homebase Storage Vaults kept at 20 ^{o}C and 4 ^{o}C, and imaged periodically with a Veeco visualisation system (Mayo

CJ., *et al.*, 2005). The PCT Pre-Crystallisation Test Kit (Hampton Research) was implemented for every new protein sample before crystallisation screening, in order to determine an appropriate concentration for crystallisation screening and get an insight on sample homogeneity. The screens used for protein samples of this thesis, are presented in Table 2.2.

Masterblock	Commercial Screen	Wells	Manufacturer
Block 1	Crystal Screen	A1-D12	Hampton Research
	Crystal Screen 2	E1-H12	Hampton Research
Block 2	Wizard 1	A1-D12	Emerald Biosystems
	Wizard 2	E1-H12	Emerald Biosystems
Block 3	PEG/Ion Screen	A1-D12	Hampton Research
	PEG 6000 Grid Screen	E1-F12	Hampton Research
	Ammonium Sulphate Grid Screen	G1-H12	Hampton Research
Block 4	Natrix Screen	A1-D12	Hampton Research
	Crystal Screen Cryo	E1-H12	Hampton Research
Block 5	PEG/LiCl Grid Screen	A1-B12	Hampton Research
	NaCl Grid Screen	C1-D12	Hampton Research
	MPD Grid Screen	E1-F12	Hampton Research
	Quik Screen	G1-H12	Hampton Research
Index	Index Screen	A1-H12	Hampton Research
SaltRX	SaltRX Screen	A1-H12	Hampton Research
PACT	PACT Premier	A1-H12	Molecular Dimensions
PEGRx	PEGRx Screen	A1-H12	Hampton Research
Morpheus	Morpheus Screen	A1-H12	Molecular Dimensions
PGA	PGA Screen	A1-H12	Molecular Dimensions
Proplex	Proplex Screen	A1-H12	Molecular Dimensions

Table 2.2: Crystallisation Screens used for screening new protein constructs

2.3.2 Optimisation of crystallisation hits

Protein crystals that were found to diffract X-rays poorly, or to be multiple were optimised in order to collect X-ray data of higher quality and resolution. A number of different strategies were followed. The first was to use a wide range of compounds included in the Additive Screen and the Silver Bullets, Silver Bullets Bio screens (Hampton Research) as additives in the original crystallisation condition. 1:1:1 drops were prepared to contain equal 100 nl volumes of protein solution, reservoir solution and a corresponding additive solution. Alternatively, a manual setup involving the dilution of the reservoir crystallisation condition was prepared, while the different drop ratios of protein solution to reservoir solution were applied at the same time. Such setups were prepared in three rows where the reservoir solution was diluted from 100% to 67% in 3% steps along the row, while each row had a certain drop ratio (1:1, 2:1, 1:2 protein to reservoir solution). Final crystallisation conditions for protein structures presented in this thesis are presented in Table 2.3.

Construct	Space Group	Protein Concentration	Crystallisation Condition	Temp (°C)	Freezing Procedure
Human EphA4 full ectodomain + Human EphrinA5 RBD (native)	H32	9.3 mg/ml	0.05 M sodium cacodylate pH 6, 0.01 M $MgSO_4$, 1.8 M Li_2SO_4, 4% benzamidine-HCl	20	0.25% v/v glycerol
Human EphA4 full ectodomain + Human EphrinA5 RBD (methylated)	H32	9.8 mg/ml	0.1 M Tris-HCl pH 8.5, 8% w/v polyethylene glycol 8000	4	0.25% v/v glycerol
Mouse C1ql1-c1q	H3	5.46 mg/ml	0.02 M Nickel(II) chloride hexahydrate, 0.02 M Magnesium chloride hexahydrate, 0.02 M Cadmium chloride hydrate, 0.1 M Sodium acetate trihydrate pH 4.5, 24% w/v polyethylene glycol monomethyl ether 2000	20	0.25% ethylene glycol
Mouse C1ql3-c1q	H3	5.37 mg/ml	0.02 M Nickel(II) chloride hexahydrate, 0.02 M Magnesium chloride hexahydrate, 0.02 M Cadmium chloride hydrate, 0.1 M Sodium acetate trihydrate pH 4.5, 24% w/v polyethylene glycol monomethyl ether 2000	20	0.25% ethylene glycol
Mouse C1ql3-c1q	$P2_12_12_1$	1.9 mg/ml *(in presence of GluK2-ATD)*	0.1 M Citrate pH 5, 2.4 M Ammonium Sulfate	20	0.25% ethylene glycol
Chicken RPTPs Ig123 + Chicken TrkC-LRR-Ig1	P1	5.5 mg/ml	0.1 M Hepes pH 7, 5% w/v Tacsimate, 10% w/v Polyethylene glycol monomethyl ether 5000	20	0.25% ethylene glycol

Table 2.3: Crystallisation and Freezing conditions for crystal structures presented in this thesis

2.3.3 Reductive lysine-methylation

To optimize crystal diffraction properties lysine methylation was pursued using established protocols (Walter T.S. *et al.*, 2006). Flexible, surface-exposed lysine residues have an increased entropy and can be a limiting factor to the formation of a well-ordered lattice. Therefore, a chemical modification was induced as a result of which the side chains of solvent-accessible lysine residues were dimethylated. Protein samples,

previously purified by size exclusion chromatography in presence of 20 mM Hepes pH 7.5, 150 mM NaCl, were concentrated to 0.05-0.1 mg/ml and mixed with 20 mM borane dimethylamine complex (the reducing agent), and 40 mM of formaldehyde (the methyl source reagent). The reaction was incubated for 2 hours at 4 ^{o}C before doubling the concentration of both reagents and further incubation for another 2 hours. 10 mM of the reducing agent was then added before the reaction was left to continue overnight at 4 ^{o}C. The methylation reaction was then quenched with 100 mM Tris pH 7.5, before concentration and injection to a Superdex 200 column previously equilibrated with 20 mM Tris pH 7.5, 150 mM NaCl. Protein purity was checked with SDS-PAGE and selected fractions were concentrated for immediate crystallisation trials.

2.4 X-ray data collection

2.4.1 Cryo-protection crystal preparation and mounting

Cryo-protecting protein crystals and collecting X-ray data under cryogenic conditions (100 ^{o}K) has been shown to be necessary in order to decrease the extent of crystal deterioration by radiation damage (Garman EF., 2010). Crystal containing drops that did not already contain some reagent that could act as cryo-protectant, were diluted with 25% glycerol or ethylene glycol stocks prepared in crystallisation solution. Then crystals were fished from the mother liquor solution, mounted in round Cryo-loops or Litho-loops (Molecular Dimensions) of matching size, promptly submerged into liquid nitrogen and stored until data collection.

2.4.2 Data collection

Crystal X-ray diffraction experiments were performed on several beamlines of Diamond Light Source (Oxford, UK), or European Synchrotron Radiation Facility (ESRF, Grenoble, France), (see crystallographic tables in relevant chapters). Prior data collection, an appropriate data collection strategy was determined for each crystal, with the special feature of Mosflm program (Battye TGG., *et al.*, 2011). After finding the optimum orientation, and required extent of rotation for a complete data set, data collection was performed with a 0.1^{o} oscillation angle step until 180^{o} of crystal rotation were collected via charged-coupled device (CCD) (Phillips WC., *et al.*, 2000) or Pilatus detectors (Bronninmann C., *et al.*, 2003). Data collection took place in cryogenic conditions (100 ^{o}K).

2.5 Structure solution

2.5.1 Data processing

Processing of X-ray diffraction data involves a number of steps. First, images are indexed to assign Miller indices (*hkl)* to each recorded reflection and determine the dimensions of the cell crystal unit cell, as well as the point group. Then, the intensities of the reflections are measured during integration. Finally intensities across data collected from the same or many crystals are merged and scaled in a single dataset. Data processing was performed using Mosflm (Leslie AGW. And Powell H., 2007) or xia2 (Winter G., 2010) data processing suites. Data processing statistics, which are available in relevant results Chapters, were monitored in order to assess data quality and determine the optimum resolution limit. Program TRUNCATE (French S. and Wilson K., 1978) of the CCP4 software

suite (Collaborative Computation Project, Number 4, 1994) was used to calculate structure factor amplitudes from intensities of reflections, given that the square of the structure factor amplitude is proportional to the intensity of the reflection (Formula C1, Appendix C).

2.5.2 Structure determination & Refinement

Structure factor phases for every structure factor determined evade detection during the X-ray diffraction experiment. The so-called "phase problem" in protein crystallography has been addressed in a number of ways (reviewed in Rupp B., 2010), in order to enable the calculation of electron density maps. All structures presented in this thesis have been solved with the method of molecular replacement (Rossman MG. and Blow DM., 1962) using program PHASER (McCoy AJ., *et al.*, 2005), included in CCP4 suite. After an approximate estimation of the number of protein molecules in the asymmetric unit, by the use of MATTHEWS_COEF program (Matthews BW., 1968) in CCP4 suite, an appropriate molecular replacement model was selected. Molecular replacement models were edited to have potential waters or ligands removed. During a phaser run, a rotation search (Formula C2, Appendix C) is performed with the model against the experimental data. The top scoring outcomes of the rotation function are then used for a translation test (Formula C3, Appendix C).. The packing of the top scoring outcomes of the translation function is evaluated for clashes between symmetrically-related molecules and the ones approved are subjected to rigid-body refinement prior to the output generation. PHASER output includes solution statistics, repositioned models according to the rotation & translation results and preliminary electron density maps. Molecular

Replacement solution was considered successful, after an evaluation based on all three criteria:

- *Log-likelihood gain (LLG)* values. LLG represents a quantitative measure of how well the molecular replacement model fits the experimental data in comparison with a fit to the same atoms, but randomly distributed. LLG is calculated as the difference between the model derived log-likelihood and the log-likelihood computed from a Wilson distribution (a probability distribution for structure factors derived from a crystal of known chemical composition, but unknown atomic positional information). LLG values for an accepted solution should be positive and gradually increase during the molecular replacement procedure.
- *Z-score* values. Z-score is a standard statistical score that measures the difference between the LLG of the model minus the LLG of a random set of rotation and translation functions, expressed in units of root mean square deviation of a random set of LLG values from the mean. For an accepted solution, Z-score should be ~7-8 or greater.
- Electron density maps qualitative evaluation. It is the most meaningful criterion for accepting a molecular replacement solution. During the evaluation, the occurrence of extra features on the density maps that were not derived from the model, reinforces the likelihood that the solution is correct.

Accepted molecular replacement solutions were then subjected to iterative rounds of model building with program Coot (Emsley P. and Cowtan K., 2004) and restrained refinement with programs REFMAC (Mushudov GN., *et al.*, 1997) and/or PHENIX (Adams PD., *et al.*, 2010). During this process, a number of variable parameters of the model

were manually adjusted (model building) and the fit of the resulting models with observed structure factors was evaluated (refinement), while taking into account geometrical constraints, atomic positions, non-crystallographic symmetry and B-factor distributions. A number of factors were closely monitored during the iterative rounds of refinement, including the values of R_{work} (Formula C4, Appendix C). and R_{free} (Formula C5, Appendix C). values and the quality of the resulting map. R_{free} is calculated from randomly selected 5% of the reflections included in the refinement, whereas the remaining 95% is represented by R_{work}. The gap between these R factors is a quantitative measure of bias introduction and differences lower than 4-5% should be expected during the course of the refinement. As refinement progresses and the maps improved, the R values should drop accordingly. Solvent molecules, ligands or ion molecules were added manually while building the models in Coot.

2.5.3 Structure validation & analysis

Refined models were submitted to MolProbity (Davis IW., *et al.*, 2007), for ultimate validation and evaluation of their stereochemical properties. Molprobity generates qualitative data information on steric problems within the protein molecules, as well as on the H-bond and van der Waals contacts in molecular interfaces. One of the main features, is the generation of Ramachandran plots, on which the polypeptide backbone angle between the N and the Cα (ϕ) and the angle between the Cα and the C=O is carbon (ψ) are plotted against each other. These plots enable the visualisation of model's residues with incorrect stereochemical attributes, known as "outliers", which can then be geometrically adjusted. LSQ algorithms, derived from original LSQMAN (Kleywegt GJ. and

Jones TA, 1997) and incorporated in Coot interface, were implemented to superpose protein domains and compare their overall architecture. Amino acid conse rvation analysis was performed with ConSURF server (Ashkenazy H., *et al.,* 2010). Protein electrostatics analyses were performed with APBS (Baker NA., *et al.*, 2010), while all figures were rendered in PYMOL (DeLano Scientific LLC).

2.6 Surface Plasmon Resonance (SPR)

2.6.1 Sample preparation & SPR binding assays

Surface plasmon resonance experiments were performed on Biacore T100 and T200 instruments (GE Healthcare), using CM5 BIAcore sensor chips (Biacore). The chips are comprised of four channels of carboxymethylated dextran attached to a gold surface. All experiments were performed at room temperature in a running buffer typically consisting of 10 mM Hepes pH 7.5, 150 mM NaCl, 2 mM $CaCl_2$, 2 mM $MgCl_2$, 0.005% v/v Tween 20. Analytes expressed in HEK293 cells were purified in the running buffer for SPR, according to procedures described in sections 2.2.1.3, 2.2.4.1, 2.2.4.2 and 2.2.4.4. The chip was primed on the SPR running buffer and normalised with the BIAnormalising solution (Biacore). The sensor surfaces of the four channels were then activated with a 1:1 mix of 100 mM NHS (N-hydroxy succinimide) and 400 mM EDC (1-ethyl-3-(3-dimethylaminopropyl) carbodiimide reagents (BIAcore amine coupling kit) for 900 sec at a flow rate of 5 µl /min. The application of EDC pre-activates the cabroxymethylated dextran groups, which upon reaction with NHS forms succinimide ester moieties that are highly reactive towards available $–NH_2$ groups. A streptavidin solution of 0.5 mg/ml in 10

mM sodium acetate pH4 was then applied to chip and 8000-10000 response units were attached on each flow cell, by amine coupling. 1M Ethanolamine pH 8.5 is eventually injected on the chip for 900 sec at 5 µl /min, to deactivate any remaining free succinimide groups and removed non coupled streptavidin.

The essence of coupling streptavidin on the chip lies on its femtomolar affinity (K_d = 1 x 10^{-14} M) to biotin. By injecting biotinilated proteins (ligands) of interest on the chip, they are immediately attached irreversibly and stably on the streptavidin coupled surface of the chip, while due to the high specificity of the interaction low and relatively crude amounts of ligands are required. The biotinilated proteins were injected gradually, in order to achieve 1000-2000 response units of bound protein, while one of the four channels of the chip remained free of biotinilated ligands and acted as the provider of a reference response level, which was subtracted from response readings of every other channel during data analysis.

In the cases where binding events between ligands and analytes were observed, appropriate analyte injection parameters were established for every experiment, through a number of test injections. During these test injections the flow rate, the injection time (association time), the dissociation time and potential regeneration strategies were varied in order to reach a binding equilibrium and be able to remove all the bound analyte from the chip surface before the initialised ligand can go through another binding cycle reproducibly. The optimised protocols for every experiment are provided in the relevant result sections.

Affinity estimates were derived from equilibrium experiments after duplicate sets of repeated protocols were run, while injecting serial N-fold dilutions of analytes (where N is

given for every individual experiment in the relevant result section). After data analysis, the binding curve was plotted as a function of bound analyte (response units of equilibrium states for each serial dilution injection) versus analyte concentration.

2.6.2 Data analysis

BIAcore evaluation software, Scrubber2 (BioLogic Software) and SigmaPlot (SyStat Software Inc) were used for data analysis. Sensograms recorded during sets of equilibrium experimental cycles were treated with subtraction of response recordings from the reference channel A binding curve was fitted assuming a 1:1 ligand to analyte binding mode, where applicable. Kd (equilibrium binding constant) and Bmax (maximum amount of analyte bound on surface) were obtained from the binding curve (Formula C6, Appendix C).

2.7 Multi-Angle Laser Light Scattering (MALLS)

MALLS experiments were performed, with the assistance of Dr Geoff Sutton, on a Wyatt MALLS system (Wyatt Technologies). Purified protein samples (see section 2.2.4) were concentrated to 0.5-1 mg/ml in MALLS running buffer (10 mM Hepes pH 7.5, 150 mM NaCl, 2 mM $CaCl_2$, 2 mM $MgCl_2$) and injected on a 30 ml Superdex 200 HR 10/30 column (GE Healthcare) attached to an Agilent chromatography system. Size exclusion chromatography elution was monitored with Optilab rEX Refractive Index detector and a Dawn Helios II Multi-Angle Light Scattering detector, for changes on the refractive index

and light scattering. Recorded data were analysed using the ASTRA V program suite (Wyatt Technology).

2.8 Fluorescence Microscopy

Live-cell imaging was performed using a wide-field inverted Nikon TE2000U fluorescence microscope, while images were captured with an attached black and wide Hamamatsu video camera (IP Labs). Recorded images were further processed with ImageJ software (http://rsbweb.nih.gov/ij/).

2.9 CPM Thermostability Assay

Fluorescent thermal stability assays were performed for Sigma-1 receptor, according to established methodology (Alexandrov AI., *et al.* 2008), to evaluate the contribution of various chemical solution conditions in overall protein stability. Thiol specific fluorochrome N-[4-(7-diethylamino-4-methyl-3coumarinyl)phenyl]maleimide (CPM) was acquired from Invitrogen (Cat no D-346), was dissolved in DMSO (Sigma Aldrich) at C_F = 4 mg/ml and stored in -80^{o}C. On the day of the experiment, it was thawed for 5 min at room temperature and was diluted to 0.1 mg/ml in 50 mM Hepes pH 7.5, 250 mM NaCl, 0.01% w/v Cholesteryl Hemisuccinate, 30 μM haloperidol, 1% w/v n-Octyl-β-D-Glucopyranoside, which was termed as the assay control buffer. Dye was used immediately after thwing and was constantly protected from light to avoid photobleaching.

For every CPM experiment of a total volume of 60 µl, 10 µg of Sigma-1 in control buffer was mixed with 0.1 mg/ml CPM and topped up with the buffer of interest. CPM experiments were prepared in parallel, in 96 well plates, to test the contribution of a variety of buffers in protein stability. Buffers tested included 100 mM NDSB256 (Affymetrix), 10% v/v glycerol (Sigma Aldrich), 6M guanidine (Sigma Aldrich), 50 mM Sodium Acetate pH 4.5 (Sigma Aldrich), 50mM Citrate pH 5.5 (Sigma Aldrich), 50 mM Cacodylate pH 6.5 (Sigma Aldrich), 50 mM Tris pH 8.5 (Sigma Aldrich), 12 mM $CaCl_2$ (Sigma Aldrich),, 35 mM $MgCl_2$ (Sigma Aldrich),, 12 mM $ZnCl_2$ (Sigma Aldrich). A Stratagene Mx3005P qPCR (Agilent Technologies) was used to heat the 96 well plate in a controlled way in temperatures ranging from 24.8 to 96.7^{o}C. The excitation wavelength was set at 387 nm, while the emission wavelength was set at 463 nm. Output fluorescence read data were analysed in Microsoft Excel and the first derivative curve (Formula C7, Appendix C) was calculated to identify melting temperatures.

Chapter 3

Preliminary structural studies of neuronal Sigma-1 receptor

Chapter 3

Preliminary structural studies of neuronal Sigma-1 receptor

3.1 Summary

Sigma-1 receptor (S1R), located primarily at the endoplasmic reticulum (ER), is a chaperone integral membrane protein that is involved in intracellular calcium homeostasis and has been targeted for drug development in schizophrenia, clinical depression, cardiovascular function, drug abuse and cancer. Recently, S1R has been reported to bind with and modulate the downstream signaling of dopamine receptor-1, while other reports implicate it in the regulation of ion channels and receptors of the cell surface. Work presented in this chapter refers to the successful expression, solubilisation from cell membranes, stabilization, large scale purification and characterization of the active full length human S1R. It thus paves the way for the crystallographic analysis of this enigmatic molecule, and in long term for an improved understanding of its functional and clinical significance.

3.2 Introduction

3.2.1 Intracellular signalling activity by non-opioid sigma-1 receptor

Sigma-1 receptor (S1R), which was originally mistakenly characterized as an opioid receptor subtype (Su TP. *et al*, 1988), is widely distributed in the central nervous system. It is primarily expressed in the cerebral cortex, the hippocampus, and cerebellum Purkinje cells (Weismann AD., *et al.*, 1988, Alonso G., *et al.* 2000, Seth P. *et al.*, 2001). The N-terminus of S1R bears a double arginine endoplasmic reticulum retention signal (Hanner M., *et al.*, 1996) and electron microscopy studies showed that it was mostly found in neuronal perikarya and dendrites, mainly associated with cytoplasmic, nuclear or endoplasmic reticulum membranes (Alonso G., *et al.* 2000). It has to be noted that it was also particularly enriched on the post-synapse. S1R is now established as a non-opioid endoplasmic-reticulum residing receptor, which acts as a ligand-regulated molecular chaperone (Hayashi T. and Su TP., 2007) and has been implicated in diseases of the central nervous system including amnesia, pain, schizophrenia, clinical depression, Alzheimer's disease, stroke, neuropathic pain and addiction (to cocaine, methamphetamine, and alcohol) (Su TP. *et al*, 2010, Guitard X. et al., 2004). S1R has active roles in endoplasmic-reticulum - mitochondrion signaling and affects calcium Ca^{2+} homeostasis and cellular bioenergetics (Hayashi T. and Su TP., 2007), while it has been demonstrated that upon activation it can translocate from the ER membranes to the cell or nuclear membranes (figure 3.1) (Morin-Surun MP., et al. 1999, Hayashi T. et al., 2000). S1R appears to be a mediator of cellular responses regulated by several voltage-gated (K^+, Na^+) and ligand-gated (IP3 receptor, small conductance Ca^{+2} activated K^+ channels, NMDA channels) ion channels, GPCRs (μ-opioid, muscarinic acetylcholine, and dopamine 1

receptors), and kinases (tyrosine kinase receptor B, phospholipase C, and src kinase), by direct interactions (Kourrich S. *et al.*, 2012).

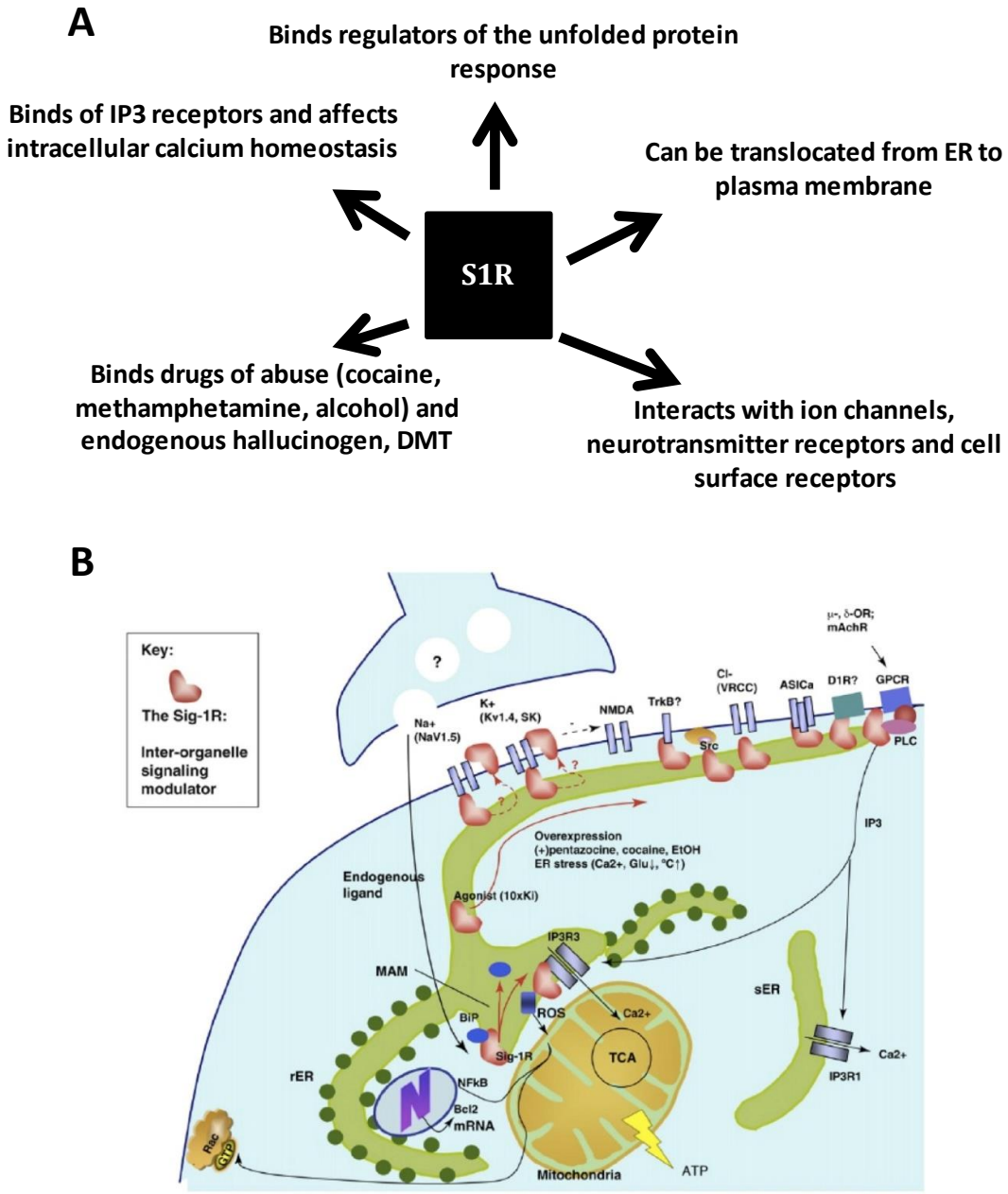


Figure 3.1: Sigma-1 receptor functional profile. **(A)** Schematic representation of Sigma-1 receptor functional highlights. **(B)** Sigma-1 receptor as an inter-organelle regulator. Modes of chaperone action, upon stress induction, are highlighted for a wide variety of molecules on the plasma membrane. (Adopted from Su TP. et al., 2010)

The specific ER subdomains, where S1R is enriched, have been demonstrated to be the points of contact between ER and mitochondria called Mitochondria Associated Membranes (MAMs) (Hayashi T. and Su TP., 2007). MAMs regulate cellular bioenergetics

(Walter L., Hajnoczky G., 2005, Csordas G. *et al.*, 2006) while they have originally been implicated in phospholipid metabolism (Vance JE., 1990). S1R has been previously shown to be a component of a tripartite complex with ankyrin-B and inositol-1,4,5-triphosphate receptor (IP3R) calcium channel (Hayashi T. & Su TP., 2001), offering grounds for a functional role of S1R on calcium release into the mitochondira and subsequent upregulation of the citric acid cycle. It was also reported that S1R agonists would lead to the displacement of ankyrin from the complex, and to the potentiation of bradykinin-induced increase in cytocolic free calcium concentration (Hayashi T. & Su TP., 2001). More recently, it has been demonstrated that S1R binds directly, in a calcium-depended manner, to the HSP70 chaperone protein Bip/GRP78/HSPA5 (Bip) (Hayashi T. and Su. TP., 2007), a key protein regulator of the unfolded protein response (UPR) (Pincus D., *et al.*, 2010). It has thus been deduced that upon S1R activation by agonists, S1R dissociates from Bip, becomes free to chaperone IP3R3 and activate antioxidant response elements (Pal A., *et al.*, 2012), and even to translocate to the plasma membrane where a number of potential target protein responses are modulated (Su TP., *et al.*, 2009).

3.2.2 Sigma-1 receptor pharmacology

S1R pharmacology is complex, since it directly binds, and is regulated by, a large number of small molecules (figure 3.2) (reviewed by Maurice T. and Su TP. 2009). They can be endogenous ligands such as progesterone (affinity in the nM range) (Su TP., *et al.*, 1988), testosterone, pregnenolone sulfate, deoxycorticosterone (affinity in the µM range) (McCann DJ. and Su TP., 1991, Maurice T., *et al.* 1996) and the potent hallucinogen N,N-dimethyltryptamine (DMT) (Fontanilla D., *et al.*, 2009). Apart from binding

benzomorphan, antidepressant and antipsychotic compounds, such as imipramine, fluovoxamine, pimozide, chlorpromazine, dextromethorphan and haloperidol with high affinities (Hayashi T., *et al.*, 2004), other exogeneous S1R binding compounds include opioids (such as (+)-pentazocine), antihistamines, phencyclidine-like compounds, b-adrenergic receptor ligands and psychostimulants, such as cocaine, methamphetamine (Nguyen EC., *et al.*, 2005) and DMT. Cocaine, in particular, has been shown to bind S1R at physiologically relevant concentrations (Sharkey J. *et al.*, 1988, Chen Y., *et al.*, 2007 and others). More recently there have been indications of a heterooligomerisation between sigma-1 and dopamine-1 receptors (D1R) in transfected cells as well as knock-out mice, where cocaine potentiated D1R downstream signaling (Navarro *et al.*, PNAS 2010). Other reports showed that treatment of NG-108 cells with cocaine, caused the translocation of sigma-1 receptors from the ER to the neurite processes as well as to the nucleus. Sigma-1 was also detected in extracellular vesicles after treating cells with cocaine, raising the possibility of it exhibiting a chaperone action outside the cell surface after exocytosis (Hayashi T., *et al.*, 2003).

Compound	Sigma-1 activity	Sigma-1 affinity (IC_{50})
DTG	Agonist	45
(+)-3-PPP	Agonist	48
(+)-SKF-10,047	Agonist	97
(+)-Pentazocine	Agonist	5.8
Haloperidol	Antagonist	2.3
Igmesine	Agonist	39
Sertraline	Agonist	6.8
BD-737	Agonist	2 (Ki)
BD-1047	Antagonist	36
Rimcazole	Antagonist	520
BMY-14,802	Antagonist	66
DuP734	Antagonist	10 (Ki)
E-5842	Antagonist	5
MS-377	Antagonist	73 (Ki)
NE-100	Antagonist	1.6
OPC-14523	Agonist	47
Panamesine	Antagonist	6
PRE-084	Agonist	44
SA4503	Agonist	17
SR31742A	Antagonist	5.3

Figure 3.2: Activity of certain sigma-1 ligands (Partially adopted from Guitard X. *et al.*, 2004)

3.2.3 Functional implications of cholesterol binding in sigma-1 receptor signalling

S1Rs have been found to localise specifically at ER subdomains that are rich in cholesterol (such as the MAMs), according to immunocytochemistry findings (Hayashi TS. *et al.*, 2003, Hayashi TS. *et al.*, 2004). Filipin staining, a histochemical approach to visualize the cellular localization of cholesterol, proved the enrichment of MAMs in cholesterol and the co-localisation with S1R (Hayashi TS. *et al.*, 2003). Membrane lipid rafts have been previously introduced as potential scaffolds for a higher order organization for signal transduction, by enabling residing protein-protein interactions (Simons K. *et al.*, 1997, Simons K. *et al.*, 2000). Stimulated trophic factor receptors have been shown to dimerise and translocate in or out of rafts to facilitate downstream signaling events (Simons K. *et al.*, 1997, Simons K. *et al.*, 2000). When S1Rs, residing at raft regions of the ER, are ligand-activated, they have been shown to transport to non-raft membranes, while certain agonists have been shown to shift S1R *in vitro*, in sucrose gradient centrifugation preparations, from TritonX100-insoluble to soluble fractions (Hayashi TS. *et al.*, 2003, Palmer CP. *et al*, 2007). It seems plausible that agonists actively compete with cholesterol for binding to sigma-1 receptors (Palmer CP. *et al*, 2007), and promote the escape of the receptor from the MAM (Hayashi TS. *et al.*, 2003, Hayashi TS. *et al.*, 2004). Conversely, the ligand-free or antagonist-bound S1R seems structurally prone to associate with cholesterol and the corresponding enriched membrane environment in the ER. A crystallographic analysis of either of the two states would tremendously increase our understanding of the receptor physiology.

3.2.4 Structural features of Sigma-1 receptor

Information on S1R topology is extremely limited, since its amino acid sequence bears no homology with any other mammalian protein, and only shares 30% sequence identity with yeast sterol isomerase C8-C7 (Moebius FF. *et al.*, 1997). More intriguingly, the mammalian sterol isomerase C8-C7 has also been cloned (Hanner M., *et al.*, 1995), and it is similar neither to the yeast homolog nor to the S1R. It has to also be noted that S1R do not exhibit sterol isomerase activity (Hanner M., *et al.*, 1996).

Human S1R has 223 amino acids, and is a 25 kDa integral membrane protein consisting of a single (Mei J. and Pasternak GW., 2000) or two transmembrane domains (Aydar E., et al. 2002) (figure 3.3.A) (residues 11-29, 80-100), according to hydropathy analyses. There is an additional less hydrophobic region (residues 180-203) which is thought to be membrane associated and contains two predicted cholesterol recognition motifs (figure 3.3.B). More recently, a novel C-terminally truncated splice variant of S1R has been reported to interfere with the function of the full length protein during ER stress conditions, and to promote apoptosis (Shioda N., *et al.*, 2012). Residues involved in drug binding are Cys94, Ser99, Tyr103, Asp126, and Glu172 with variations in sensitivity between agonists and antagonists (Yamamoto H., *et al.*, 1999, Seth P., *et al.*, 2001, Chen Y., *et al.*, 2007), whereas residues implicated in sterol or cocaine binding include Tyr173, Asp188 and Tyr206 (Su TP. and Hayashi T., 2010) within the cholesterol binding region. The implication of S1R in many diseases, makes it a potentially promising target for therapeutic intervention. An atomic insight of sigma-1 receptor alone and/or in presence of various ligands, would provide clues towards understanding its complex physiology, as well as its roles in pathological states.

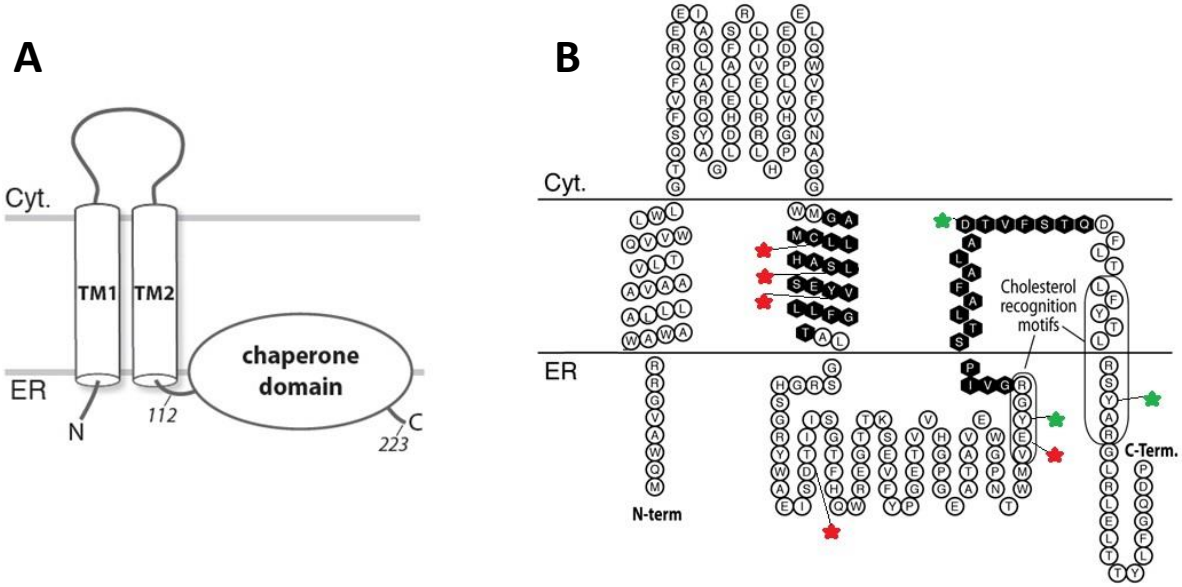


Figure 3.3: Sigma-1 receptor topology embedded in ER membrane. **(A)** Schematic representation (Adopted from Ortega-Roldan JL., *et al.*, 2013). (**B**) Cartoon snake-plot representation. Residues reported to be involved in drug binding (Cys94, Ser99, Tyr103, Asp126, and Glu172) are highlighted with red stars, while residues putatively involved in sterol or cocaine binding are highlighted with green stars.

3.3 Aims

The main research aim was to generate structural information on Sigma-1 receptor initially in complex with an antagonist. Results related to a number of parameters that were optimized before crystallographic analysis, including expression technology optimization, screening methodologies as well as small and large scale purification, are provided in this chapter. Crystallisation efforts are currently ongoing.

3.4 Expression and screening for optimal membrane extraction

Full length constructs of the human Sigma-1 receptor (Uniprot: Q99720) were designed as listed in Appendix B. The cloning strategy and procedures used to create these constructs are described in detail in section 2.1.2. Small scale expression trials in HEK293 cells and subsequent western blot analysis (see section 2.2.1.2) indicated expression of these constructs in the cell pellet fractions (figure 3.4.A). Constructs C-terminally tagged with monoVenus fluorescent protein, were used to transfect HEK293T cells and imaged with a fluorescent microscope (figure 3.4.B), as described in section 2.9.

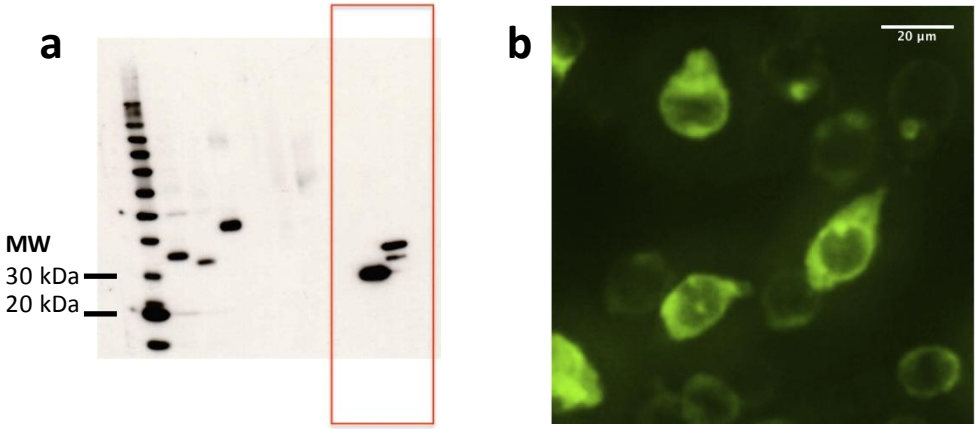


Figure 3.4: (**A**). Anti1D4 Western Blot. In the red box, protein products from sigma1::pHL-1D4, and sigma1::pHL-SBP-1D4 transfections are indicated. (**B**). Fluorescence image of HEK293T cells transfected with sigma1::pHL-monoVenus plasmids (40X magnification).

Sigma-1 receptor extraction from 293T membranes was tested on a small and high-throughput scale by Fluorescence Size Exclusion Chromatography as described in section 2.2.2. The relative elution profiles in the presence of various detergents, enabled the gradual optimization of the solubilisation reagents and conditions (figure 3.5). The addition of a cholesterol soluble analog (cholesteryl hemisuccinate, Sigma Aldrich) (figures 3.6.A, 3.7) and the use of antagonists proved to optimise substantially the elution

profiles in the presence of most detergents. High affinity Sigma1 receptor antagonists were selected, fenpropimorph (0.05 nM) and haloperidol (3.1 nM), and were also introduced to the screening process (figures 3.6.B,C, 3.7).

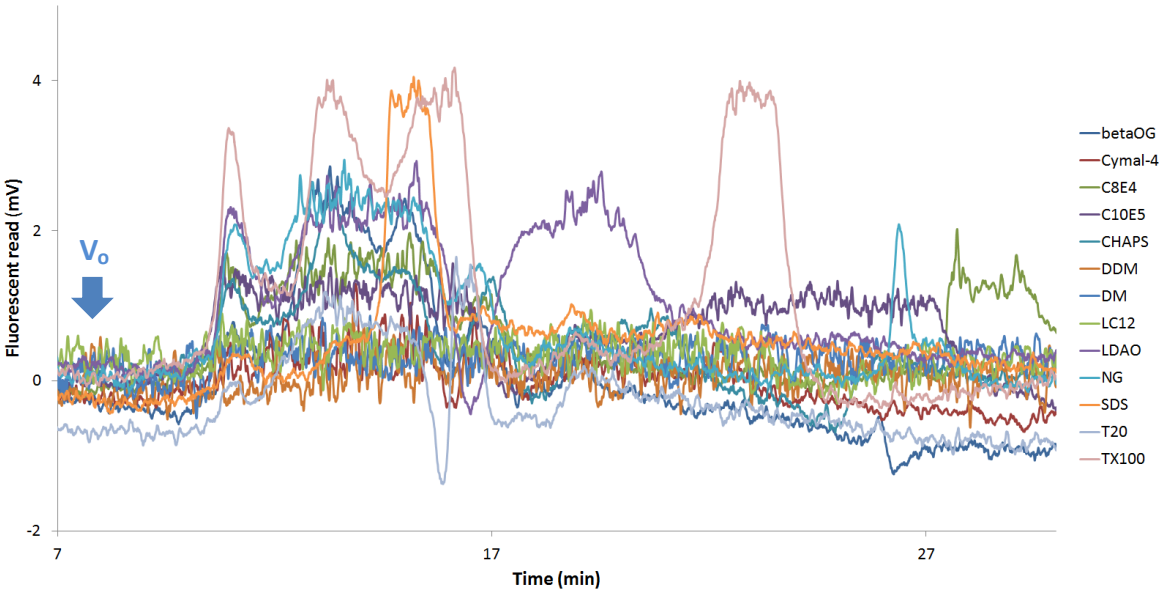


Figure 3.5: Fluorescence Size Exclusion Chromatography (FSEC) elution profiles of Sigma-1 receptor solubilisation screen, in 13 different detergents.

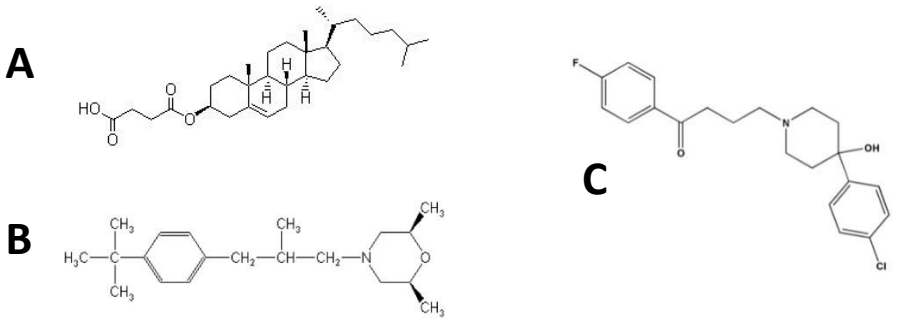
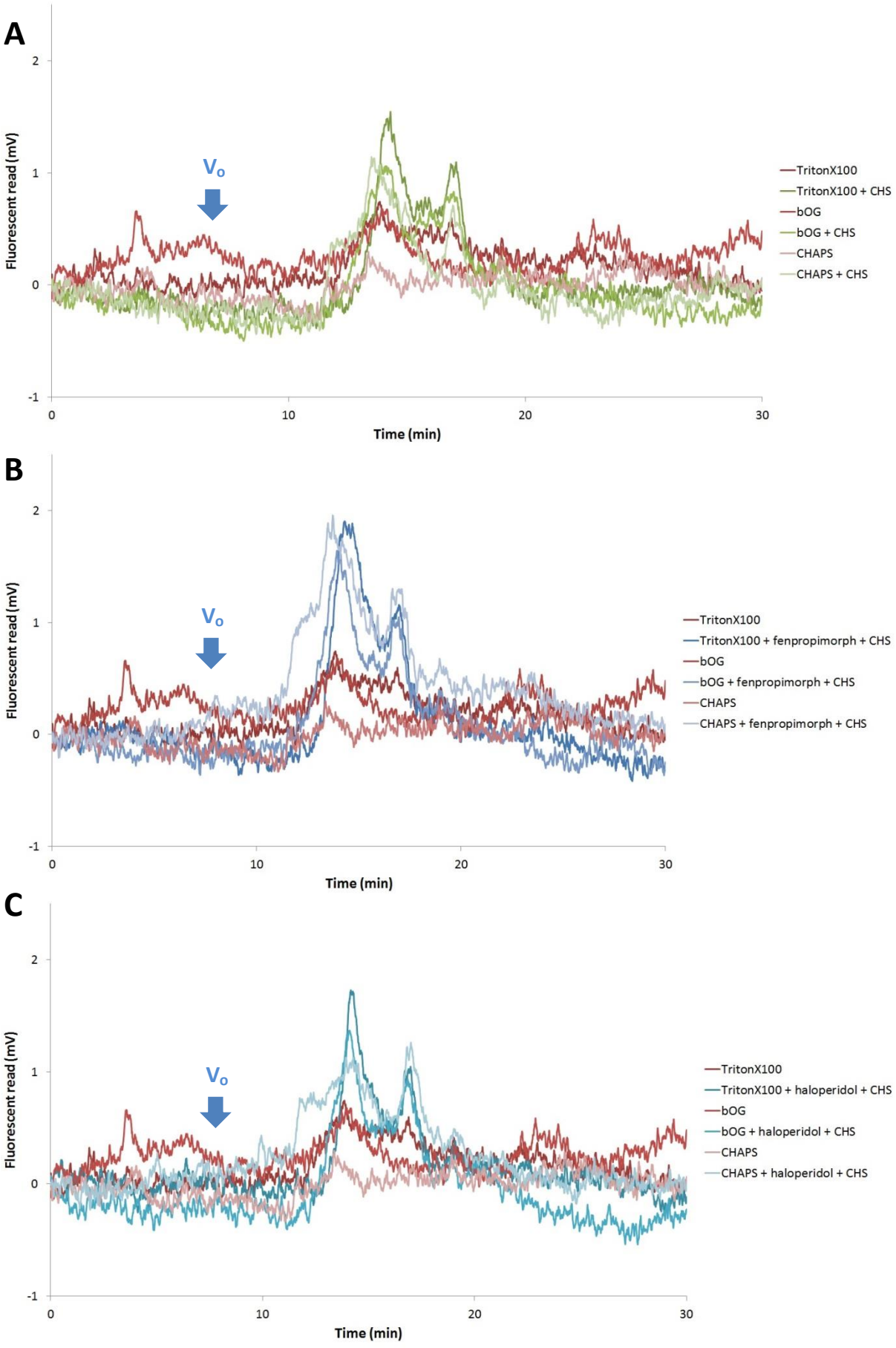


Figure 3.6: Compound introduced to optimize S1R solubilisation efficiency.**(A)** Cholesteryl Hemisuccinate. **(B,C)** Sigma1-receptor antagonists, **(B)** fenpropimorph (0.05 nM), **(C)** Haloperidol (3.1 nM) (Hayashi T., *et al.*, 2004).


A
Fluorescent read (mV)
Time (min)
Vo
TritonX100
TritonX100 + CHS
bOG
bOG + CHS
CHAPS
CHAPS + CHS
B
Fluorescent read (mV)
Time (min)
Vo
TritonX100
TritonX100 + fenpropimorph + CHS
bOG
bOG + fenpropimorph + CHS
CHAPS
CHAPS + fenpropimorph + CHS
C
Fluorescent read (mV)
Time (min)
Vo
TritonX100
TritonX100 + haloperidol + CHS
bOG
bOG + haloperidol + CHS
CHAPS
CHAPS + haloperidol + CHS

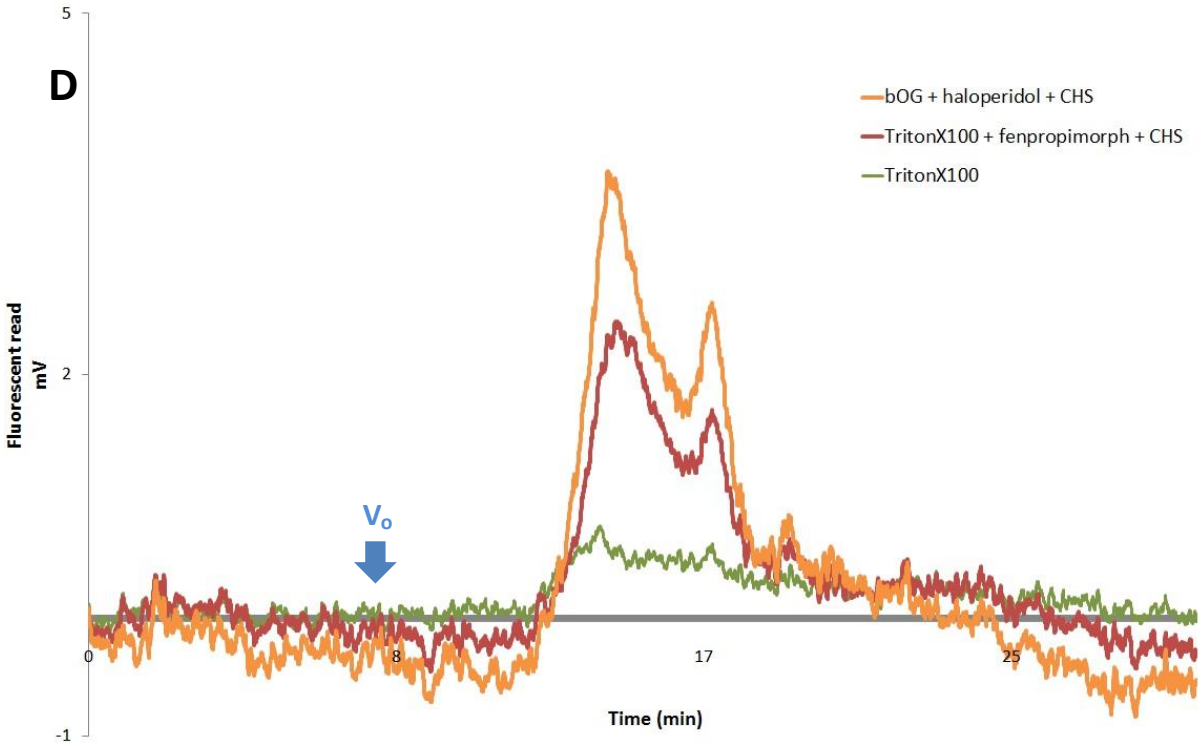


Figure 3.7: Optimisation of FSEC solubilisation screening of Sigma-1 receptor in presence of v n-Octyl-β-D-Glucoside, CHAPS and TritonX100. **(A)** (previous page) FSEC elution profiles of Sigma-1 receptor, solubilized in presence of 0.2% v/v CHS. **(B)** (previous page) FSEC elution profiles of Sigma-1 receptor, solubilized in presence of 0.2% v/v CHS and 1 mM fenpropimorph. **(C)** (previous page) FSEC elution profiles of Sigma-1 receptor, solubilized in presence of 0.2% v/v CHS and 1 mM haloperidol. **(D)** Overlay of select FSEC elution profiles of Sigma-1 receptor, solubilized in presence of CHS and antagonists.

Extraction efficiency appeared to improve in the presence of 0.2% v/v cholesterol, any of the two antagonists and one of the following detergents: 2% w/v n-Octyl-β-D-Glucoside (Anatrace, Affymetrix Inc.), 2% w/v CHAPS (Anatrace, Affymetrix Inc.), 1% v/v Triton X-100 (Anatrace, Affymetrix Inc.) (Figure 3.7). n-Octyl-β-D-Glucoside was the final detergent of choice due to the significantly smaller micelle size, compared to CHAPS and Triton-X100 (see Chapter 2, Table 2.1).

3.5 Purification of full-length sigma-1 receptor

Sigma-1::pHL-1D4 constructs were used for small scale purification trials which eventually enabled the tuning of the large scale 1D4 antibody affinity purification step, performed as described in section 2.2.4.3. The solubilisation supernatant had to be mixed with 1D4 beads in the optimum ratio that would maximize the elution efficiency, as shown in western blot analyses in figure 3.8. The final volume ratio between solubilsation supernatant and 1D4-beads used for large scale purifications was 1:15.

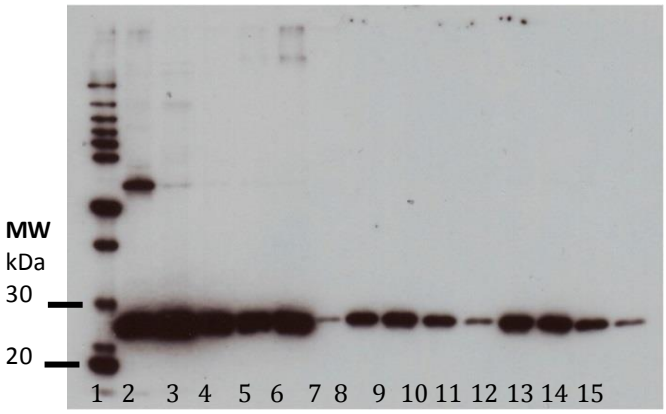


Figure 3.8: 1D4/AntiHis western blotting of small scale 1D4 purification elutions. Here are illustrated 2 different protein to 1D4 ratios (**Sample A, Sample B**). **(1)** Marker. (**2)** Ultracentrifugation pellet, after solubilisation. **(3)** Ultracentrifugation supernatant after solubilisation. **(4)** Aliquot of supernatant in absence of 1D4 beads. **(5)** Aliquot of supernatant in presence of 1:30 volume of 1D4 beads (**Sample A**). **(6)** Aliquot of supernatant in presence of 1:15 volume of 1D4 beads (**Sample B**). **(7)** Flow-through of Sample A. **(8-10)** Sample A elutions. **(11)** Flow-through of Sample B. **(12-15)** Sample B elutions.

1D4 column elutions were pooled and concentrated using a 50 kDa concentrator (Vivascience, Sigma-Aldrich Inc.). In terms of concentrating the protein, the choice of detergent was of critical importance, since no large scale purification or any evidence on the functional oligomeric state of the receptor has been reported so far. Sigma-1 receptor could adopt a high oligomeric organization in solution, based on the Superose 6 elution profile (Figures 3.9). A peak at ~16 ml indicates a mono-disperse and homogeneous

sigma1 receptor sample (Figure 3.10), at a pure enough state for crystallization trials. Sigma1 receptor, in n-Octyl-β-D-Glucoside micelles in presence of cholesterol, appears to match the retention time needed by aldolase (Mr 158 kDa) to elute in Superose 6. So Sigma-1 receptor could adopt trimeric or tetrameric organisations in solution, according to this preliminary and rough estimation. A sharp void peak at 8.31 ml could well be attributed to lipid of detergent aggregates.

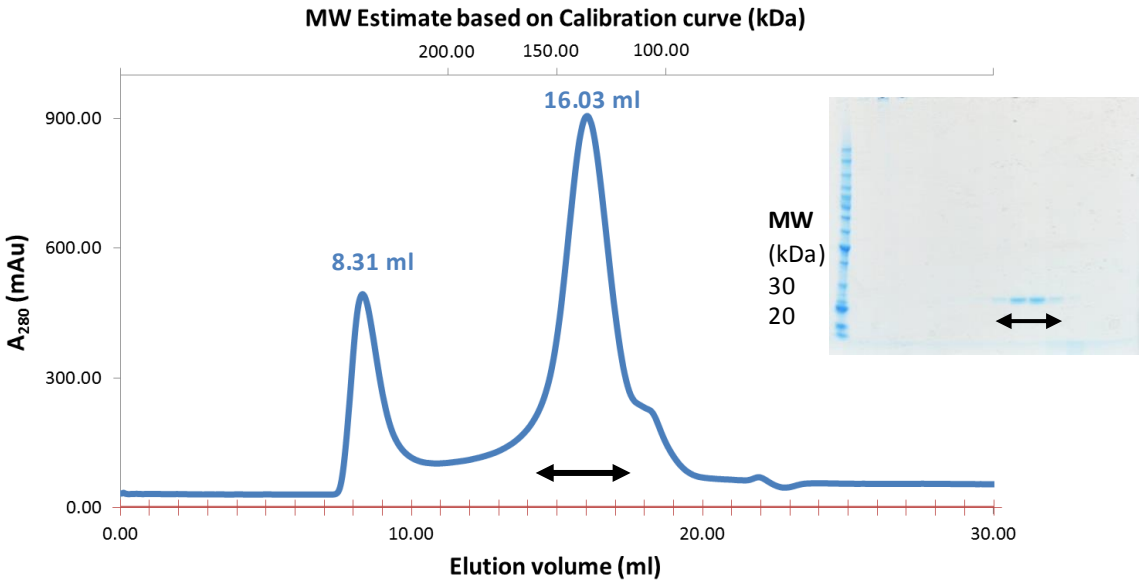


Figure 3.9: Sigma-1 receptor Superose 6 elution profile and SDS-PAGE. Arrows indicate the fractions of the peak spanning from 15 to 18 ml V_e.

Eluted sigma1 receptor was concentrated and the final yield was found to be **~2 mg** from ~17gr of 293T cells (collected from 24 Roller bottles), while preliminary negative staining highlighted the mono-dispersity of the sample (Figure 3.10). Traditional high through-put sitting drop crystallization as well as cubic-phase crystallization methodologies and UV imaging are currently being implemented in order to pursue the sigma-1 receptor structure.

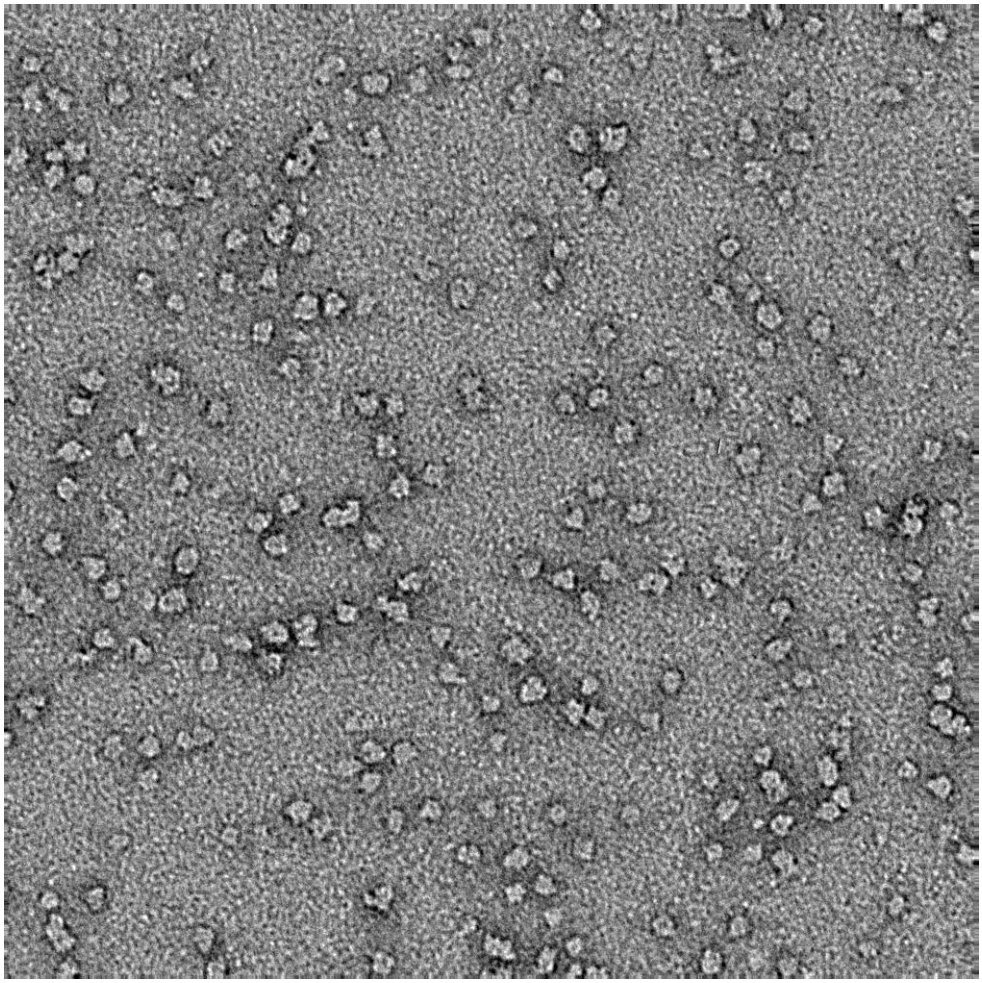


Figure 3.10: Negative staining of Sigma-1 receptor Superose 6 peak fractions (figure 4.9) (experiment performed by collaboration with Dr.Terunawa Nakagawa, UCSD, USA).

3.6 Stability optimisation of Sigma-1 receptor detergent micelle

Sigma-1 receptor bears a single cysteine (Figure 3.11) in one of its transmembrane regions and thus was an excellent target for the CPM thermofluor assay, originally described by the Stevens laboratory (Scripps Institute, USA) (Alexandrov AI., et al., 2008). The assay was performed as described in section 2.11. Gradual unfolding was induced by slow increase of temperature, in presence of the CPM dye and a number of buffers of interest, which were being tested for an effect on the overall protein stability. As unfolding took place, the transmembrane core of the protein became exposed to the solvent and Cys94 became available for chemical modification with the diffusible fluorescent probe.

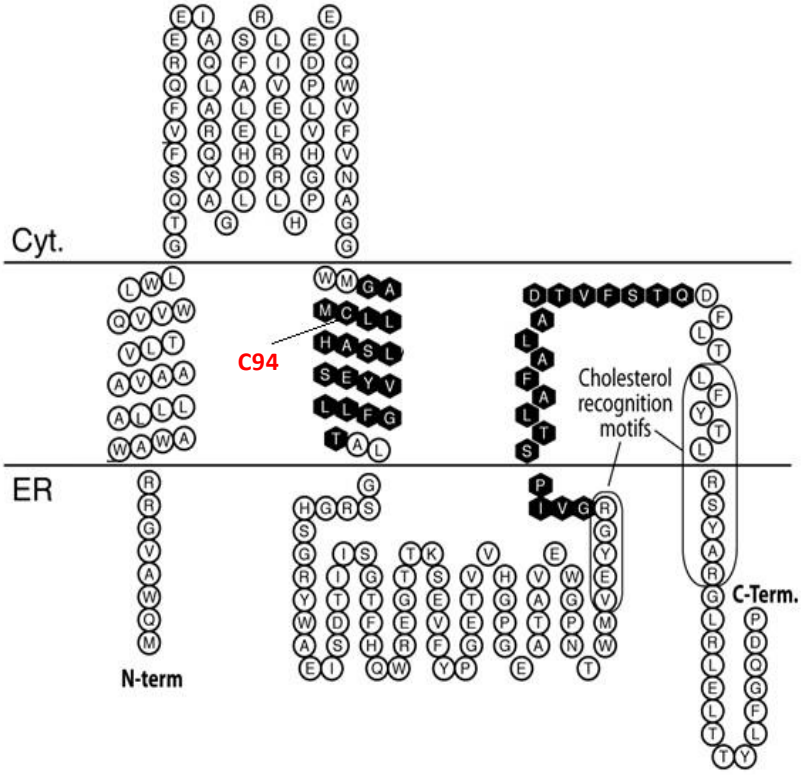


Figure 3.11: Schematic snake plot representation of Sigma-1 receptor sequence on the ER membrane. Cysteine 94 and cholesterol binding motifs of the protein are highlighted.

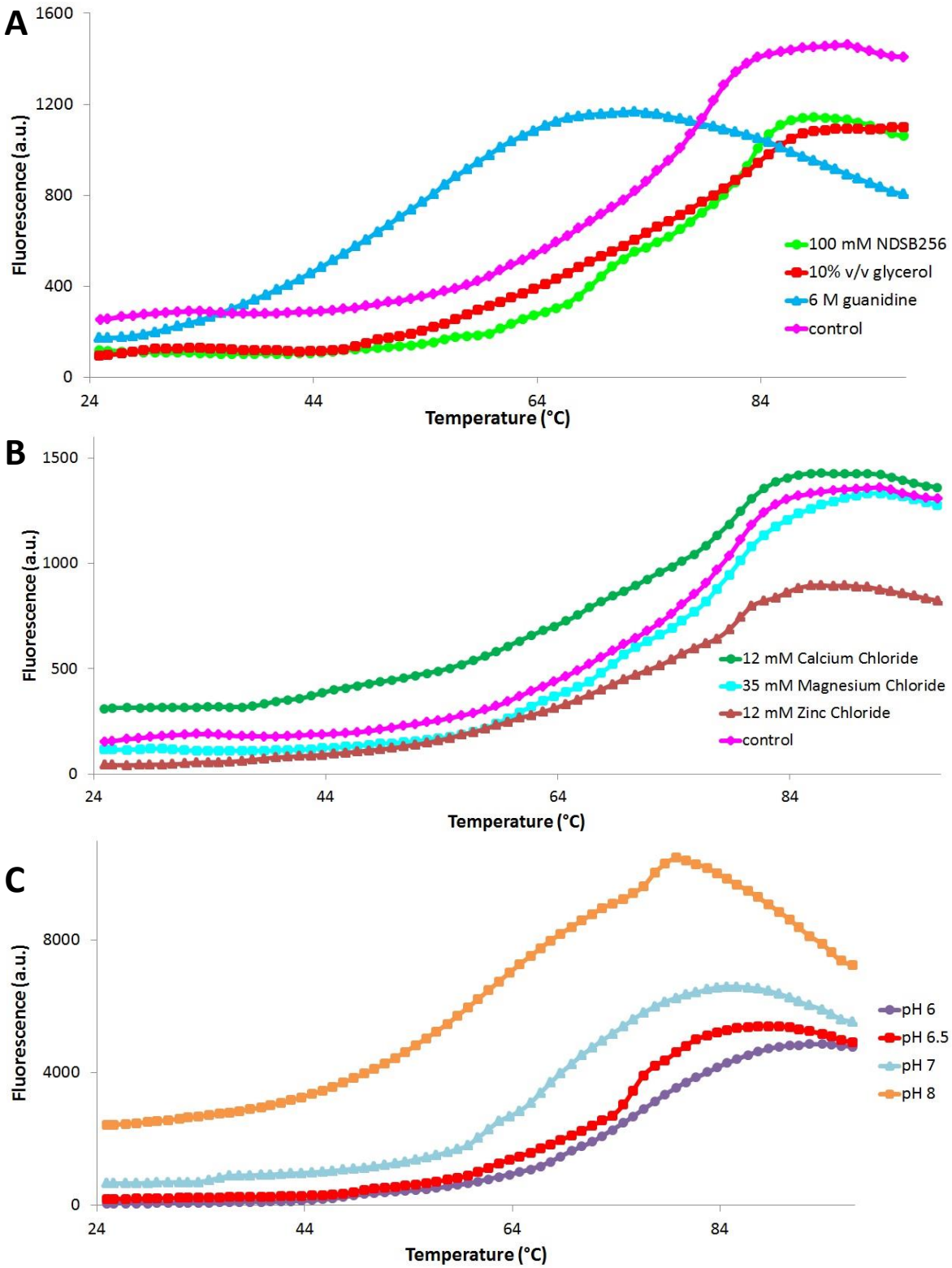


Figure 3.12: Solubilised Sigma-1 receptor melting curves, in presence of 0.1 mg/ml CPM. Control buffer was 50 mM Hepes pH 7.5, 250 mM NaCl, 0.01% w/v Cholesteryl Hemisuccinate, 30 µM haloperidol, 1% w/v n-Octyl-β-D-Glucopyranoside. **(A)** Respresentative curves in presence of specific buffers (NDSB256, Guanidine, Glycerol). **(B)** Respresentative curves in presence of metal ions ($CaCl_2$, $MgCl_2$, $ZnCl_2$). **(C)** Respresentative curves in presence of buffers with variable pH values (pH6, pH 6.5, pH 7, pH 8).

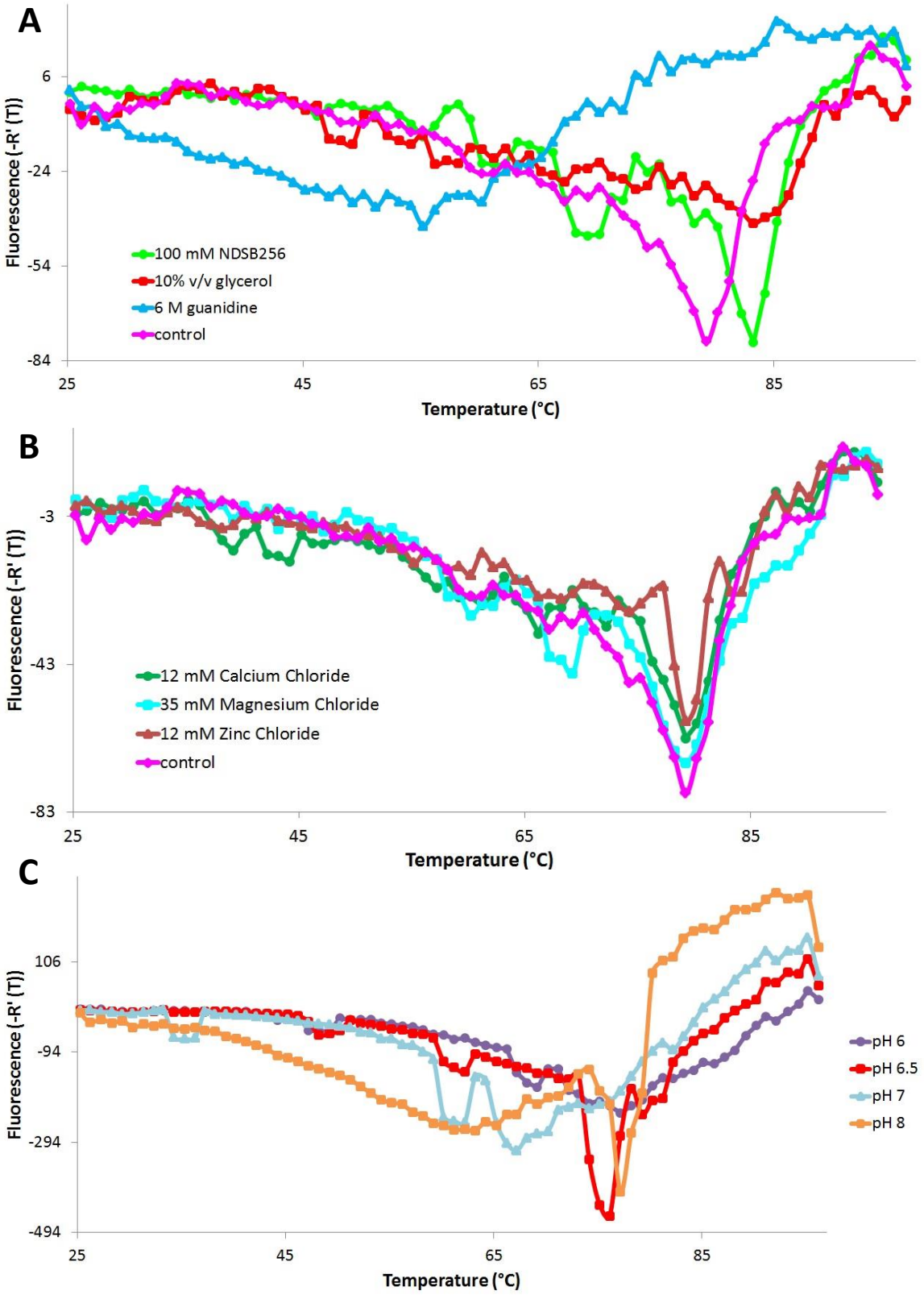


Figure 3.13: Derivatised and multiplied by (-1) melting curves of solubilised Sigma-1 receptor, in presence of 0.1 mg/ml CPM. Control buffer was 50 mM Hepes pH 7.5, 250 mM NaCl, 0.01% w/v Cholesteryl Hemisuccinate, 30 µM haloperidol, 1% w/v n-Octyl-β-D-Glucopyranoside. Melting temperature (T_m) for control buffer: 79.2°C. **(A)** Melting temperatures (T_m): 100 mM NDSB256, 83.2°C; 10% v/v glycerol: 83.2°C; 6M guanidine: 55.2°C. **(B)** Melting temperatures (T_m): 12 mM $CaCl_2$, 80.2°C; 35 mM $MgCl_2$: 79.2°C; 12 mM $ZnCl_2$: 79.2°C. **(C)** Melting temperatures (T_m) for variable pH values: pH6, 77.1°C; pH 6.5: 76.1°C; pH 7: 66.2°C; pH 8: 77.1°C.

It emerged from the melting curves (Figure 3.12) and the calculation of melting temperatures (T_m) (Figure 3.13), that the control Sigma-1 receptor micelle exhibits extraordinary thermostability with a reported Tm of 79.2^{o}C. While a pH variance did not appear to have an effect in increasing the thermostability (Figure 3.13.C), utilizing special buffer components such as NDSB256 and glycerol (Figures 3.12.A & 3.13.A) appeared to increase the Tm values up to 4^{o}C (Figure 3.13.A). Additionally, a slight shift in the T_m has been observed in presence of $CaCl_2$ (Figure 3.13.B), raising the possibility of a direct interaction, given the established role of the protein in the regulation of intracellular calcium signaling (Hayashi T. and Su TP, 2007).

3.7 Future perspectives

Solubilised Sigma-1 receptor, in complex with haloperidol and CHS, has currently reached the stage of nanolitre scale crystallization screening. Further optimization of the membrane extraction process is under way for the human S1Rs. The studies will be expanded towards the crystallographic elucidation of the thermophilic *Paralvinella sulfincola* invertebrate S1R homolog, since proteins that are evolved to function at higher temperatures have lower overall flexibility at lower temperatures and may become trapped in a single conformation (Shin DS., *et al.*, 2009). They thus have an increased crystallization potential (Shin DS., *et al.*, 2009). Within a collaboration with Dr. Jason Schnell (Department of Biochemistry, University of Oxford), structural information on the overall dynamics of the receptor will be provided by NMR and additional clues will be offered for the construct optimization towards successful crystallization in apo, or via fusion with crystallization protein agents, currently used in the membrane protein crystallography field (Chun E., *et al.*, 2012). Since Sigma-1 receptor does not have any

known mammalian homologs for which structural information is available, selenomethionine labeling of S1Rs produced in mammalian cells will be pursued, according to established protocols (Aricescu AR., *et al.*, 2006), to enable experimental phasing. Determining the crystal structure of S1R will offer unprecedented insight into its intricate pharmacology and will explain how a single receptor can distinguish between such a diverse range of small ligand molecules, such as DMT and others mentioned in this chapter. Such structural information will eventually provide a basis for the formulation of functional hypotheses regarding how S1R regulates cellular bioenergetics and synaptic connectivity and how it can be targeted for novel drug development for a range of neurological disorders.

Chapter 4

Structural studies of the EphA4/ephrinA5 signalling complex

Chapter 4

Structural studies of the EphA4/ephrinA5 signalling complex

4.1 Summary

Human erythropoetin-producing hepatocellular receptors (Eph), the major sub-family of receptor-tyrosine kinases (RTK), act after interaction with ephrin ligands which are typically tethered on neighbouring cells. Eph receptors act as a guidance system in many aspects of neural development, as well as other tissues, and are involved in certain types of cancer. Work presented in this chapter contributed to the structural elucidation of the complete extracellular region of EphA4 receptor in complex with EphrinA5. A constructive comparison of the new EphA4 - ephrinA5 structure with the previously determined structure of EphA2 – ephrinA5, enabled a range of functional experiments that extend the understanding of Eph signalling.

4.2 Introduction

4.2.1 Signalling by Eph receptors

Most processes involved in the development and maintenance of organism function depend on communication of information between cells. Such communication also enables them to respond appropriately to environmental factors and variations. A considerable number of genes in eukaryotes encode for proteins that function as membrane spanning cell surface receptors, which, upon receipt of external stimuli, internalise signal information to the cell.

Eph receptors constitute the largest receptor tyrosine kinase (RTK) family in vertebrates and have essential roles in a wide range of cellular responses (Kullander K., and Klein R., 2002, Pasquale EB., 2005). Eph family members are expressed in every germ layer affecting cell segregation and positioning, vascular remodeling, topographic mapping as well as cell migration and tracking (as reviewed by Klein R., 2012 and Wilkinson DG., 2001). They have been also implicated in adult tissue homeostasis (Zhao C., *et al.*, 2006), insulin secretion (Konstantinova I., *et al.*, 2007), and several cell pathological processes leading to diabetes and cancer (Pasquale EB., 2008). Their clinical significance in tumor progression and metastasis has been a topic of intense research focus (Pasquale EB., 2010, Brantley-Sieders DM., 2012 , Nievergall E., *et al.*, 2012). Eph signaling, in the adult brain, has been shown to affect dendritic spine development and neuronal-glia communication, while the bidirectional signaling nature of Eph receptors with their

ephrin ligands regulates synaptic plasticity (Gerlai R., 2001, Murai KK., *et al.*, 2002, Yamaguchi Y. and Pasquale EB., 2004, Klein R., 2008).

Since the first report of cloning an Eph receptor, EphA1 (Hirai H., *et al.,* 1987), 14 receptor members have been identified in the Eph family, which are divided in classes A (EphA1 – EphA8) and B (EphB1 - EphB5) according to sequence similarity and ligand specificity. Their ligands, identified as ephrins (Bartley TD., *et al.*, 1994), consist of an N-terminal extracellular receptor-binding domain (RBD) and are also divided into two subclasses, the A-subclass (ephrinA1-ephrinA5), which are linked to the plasma membrane by a glycosylphosphatidylinositol (GPI) anchor, and the B-subclass (ephrinB1-ephrinB3), members of which have a trans-membrane domain (Eph Nomenclature Committee, 1997, Zhou R., 1998). Binding affinities between Eph receptor and their Ephrin partners can vary, however binding is mostly restricted within classes (Gale NW., *et al.*,1996).

The domain organization is tightly conserved across species. The extracellular side of the Eph receptors (alternatively called as the “ectodomain” region) consists of a ligand-binding domain (LBD), a cysteine-rich region with a sushi and an epidermal growth factor-like (EGF) domain, and two fibronectin type III domains (FN1 and FN2). The ectodomain is followed by a single transmembrane helix (TM), while the cytoplasmic region entails a juxtamembrane region (JM) with a number of conserved tyrosine (Y) rediues, a tyrosine kinase domain, a sterile-α motif (SAM) domain and a C-terminal PSD-95, DLG and ZO1 domain (PDZ)-binding motif (Klein R., 2012). Ephrins have a globular extracellular receptor-binding domain (RCB), which is either GPI-anchored on the cell surface (in the case of Ephrin-As), or followed by a TM helix and an intracellular portion with conserved tyrosine residues and a C-terminal PDZ-binding motif (Ephrin-Bs) (Klein R., 2002), (Figure 4.1).

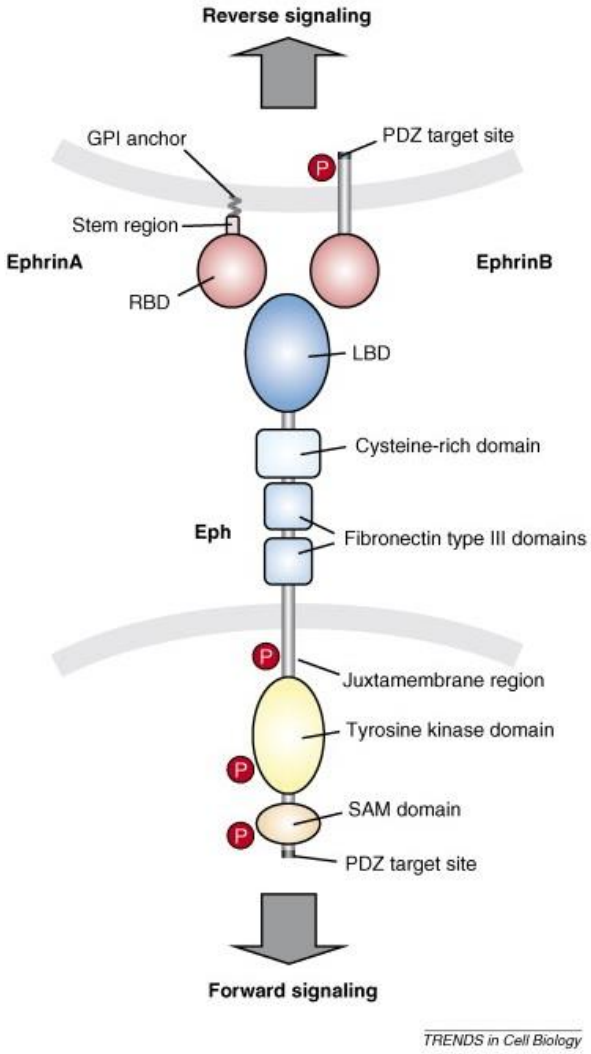


Figure 4.1: Schematic representation of Eph receptor/ephrin domain organization. A cell expressing an Eph receptor (bottom) and a cell expressing ephrinA and ephrinB (top) are indicated. (Image adopted from Egea J. and Klein R., 2007)

Since Eph receptors and ephrins are membrane attached, their binding events and activation require cell–cell interactions. The bidirectional nature of Eph/Ephrin activation accords with the recruitment of effectors on both sides of the *trans* signaling complex (Xu N. and Henkemeyer M., 2012, Pasquale EB., 2010, Egea J. and Klein R., 2007), while a *cis* regulatory interplay with other cell surface signaling hubs provides an additional layer of complexity in signal transduction read-outs (Arvanitis D. and Davy A., 2008). The

influence of Eph/ephrin activation on cell behaviour differs widely (Figure 4.2) depending on the cell type, but can generally be attributed to repulsion of neighbouring cells, or of cellular processes, mediated by transendocytocis (Marston DJ., *et al.*, 2003, Zimmer M., *et al.*, 2003) or proteolytic cleavage (Hattori M*., et al.*, 2000, Janes PW., *et al.*, 2005, Janes PW., *et al.*, 2009). However, adhesive responses have also been reported (Dravis C. *et al.*, 2004, Holmberg J., *et al.*, 2000, Daar IO., 2012). In molecular terms, the signalling pathways that act downstream of Eph and ephrins regulate cytoskeletal responses, via the positive regulation of Rho family GTPases or the intriguing negative regulation of the Ras GTPases (Noren NK. and Pasquale EB., 2004).

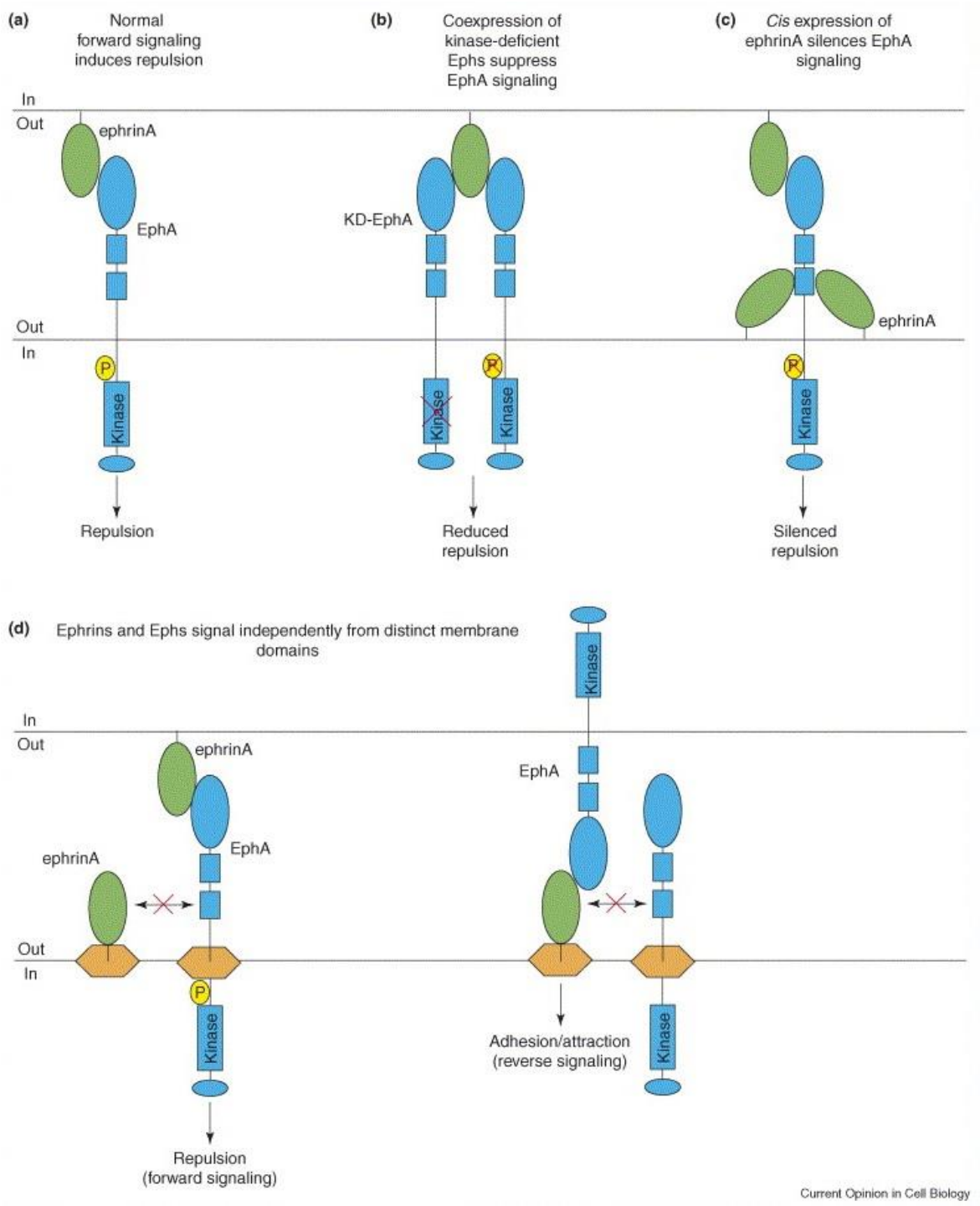


Figure 4.2: Regulation of ephrin–Eph signaling to determine repulsion or adhesion. **(a)** Normal forward signaling induces repulsion of the EphA-expressing cell after interaction with ephrinA in *trans*. **(b)** Coexpression of kinase-deficient Ephs with kinase-active Ephs suppresses phosphorylation of the kinase active Eph to reduce forward signaling and repulsion of the Eph expressing cell. **(c)** Cis expression of ephrinA silences forward signaling by interacting with EphA's first fibronectin III domain, which prevents the EphA cytoplasmic phosphorylation necessary for signaling. **(d)** Expression of ephrinA and EphA from distinct domains within the same cell membrane prevents their *cis* interaction, allowing either forward (repulsion) or reverse (adhesion/attraction) signaling. (Image and caption adopted from Halloran MC. and Wolman MA., 2006)

Upon ephrin binding, Eph receptors are phosphorylated and the kinase domain gets activated in order to initiate downstream signaling (Pasquale EB., 2005). However, It became evident that Eph receptors may implement a more complex mode of oligomerisation to induce signaling, than a ligand-induced dimerisation model, as in the case of the human growth hormone receptor (Cunningham BC. *et al.*, 1991), or in the case of the nerve growth factor TrkA receptor (Wiesmann C. *et al.*, 1999). The activation of Eph receptors depends highly on the spatial arrangement of their structure into signaling clusters (Pasquale EB., 2008, Himanen JP., *et al.*, 2007). Early crystal structures of N-terminal Eph LBDs bound to ephrin RBDs consistenly showed an ephrin loop (GH loop) protruding into a hydrophobic groove of the receptor and provide insights into ligand-receptor specificity, but failed to consistently support a model for ligand mediated signal transduction across the membrane (Himanen JP., 2012, Himanen JP. *et al.*, 2001). In addition, the crystal structure of EphB2 LBD–ephrinB2 RBD complex, reported by Himanen JP., *et al.*, 2001, revealed a tetramerisation interface mediated by a LBD loop designated as the HI loop. Five subsequent Eph LBD–ephrin RBD crystal structures lacked the originally observed tetramerisation interface (Himanen JP. *et al.*, 2004, Chrencik, J.E. *et al*.,2006, Himanen JP. *et al.*, 2009, Bowden TA. *et al.*, 2009). Functional mutagenesis analyses have provided additional hints on the role of other regions of the Eph ectodomain in signaling propensity, upon ephrin triggering (Smith FM., *et al.*, 2004). Structural studies of multidomain complexes of Eph receptors have also been prompted to investigate the observed Eph-Eph interactions necessary to propagate clustering formation beyond the points of ephrin binding ("seeding points") (Wimmer-Kleikamp S. *et al.*, 2004).

Previous endeavours, in the Jones lab and from others, sought to provide structural

insight into a full Eph receptor ectodomain architecture and its interactions and gave rise to the first full ectodomain structures of an Eph receptor in complex with an ephrin ligand (EphA2-ephrinA5) (Seiradake E. *et al.*, 2010, Himanen JP. *et al*., 2010) (figure 4.3).

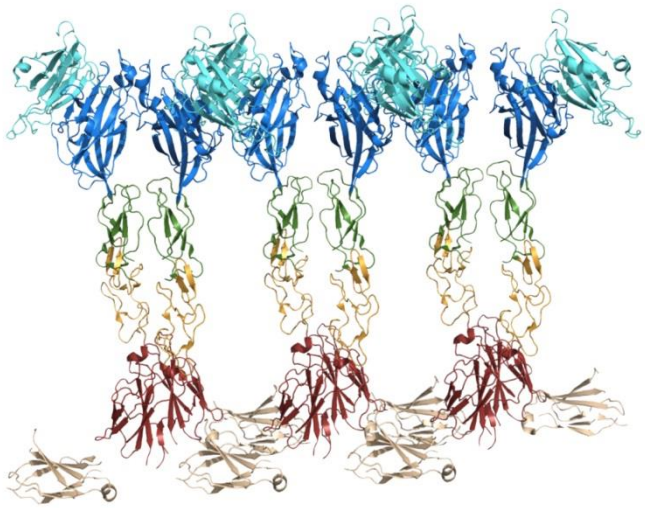


Figure 4.3: EphA2 array formations upon binding of EphrinA5-RBD. EphA2 ectodomains (comprised of domains LBD, sushi, EGFlike, FN1 and FN2) appear in an in-register array-like organization. (PDB 2X11) (Seiradake E., *et al.*, 2010).

Those studies reported that it was not possible to detect any oligomerisation in solution for either various ectodomains alone ($EphA2_{ecto}$, $EphB2_{ecto}$ and $EphB3_{ecto}$) or in complex with soluble Ephrin-RBDs (EphrinA5, EphrinA2 and EphrinB2). Such findings are in accordance with a need for the receptor/ligand system to be membrane attached to promote dimerization or aggregation and subsequent functional activation (Davis S. *et al.*, 1994). However, in the extremely high concentrations generated by a protein crystal environment, the visualisation of potential cluster arrangements was possible, while structure-based functional mutagenesis approaches highlighted their functional significance for receptor activation (Seiradake E. *et al.*, 2010, Himanen JP. *et al*., 2010). The model derived from these studies described a steric 'seeding' mechanism where low Ephrin amounts can trigger the formation of extended arrays of an Eph receptor and

subsequent signaling activation and amplification.

It was essential to investigate whether such a proposed nucleation mechanism, for ectodomain-driven array-based signalling, provides a unifying model for receptor signalling across the Eph family.

The work presented here is focused on EphA4, an Eph family member involved in the developing and the adult nervous system (Flanagan JG. *et al.*, 1998, Wilkinson DG. *et al.*, 2001). It is particularly enriched in brain regions that undergo extensive synaptic remodelling and is important for learning and memory processes (Bourgin C. *et al.*, 2007, Richter M. *et al.*, 2007). Due to its involvement in various physiological and pathological conditions, it has been marked as an interesting drug target for diseases such as spinal cord injury, as well as abnormal blood clotting and certain types of cancer (Prevost N. *et al.*, 2005, Goldshmit Y. *et al.*, 2004, Benson MD. *et al.*, 2005, Easty DJ. *et al.*, 1997, Ashida S. *et al.*, 2004, Iiizumi M. *et al.*, 2006, Yao V. *et al.*, 2005).

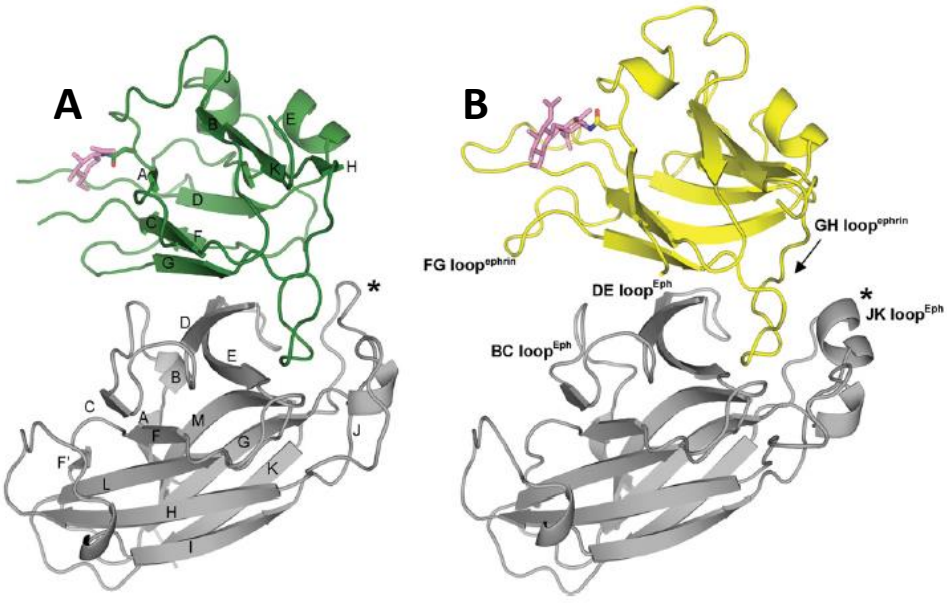


Figure 4.4: Cartoon representations of EphA4-LBD-ephrinB2-RBD **(A)** and EphA4-LBD-ephrinA2-RBD **(B)** complexes. Secondary structure elements are labeled according to standard nomenclature in **(A)** and the main interaction loops are labeled in **(B)**. The J-K Eph loops are marked with an asterisk and undergo major conformational changes dependent on the class of ephrin ligand bound. N-acetyl-glucosamine moieties observed at Asn-linked glycosylation sites are shown as pink sticks (image and caption adapted from Bowden TA., et al., 2009).

Previous structural analyses of the EphA4 LBD in apo form or in complex with various ephrins (figure 4.4), have provided arguments for a debate on the properties that mandate class-dependent Eph receptor specificity and promiscuity (Qin H. *et al.*, 2008, Bowden TA. *et al*, 2009, Qin H. *et al.*, 2009, Singla N. *et al.*, 2010), the reciprocal family-wide breadth of which is illustrated in figure 4.5.

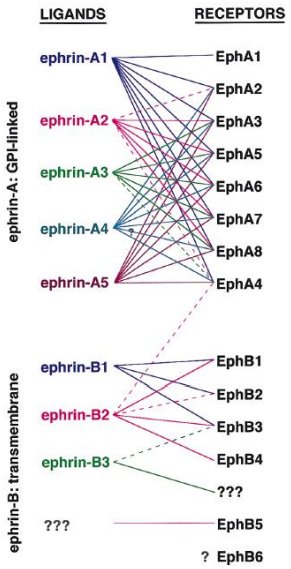


Figure 4.5: Schematic representation of the promiscuity in Eph receptor-ligand interactions (adapted by Zhou R., 1998)

4.3 Aims

The main aim of this chapter was to gain a structural insight of the complete extracellular region of Ephrin A4 receptor in complex with Ephrin ligands, and perform comparisons with previous structural data for the Eph family.

4.4 Expression and purification of EphA4 and EphrinA5

4.4.1 Expression of EphA4 and EphrinA5

Continuing preliminary work in Prof. Jones lab, from Dr. Elena Seiradake, the full extracellular region of hEphA4 and the receptor binding domain of hEphrinA5 were expressed in HEK293 cells (Reeves PJ., *et al.*, 2002), as described in detail in section 2.2.1, at high levels, as shown in Table 4.1. Predicted N-glycosylation sites, according to the NetNGlyc 1.0 server (Gupta R. and Brunak S., 2002), are provided in Figure 4.6. Construct boundaries are presented in Appendix B.

	Cell volume	Yield
EphA4 [LBD-sushi-EGF-FN1-FN2]	~3 L [6 Hyper flasks]	8.6 mg
EphrinA5 [RBD]	~ 3 L [12 Roller Bottles]	3.29 mg

Table 4.1: Expression levels of hEphA4 and hEphrinA5

```
Name:  hEphA4ecto       Length:  534
VTGSRVYPANEVTLLDSRSVQGELGWIASPLEGGWEEVSIMDEKNTPIRTYQVCNVMEPSQNNWLRTDWITREGAQRVYI      80
EIKFTLRDCNSLPGVMGTCKETFNLYYYESDNDKERFIRENQFVKIDTIAADESFTQVDIGDRIMKLNTEIRDVGPLSKK     160
GFYLAFQDVGACIALVSVRVFYKKCPLTVRNLAQFPDTITGADTSSLVEVRGSCVNNSEEKDVPKMYCGADGEWLVPIGN     240
CLCNAGHEERSGECQACKIGYYKALSTDATCAKCPPHSYSVWEGATSCTCDRGFFRADNDAASMPCTRPPSAPLNLISNV     320
NETSVNLEWSSPQNTGGRQDISYNVVCKKCGAGDPSKCRPCGSGVHYTPQQNGLKTTRVSITDLLAHTNYTFEIWAVNGV     400
SKYNPNPDQSVSVTVTTNQAAPSSIALVQAKEVTRYSVALAWLEPDRPNGVILEYEVKYYEKDQNERSYRIVRTAARNTD     480
IKGLNPLTSYVFHVRARTAAGYGDFSEPLEVTTNTVPSRIIGDGANSTHHHHHH
.....      80
.....     160
.....N.....     240
.....     320
N.....N.....     400
.....     480
.....     560

(Threshold=0.5)
---------------------------------------------------------------------
SeqName      Position  Potential   Jury    N-Glyc
                                 agreement result
---------------------------------------------------------------------
hEphA4ecto   216 NNSE   0.5673     (7/9)   +
hEphA4ecto   321 NETS   0.6514     (9/9)   ++
hEphA4ecto   389 NYTF   0.5918     (6/9)   +
hEphA4ecto   526 NSTH   0.3348     (7/9)   -
---------------------------------------------------------------------

Name:  hEphrinA5-RBD    Length:  152
ETGAVADRYAVYWNSSNPRFQRGDYHIDVCINDYLDVFCPHYEDSVPEDKTERYVLYMVNFDGYSACDHTSKGFKRWECN      80
RPHSPNGPLKFSEKFQLFTPFSLGFEFRPGREYFYISSAIPDNGRRSCLKLKVFVRPTNSCMKGTKHHHHHH
.....N.....      80
.....     160

(Threshold=0.5)
---------------------------------------------------------------------
SeqName      Position  Potential   Jury    N-Glyc
                                 agreement result
---------------------------------------------------------------------
hEphrinA5-RBD   14 NSSN   0.7336     (9/9)   ++
---------------------------------------------------------------------
```

Figure 4.6: Prediction of N-glycosylation sites for hEphA4ecto and hEphrinA5-RBD NetNGlyc 1.0 server (Gupta R. and Brunak S., 2002).

4.4.2 Purification of native EphA4 and EphrinA5

In figure 3.5, the Ni-affinity purification of both EphA4 (~58kDa) and EphrinA5 (~18kDa) is shown (panels A, B), performed as described in section 2.2.4.2. An additional Ni-affinity step was carried out after an overnight deglycosylation reaction (figure 4.7, panels C,D). When mixing the eluted proteins in 1:1.5 molar ratio (EphA4:EphrinA5), they co-eluted in gel filtration due to a strong interaction (figure 4.8.A).

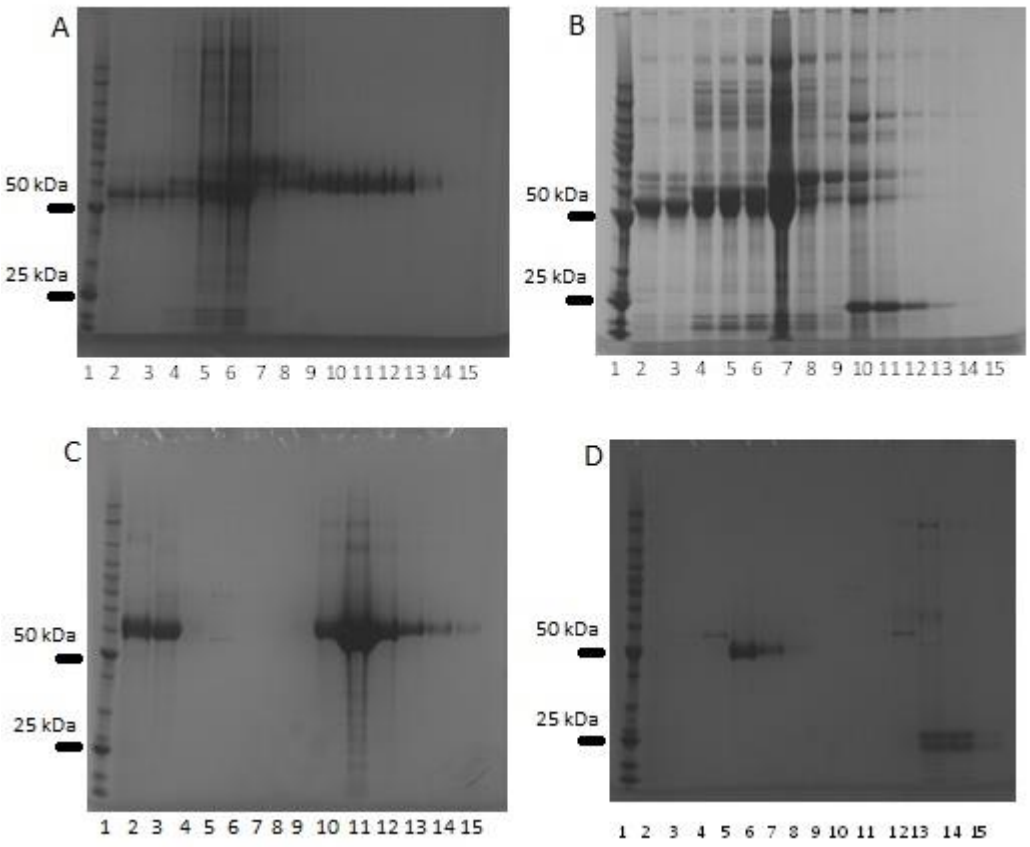


Figure 4.7: **(A)** SDS-PAGE of Ni-affinity purification of EphA4 (high imidazole fractions: 8-15). **(B)** SDS-PAGE of Ni-affinity purification of EphrinA5 (high imidazole fractions: 10-15). **(C)** SDS-PAGE of Ni-affinity purification, after EndoH deglycosylation, of EphA4 (fraction 2: before EndoH, fraction 3: after EndoH, high imidazole fractions: 11-15). **(D)** SDS-PAGE of Ni-affinity purification, after EndoH deglycosylation, of EphrinA5 (high imidazole fractions: 13-15).

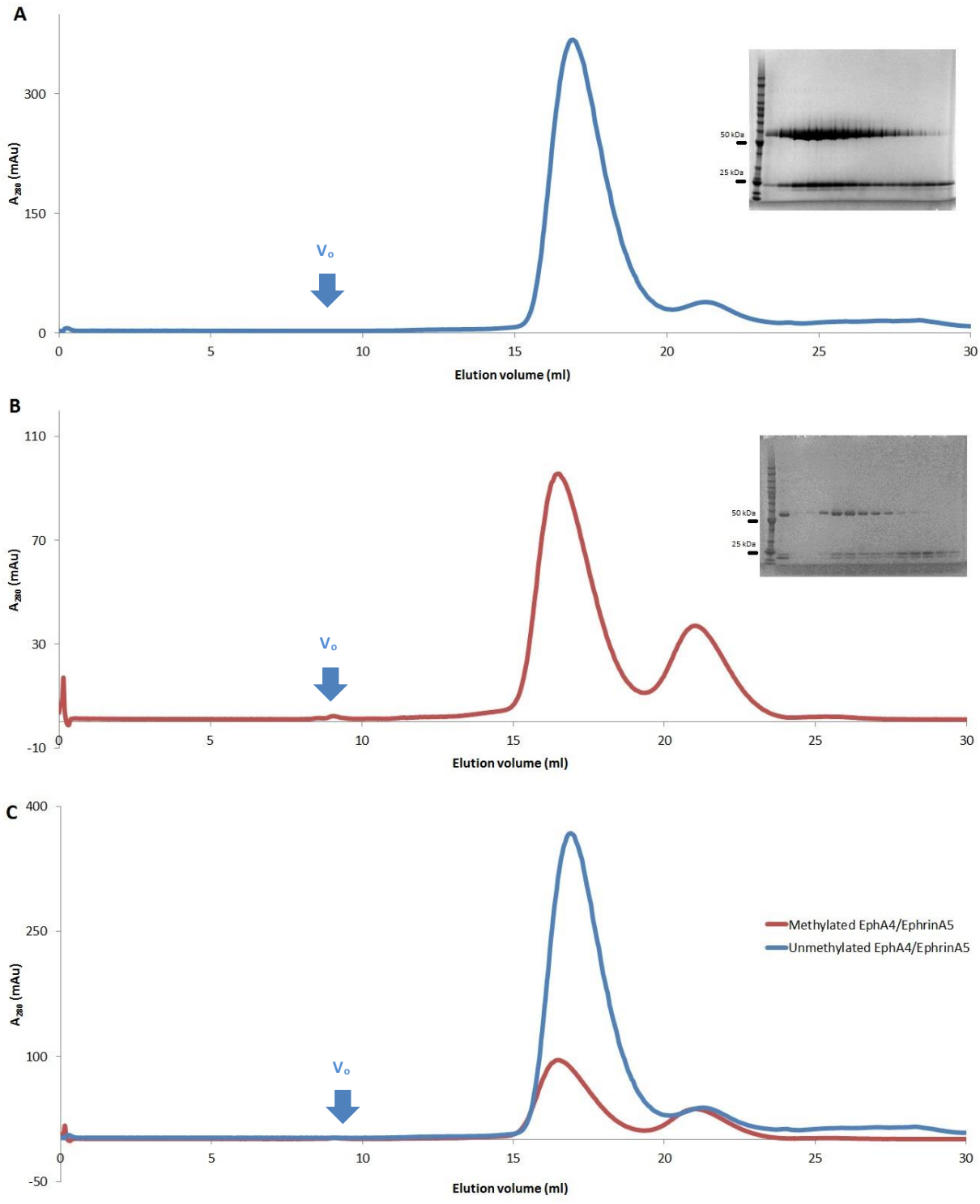


Figure 4.8: **(A)** S200 elution profile of the complex EphA4/EphrinA5 and SDS-PAGE. **(B)** S200 elution profile of the methylated complex EphA4/EphrinA5 and SDS-PAGE. **(C)** Comparison of the gel filtration elution profiles of the methylated complex.

4.4.3 Purification of lysine-methylated EphA4 and EphrinA5

The presence of a certain number of lysines in EphA4 and EphrinA5 sequences (figure 4.9), suggested a route of deducing of surface entropy by methylating surfaced-exposed lysines (Walter TS., *et al.*, 2006). The pure complex was subjected to methylation, as described in section 2.3.3, and the resulting 13/30 S200 elution profile showed that the complex was present with a shift in the elution volume (figures 4.8.B and 4.8.C).

EphA4

VTGSRVYPANEVTLLDSRSVQGELGWIASPLEGGWEEVSIMDE**K**NTPIRTYQVCNVMEPSQNNWLRTDWITREGAQ
RVYIEI**K**FTLRDCNSLPGVMGTC**K**ETFNLYYYESDND**K**ERFIRENQFV**K**IDTIAADESFTQVDIGDRIM**K**LNTE
IRDVGPLS**KK**GFYLAFQDVGACIALVSVRVFY**KK**CPLTVRNLAQFPDTITGADTSSLVEVRGSCVNNSEE**K**DVP
KMYCGADGEWLVPIGNCLCNAGHEERSGECQAC**K**IGYY**K**ALSTDATCA**K**CPPHSYSVWEGATSCTCDRGFFRAD
NDAASMPCTRPPSAPLNLISNVNETSVNLEWSSPQNTGGRQDISYNVVC**KK**CGAGDPS**K**CRPCGSGVHYTPQQNG
L**K**TT**K**VSITDLLAHTNYTFEIWAVNGVS**K**YNPNPDQSVSVTVTTNQAAPSSIALVQA**K**EVTRYSVALAWLEPDR
PNGVILEYEV**K**YYE**K**DQNERSYRIVRTAARNTDI**K**GLNPLTSYVFHVRARTAAGYGDFSEPLEVTTNTVPSRIIG
DGANSTHHHHHH

EphrinA5

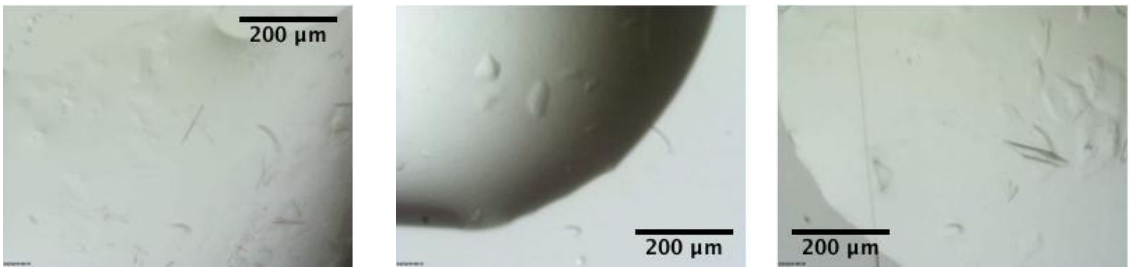
ETGAVADRYAVYWNSSNPRFQRGDYHIDVCINDYLDVFCPHYEDSVPED**K**TERYVLYMVNFDGYSACDHTS**K**GF**K**
RWECNRPHSPNGPL**K**FSE**K**FQLFTPFSLGFEFRPGREYFYISSAIPDNGRRSCL**K**L**K**VFVRPTNSCM**K**GT**K**HH
HHHH

Figure 4.9: Overview of lysine residues present in EphA4 and EphrinA5 constructs, amounting to 4.7% for EphA4 and 5.9% for EphrinA5.

4.5 Crystal optimization of existing hits and crystallographic analysis of EphA4/EphrinA5 complex

The native EphA4/EphrinA5 complex was concentrated to 9.32-9.5 mg/ml and was used for nanolitre scale crystallization trials. A number of initial crystallization conditions identified by Dr. Elena Seiradake (figure 4.10) found to diffract not better than 15 Å, were pursued for optimization in extensive additive screening (Hampton Rerearch Inc.). Crystals were optimized as proved by their diffraction properties, and a new condition emerged (figure 4.11). A dataset was collected from an optimized crystal, diffracting up to 5.5 Å resolution. The methylated sample was concentrated to 9.8 mg/ml and used in high-throughput crystallization trials which enabled the growth of the best diffracting crystals so far (figure 4.12). A dataset was collected from a single crystal, diffracting up to 4.7 Å resolution.. Data collection statistics for both datasets are reported in Table 4.2.

This project was pursued as a rotation during the first year of the doctoral programme, so due to time limitations and impending international competition there was a pressure to pursue a publication as soon as possible. Therefore, all collected data were further processed by Dr. Elena Seiradake, who also performed the structural determinations, as reported in the relevant original publication (Seiradake E., *et al*. 2013).



0.010 M Magnesium Sulphate
1.800 M Lithium Sulphate
0.050 M Sodium Cacodylate pH 6.0

15 %v/v 2-Propanol
0.020 M Magnesium Chloride
0.050 M MES pH 6.0

15 %v/v Polyethylene Glycol 400
0.080 M Magnesium Acetate
0.050 M Sodium Cacodylate pH 6.5

Figure 4.10: Initial EphA4/ephrinA5 crystals grown by Dr. Elena Seiradake.

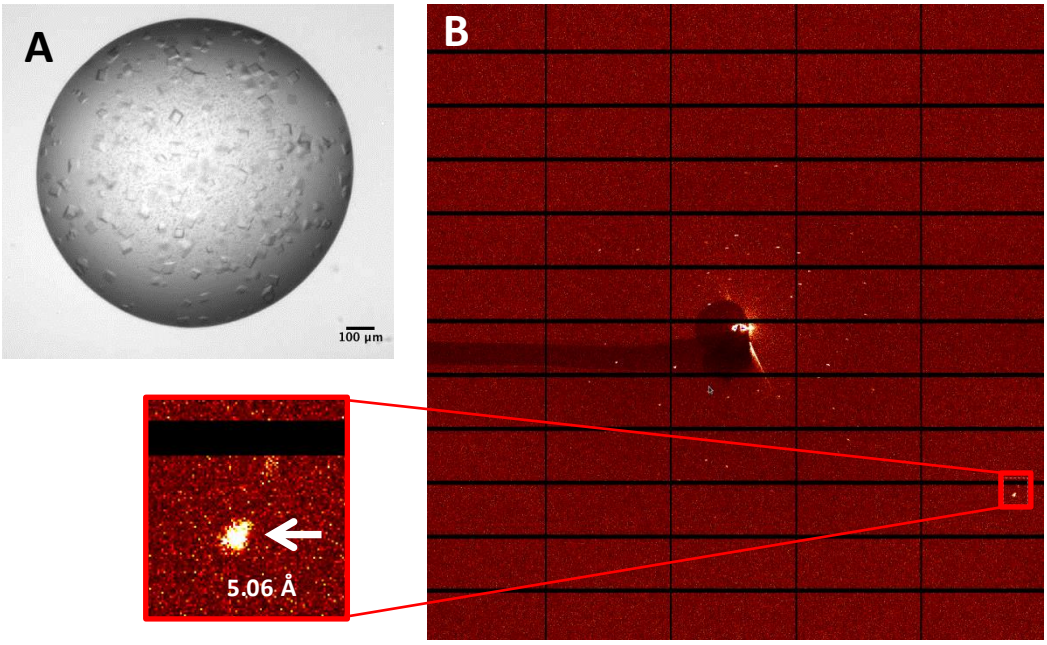


Figure 4.11: Low resolution diffraction of native hEphA4ecto/hEphrinA5-RBD crystals. **(A)** Representative crystals obtained from additive screening optimization (Hampton Rerearch Inc.), grown in 0.05 M sodium cacodylate pH 6, 0.01 M $MgSO_4$, 1.8 M Li_2SO_4, 4% benzamidine-HCl. **(B)** A ~5.5 Å data set was collected.

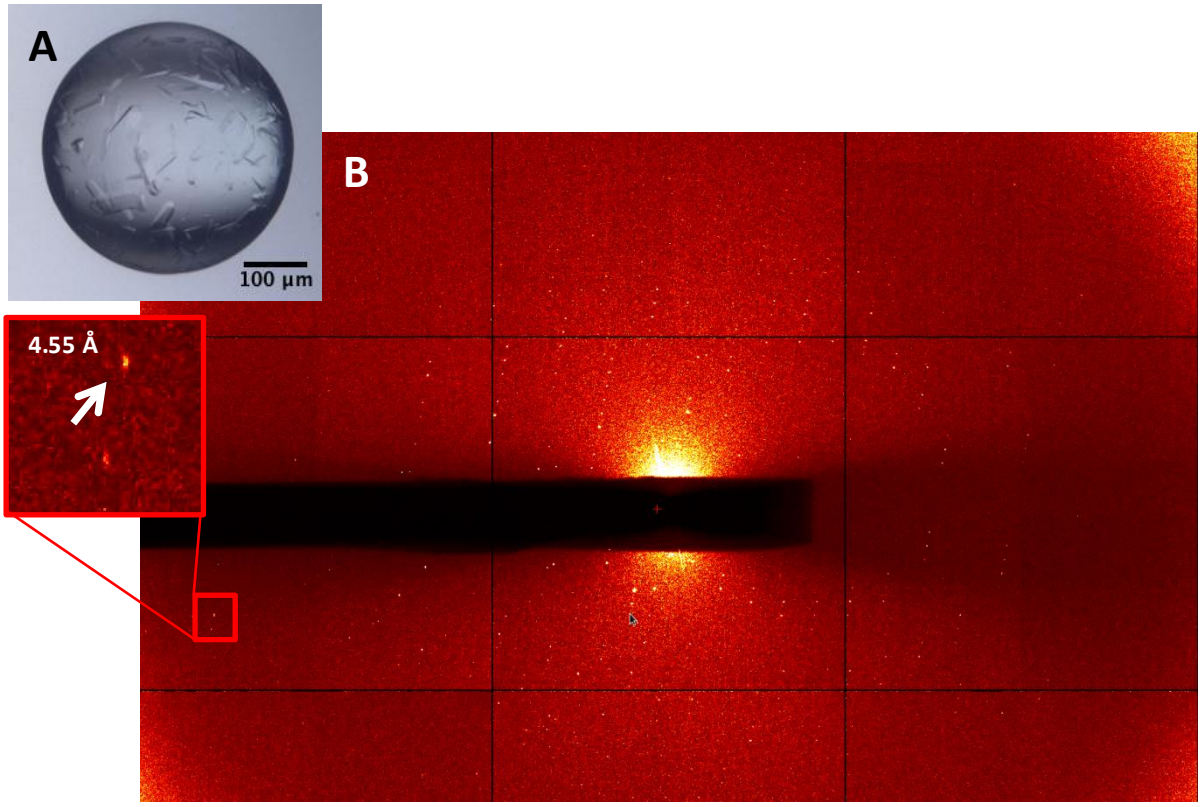


Figure 4.12: Low resolution diffraction of lysine methylated hEphA4ecto/hEphrinA5-RBD crystals. **(A)** Representative crystals grown at 4°C, in 0.1 M Tris-HCl pH 8.5, 8% w/v polyethylene glycol 8000. **(B)** A ~4.5 Å data set was collected.

Data Collection Statistics		
Protein	$hEphA4_{ecto}$+hEphrinA5-RBD methylated	$hEphA4_{ecto}$+hEphrinA5-RBD native
Beamline	Diamond-I04	Diamond-I24
Resolution (Å)	51.16-4.7 (4.82-4.7)	154.58-5.5 (6.15-5.5)
Spacegroup	H32	H32
Cell dimensions a, b, c (Å) α, β, γ (°)	 257.060 257.060 253.570 90.000 90.000 120.000	 203.20 203.20 323.49 90.00 90.00 120.00
Wavelength (Å)	0.9795	0.9786
Unique reflections	16934 (1230)	8588 (2407)
Completeness (%)	99.9 (100)	100 (100)
R_{merge} (%)	32 (147)	65 (374)
I/σI	8.7 (2.2)	3.1 (0.8)
Multiplicity	11.3 (11.5)	8.6 (8.6)

Table 4.2: Crystallographic data collection statistics for $EphA4_{ecto}$/EphrinA5 crystal structures. Numbers in brackets refer to the high resolution shell.

The structures of $EphA4_{ecto}$/EphrinA5-RBD indicated a similar domain arrangement with the one previously shown in EphA2 structures (Seiradake E., *et al.*, 2010, Himanen JP., *et*

al., 2010) (figure 4.13). The structure shows unique features in terms of how molecules are packed to form the lattice, mainly between contacts in the sushi domains. However in the case of the lysine-methylated sample, the ligand binding domain of the EphA4 presents an additional contact site at the HI loop (figures 4.13, 4.14).

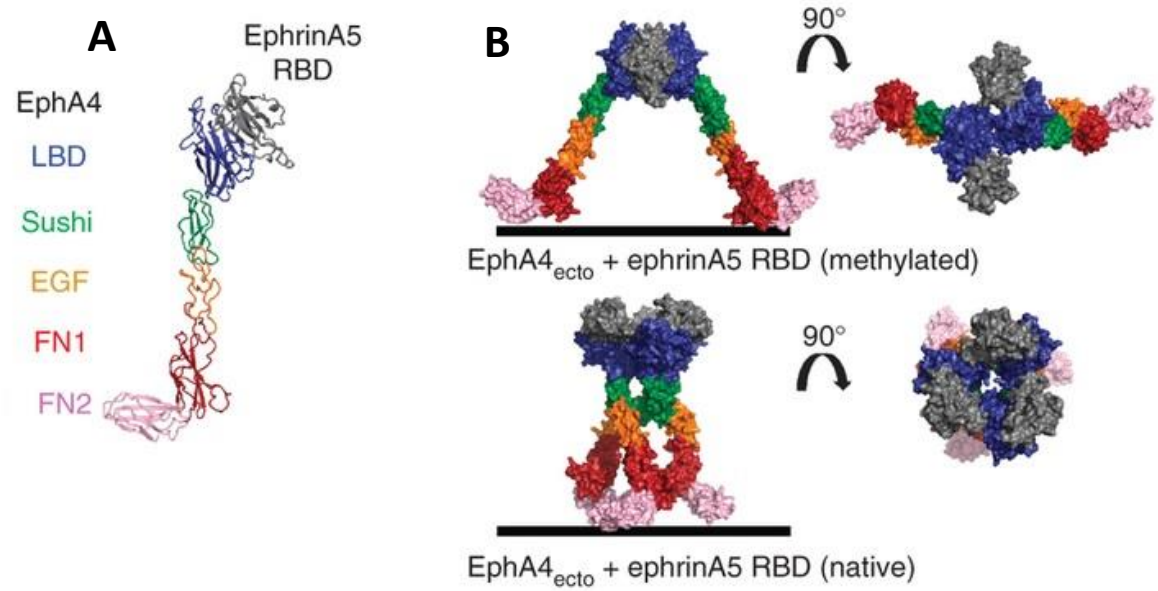


Figure 4.13: Structural arrangements of EphA4 ectodomain ($EphA4_{ecto}$) in complex with EphrinA5 receptor binding domain (RBD), as observed in the crystals. **(A)** Domain organization shown in cartoon representations, with distinct coloring. $EphA4_{ecto}$ comprises of ligand binding domain (LBD), sushi domain, epidermal growth factor-lie domain (EGF), fibronectin type III domains 1 and 2 (FN1, FN2). **(B)** Lattice assemblies of EphA4/EphrinA5, as observed in the crystal structures, indicating clustering modes of receptors on the same cell surface. (Image adopted from Seiradake E., *et al.* 2013)

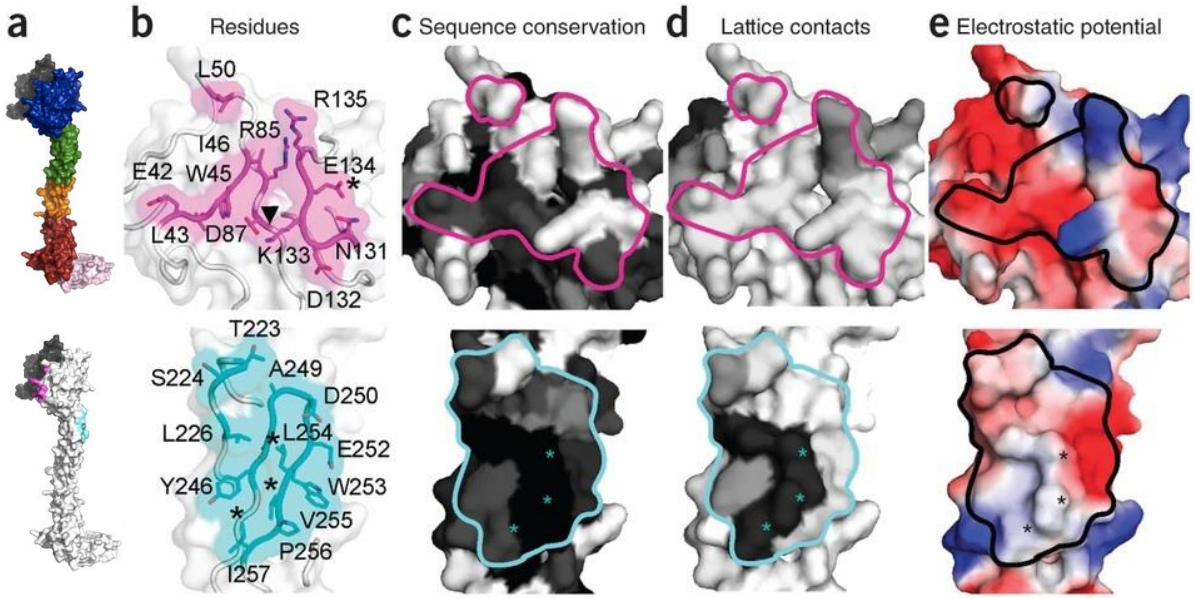


Figure 4.14: Properties of EphA4 HI-loop and sushi dimerization regions. **(a)** Surface of $EphA4_{ecto}$ in complex with ephrinA5 RBD, shown in two color schemes. Top, domains are colored separately: gray, ephrinA5-RBD; blue, EphA4-LBD; green, EphA4-sushi; orange, EphA4-EGF-like; red, EphA4-FN1; pink, EphA4-FN2. Bottom, colors are: white, $EphA4_{ecto}$; gray, ephrinA5-RBD; magenta, HI loop and adjacent regions implicated in clustering for EphA2 (Seiradake E. *et al.*, 2010); cyan, sushi dimerization surface. **(b–e)** Zoomed-in view of the EphA4 HI-loop region (magenta) and sushi dimerization surfaces (cyan). In **(b)**, residues are shown as sticks. Arrowhead marks Lys133. Asterisks mark Glu134 (equivalent to Gly131 in EphA2, which is mutated to tyrosine in $EphA2^{HI}$) and the surface residues Leu254, Val255 and Ile257 on the sushi domain (mutated to aspartate in functional mutagenesis experiments described in Seiradake E., *et al.* 2013). In **(c)**, colors are according to sequence conservation among human EphAs, ranging from black (highly conserved) to white (not conserved). The HI-loop area and sushi dimerization surface are encircled. In **(d)**, colors are according to the frequency of residues mediating lattice contacts in the four crystal structures presented, ranging from black (involved in all lattices) to white (not involved in any lattices). In **(e)**, colors are according to electrostatic potential, calculated for vacuum. Blue, positive charge; red, negative charge; white, neutral; units in PyMoL adjusted to ± 63. (Image and caption partially adopted from Seiradake E., *et al.* 2013)

4.6 Comparison of EphA4/EphA2 ectodomain structures and implications for EphrinA5-mediated signalling

Data on Eph function have proposed a need for the receptors to form oligomers via the extracellular region in order for signal to propagate through the membrane (Wimmer-Kleikamp, S.H., et al., 2004, Egea J. et al, 2005). Studies have shown that cytoplasmic regions of EPH receptors are also required in a two-step signalling initiation process (Lackmann M., *et al.*, 1998), which may involve additional contacts mediated by SAM domains on the C-terminus (Thanos CD., *et al.*, 1999). The cellular membrane context where these interactions take place apparently has an additional effect on the ability of Eph receptors to cluster, a process directly involving cytoskeletal reorganization (Salaita K. *et al.*, 2010, Groves JT. and Kuriyan J., 2010). Crystallographic approaches combined with functional analyses targeting Eph signaling complexes have been recently expanded to investigate the contributions of the full extracellular regions on signaling propensity (Seiradake E. *et al.*, 2010, Himanen JP. *et al.*, 2010). By focusing on EphA2 receptor complexes with EphrinA5 and EphrinA1, it has been observed that cluster formation is mediated by interactions between sushi domains in adjacent receptors, as well as parallel in interactions between the ligand binding domains in the HI loop region (figure 4.15).

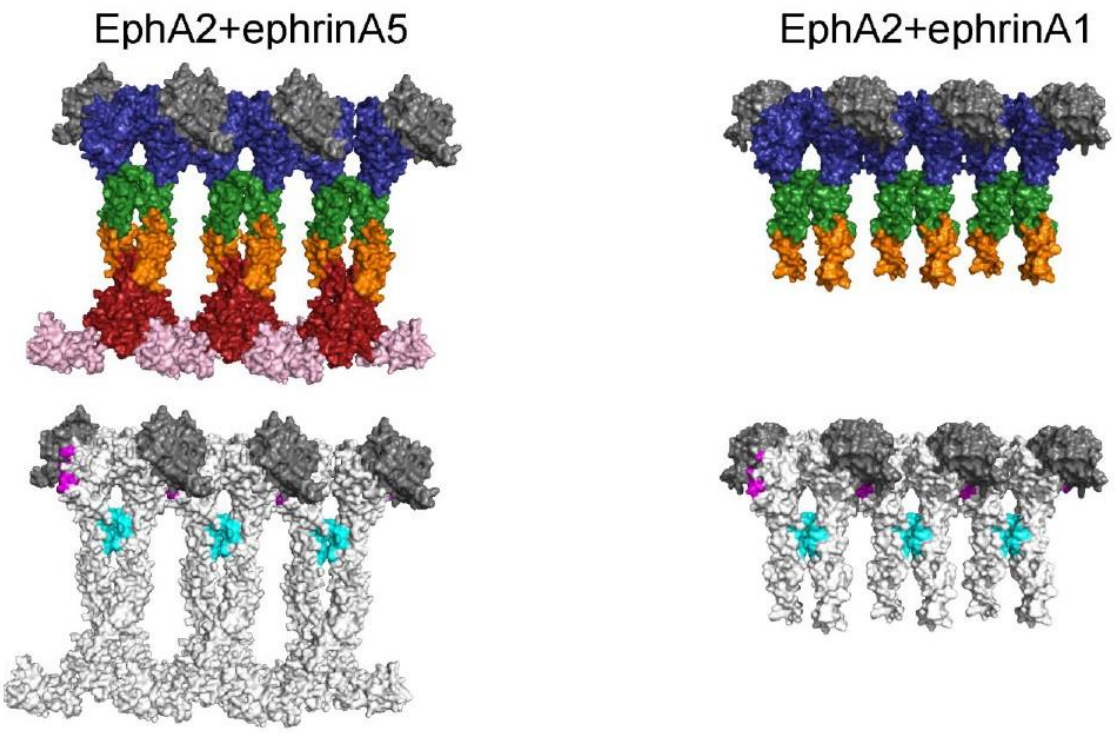


Figure 4.15: $EphA2_{ecto}$/EphrinA5 (PDB 2X11, Seiradake E. *et al.*, 2010) and $EphA2_{LBD\text{-}sushi\text{-}EGF\text{-}like}$/EphrinA1 (PDB 3MBW, Himanen JP. *et al.*, 2010) structural arrangements observed in crystals. Surface representations are either colored by domain (LBD = blue, sushi = green, EGF-like = orange, FN1 = red, FN2 = pink) or are depicted in white with contact interfaces of the sushi or LBD domains highlighted in cyan and magenta, respectively. Ephrin-RBDs are depicted in grey. (Image and caption partially adopted from Seiradake E. *et al.* 2013)

The EphA4 ectodomain structural analysis in complex with EphrinA5-RBD has revealed a strikingly different arrangement than the one observed in the EphA2 studies. Defined units, stabilised in dimeric or circular arrangements (figure 4.13), are held together by interactions between the sushi domains. The less conserved HI loop region (figure 4.16) appears to be involved, as a potential receptor clustering interface, only in the case of the lysine methylated sample. However there is a lysine residue in the HI loop region (K133, figure 4.14), therefore the contribution of the native/non-methylated HI loop to the clustering propensity, is doubtful.

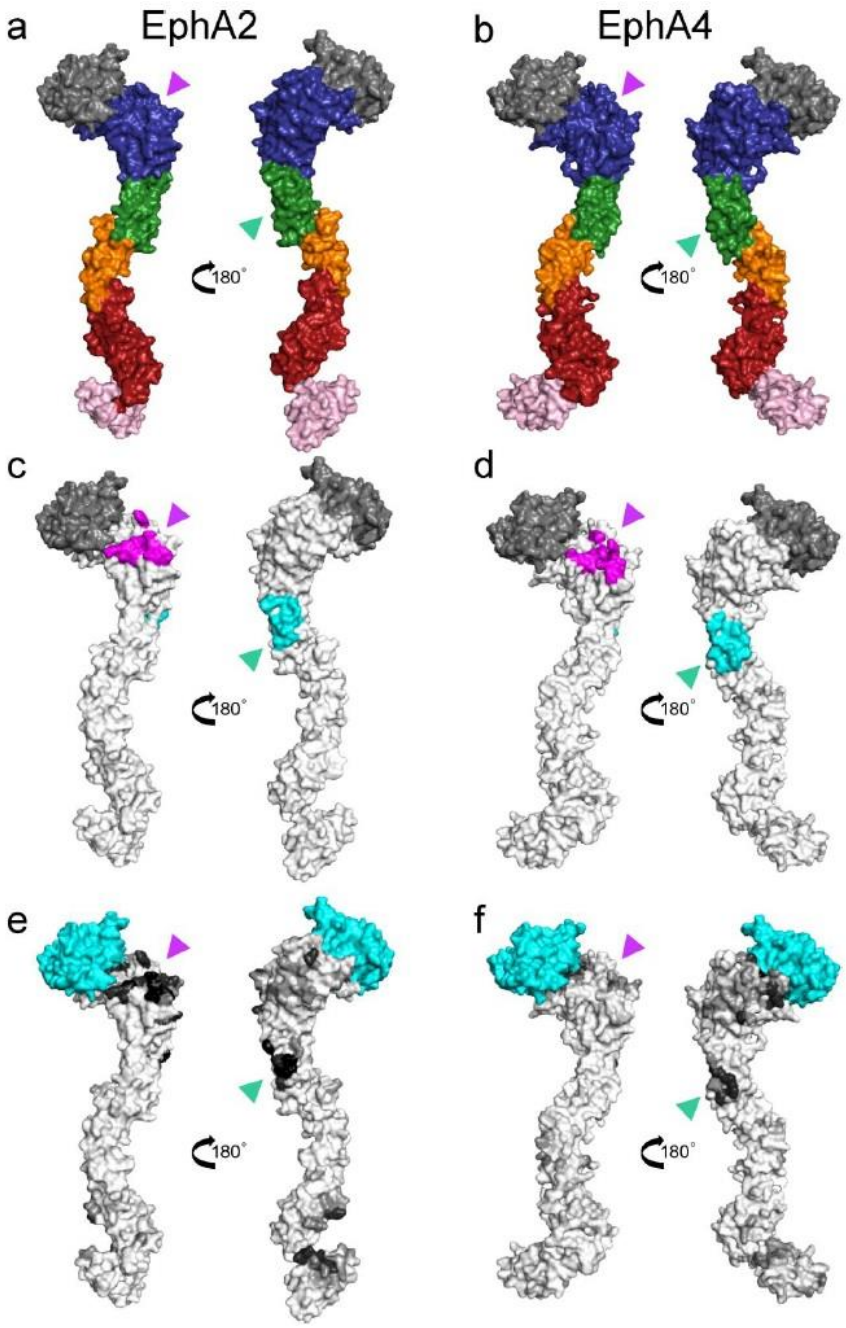


Figure 4.16: Surface representations of EphA2ecto and EphA4ecto in complex with ephrinA5 RBD are shown. Pink and blue arrows point to surfaces providing contacts in the EphA2ecto arrays on the LBD and the sushi domain, respectively. **(a)** EphA2ecto in complex with ephrinA5 RBD. Colours are according to domain: LBD (dark blue), sushi (green), EGF-like (orange), FN1 (dark red), FN2 (light pink), ephrinA5 RBD (grey). **(b)** As panel a, but showing the corresponding EphA4ecto structure. **(c)** As panel a, but colours are white (EphA2), grey (ephrinA5), magenta (HI-loop and adjacent regions), cyan (sushi dimerisation surface). **(d)** As panel c, but showing the corresponding EphA4ecto structure. **(e)** As panel a, but the EphA2ecto surface is coloured according to the frequency of residues mediating lattice contacts in the four crystal structures known (in PDB: 2X10, 2X11, 3FL7, 3MBW). Colours range from black = involved in all lattices, to white = not involved in any lattices. **(f)** As panel e, showing frequencies for the corresponding EphA4ecto structures (in PDB: 4BK4, 4BK5, 4BKA, 4BKF). Notably, residues in the EphA4 HI-loop are less frequently involved in mediating lattice contacts compared to those in the EphA2 HI-loop. (Image adopted from Seiradake E. *et al.* 2013, caption partially adopted from Seiradake E. *et al.* 2013)

4.7 Discussion and future perspectives

It becomes evident that the Eph signaling propensity is significantly modulated by specific characteristics of various Eph ectodomains, in a non-generic way. Expanding structure-function studies in a platform where additional homotypic or even heterotypic Eph clusters (Janes PW., et al., 2011), are evaluated for effects on signal transduction will become increasingly instrumental in our understanding of the molecular attributes of Eph function. In addition, it would be essential to evaluate the necessity of EphA clustering for signal transduction across the membrane, within a more physiological context. That could be feasible by complementing crystallographic findings for ectodomain and full-length EphA4 and other Eph receptors with cryo-electron tomography insights, which would contribute to the mechanistic understanding directly at cell-cell contact sites. That would be very interesting since, there have been reports suggesting that the potential modulation of co-expressed EphA/ephrin molecules, by the local membrane environments leads to segregation of EphA receptors and ephrins in distinct compartments and promotes distinct functional effects (Marquardt T., *et al.*, 2005, Klein R., 2005). In addition, it needs to be evaluated whether the different clustering modes of Eph receptors, and their effects in spatial organization at the membrane, are implicated in their ability to respond to different ligand densities they encounter (Huynh-Do U., *et al.*, 1999, McLaughlin T., et al., 2003). Is the regulation of their clustering a core mechanism for the recruitment of effectors and promotion of cellular attachment responses (Stein E., *et al.*, 1998)? Is the regulation of their clustering a core mechanism for the concentration-dependent transition from retinal axon growth promotion to inhibition (Hansen MJ., *et al.*, 2004)?

Chapter 5

Proteoglycan regulation of RPTPσ-TrkC mediated synaptogenesis

Chapter 5

Proteoglycan regulation of RPTPσ-TrkC mediated synaptogenesis

5.1 Summary

Type IIa receptor protein tyrosine phosphatases (RPTPs) are cell surface receptors shown to be involved in neuronal growth and guidance, as well as excitatory synapse formation. Extracellular regions of type IIa RPTPs, namely the LAR, σ and δ, have been shown to interact, via a shared binding site, with a diverse range of heparan sulfate proteoglycans (HSPGs) and chondroitin sulfate proteoglycans (CSPGs). Such events have been previously shown to act as switches in RPTP-mediated signaling, leading to different neuronal extension outcomes. RPTPσ has been reported to interact with a postsynaptic neurotrophin receptor tyrosine kinase (Trk), TrkC, facilitating bidirectional adhesion and excitatory synaptic organization. Work presented in this chapter provides crystallographic insight into the complex between RPTPσ/TrkC interacting domains, highlighting an overlap of the proteoglycan and TrkC binding sites on RPTPσ. Surface plasmon resonance experiments with structure-based mutants and wild-type proteins were performed to characterise the interaction between RPTPσ-TrkC, as well as the competition between TrkC and proteoglycans for RPTP binding. Studying this trans-synaptic interaction assists in the formulation of a prototypical molecular mechanism which describes in atomic detail how extending axons recognise and mark cellular targets for subsequent synapse establishment.

5.2 Introduction

5.2.1 Protein Tyrosine Phosphorylation and signalling

The reversible phosphorylation of tyrosine residues is a common and critical mechanism in signal transduction, occurring by the balanced action of tyrosine kinases (PTKs) and tyrosine phosphatases (Hunter T., 1995, Sun H., and Tonks NK., 1994). The first indication that proteins can be phosphorylated came in the 1950s when work by Fischer and Krebs on glycogen metabolism showed that the active form of phosphorylase a and the inactive form of phosphorylase b are phosphorylated and dephosphorylated forms of the single enzyme (Krebs EG., 1992, Fischer EH., 1992). Tyrosine phosphorylation has been a topic of intense research for more than 3 decades, since the early 1980s when $pp60^{src}$, the protein responsible for the transformation of chicken cells by Rous sarcoma virus, was found able to phosphorylate tyrosine (Hunter T. and Sefton BM., 1980). The same year the epidermal growth factor (EGF) receptor was also found to possess a tyrosine kinase catalytic activity (Ushiro H. and Cohen S., 1980). A number of kinases were subsequently identified providing grounds for the hypothesis that the regulation of protein phosphorylation is a critical mechanism for the control of enzymatic activity (Denu JM. And Dixon JE., 1998). However, it took eight years after the original identification of a protein kinase, for a protein with a tyrosine phosphatase activity, PTP1B, to be characterised (Tonks NK., et al., 1988, Tonks NK., et al., 1988). CD45 was the first receptor protein tyrosine phosphatase (RPTP) to be characterised (Tonks NK., 1988), after its sequence analysis indicated a high degree of similarity with PTP1B. Low-stringency screens of mouse brain cDNA libraries with probes based on the cytoplasmic domains of CD45, enabled the identification of additional family members (Kaplan R., *et al.*, 1990,

Sap J., *et al.*, 1990). Structural and evolutionary analyses of the RPTP family members resulted in the identification of 6 separate classes with members from both vertebrate and invertebrate organisms (Andersen JN., *et al.*, 2001). With the completion of the human genome it is now established that a total 107 human PTP genes give rise to a family with very modular structures and domain combinations (Figure 5.1) (Alonso A. *et al.*, 2004). Certain phosphatases are currently established to have diverse roles in cell-substrate adhesion (reviewed by Stoker AW., 2005), cell-cell adhesion (reviewed by Beltran PJ. and Bixby JL., 2003. Stoker AW., 2005), hormone receptor downstream signalling transduction (as reviewed by Espanel X., *et al.*, 2001), while a range of studies have implicated them in axon guidance and nervous system development (reviewed by Stoker AW., 2001, Johnson KG. and Van Vactor D., 2003, Paul S. and Lombroso PJ., 2003, Ensslen-Craig SE., Brady-Kalnay SM., 2004).

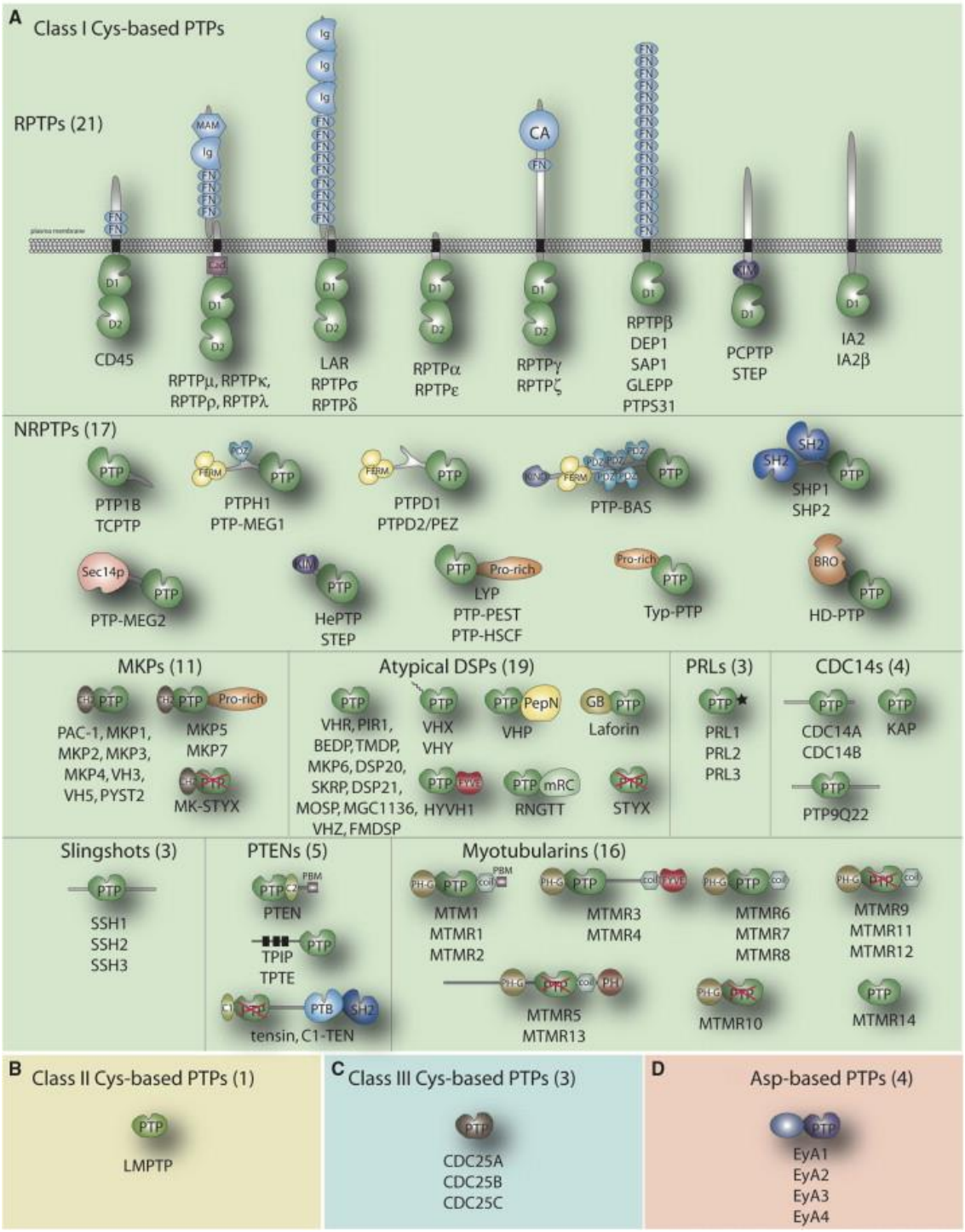


Figure 5.1: Domain structure of all PTPs. Schematic view of the domain composition of all members of the four PTP families. Abbreviations: BRO, baculovirus BRO homology; C1, protein kinase C conserved region 1; C2, protein kinase C conserved region 2; CA, carbonic anhydrase-like; CAAX box, farnesylation signal; CH2, cdc25 homology region 2; CRAL/TRIO, cellular retinaldehyde binding protein/trio homology (Sec14p homology); FERM, band 4.1/ezrin/radixin/moesin homology; FN, fibronectin-like; FYVE, Fab1/Yotb/Vac1p/early endosomal antigen-1 homology; Ig, immunoglobulin-like; KIM, kinase interaction motif; KIND, kinase N lobe-like domain; MAM, meprin, A2, RPTPμ homology; PBM, PDZ binding motif; PDZ, postsynaptic density-95/discs large/ZO1 homology; PH, pleckstrin homology (including GRAM domains); PTB, phosphotyrosine-binding domain; SH2, src homology 2; SH3B, src homology 3 domain binding motif; SH4, src homology 4 (myristylation signal); coil, coiled-coil domain; GB, glycogen binding; mRC, mRNA

capping; PBM, PDZ binding motif; pepN, N-terminal peptidase-like; PH-G, pleckstrin homology-"GRAM" domain; Pro-rich, proline-rich; Sec14, Sec14p homology (or CRAL/TRIO). Small black boxes signify transmembrane stretch. Red crosses over a PTP domain signify catalytically inactive domain. Figure and caption fully adopted from (Alonso A. *et al.*, 2004)

A set of signature motifs in the catalytic active site of phosphatases (Figure 5.2), is required for the hydrolysis of the phosphoric acid monoester of a phosphorylated tyrosine into a phosphate ion and a tyrosine with a free hydroxyl group. The most significant motif is the CX_5R (known as the P-loop), which bears both the cysteine responsible for the nucleophilic attack leading to a cysteinyl-phosphate reaction intermediate, and the arginine for the stabilisation of the reaction transition state (Zhang ZY., *et al.*, 1993, Pannifer ADB., *et al.*, 1998). There is also the KNRY loop, which is involved in phosphotyrosine recognition (Barford D., *et al.*, 1994, Barr AJ., *et al.*, 2009), and a conserved WPD loop with a critical aspartate residue, which acts as a general acid/base in the catalytic mechanism. The WPD loop is highly mobile and adopts many conformations, as seen in crystal structures (Pannifer ADB., *et al.*, 1998, Nam HJ., *et al.* 2005). When the phosphotyrosine-bearing substrate is bound in the active site, the WPD loop adopts a closed conformation, facilitating the protonation of the oxygen of the leaving group in the tyrosine residue. The regeneration of the active site takes place, when the aspartate of the WPD loop acts as a general base by accepting a proton from a water molecule, which leads to the regeneration of the cysteine-SH resting state and the exit of a phosphate ion from the active site (Denu JM. And Dixon JE, 1995, Denu JM., *et al.*, 1996). A postulated secondary substrate binding site, close to the CX_5R loop, was originally identified in PTP1B (Puius YA., *et al.*, 1997, Salmeen A., *et al.*, 2000). However, a

recent large-scale structural analysis showed that this site is also present in a number of RPTPs, and its accessibility is controlled by the multiple conformations of a "second-site loop" (Barr AJ., *et al.*, 2009).

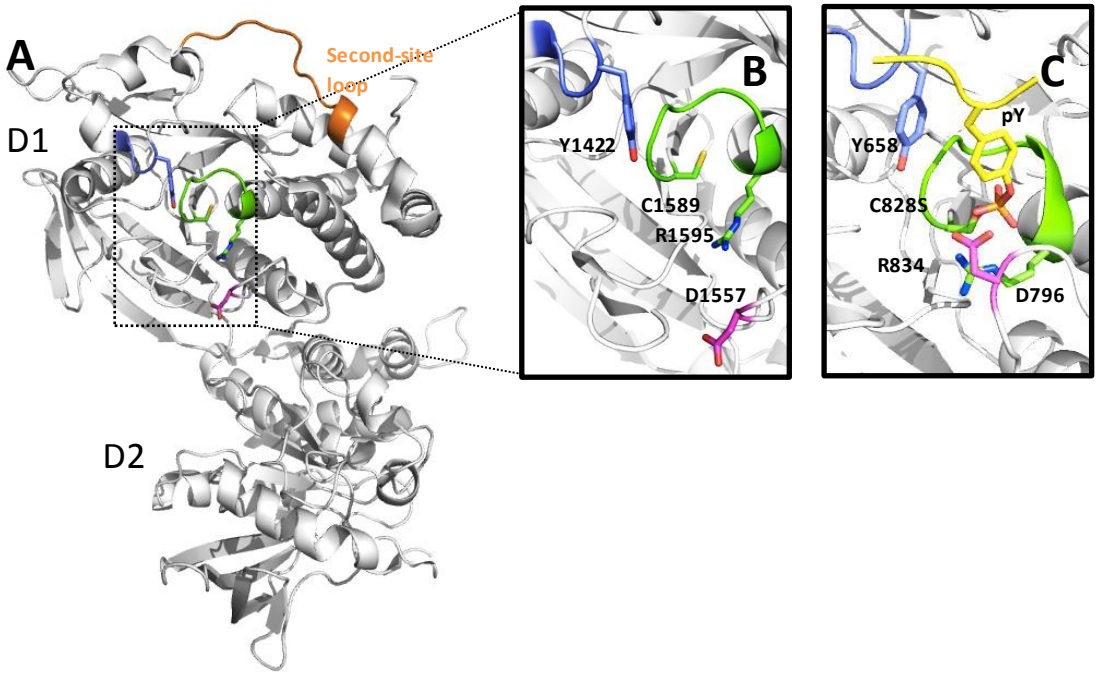


Figure 5.2: Residues involved in the phosphatase catalytic activity. **(A)** Cartoon representation of the tandem phosphatase domains (D1, D2) from RPTPσ (PDB: 2FH7, Almo S., *et al.*, 2007). Key structural motifs are highlighted: blue, phosphotyrosine loop; green, CX_5R loop; pink, catalytic aspartate of the WPD loop; orange, second-site loop. **(B)** A close view of the active site of D1 domain from RPTPσ (PDB: 2FH7, Almo S., *et al.*, 2007), highlighting the open conformation of the WPD loop, in the absence of a phosphotyrosine substrate. **(C)** A close view of the active site of D1 domain from CD45 C828S substrate-trapping mutant in complex with a NPTpYS phosphopeptide (PDB: 1YGU, Nam HJ., *et al.*, 2005), highlighting the closed conformation of the WPD loop, in presence of a phosphotyrosine substrate (yellow).

5.2.2 Regulation of Protein Tyrosine Phosphatases (PTP)

Since phosphatase activity is instrumental in a variety of cellular responses and the aetiology of disease (Tonks NK., 2006), the action of PTPs is tightly regulated with a range of mechanisms. Protein-protein recognition domains, as well as compartmentalisation-targeting domains, direct PTPs to the appropriate subcellular location where they ought to act (Mauro LJ. and Dixon JE. 1994). RPTPs, residing at the plasma membrane, control tyrosine phosphorylation in response to stimulation of Protein Tyrosine Kinase receptors (Ostman A. and Bohmer FD., 2001). RPTPs additionally modulate signal transduction events initiated by cell adhesion with the extracellular matrix (Burridge K., *et al.*, 2006, Sallee JL., *et al.*, 2006). PTPs of the cytoplasm are recruited to phosphorylated cell surface receptors and other scaffolding adaptor protein partners via highly specific protein-protein interaction events performed by SH2 domains (Neel BG., *et al.*, 2003). It has been shown that regions in the structure of non-transmembrane PTPs may have an affinity for phospholipids, as in the case of SHP1 in T lymphocytes and the regulation of T-cell receptor signalling (Sankarshanan M., *et al.*, 2007). Phosphotyrosine-independent interactions have also been demonstrated to be critical for recruitment of PTP, as in the case of PTP1B and insulin receptor (Li S., *et al.*, 2005). Some PTPs are spatially restricted via their interaction with the endoplasmic reticulum (ER), as in the case of PTP1B which bears 35 highly hydrophobic residues on the C-terminus which target the protein to the cytoplasmic face of the ER (Frangioni JV., *et al.*, 1992, Tonks NK., 2003). FRET analyses have indicated that there is a spatial segregation of ER-embedded PTP1B activity in the perinuclear compartment, while the peripheral population exhibits lower activity (Yudushkin IA., *et al.*, 2007).

Alternative splicing events can be instrumental in the regulation of PTP activity. A prominent example is the T-cell PTP (Ibarra-Sanchez MJ., *et al.*, 2000) and its interplay with nucleus-residing phosphorylated STAT family members (Shcindler C., *et al.*, 2007). Alternative splicing products of T-cell PTP can have different nuclear localisation signals, and only the 45 kDa T-cell PTP can effectively shuttle into the nucleus and suppress STAT1 signaling (ten Hoeve, *et al.*, 2002). Alternative splicing can give rise to variant RPTPs in the extracellular region (Pulido R., *et al.*, 1995, Zhang JS. and Longo FM., 1995), which affects their ligand binding recognition profile (Sajnani-Perez G., *et al.*, 2003, Lee S., *et al.*, 2007) or generates ectodomain secreted truncations that engage in ligand interactions (Zhang JS. and Longo FM., 1995, Tabiti K., *et al.*, 1996, Yang T., *et al.*, 2005).

Another mechanism involved in PTP regulation is the proteolytic processing of PTP precursors. The extracellular regions of RPTP precursors are targeted by furin-like proteinases and subtilisin-like convertases during biogenesis, and the mature products are composed of transmembrane/intracellular parts which remain non-covalently associated with extracellular regions (Jiang YP., *et al.*, 1993, Streuli M., *et al.*, 1992). Additional proteolysis can occur when cells reach high densities (Anders L., *et al.*, 2006), which acts as a trigger for shedding of the extracellular region, internalisation and intracellular redistribution of the remaining protein (Aicher B., *et al.*, 1997). ADAM10, a mettalloprotease, performs the shedding in the case of RPTPμ and RPTPκ, while γ-secretase is responsible for subsequent intra-membrane cleavage (Anders L., *et al.*, 2006). Similar processing events have been reported recently for LAR (Haapasalo A., *et al.*, 2007). The crystal structure of the full extracellular region of RPTPμ revealed that it forms homophilic (trans) antiparallel dimers that act as sensors of the cell-cell junctions

and regulate the phosphatase action by a "spacer-clamp" mechanism. Shedding of the ectodomain serves then to allow for truncated RPTPμ molecules to exit the junction (Aricescu AR., *et al.*, 2007).

The elevation of reactive oxygen species (ROS) in response to cell adherence and density, UV radiation and cell migration, can negatively regulate the activity of phosphatases through the reversible oxidation of their catalytic site (Rhee SG., 2006, Salmeen A. and Barford D., 2005). Crystallographic analyses of oxidised PTP1B and RPTPα showed the catalytic cysteine to be involved in a sulphonamide species with the backbone nitrogen of a neighboring serine (Salmeen A., *et al.*, 2003, van Montfort RL., *et al.*, 2003). Such a temporary inactivation of phosphatases is believed to shift reversibly the balance of signalling outcomes through PTK pathways, thus affecting the delicate control of tyrosine phosphorylation on the cell (Tonks NK., 2005, Ostman A. and Bohmer FD., 2001).

Dimerisation of transmembrane proteins, induced by ligand binding to the extracellular parts has been an established model of catalytic domain activation in the case of PTKs (Lemmon MA. and Schlessinger J., 1994). According to the model, ligand binding events bring receptors in proximity and transphosphorylation takes place via their catalytic domains (Schlessinger J., 1988, Heldin CH., 1995). In the case of epidermal growth factor receptor (EGFR) the separate catalytic domains were found to be autoinhibited, and the receptor activation was facilitated by intermolecular interaction similar to those of Src and cyclin-dependent kinases (Zhang X., *et al.*, 2006). However, dimerization appears to lead to receptor inactivation in the context of RPTPs, as it has been demonstrated for RPTPα and CD45 (Jiang G., *et al.*, 1999, Jiang G., *et al.*, 2000, Takeda A., *et al.*, 2004). The crystal structure of RPTPα catalytic domain suggested that dimerised RPTPs were

subjected to inhibition due to a wedge mechanism (Jiang G., *et al.*, 1999). In the structure the symmetrical dimer of catalytic domain D1, each of the catalytic domains appear to extend a loop into the active site of the other, while structure-based mutants on this "wedge" region restored the catalytic activity (Jiang G., *et al.*, 1999). The wedge mechanism has not been observed in structures of catalytic domains from LAR, CD45 and RPTPσ, where D1 domains appear to be monomeric (Nam HJ., *et al.*, 1999, Nam HJ., *et al.*, 2005, Almo S., *et al.*, 2007). Tandem catalytic domains appear to be monomeric in solution as well, with the exception of RPTPγ (Barr AJ., et al., 2009). The crystal structure of RPTPγ revealed a "head-to-toe" arrangement, where a D2 domain blocks the D1 domain of the opposing molecule in the assymetric unit, suggesting a unique mechanism for the RPTP subfamily V (Barr AJ., et al., 2009).

5.2.3 An overview of the receptor protein tyrosine phosphatase subfamily

5.2.3.1 RPTP domain organisation and classification

The RPTP family (a subset of the PTP superfamily) contains 21 type I membrane protein members organised in 8 distinct subfamilies, based on domain composition (Figure 5.3). Members of the RPTP family are mediators of signalling events affecting cell growth, neural development and immune response (Tonks NK., 2006, Alonso A. *et al.*, 2004). The 21 family members are comprised of a single transmembrane helix, a variable domain composition in the extracellular region (subfamily specific) and either one or two phosphatase domains on the intracellular side (Figure 5.3). Work presented in this thesis focuses on RPTPσ, which is a member of the type IIa subfamily of RPTPs, and consists of

three immunoglobulin (Ig)-like domains, followed by nine fibronectin (FN) type III repeats. The RPTP type IIa precursors are cleaved intracellularly by subtilisin-like endopeptidase and their extracellular region remains non-covalently attached with the rest of the protein (Pulido R., *et al.*, 1995, Streuli M., *et al.*, 1992).

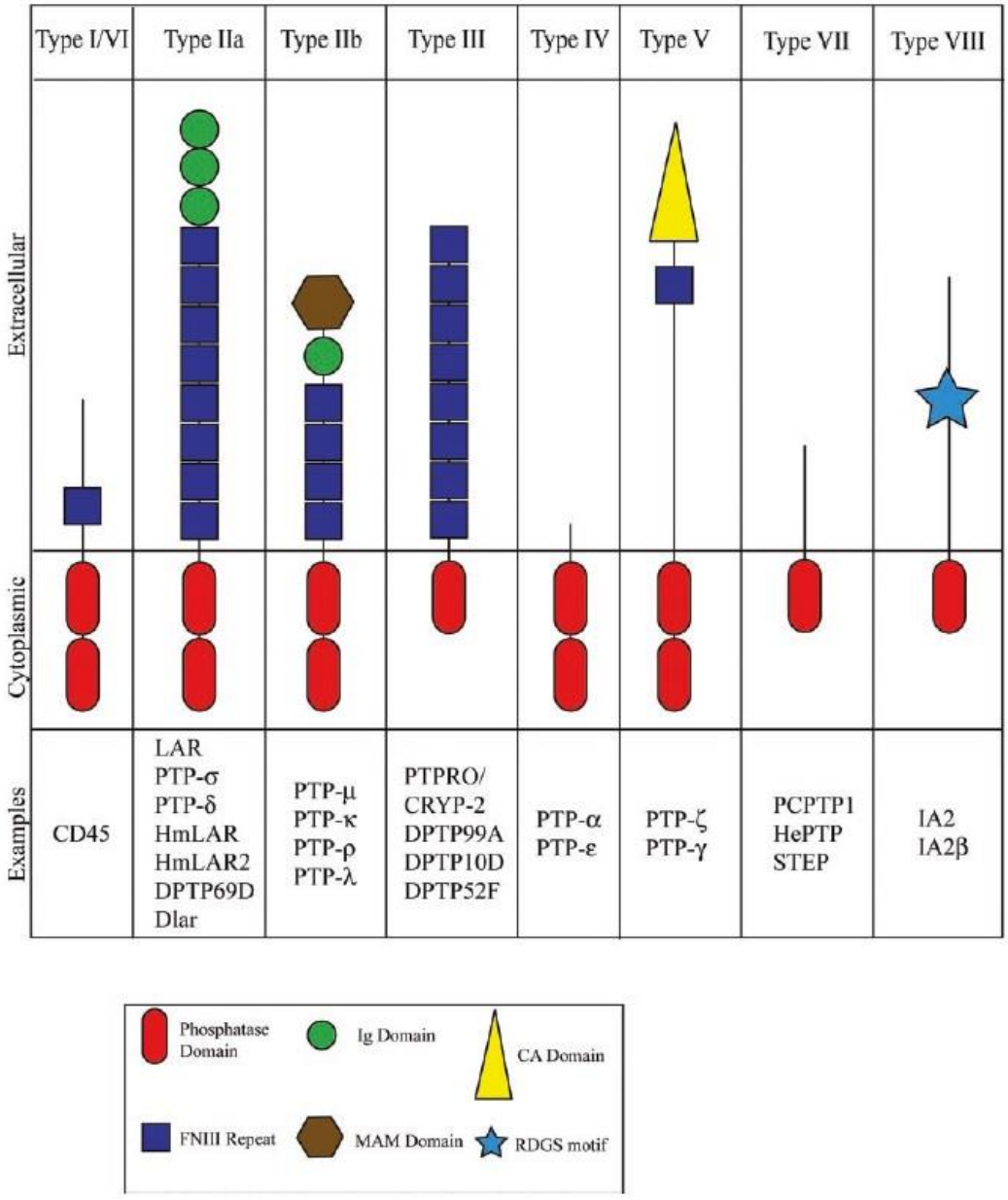


Figure 5.3: Schematic representation of the eight subfamilies of receptor protein tyrosine phosphatases (RPTPs). Certain family members deviate from the domain representation presented above. For example, Dlar has 9 instead of 8 FNIII domains while DPTP99A has 2 instead of 1 phosphatase domain. (Figure adopted from Johnson KG., and Van Vactor D., 2003)

The three vertebrate type IIa RPTPs have distinct expression patterns in the developing nervous system, and alternative splicing increases their structural diversity (Pulido R., et al., 1995 , Stoker AW., 1994, Schaapveld R., *et al.*, 1997, Zhang JS. and Longo FM., 1995, Johnson KG., and Holt CE., 2000, Stoker AW., *et al.*, 1995). RPTPσ is predominantly expressed in the nervous system, however longer isoforms can be also detected in the lung and heart at significantly lower levels (Yan H., *et al.*, 1993). RNA in situ hybridisation analyses showed that LAR is expressed in basal lamina-associated epithelial tissues of (neuro)ectodermal, neural crest/ectomesenchyme and endodermal origin, while RPTPδ and RPTPσ are found in tissues of neuronal and mesodermal origin (Schaapveld R., *et al.*, 1997).

5.2.3.2 Type IIa RPTP knock-out studies

Animal studies showed that knocking out type IIa RPTPs leads to multiple neurological defects. Mice lacking RPTPσ exhibit abnormal limb flexion, consistent with cerebellar defects and neuroendocrine defects (Wallace MJ., *et al.*, 1999, Elchebly M., *et al.*, 1999), have enhanced levels of nerve regeneration after spinal cord injury (McLean J., *et al.*, 2002, Shen Y., *et al.*, 2009, Fry EJ., *et al.*, 2010), and show susceptibility to ulcerative colitis (Muise AM., *et al.*, 2007). Mice lacking RPTPδ exhibit spatial learning and memory impairment and semi-lethality due to insufficient food intake (Uetani N., *et al.*, 2000), while an association with restless leg syndrome has also been reported (Schormair B., *et al.*, 2008). Double knock-out mutant mice of RPTPδ and RPTPσ exhibit total paralysis due to severe motor neuron axon targeting defects (Uetani N., *et al.*, 2006). LAR deficient models (with a portion of the extracellular region still detectable though) are less

severely affected. However, they display impaired mammary gland development (Schaapveld R., *et al.*, 1997), forebrain cholinergic innervation defects (Yeo TT., *et al.*, 1997), and hyperactivity and spatial learning impairment (Kolkman MJM., *et al.*, 2004). In *Drosophila*, where there is only a single type IIa RPTP member, deletion of dLAR leads to severe axon guidance defects (Krueger NX., *et al.*, 1996), suggesting that functional redundancy may be present in vertebrate RPTPs.

5.2.3.3 Type IIa RPTP ligands

The modular structure of RPTPs implies the presence of a non-specific multicomponent ligand binding network that regulates RPTP localization, oligomerisation, conformation and ultimately signal transduction. However, identifying ligands for the RPTPs has been an inherently difficult task, leaving still a number of receptors orphan. A number of RPTPs have been reported to exhibit homophilic interactions, such as the already mentioned RPTPμ interactions at the adherens junctions (Aricescu AR., *et al.*, 2007) and the homophilic interaction effects of RPTPδ and LAR on the promotion of neurite outgrowth (Wang J. and Bixby JL., 1999, Yang T., *et al.*, 2003). Heterotypic partners for RPTPs have also been identified. RPTPσ binds to the heparan sulfate proteoglycans Agrin and Collagen XVIII (Aricescu AR., *et al.*, 2002), neurocan chondroitin sulfate proteoglycan (Shen Y., *et al.*, 2009), cell surface nucleolin on developing muscle tissues (Alete DE., *et al.*, 2006), α-latrotoxin (Krasnoperov V., *et al.*, 2002), tyrosine receptor kinases A and C (Faux C., *et al.*, 2007), Netrin-G ligand 3 (NGL3) (Kwon WK., *et al.*, 2010), Slitrks1-3 (Yim YS., *et al.*, 2013) and intracellular Liprin-α (Serra-Pages C., *et al.*, 1995). RPTP LAR has been reported to bind heparan sulphate proteoglycans Syndecan and Dallylike (Fox AN.

and Zinn K., 2005, Johnson KG., *et al.*, 2006), NGL3 (Woo J., *et al.*, 2009), Laminin/Nidogen complex (O'Grady P., *et al.*, 1998), intracellular Liprin-α (Serra-Pages C., *et al.*, 1998) and Rac/Rho-specific guanine nucleotide exchange factor domain containing Trio (Debant A., *et al.*, 1996). RPTPδ has been reported to bind NGL3 (Kwon WK., *et al.*, 2010), intracellular Liprin-α (Serra-Pages C., *et al.*, 1995) and all Slitrks (1-6) (Yim YS., *et al.*, 2013).

5.2.3.4 Type IIa RPTP involvement in synapse formation

It has been shown that type IIa RPTPs have roles in excitatory and inhibitory synaptic development (figure 5.4). LAR has been reported to be concentrated in matured synapses of rat hippocampal cultures and RNAi knockdown of LAR or dominant-negative disruption of its function resulted in loss of excitatory synapses (Dunah AW., *et al.*, 2005). LAR has also been shown to be required for post-synaptic clustering of AMPA receptors (Wyszynski M., *et al.*, 2002). Liprin-α, an intracellular scaffolding factor involved in pre-synaptic organisation (Serra-Pages C., *et al.*, 1995), binds to the D2 phosphatase domain of LAR and mediates the dephosphorylation of β-catenin (Dunah AW., *et al.*, 2005). LAR signalling effect is subsequently transduced to the actin cytoskeleton, through the β-catenin/N-cadherin interaction (Siu R., *et al.*, 2007), and regulates synaptic adhesion. The interaction between NGL3/LAR leads to excitatory presynaptic differentiation (Woo J., *et al.*, 2009), the interaction between NGL3/RPTPσ was shown to induce post-synaptic PSD-95 clustering on dendrites and pre-synaptic differentiation (Kwon SK., *et al.*, 2010), while the NGL3/RPTPδ interaction was found to only induce pre-synaptic differentiation (Kwon SK., *et al.*, 2010). Interestingly RPTPδ has been demonstrated to be involved in inhibitory

synapse development via its direct *trans*-synaptic interaction with Slitrk3 (Takahashi H., *et al.*, 2012, Yim YS., *et al.*, 2013). RPTPδ has been involved in excitatory synaptic formation via its interaction with Interleukin-1 receptor accessory protein (IL-1RAcP) (Yoshida T., *et al.*, 2012). Recent studies have demonstrated bidirectional excitatory synapse establishment via the nanomolar interaction between TrkC and RPTPσ (Takahashi H., *et al.*, 2011). TrkC was shown to mediate clustering of post-synaptic proteins in dendrites and glutamatergic synaptic adhesion in a neurotrophin-independent manner (Takahashi H., *et al.*, 2011).

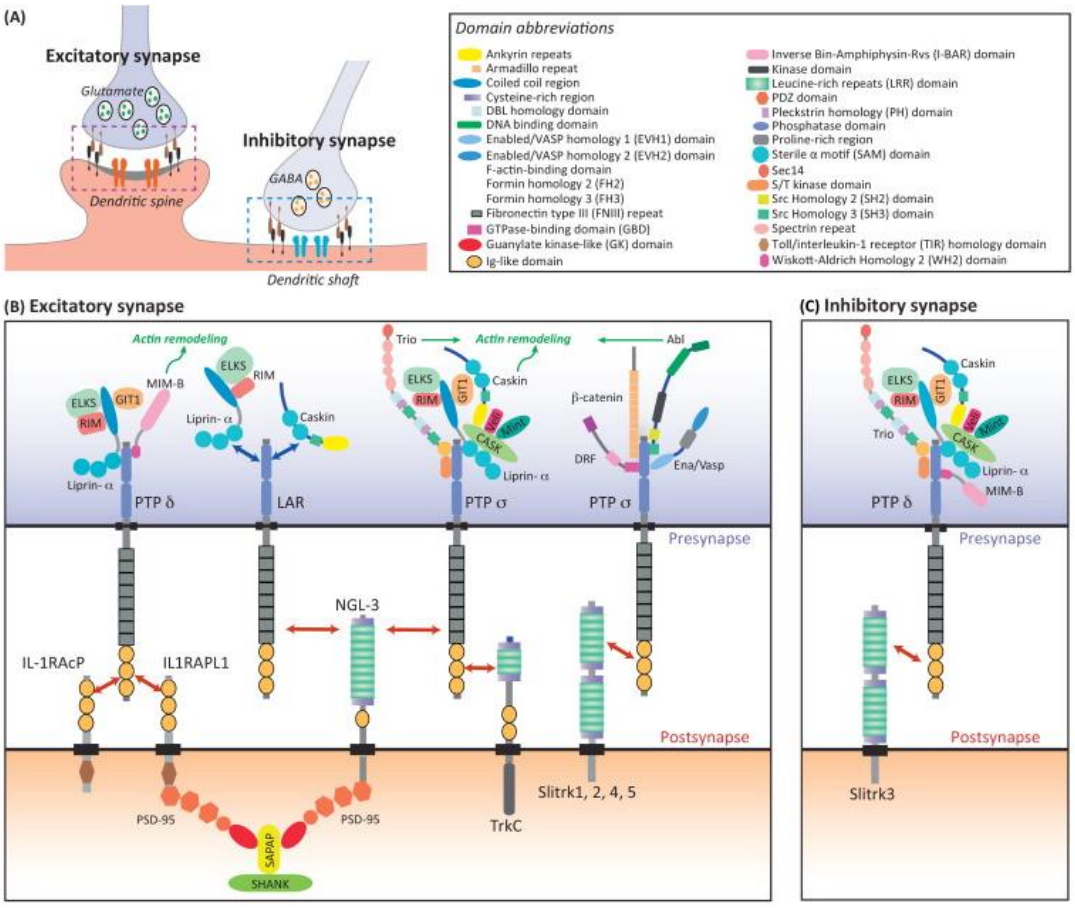


Figure 5.4: Schematic representation of the control of excitatory and inhibitory synaptic establishment by type IIa RPTPs and their *trans*-synaptic interactions (Figure adopted Um JW. and Ko J., 2013).

5.2.4 Proteoglycan regulation of axon guidance

Proteoglycans are bimodal macromolecules that have a protein core with glycosaminoglycan (GAG) chains of repeated saccharide units covalently attached. GAG chains are characterised by their sulfation pattern, which is enzymatically modified and provides negatively charged domains available for interactions with proteins (Bernfield M., *et al.*, 1999). Proteoglycans have been reported to play instrumental roles in axon guidance (de Wit J. and Verhaagen J., 2007). Heparin sulphate proteoglycans (HSPGs) normally potentiate axon growth while chondroitin sulphate proteoglycans (CSPGs) lead to inhibition of neuronal extension (Bandtlow CE. and Zimmermann DR., 2000, Van Vactor D., *et al.*, 2006, Lee JS. and Chien CB., 2004, Silver J. and Miller JH., 2004). CSPGs have been found in areas where neural crest cells cannot migrate, and inhibition of CSPGs biosynthesis affects the neural crest cells migration patterns (Kubota Y., *et al.*, 1999). Additionally, axonal penetration has been demonstrated to be inhibited by the presence of CSPGs (Landolt RM., *et al.*, 1995, Oakley RA. and Tosney KW., 1991, Oakley RA., *et al.*, 1994, Ring C., *et al.*, 1996). Recent studies link such effects with direct interactions of CSPGs with RPTPσ (Shen Y., *et al.*, 2009, Coles CH., *et al.*, 2011). Retinal axons have been demonstrated to be able to grow into areas that were originally repulsive after treating them with chondroitin ABC lyase (Brittis PA., *et al.*, 1992). HSPGs have been demonstrated to stimulate neurite growth through interaction and activation of amyloid protein precursor (Small D., *et al.*, 1994, Williamson TG., *et al.*, 1995), laminin (Bronner-Fraser M. and Lallier T., 1988) and fibroblast growth factor-2 (FGF2) (Walicke PA., 1988). There are also data demonstrating the presence of glypican-2 and syndecan-3 in rat axonal tracts during active growth and the recognition of syndecan-3 by an extracellular

growth promoting factor, heparin-binding growth-associated molecule (HB-GAM) (Ivins JK., *et al.*, 1997, Raulo E., *et al.*, 1994, Kinnunen A., *et al.*, 1998, Kinnunen A., *et al.*, 1999). Recent crystallographic analysis of RPTPσ revealed that a shared, conformationally plastic binding site for HSPGs and CSPGs facilitates the regulation of receptor oligomerisation and subsequent control on neuronal extension (Coles CH., *et al.*, 2011).

5.2.5 Proteoglycan mediation of synapse formation

The role of HSPGs in the establishment of synapses and synaptic plasticity has been demonstrated. Early studies implicated agrin signalling in the organisation of the neuromuscular junction (Nitkin RM., *et al.*, 1987, Reist NE., *et al.*, 1987). The role of agrin in the stabilisation of the developing synapse has been revealed by stimulating the MuSK-mediated phosphorylation of acetylcholine receptors and inducing their clustering (Herbst R. and Burden SJ., 2000). Syndecan-2 has been found to be responsible for the induction of filopodia formation before spinogenesis, via the neurofibromin-PKA-Ena/VASP pathway (Lin YL., *et al.*, 2007). CSPGs have been implicated in the postnatal developmental maturation of CNS, as the main building block of specialised extracellular matrix scaffolding structures called perineuronal nets (PNNs). PNNs primarily consist of CSPGs of the lectican family (aggrecan, neurocan, versican and brevican), phosphacan, tenascin-R, hyaluronan synthase (HAS) and other link proteins (Kwok JCF., *et al.*, 2010). The organisation of CSPGs into perineuronal nets coincides with the critical period termination of plasticity in the visual cortex (Pizzorusso T., *et al.*, 2002). A recent study utilising *in vivo* imaging*, in vitro* two photon microscopy and electrophysiology after enzymatic digestion of CSPG GAG chains, demonstrated a higher motility of cortical

motility and plasticity in the adult visual system (de Vivo L., *et al.*, 2013). The enzymatic removal of CSPG GAG chains had also a severe effect on hippocampal long-term potentiation and long-term depression in splice cultures (Bukalo O., et al., 2001). The molecular mechanism by which the CSPGs affect synaptic plasticity remains elusive.

It has been shown in the *Drosophila* that HSPGs Syndecan and Dallylike can control different aspects of neuromuscular junction organisation. Syndecan has been demonstrated to induce the growth of presynaptic terminals, while Dallylike controls the active zone stabilisation (Johnson KG., et al., 2006). Both proteins have been found to exert their synaptic effects through their interaction with the *Drosophila* dLAR, showing that Syndecan promotes, while Dallylike inhibits LAR or the control of synapse morphogenesis (Figure 5.5).

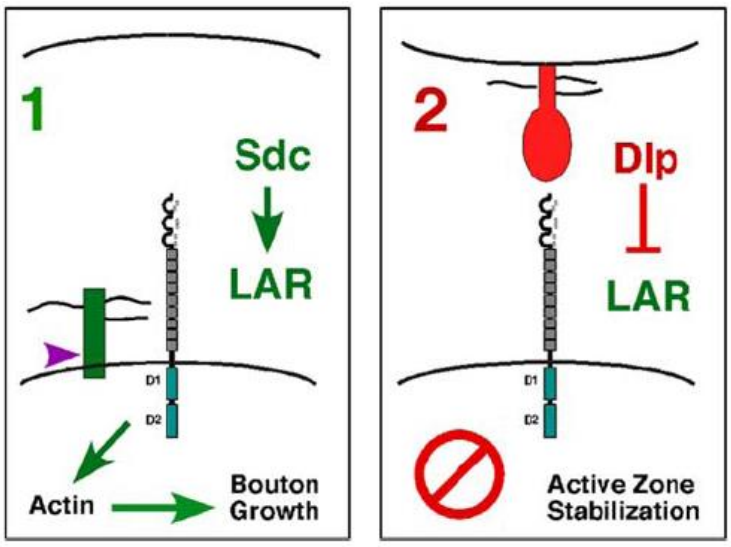


Figure 5.5: Schematic representation of Syndecan and Dallylike interplay with dLAR, in the the regulation of neuromuscular junction morphogenesis in *Drosophila*. Syndecan (Sdc) (green) promotes LAR to induce bouton growth **(1)**, in a phosphatase dependent manner. Dallylike (Dlp) (red) inhibits LAR activity and thus suppress growth signals required for active zone formation **(2)**. (Figure adopted from Johnson KG., *et al*., 2006)

Recently it was demonstrated that mammalian homologs of dallylike, glypicans 4 and 6 can be secreted from astrocytes and promote synaptic clustering of AMPA receptors and subsequent excitatory synapse formation in retinal ganglion cells, even though they are not interacting with AMPA receptors (Allen N., *et al.*, 2012). Whether glypicans exert their synaptic effects by simultaneous in *cis* interaction with co-receptors, such as LAR-RPTPs or neurexins, is currently an open question. Post-synaptic LRRTM4 has also been involved in *trans*-synaptic modulation of excitatory synaptic establishment and function via interaction with HSPGs (Siddiqui TJ., *et al.*, 2013, de Wit J., *et al.*, 2013). Knocking down LRRTM4 in cortical pyramidal neurons decreases the number of dendritic spines (de Wit J., *et al.*, 2013) and impairs activity dependent AMPA receptor trafficking (Siddiqui TJ., *et al.*, 2013). The transynaptic interaction is confirmed by the bidirectional effect of the HSPG regulation, since LRRTM4 promotes Glypican-4 clustering in contacting axons and glypican-4 induces LRRTM4 clustering in contacting dendrites in a HS-dependent manner (de Wit J., *et al.*, 2013). It remains to be seen whether involving other known *trans*-synaptic adhesion events are dependent on proteoglycan control (Figure 5.6).

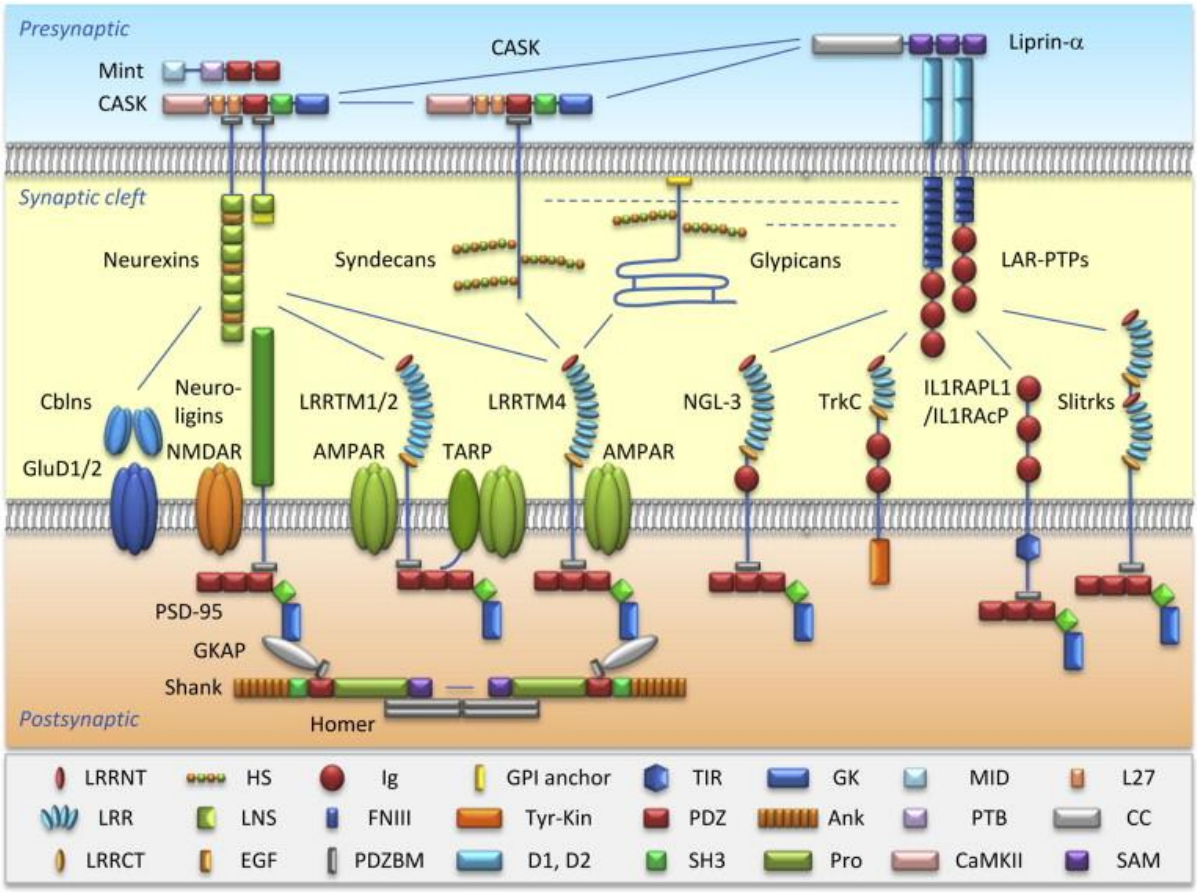


Figure 5.6: Schematic representation of *trans*-synaptic interactions documented to mediate excitatory synapse development. Established trans-synaptic interactions involving neurexins, LAR-RPTPs and HSPGs are depicted with straight lines. Potential interactions are depicted with dotted lines (Figure adopted from Song YS. and Kim E., 2013)

5.2.6 An overview of neurotrophin signalling

Neurotrophic factors constitute a family of diffusible proteins that promote neuronal survival and differentiation as well as neurite outgrowth (Reichardt LF., 2006). The first family member to be discovered, the Nerve Growth Factor (NGF), was identified as a factor that could explain deleterious effects of target tissue removal on the subsequent survival of motor and sensory neurons (Hamburger V. and Levi-Montalcini R., 1949). Later, it was demonstrated that NGF exhibits trophic effects in a variety of cell

populations in the CNS as well, such as during the development and survival of basal forebrain cholinergic neurons (Dreyfus CF., 1989).

According to the general model of neurotrophic factor action, these trophic agents are produced in limited amounts by neuronal or non-neuronal target cells and are detected by the axonal projections of innervating neurotrophin-sensitive neurons during development (Thoenen H., 1995). NGF has been demonstrated to be internalised through receptor-dependent mechanisms and transported by cytoskeletal mediators in vesicular structures across axons (Thoenen H. and Barde YA., 1980, Grimes ML., *et al.*, 1996, Grimes ML., *et al.*, 1997, Howe Cl., *et al.*, 2001). The establishment of a retrograde information flow up the axon to the cell body leads to gene expression and survival (Ginty DD. and Segal RA., 2002). Cells that do not exhibit this neurotrophin-triggered retrograde response fail to differentiate (Barde YA., 1989), degenerate and succumb to neuronal cell death, naturally occurring during early development (Ginty DD. and Segal RA., 2002). The second member of the family, Brain-derived neurotrophic factor (BDNF) was purified from pig brains and was characterised as a factor that exhibits trophic effects on CNS cell populations that did not respond to NGF (Barde YA., *et al.*, 1982). The high amino-acid sequence conservation (Leibrock J., et al., 1989) and the similar functional effects with NGF provided leads to isolate and characterise other members of the family, which currently consists of four members in mammals: NGF, BDNF, Neurotrophin-3 (NT-3) and Neurotrophin-4 (NT-4). All neurotrophic factors are derived from precursor molecules, the proneurotrophins (30-35 kDa), which upon maturation are cleaved to the final products (12-13 kDa) (Lu Y. and Gottschalk W., 2000). The maturation process by proteolytic cleavage is tightly regulated and refines functional specificity (Lee R., *et al.*,

2001). All neurotrophins, before and after maturation, bind with high affinities to a member of the Tumor Necrosis Factor family of receptors, the p75 receptor (Johnson D., *et al.*, 1986, Dechant G. and Barde YA., 2002), while the mature products bind Tropomyosin receptor tyrosine kinases (Trks) with defined specificities (Kaplan DR., *et al.*, 1991, Klein R., et al., 1991, Kaplan DR. and Miller FD., 2000) (Figure 5.7). Mature NGF activates TrkA, BDNF and NT-4 activate TrkB, while NT-3 activates TrkC (Chao MV. and Hempstead BL., 1995) (Figure 5.7).

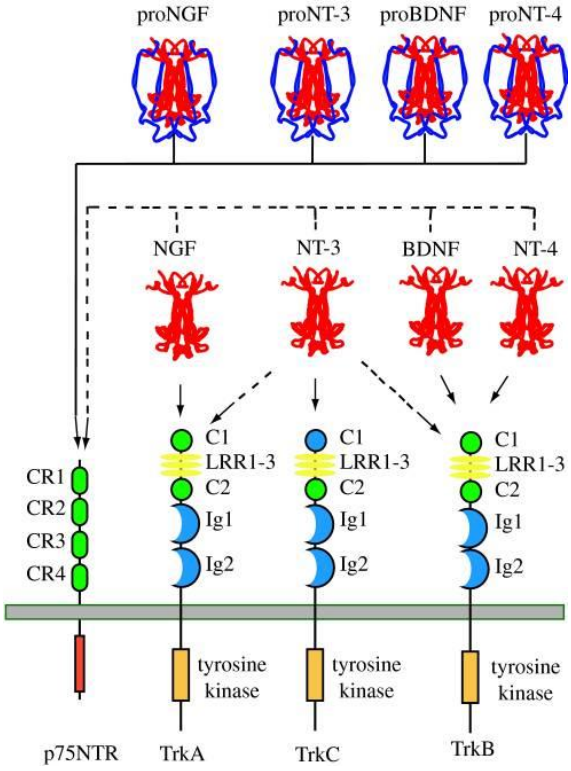


Figure 5.7: Neurotrophin–receptor interactions. This illustrates the major interactions of each of the four mammalian neurotrophins. Each proneurotrophin binds p75NTR, but not the Trk receptors. Following maturation through proteolysis of the proneurotrophins, each mature neurotrophin is able to bind and activate p75NTR, but exhibits more specific interactions with the three Trk receptors. (Image and caption partially adopted from Reichardt LF., 2006)

As mentioned in Chapter 3, autophosphorylation as a result of ligand-mediated oligomerisation is an established model for receptor protein tyrosine kinases (Weiss A. and Schlessinger J., 1998) and typically applies to Trk receptors, which are dimerised by neurotrophin binding and are transphosphorylated in the activation loop of their kinase domains (Huang EJ. And Reichardt LF., 2003). Phosphorylated residues in the cytoplasmic region of Trk receptors act as the keylocks for several adaptor macromolecules and enzymes, containing Src homology 2 or other phosphotyrosine-binding domains that will facilitate the propagation of the signal seeded by neurotrophin on the extracellular side (Segal RA. and Greenberg ME., 1996). Trk receptor activation by neurotrophins leads to the subsequent activation of Ras, phosphatidylinositol—3-kinase, Rac and phospholipase C-γ1 pathways (Segal RA. and Greenberg ME., 1996, Huang EJ. And Reichardt LF., 2003). Neurotrophin signalling via trk receptors have been increasingly implicated in promoting the genesis, maturation and stability of excitatory glutamatergic and inhibitory synapses in the CNS (reviewed in Vicario-Abejon C., et al., 2002).

Structural data for NGF, NT-3 and NT-4, as well as heteromers formed between BDNF and NT-3 or NT-4 monomer revealed a highly conserved dimeric fold with attributes observed in other growth factors, such as the platelet derived growth factor and the transforming growth factor-β (TGF-β) (McDonald NQ., *et al.*, 1991, Robinson RC., *et al.*, 1995, Butte MJ., *et al.*, 1998). Structural analyses of interactions with receptors have also become available. NGF has been demonstrated to form homodimeric complexes with the C-terminal immunoglobulin ligand-binding domain of TrkA (Wiesmann C., *et al.*, 1999), while a crystallographic analysis of NGF interaction with p75 receptor showed a 2:1 stoichiometry which left one side of NGF still available (He XL. and Garcia KC., 2004). A

structural investigation between NGF and the complete extracellular region of TrkA demonstrated that a direct TrkA-p75 interaction within a trimeric arrangement seeded by NGF is unlikely, suggesting that the signalling effects of the pathways activated by these two receptor systems converge on downstream nodes (Wehrman T., *et al.*, 2007).

Mutations in human genes of neurotrophin or neurotrophin receptors have been associated with a number of genetic diseases. Thirty seven distinct nonsense, missense, frameshift and splice-site trkA mutations have been identified in congenital insensitivity to pain with anhydrosis (CIPA) patients (Indo Y., 2001). The dominant Y722C *de novo* missense mutation in trkB receptor has been shown to impair receptor autophosphorylation and MAP kinase signaliing in a patient with hyperphagic obesity and nociception, learning and memory impairment (Yeo GS*., et al.*, 2004). Lastly, a val66met polymorphism was shown to impact hippocampal function and episodic memory in human subjects, by affecting intercellular trafficking and activity-dependent secretion of BDNF (Egan MF., *et al.*, 2003).

5.3 Aims

The aim of this project was to generate structural information for TrkC/RPTPσ interacting domains and dissect, through subsequent biophysical analyses and cellular studies (from collaborators), the molecular mechanism that enables the proteoglycan regulation of TrkC/RPTPσ to exert effects on excitatory synapse establishment and function.

5.4 Expression and purification of RPTPσ and TrkC proteins

5.4.1 Small scale expression of RPTPσ and TrkC proteins

Constructs targeting the extracellular region of mouse TrkC, containing the leucine rich repeat region (LRR) as well as the first subsequent immunoglobulin-like domain (Ig), and the N-terminal region of the extracellular portion of the human RPTPσ, containing three Ig domains, were expressed in HEK293T cells as described in section 2.2.1.2 (Figure 5.8). Constructs included wild-type proteins, as well as structure-based mutants derived from previous work performed by Dr. Charlotte Coles. The full list of constructs used in experiments presented in this chapter, is presented in Appendix B.

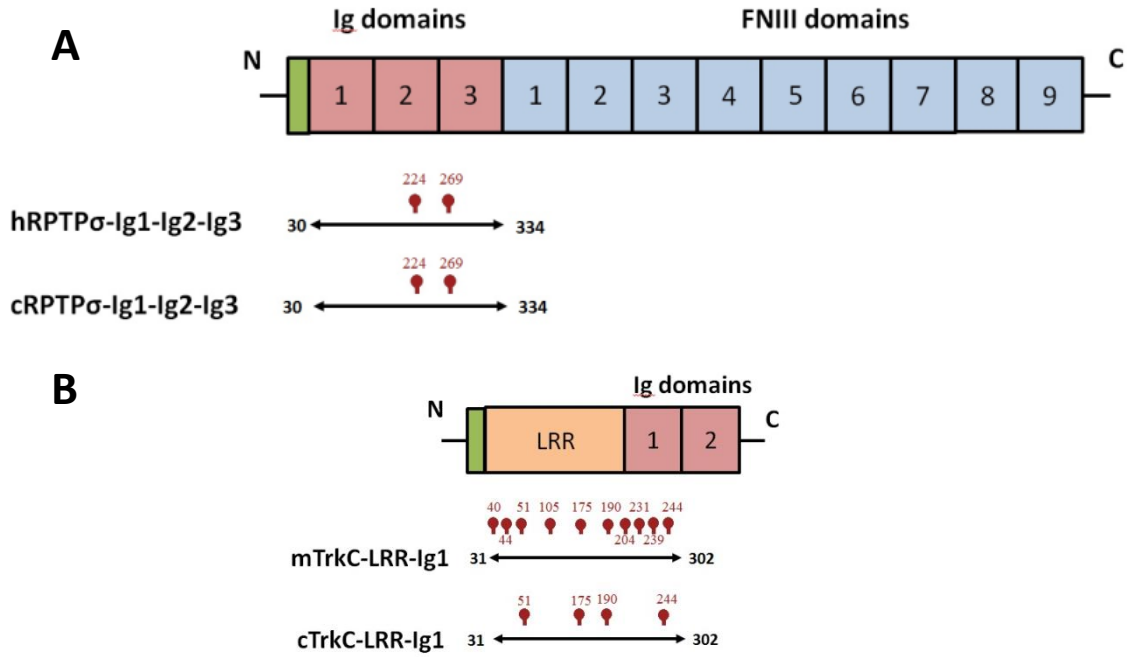


Figure 5.8: Schematic domain representation and boundaries for protein constructs used within the experimental context of this chapter for RPTPσ **(A)** and TrkC **(B)**. A full list of designed site mutants are provided in Appendix B. Predicted N-linked glycosylation sites are depicted as brown blobs (NetNGlyc 1.0 server, CBS, Denmark, Gupta R. and Brunak S., 2002).

5.4.2 Large scale expression of RPTPσ and TrkC proteins

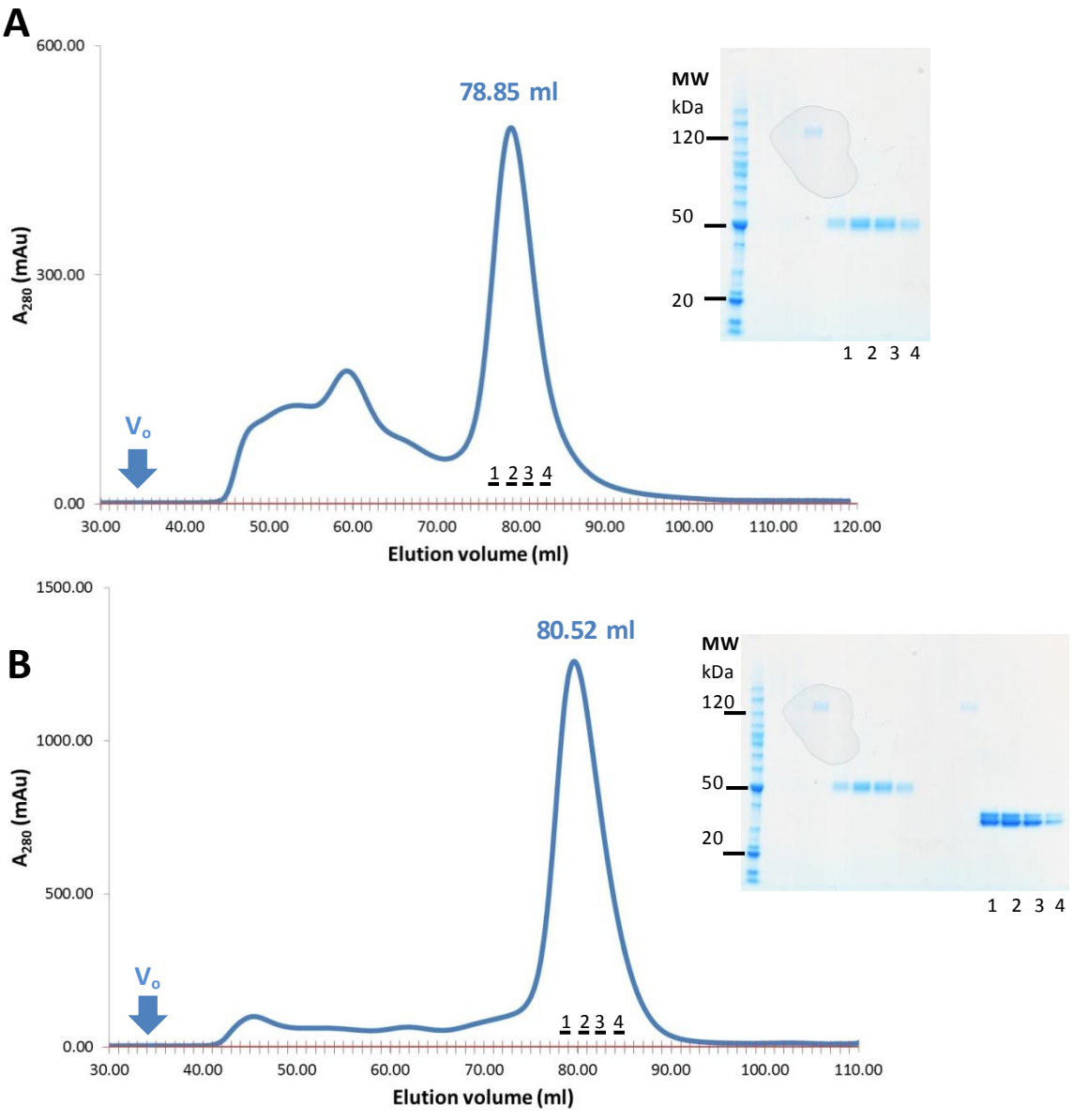
Mouse TrkC-(LRR-Ig1), human RPTPσ-(Ig1-Ig2-Ig3) as well as their chicken homologs, were expressed in HEK293 cells, as described in detail in section 2.2.1, at high levels, as shown in Table 5.1. A mutant hRPTPσ-(Ig1-Ig2-Ig3)-QuadK, required for the biophysical experiments described in section 5.5, was also expressed in large scale. In the case of chicken proteins, HEK293S cells were used for expression due to the prediction of multiple N-glycosylation sites (using the NetNGlyc 1.0 server, CBS, Denmark, Gupta R. and Brunak S., 2002) (figure 5.8), while in the case of proteins derived from mouse or human HEK293T cells were used as the expression system, since these homologs were used for biophysical assays and the native glycosylation pattern was required. Construct boundaries are presented in Appendix B.

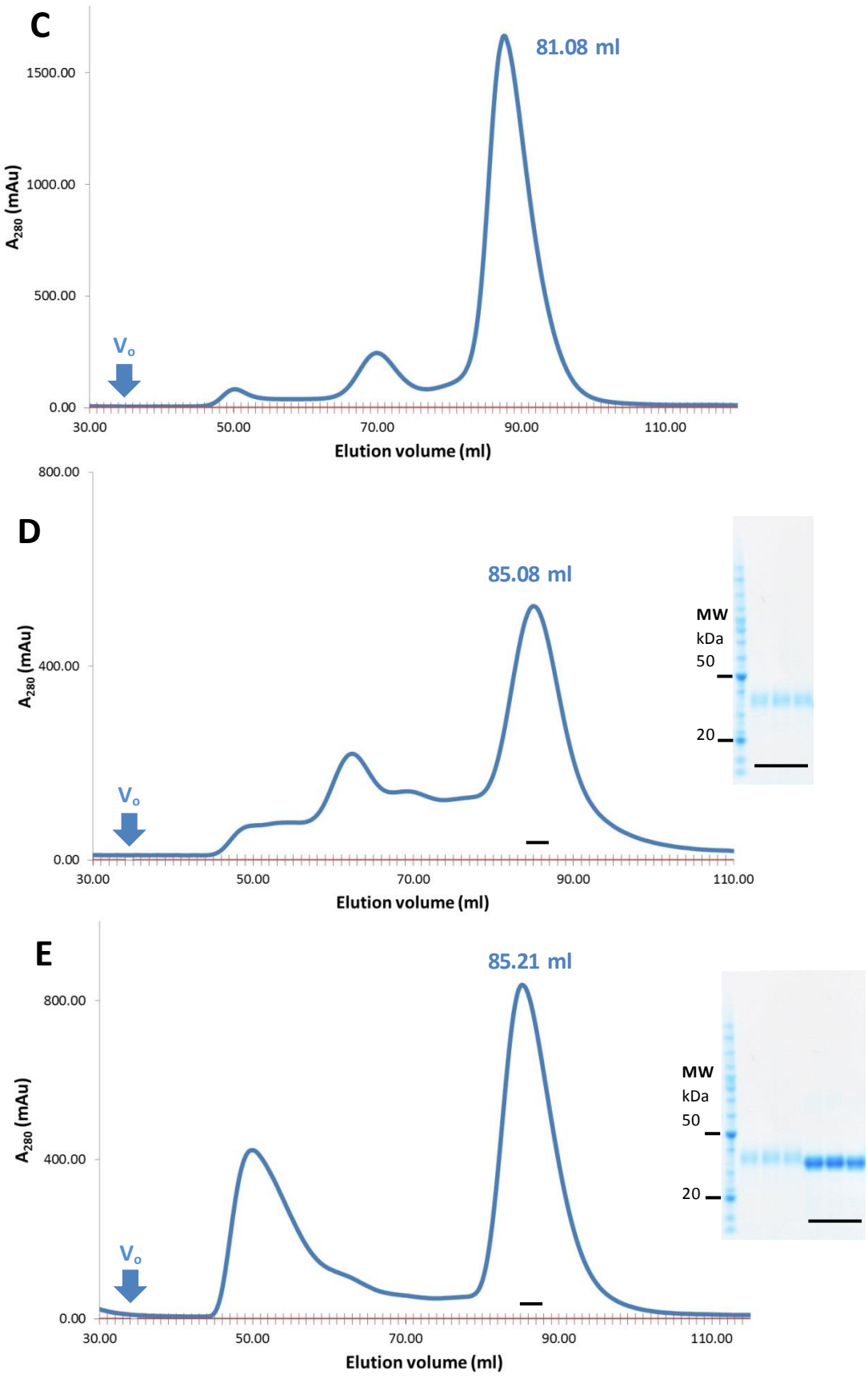
	Cell volume	**Yield**
Chicken TrkC-(LRR-Ig1)	~ 3 L [12 Roller Bottles]	2.011 mg
Chicken RPTPσ-(Ig1-Ig2-Ig3)	~ 3 L [12 Roller Bottles]	55.39 mg
Mouse TrkC-(LRR-Ig1)	~ 2 L [8 Roller Bottles]	2.42 mg
Human RPTPσ-(Ig1-Ig2-Ig3)	~ 1 L [4 Roller Bottles]	~ 7 mg
Human RPTPσ-(Ig1-Ig2-Ig3)-QuadKmutant	~1.5 L [6 Roller Bottles]	~ 9 mg

Table 5.1: Expression levels of RPTPσ and TrkC. Yields stated for TrkC proteins correspond to final amounts at the end of the purification process, while RPTP yields correspond to amounts calculated after the IMAC step.

5.4.3 Purification of RPTPσ and TrkC proteins

Ni-affinity purification of cRPTPσ-Ig1-Ig2-Ig3 (~35.9 kDa), hRPTPσ-Ig1-Ig2-Ig3 (~36 kDa), cTrkC-LRR-Ig1 (~39.8 kDa) and mTrkC-LRR-Ig1 (~46.3 kDa) was performed as described in section 2.2.4.2. High imidazole elution fractions were subsequently gel purified, as described in section 2.2.4.4 (Figure 5.9). As soon as the cRPTPσ/cTrkC complex was reconstituted with a molar ratio 1:1.1, it was subjected to a deglycosylation reaction for 2 hours (Figure 5.9.F). The two components of the deglycosylated complex co-eluted on gel-filtration, which indicated a nM affinity interaction (Figure 5.9.F).




C
81.08 ml
1500.00
1000.00
500.00
0.00
A280 (mAu)
Vo
30.00
50.00
70.00
90.00
110.00
Elution volume (ml)
D
85.08 ml
800.00
400.00
0.00
A280 (mAu)
Vo
MW
kDa
50
20
30.00
50.00
70.00
90.00
110.00
Elution volume (ml)
E
85.21 ml
800.00
400.00
0.00
A280 (mAu)
Vo
MW
kDa
50
20
30.00
50.00
70.00
90.00
110.00
Elution volume (ml)

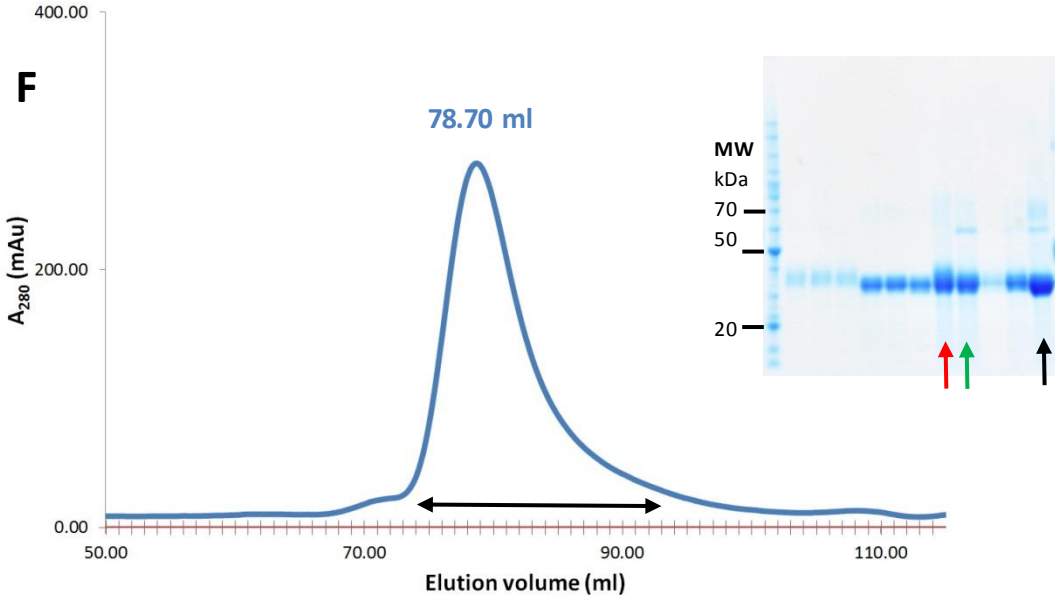


Figure 5.9: Gel filtration profiles of RPTPσ and TrkC protein constructs, accompanied by SDS-PAGE, where appropriate. **(A)** S200 elution profile of mTrkC-(LRR-Ig1) and SDS-PAGE. **(B)** S200 elution profile of hRPTPσ-(Ig1-Ig2-Ig3) and SDS-PAGE. **(C)** S200 elution profile hRPTPσ-(ig1-Ig2-Ig3)-QuadK mutant. **(D)** S200 elution profile of cTrkC-(LRR-Ig1) and SDS-PAGE. **(E)** S200 elution profile of cRPTPσ-(Ig1-Ig2-Ig3) and SDS-PAGE. **(F)** S200 elution profile of the deglycosylated cTrkC-(LRR-Ig1)/cRPTPσ-(Ig1-Ig2-Ig3) complex and SDS-PAGE. The black arrow on the SDS-PAGE highlights the final sample, after pooling indicated fractions and concentration. The effect of the deglycosylation reaction is also highlighted on the SDS-PAGE: the red arrow highlights the complex before the deglycosylation reaction, while the green arrow highlights the complex after the deglycosylation reaction.

5.5 Structure determination of cRPTPσ-cTrkC complex

The deglycosylated cRPTPσ-cTrkC complex was concentrated to 5.5 mg/ml and was used for nanolitre-scale crystallization trials, as described in section 2.3.1. Three-dimensional crystals were grown approximately 72 hours after setup, which diffracted up to 3.25 Å resolution (Figure 5.10). A 360° diffraction data set was collected with 0.2° oscillation step on a Pilatus 6M-F detector at Diamond I03 beamline (Diamond Light Source, Oxfordshire, UK). Data collection statistics are available in Table 5.2. An existing structure of the cRPTPσ-(Ig1-Ig2)/cTrkC-(LRR-Ig1), previously determined by Dr. Charlotte Coles,

was used as a search model for molecular replacement using Phaser (McCoy AJ.,et al., 2005), yielding a solution (LLG=5567, TFZ=41.7) with three complexes in the asymmetric unit, while the solvent content was calculated to be 65.61% (Figure 5.11.A). The initial electron density maps after refinement with tight Non Crystallographic Symmetry restraints in Phenix (Adams PD., *et al.*, 2010), revealed features that were disordered in the previous structure (Figure 5.11.B.C). Iterative rounds of manual model building in Coot (Emsley P. and Cowtan K., 2004), followed by refinement using Refmac (Mushudov GN., *et al.*, 1997) or Buster (Bricogne G., *et al.*, 2011) were performed. Refinement statistics are also available in Table 5.2.

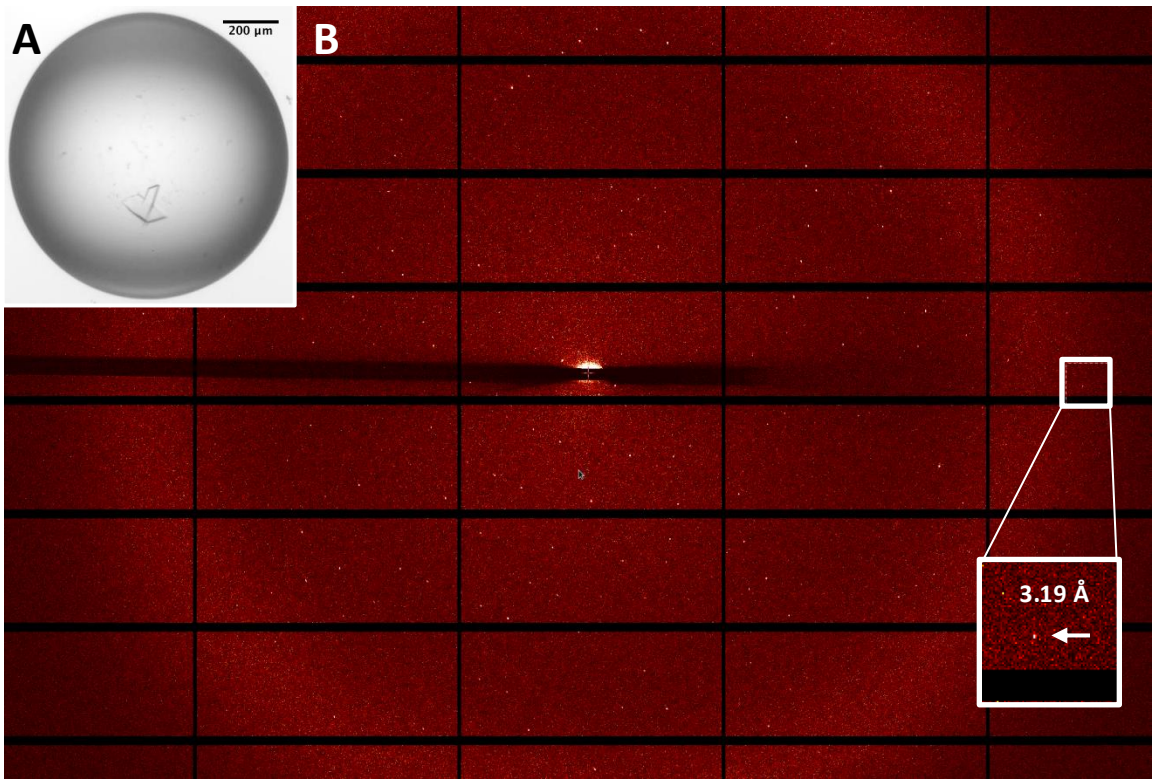


Figure 5.10: Diffraction of deglycosylated cRPTPσ-(Ig1-Ig2-Ig3)/cTrkC-(LRR-Ig1) crystals. **(A)** Representative crystals obtained from additive screening optimization (Hampton Rerearch Inc.), grown in 0.1 M HEPES pH 7.0, 5 %w/v Tacsimate pH 7.0, 10 %w/v Polyethylene Glycol Monomethyl Ether 5000. **(B)** X-ray diffraction data, reaching ~3.2 Å resolution, were collected.

Data Collection Statistics	
Protein	cRPTPσ-(Ig1-Ig2-Ig3)/cTrkC-(LRR-Ig1)
Beamline	Diamond-I03
Resolution (Å)	85.64-3.25 (3.34-3.25)
Spacegroup	P1
Cell dimensions a, b, c (Å) α, β, γ (°)	 84.42, 93.12, 99.38 73.37, 89.45, 74.23
Wavelength (Å)	0.97625
Unique reflections	43143 (3169)
Completeness (%)	98.6 (98.4)
R_{merge} (%)	10 (38.9)
I/σI	5.6 (1.8)
Redundancy	1.8 (1.8)
Refinement Statistics	
Resolution range (Å)	85.64-3.25 (3.34-3.25)
Number of reflections	40971 (3169)
R_{work} (%)	20.71 (30.6)
R_{free} (%)	23.30 (32.90)
No. of atoms	10630
No. of NAGs	1
Average B factors (Å^2)	126.3
R.M.S.D. bonds (Å)	0.006
R.M.S.D. angles (°)	1.095
Ramachandran plot (% residues)	
Favoured	95.7
Additionally allowed	4.1
Disallowed	0.2

Table 5.2: Crystallographic data statistics for cRPTPσ-(Ig1-Ig2-Ig3)/cTrkC-(LRR-Ig1) crystal structure. Numbers in brackets refer to the high resolution shell.

The crystal of cRPTPσ-(Ig1-Ig2-Ig3)/cTrkC-(LRR-Ig1) complex revealed a 1:1 interaction of the two partners (Figure 5.12). The binding interface between the two proteins is extended and contacts are stabilised by a putative hydrogen bonding network localised in three separate sites (Figure 5.14). Only the first two domains are observed in our crystal structure, adopting a conserved V-shaped arrangement previously described in apo structures (Coles CH., *et al.*, 2011). The TrkC-LRR, TrkC-Ig1 domains adopt a boomerang shaped conformation also observed in crystallographic analyses of Trk family members

(Wehrman T., *et al.*, 2007). The most striking feature of our structure is located in site 1 (Figure 5.14), of the extended binding interface, where one can see an involvement of a conserved loop known to bind proteoglycans (Figure 5.11, Coles CH., et al., 2011), in mediating the overall contact of RPTPσ residues within site 1, with TrkC-Ig1 residues.

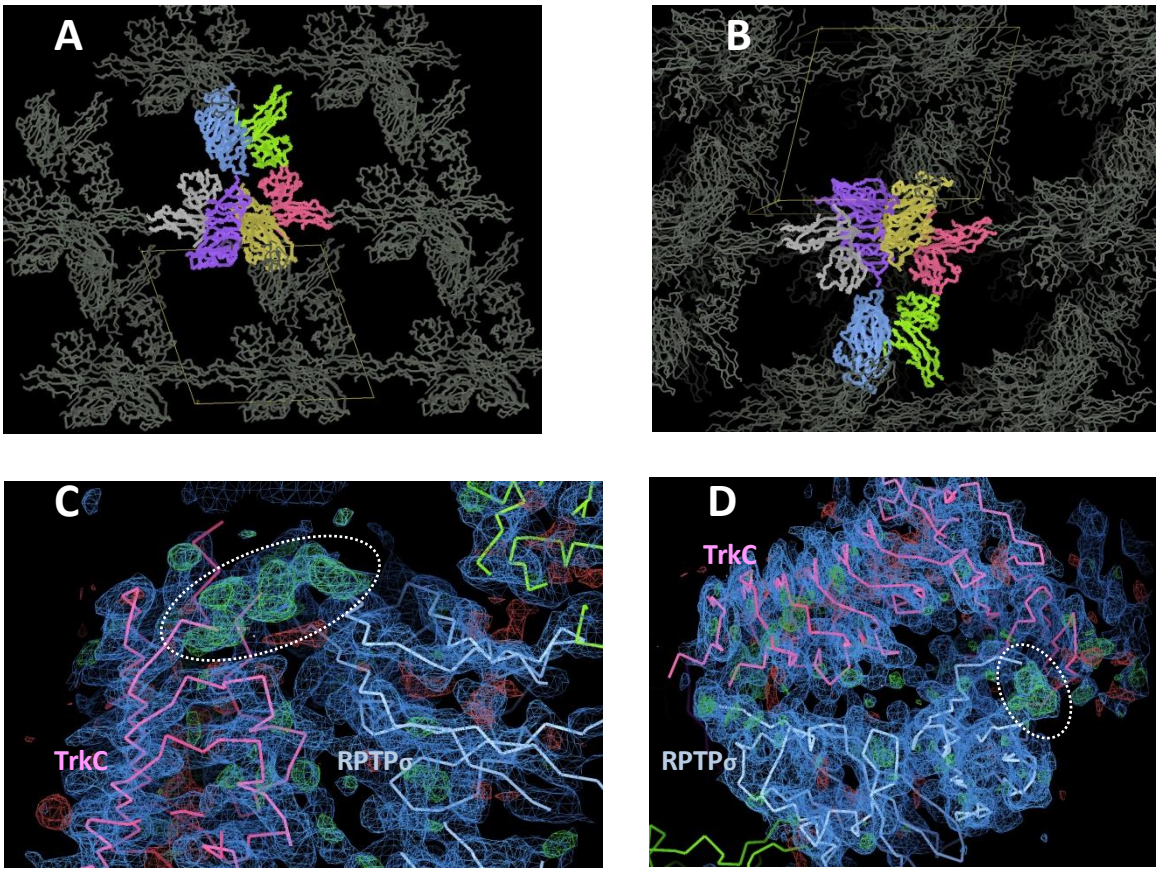


Figure 5.11: Crystal packing and initial electron density maps of cRPTPσ/cTrkC complex. **(A)** Packing of cRPTPσ/cTrkC complex molecules in the crystal. TrkC molecules are coloured in purple, yellow and blue, while RPTPσ molecules are coloured in grey, pink and green. Three copies of the complex are visible in the asymmetric unit ($TrkC_{purple}$- $RPTP\sigma_{grey}$, $TrkC_{yellow}$- $RPTP\sigma_{pink}$, $TrkC_{blue}$-$RPTP\sigma_{green}$). **(B)** 180^{o} horizontal rotation of packing view in panel A. **(C)** Unmodelled features are highlighted extending on TrkC. **(D)** Unmodelled features are highlighted on RPTPσ. $2F_c$-$2F_o$ maps (blue) and F_o-F_c maps (green/red) are contoured at 1, 3 σ respectively.

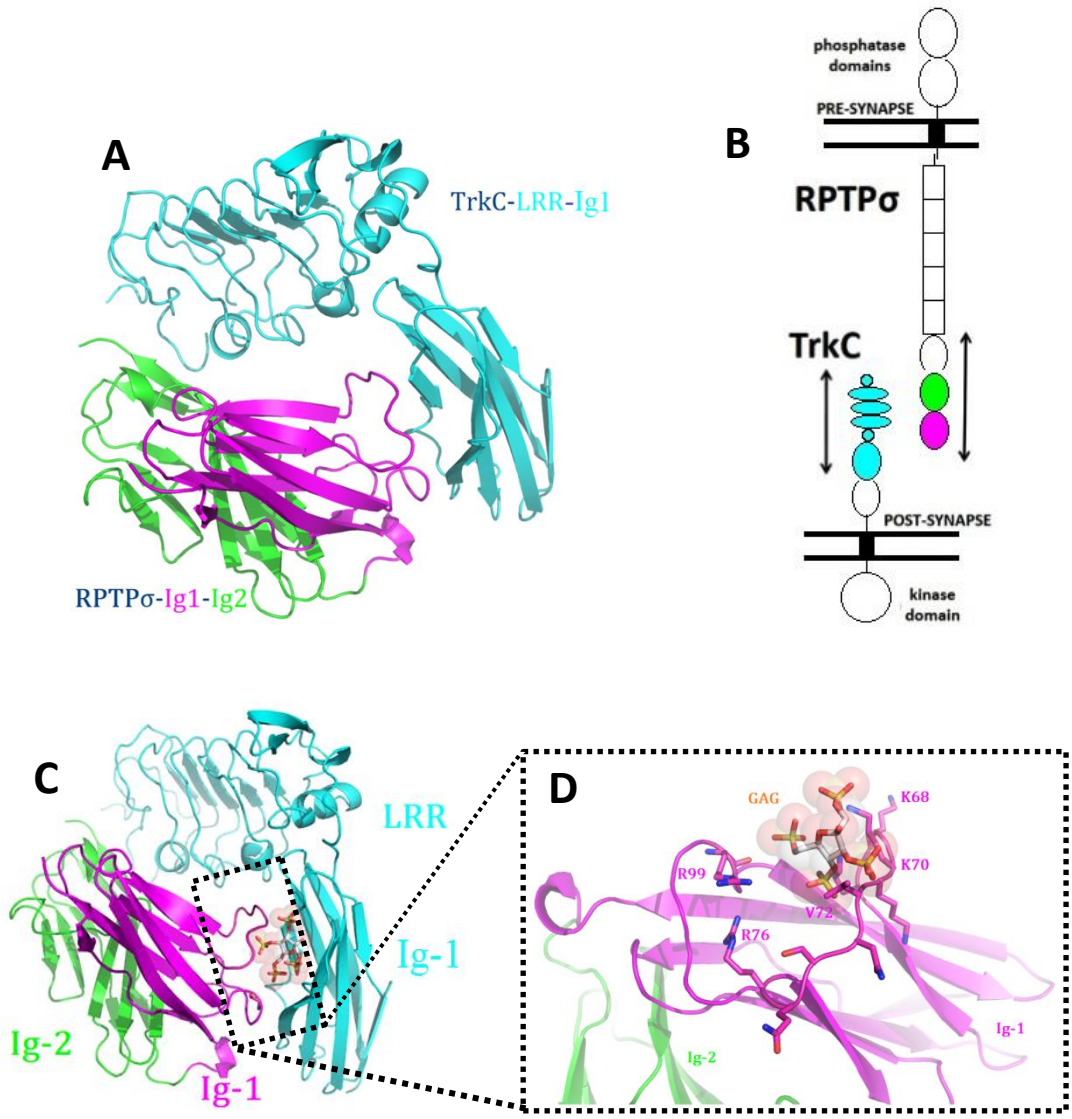
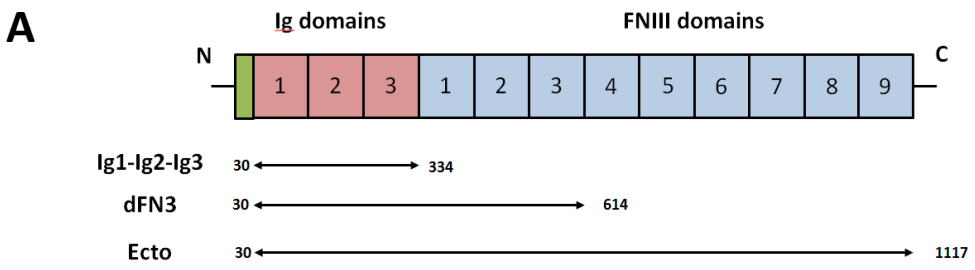


Figure 5.12: Crystal structure of cRPTPσ/cTrkC complex. **(A)** Cartoon representation of cRPTPσ-Ig1-Ig2/cTrkC-LRR-Ig1 complex structure. **(B)** Schematic representations of domain organisation of RPTPσ and TrkC proteins. Arrows indicate the constructs used in the co-crystallisation experiment (cRPTPσ-Ig1-Ig2-Ig3, cTrkC-LRR-Ig1). Domains for which there was interpretable electron density in our crystal structure are coloured cyan (cTrkC-LRR-Ig1), magenta (cRPTPσ-Ig1) and green (cRPTPσ-Ig2). **(C)** Cartoon representation of cRPTPσ-Ig1-Ig2/cTrkC-LRR-Ig1 complex structure. Sucrose octasulfate (SOS) is superimposed on its crystallographically determined binding site (PBD: 2YD8, Coles CH., *et al.*, 2011, and simulates GAG binding. **(D)** A close up of the superimposed SOS from the LAR-Ig1-Ig2/SOS complex (PDB: 2YD8), in the context of cRPTPσ-Ig1-Ig2.

5.6 Biophysical characterisation of hRPTPσ-mTrkC interaction, and competition with proteoglycans

5.6.1 Minimal unit of hRPTPσ required for interaction of mTrkC

According to the study that identified the bidirectional excitatory synaptic organising activity of TrkC/RPTPσ complex (Takahashi H., *et al.*, 2011), in cell-based assays, this requires the extracellular LRR and Ig1 domains of TrkC and the three N-terminal Ig domains of RPTPσ. Here we tried to confirm that the minimal unit of RPTPσ for mTrkC-LRR-Ig1 binding is the hRPTPσ-Ig1-Ig2-Ig3 using Surface Plasmon Resonance (SPR). hRPTPσ Ig1-Ig2-Ig3, dFN3 and Ecto constructs (as defined in Figure.5.13.A) were expressed in HEK293T cells and coupled to three channels of a CM5 chip, as described in section 2.6. mTrkC-LRR-Ig1 construct was used as an analyte, expressed in HEK293T cells and purified with the native glycosylation pattern, as described in section 2.2. All three hRPTPσ constructs appeared to bind mTrkC-LRR-Ig1, even though the K_d value for the ectodomain indicated a slightly tighter interaction (Figure 5.13). One can thus deduce that the hRPTPσ Ig1-Ig2-Ig3 is indeed the minimal unit required for interaction with mTrkC, without neglecting the possibility that the interaction is further stabilised by the presence of some of the other domains of the hRPTPσ ectodomain region.



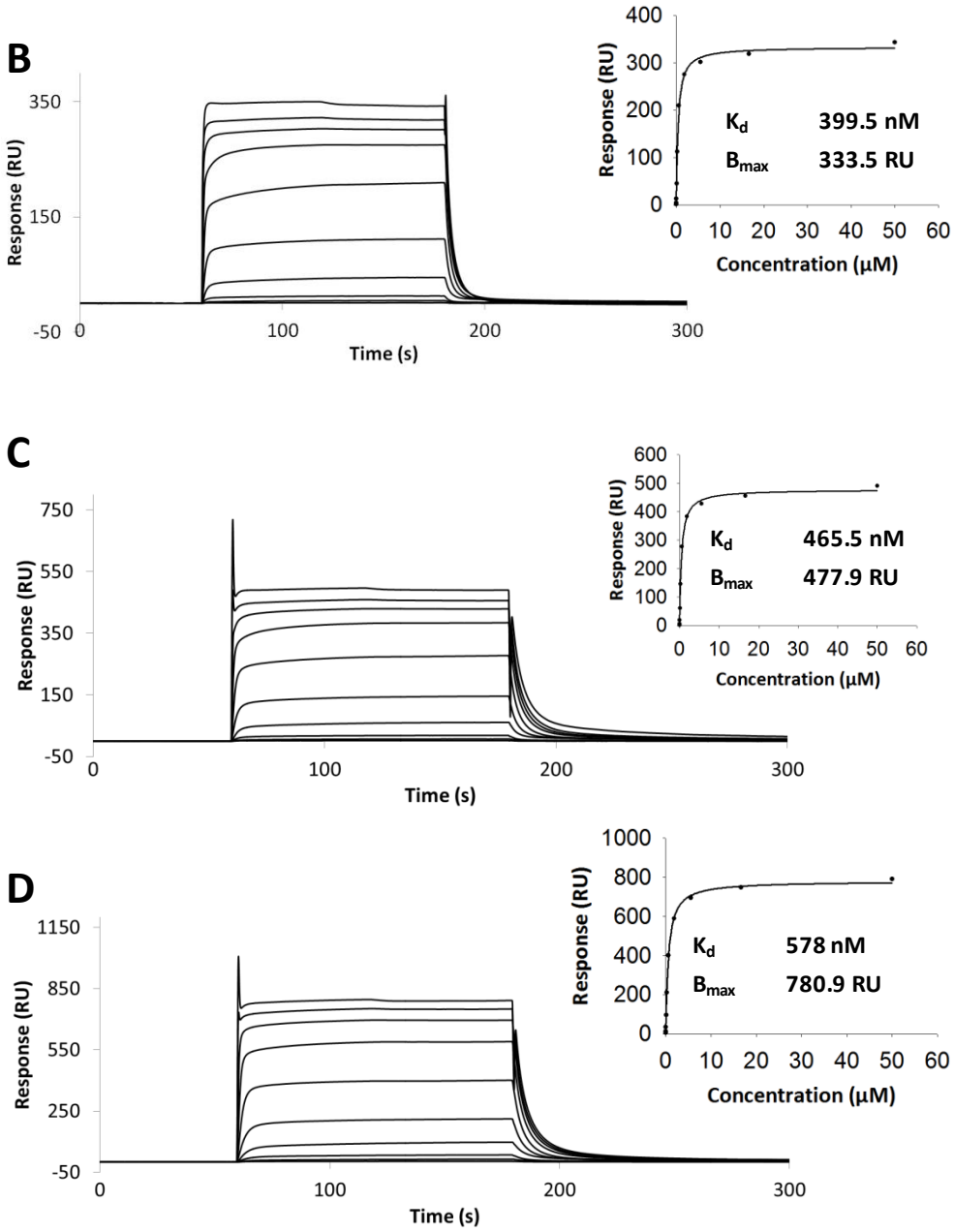


Figure 5.13: mTrkC binding to hRPTPσ ectodomain deletion constructs, to identify minimal hRPTPσ binding unit. A serial three-fold dilution series of mTrkC-LRR-Ig1 was tested for binding on different hRPTPσ constructs. Top mTrkC-LRR-Ig1 concentration tested was 50 µM. **(A)** Schematic representation of hRPTPσ deletions. **(B)** Binding of mTrkC-LRR-Ig1 to hRPTPσ-Ecto. **(C)** Binding of mTrkC-LRR-Ig1 to hRPTPσ-dFN3. **(D)** Binding of mTrkC-LRR-Ig1 to hRPTPσ-Ig1-Ig2-Ig3.

5.6.2 Biophysical analysis of structure-based mutants targeting the hRPTPσ-mTrkC interfaces

A set of structure-based mutants were generated targeting all three apparent interaction interfaces of hRPTPσ/mTrkC complex, identified in the crystal structure (Figure 5.14). The mutants that were generated were: mTrkC-LRR-Ig1-(D224A, D226A), mTrkC-LRR-Ig1-(N68Q, N72Q), hRPTPσ-Ig1-Ig2-Ig3-(R96A, R99A), hRPTPσ-Ig1-Ig2-Ig3-(Y223S), hRPTPσ-Ig1-Ig2-Ig3-(R241A, R242A) and hRPTPσ-Ig1-Ig2-Ig3-(K68A, K69A, K71A, K72A) (QuadK). According to my wild-type measurements mTrkC-LRR-Ig1 exhibits a nanomolar affinity for hRPTPσ-Ig1-Ig2-Ig3 (Figure 5.13.D, Figure 5.15.A).

It was found with SPR that mutants targeting polar interactions at hRPTPσ/mTrkC interaction site 1 (Figure 5.14.B), namely mTrkC-LRR-Ig1-(D224A, D226A) (Figure 5.15.B) and hRPTPσ-Ig1-Ig2-Ig3-(R96A, R99A) (Figure 5.15.C) would abolish any binding between TrkC and RPTPσ.

Mutant hRPTPσ-Ig1-Ig2-Ig3-(Y223S), which targets hRPTPσ/mTrkC interaction site 2 (Figure 5.14.D), decreased binding to TrkC greatly (more than 1000 fold), but left the proteoglycan binding intact since the site 1 was not affected (Coles CH., *et al.*, 2011) (Figure 5.15.E).

Mutant mTrkC-LRR-Ig1-(N68Q, N72Q) which targets hRPTPσ/mTrkC interaction site 3, by removing glycosylation sites from a helical TrkC region protruding onto hRPTPσ-Ig2 (Figure 5.14.E), appeared to enhance binding (approximately 2 fold) between TrkC and RPTPσ (Figure 5.15.D), when compared to the wild-type measurement (Figure 5.15.A).

Mutant hRPTPσ-Ig1-Ig2-Ig3-(R241A, V242A) which targets hRPTPσ/mTrkC interaction site 3, also decreased binding to TrkC, but to a lesser extent than Y223S (Figure 5.15.F).

Finally, mutant hRPTPσ-Ig1-Ig2-Ig3-(K67A, K68A, K70A, K71A) (QuadK) revealed that by altering the loop that is primarily responsible for proteoglycan binding (Coles CH., *et al.*, 2011), hRPTPσ can still bind to TrkC (Figure 5.15.G).

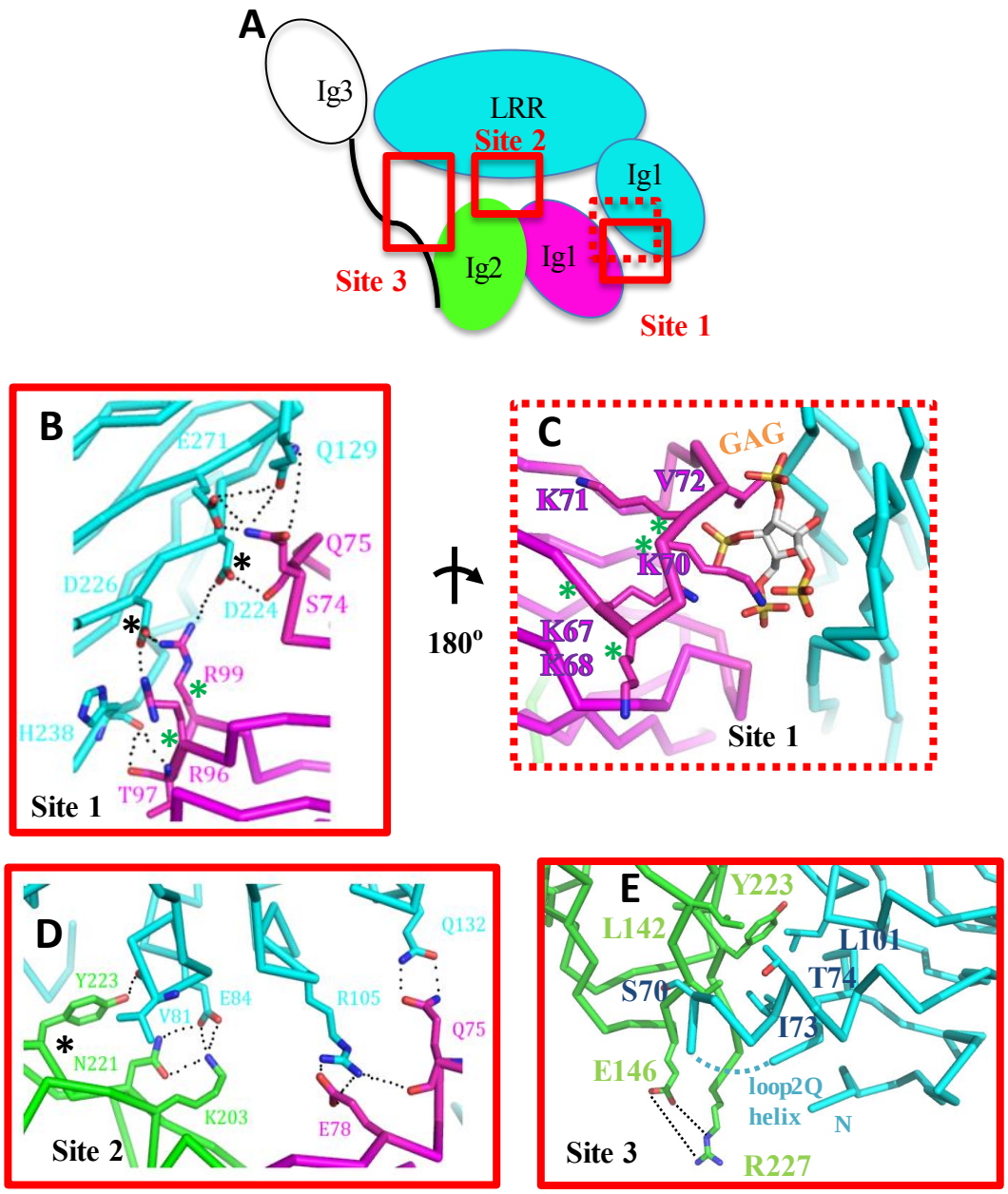
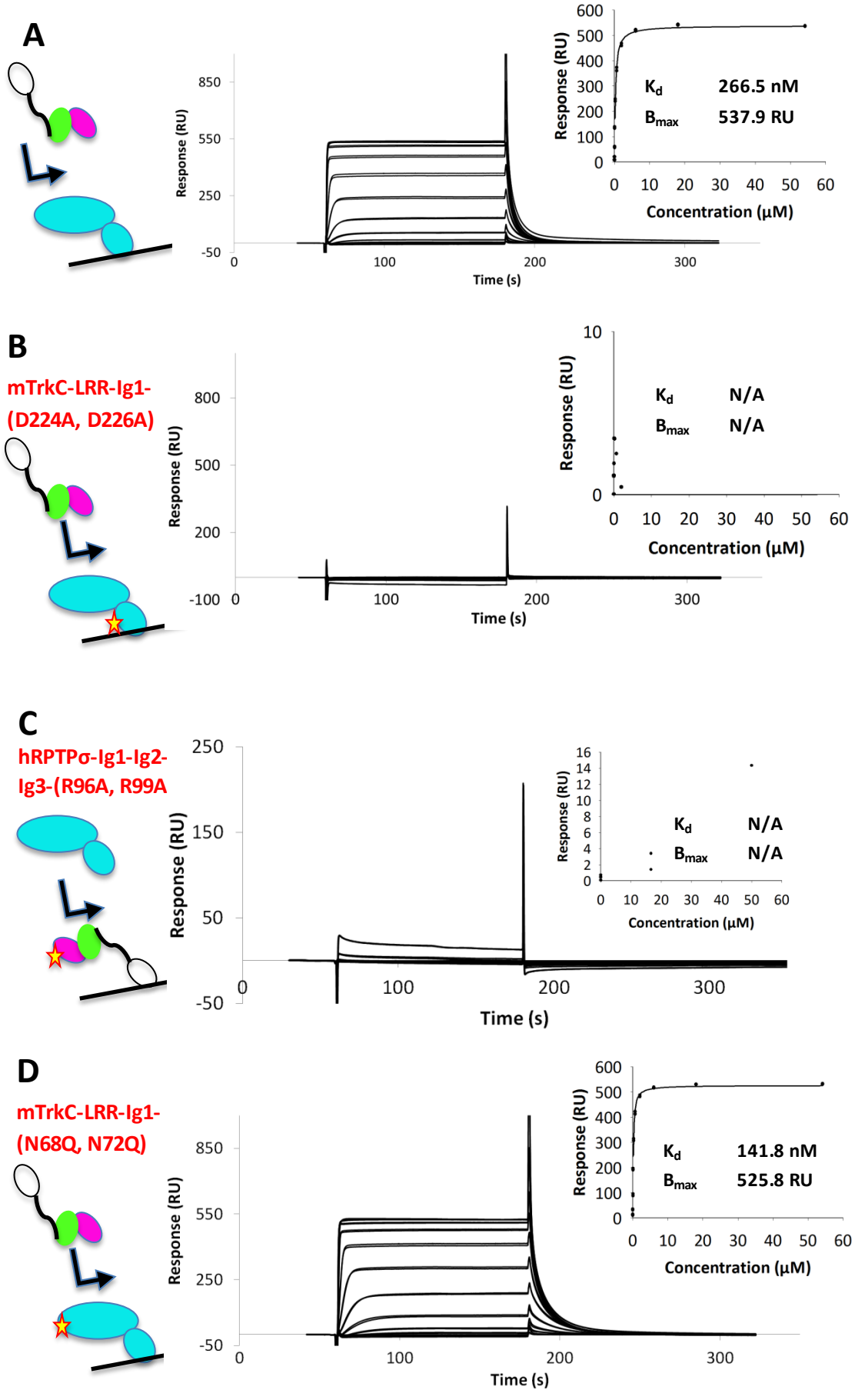


Figure 5.14: A structural view of the binding interfaces that the cRPTPσ-Ig1-Ig2/cTrkC-LRR-Ig1 complex structure revealed. **(A)** A schematic representation of cRPTPσ-Ig1-Ig2-Ig3/cTrkC-LRR-Ig1 complex, with red boxes highlighting the three observed binding interfaces. The colouring scheme is adopted from figure 5.12. cRPTPσ-Ig3 is depicted in white, since the x-ray data did not provide conclusive density in order to locate and build the domain. **(B)** A close-up of Site 1. In mutant mTrkC-LRR-Ig1-(D224A, D226A) (black asterisks), aspartates 224 and 226 were mutated to alanines, while in mutant hRPTPσ-Ig1-Ig2-Ig3-(R96A, R99A) (dark green asterisks), arginines 96 and 99 were mutated to alanines. **(C)** A close-up of the GAG binding site, which partially overlaps with Site 1. In mutant hRPTPσ-Ig1-Ig2-Ig3-(K67A, K68A, K70A, K71A) (dark green asterisks), lysines 67, 68, 70 and 71 were mutated to alanines. **(D)** A close-up of Site 2. In mutant hRPTPσ-Ig1-Ig2-Ig3-(Y223S) (black asterisk), tyrosine 223 is mutated to serine. **(E)** A close-up of Site 3. A helical region could be built on our structure at the end of the extremely flexible loop2Q, which is involved in binding hRPTPσ-Ig2.


A
Response (RU)
850
550
250
-50
0
100
200
300
Time (s)
Response (RU)
600
500
400
300
200
100
0
0 10 20 30 40 50 60
Concentration (µM)
Kd 266.5 nM
Bmax 537.9 RU
B
mTrkC-LRR-Ig1-
(D224A, D226A)
Response (RU)
800
500
200
-100
0
100
200
300
Time (s)
Response (RU)
10
0
0 10 20 30 40 50 60
Concentration (µM)
Kd N/A
Bmax N/A
C
hRPTPσ-Ig1-Ig2-
Ig3-(R96A, R99A
Response (RU)
250
150
50
-50
0
100
200
300
Time (s)
Response (RU)
16
14
12
10
8
6
4
2
0
0 10 20 30 40 50 60
Concentration (µM)
Kd N/A
Bmax N/A
D
mTrkC-LRR-Ig1-
(N68Q, N72Q)
Response (RU)
850
550
250
-50
0
100
200
300
Time (s)
Response (RU)
600
500
400
300
200
100
0
0 10 20 30 40 50 60
Concentration (µM)
Kd 141.8 nM
Bmax 525.8 RU

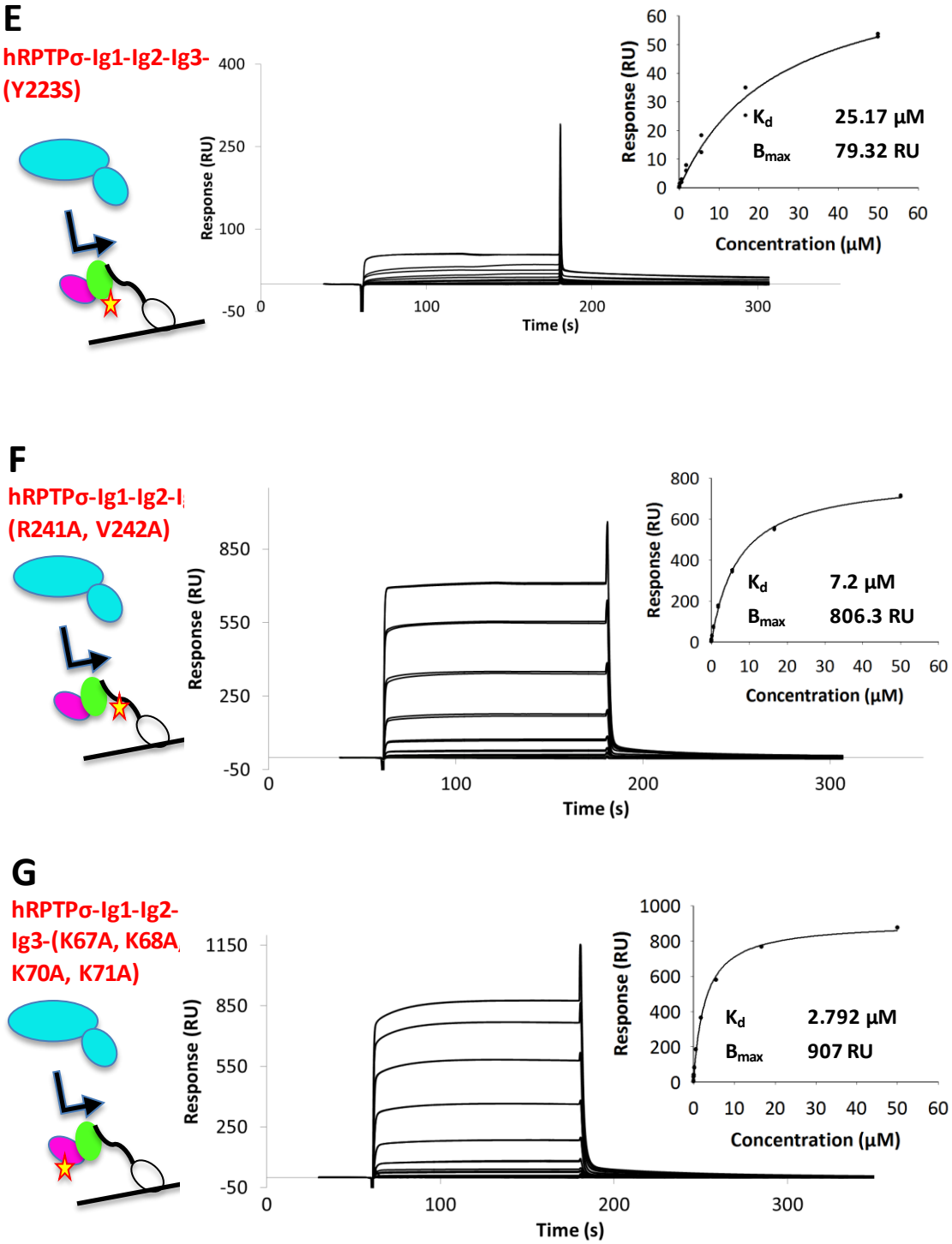
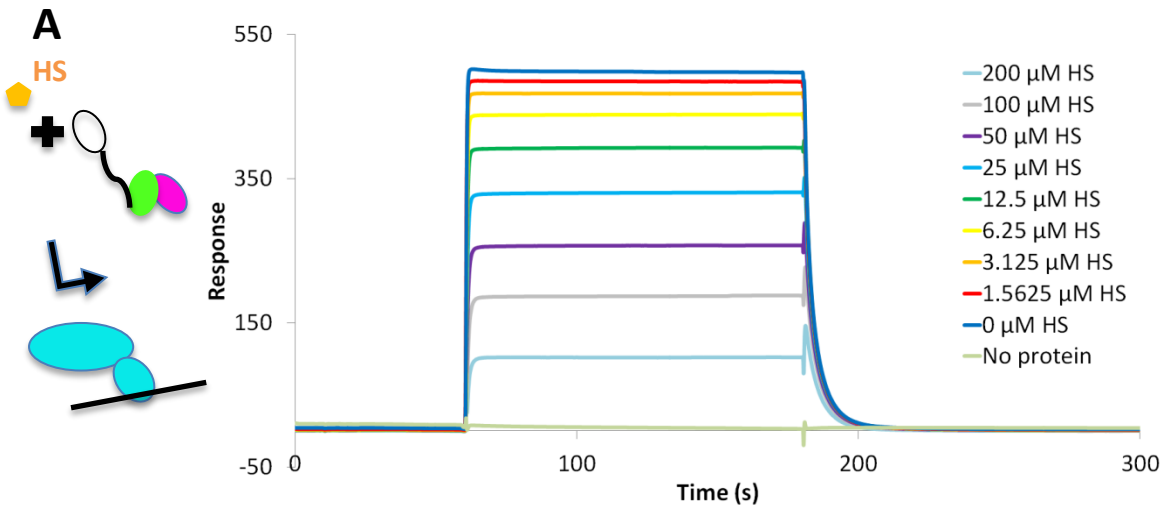


Figure 5.15: Biophysical analysis of structure-based mutants targeting mTrkC/hRPTPσ complex formation. A serial three-fold dilution series of analytes was tested for binding on different immobilised constructs. Top analyte concentration tested was 50 μM. Each mutant and corresponding experimental orientation, is schematically represented on the left side of each panel. hRPTPσ-Ig1-Ig2-Ig3/mTrkC-LRR-Ig1 colouring scheme is adopted from figure 5.11. hRPTPσ-Ig3 is depicted in white. Stars represent the relative position of point mutations on the domain of interest. **(A)** Binding of hRPTPσ-Ig1-Ig2-Ig3 (wild-type) to mTrkC-LRR-Ig1. **(B)** Binding of hRPTPσ-Ig1-Ig2-Ig3 (wild-type) to mTrkC-LRR-Ig1-(D224A, D226A). **(C)** Binding of mTrkC-LRR-Ig1 (wild-type) to hRPTPσ-Ig1-Ig2-Ig3-(R96A, R99A). **(D)** Binding of hRPTPσ-Ig1-Ig2-Ig3 (wild type) to mTrkC-LRR-Ig1-(N68Q, N72Q). **(E)** Binding of mTrkC-LRR-Ig1 (wild-type) to hRPTPσ-Ig1-Ig2-Ig3-(Y223S). **(F)** Binding of mTrkC-LRR-Ig1 (wild-type) to hRPTPσ-Ig1-Ig2-Ig3-(R241A, V242A). **(G)** Binding of mTrkC-LRR-Ig1 (wild-type) to hRPTPσ-Ig1-Ig2-Ig3-(K67A, K68A, K70A, K71A).

5.6.3 mTrkC competes with heparan sulfate for hRPTPσ binding

Surface Plasmon Resonance experiments were designed to evaluate whether a concentration gradient of soluble heparan sulfate could disrupt binding of free hRPTPσ-Ig1-Ig2-Ig3 to immobilised mTrkC-LRR-Ig1. Heparan sulfate can indeed compete with mTrkC for hRPTPσ binding (Figure 5.16.A), while the competition effect is lost when the primary hRPTPσ responsible for proteoglycan binding is mutated (Figure 5.16.B). This result reinforces the observations from the crystal structure and supports the view that the binding site on RPTPσ for TrkC and proteoglycans is partially overlapping, enabling RPTPσ to mechanistically respond to either partner.



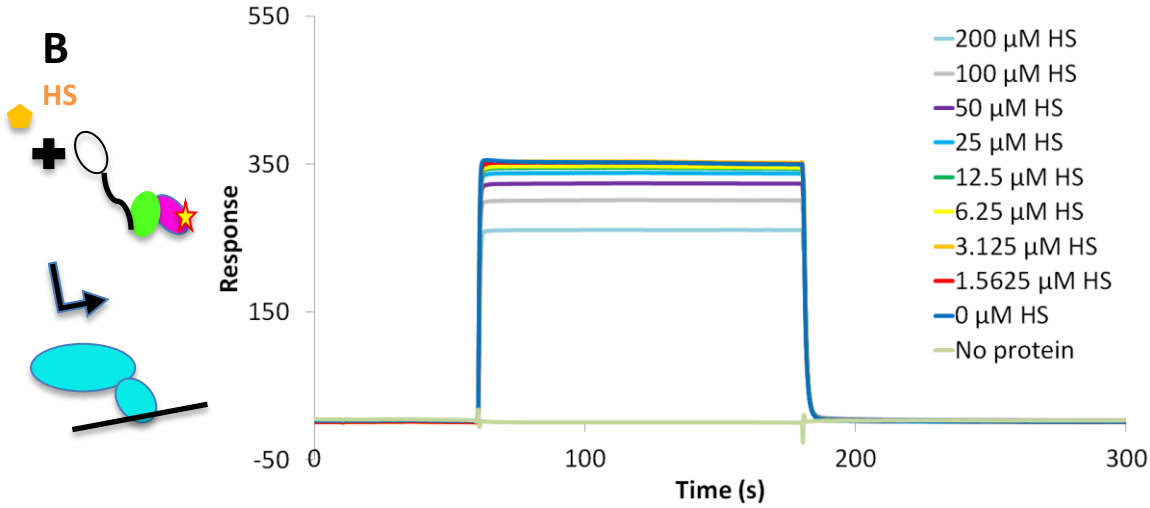


Figure 5.16: Competition analysis mTrkC/hRPTPσ complex by heparan sulfate. A serial two-fold dilution series of heparan sulfate was tested for competing the interaction between 10 µM hRPTPσ-Ig1-Ig2-Ig3 and immobilised mTrkC-LRR-Ig1. The highest heparan sulfate concentration tested was 200 µM. Each partner involved and the corresponding experimental orientation, is schematically represented on the left side of each panel. GAG is depicted in orange, while hRPTPσ-Ig1-Ig2-Ig3/mTrkC-LRR-Ig1 colouring scheme is adopted from figure 5.11. hRPTPσ-Ig3 is depicted in white. The star in panel B represents the relative position of K68A, K69A, K71A, K72A mutations on hRPTPσ-Ig1 domain. **(A)** Heparan sulphate competition of hRPTPσ-Ig1-Ig2-Ig3-(wild-type)/mTrkC-LRR-Ig1-(wild-type) binding. **(B)** Heparan sulphate competition of hRPTPσ-Ig1-Ig2-Ig3-(K67A, K68A, K70A, K71A)/mTrkC-LRR-Ig1-(wild-type) binding.

5.7 Conclusions and future perspectives

In conclusion, the results presented in this chapter provide mechanistic information on the interplay of proteoglycans with an established *trans*-synaptic interaction between RPTPσ and TrkC (Takahashi H., *et al.*, 2011). While HSPGs have been shown to cluster RPTPσ on the face of a growing axon (Coles CH., *et al.*, 2011), a molecular description of those events that cause a switch from axonal growth to synaptic adhesion events leading to synaptic establishment has been missing. Since the results presented in this chapter highlight an unexpected competition between GAG and TrkC for RPTPσ binding, a testable hypothesis can now be formulated as to whether this competition represents the switch signal from neuronal growth to synaptic establishment. The mutants described in

this chapter are currently being tested in co-culture cellular settings, with a number of soluble GAGs as well as proteoglycans, for effects on synapse formation, in collaboration with Prof. Ann Marie Craig (University of British Columbia, Canada). Additionally, whole cell electrophysiology is planned to test whether GAG modulation of RPTPσ-TrkC binding can influence glutamate release and synapse function. Further biophysical studies will aim to evaluate whether GAGs can have any effect in the context of RPTPσ/NGL3 and RPTPσ/Slitrk2 *trans*-synaptic interactions, which have also been reported to regulate excitatory synapse formation (Kwon SK., *et al.*, 2010, Yim YS., *et al.*, 2013).. However, the RPTPσ/NGL3 interaction is mediated via the RPTPσ-FNIII region (Kwon SK., *et al.*, 2010), while RPTPσ/Slitrk2 interaction is mediated with the same RPTPσ region as TrkC (Yim YS., *et al.*, 2013).

Chapter 6

Structural investigations of C1q-like proteins and characterisation of their synaptic interactions

Chapter 6

Structural investigations of C1q-like proteins and characterisation of their synaptic interactions

6.1 Summary

Complement C1q is the prototypical member of a family characterised by the presence of a C-terminal globular domain (gC1q). The gC1q domain is included in all members of the family, including adiponectin, cerebellin and the structurally-related cytokine tumor necrosis factor family, expanding its functional versatility beyond immunity. The subfamilies of Cerebellin and C1q-like (C1ql) predominantly function in the brain. While Cerebellins have been established as bearing roles in trans-synaptic arrangements in the cerebellum, the functions of C1ql subfamily members remain largely unknown. Members of the C1ql subfamily were recombinantly expressed, purified and led to the determination of the first crystal structures from this subfamily. Surface plasmon resonance experiments enabled mapping interactions between C1ql proteins and specific domains of postulated postsynaptic partners. Further biochemical analysis, with Multiple Angle Light Scattering, confirmed the formation of these complexes and paved the way for high-throughput co-crystallisation screening. Structure guided site-directed C1ql mutants were shown to abolish the interactions with postsynaptic partners in surface plasmon resonance experiments, without affecting folding or expression. Structural investigation of a prototypical trans-synaptic complex involving a C1ql family member can provide novel insights into the molecular mechanisms of synapse formation and function and may open a way towards the design of novel theurapeutics for mental disorders.

6.2 Introduction

6.2.1 The action of Complement C1q in the nervous system

The classical complement pathway, which is initiated with recognition events of the C1q component, is a fast and robust mediator of innate surveillance and homeostasis that targets and discards pathogenic threats (Ricklin D., *et al.*, 2010). The blood-brain barrier occludes entry of blood residing cells and proteins, therefore the protection from microorganisms as well as molecular housekeeping for the maintenance of a healthy network of neurons and glial cells is conferred by innate immunity mechanisms (as reviewed in Veerhuis R., *et al.*, 2011). The functions of the members of the complement pathway extend beyond immunological roles in the brain though, as with other immune related molecule described above (Veerhuis R., *et al.*, 2011). C1q is expressed in the visual system during development and through the classical cascade activation facilitates developmental synaptic elimination which is crucial for the refinement of the visual circuitry neuronal connections (Stevens B., *et al.*, 2007). In addition, C1q has been demonstrated to participate in the mechanisms offering protection against neurotoxicity and β-amyloid induced neuronal death (Benoit ME., and Tennet AJ., 2011, Benoit ME., *et al.*, 2013). It was shown recently that C1q protein levels are boosted by as much as 300-fold in the normal aging mouse brain, and that this increase was in close proximity to synapses in certain areas known to be severely affected in neurodegenerative diseases (the hippocampus, the substantia nigra and the piriform cortex) (Stephan AH., *et al.*, 2013). Adult systemic C1q knock-out mice were indicative of increased synaptic plasticity and their aging hippocampi were undergoing extensive C3-independent circuit remodelling (Stephan AH., *et al.*, 2013). Since C3 cascade member appears only in low

levels in the adult and aging brain it is postulated that C1q is one of the molecular effectors of the aging central nervous system, independently from the roles it exhibits during the developmental synaptic elimination (Stephan AH., *et al.*, 2013). Intriguingly, C1q has been reported to promote the canonical Wnt signalling pathway activation and aging-associated defects in tissue regeneration (Naito AT., *et al.*, 2012). It should be noted that Wnt signalling has been shown to exhort both promoting effects, as in the case of Wingless in Drosophila (Packard M. et al., 2002) and inhibiting outcomes, as in the case of lin-44 in the nematode neuromuscular junction (Klassen MP., and Shen K., 2007) in synapse formation. Whether an interplay between C1q and Wnt signalling bears roles in neurological disorders of the aging brain, remains to be demonstrated.

6.2.2 An overview of the C1q family

The C1q family of proteins, characterised by containing the signature C1q domain on the C-terminus (Figure 6.1), is comprised of 32 members in human and 29 members in mice. There is a wide variety of domain organisations at the N-terminal regions of members of this family, which was brought to such levels of diversity probably through gene duplication events (Ghai R., *et al.*, 2007).

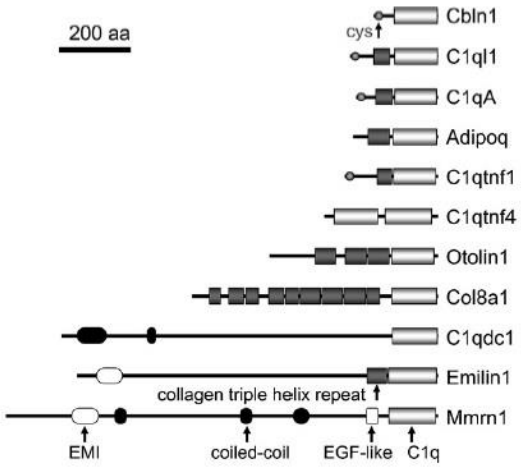


Figure 6.1: Schematic domain organisation of representative C1q family members. The signature gC1q domain is universaly present (light grey boxes) and forms a trimeric unit. Various domain combinations on the N-terminus are involved in higher order multimerisation (Image and caption partially adopted from Yuzaki M., 2008).

Interestingly, the C1q domain appears to be present even during early evolutionary stages, such the prokaryotes, as a standalone globular head protein, while its most ancient forms were not secreted (Carland TM. and Gerwick L., 2010). Phylogenetic analyses suggest that we can divide the mouse family members in four distinct groups according to overall domain and sequence conservation: C1q, Emilin, Cerebellin and C1q-like (Figure 6.2).

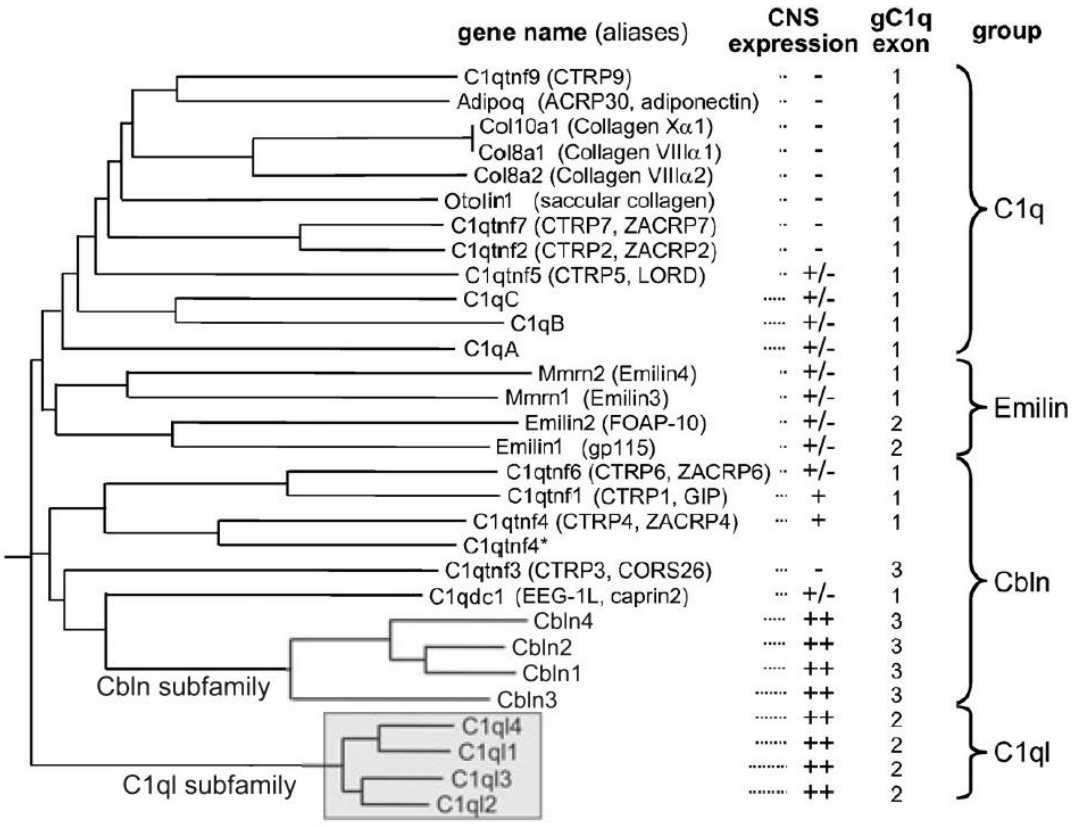


Figure 6.2: Phylogenetic analysis of mouse C1q family members. The gene name, its expression in the CNS as suggested by an analysis of the expressed sequence tag counts (National Center for Biotechnology Information, ESTProfile Viewer), the numbers of exons encoding each gC1q domain, and the assignment of four groups of homology-related sequences are indicated on the right side of the phylogenetic tree. (Figure and caption partially adopted from Yuzaki M., 2008).

While the overall structure of the individual members is very variable, the signature gC1q domain is tightly conserved across the family, as revealed in alignments where one can observe eight invariant residues responsible for the structural integrity of the gC1q domain oligomerisation into trimers (Figure 6.3).

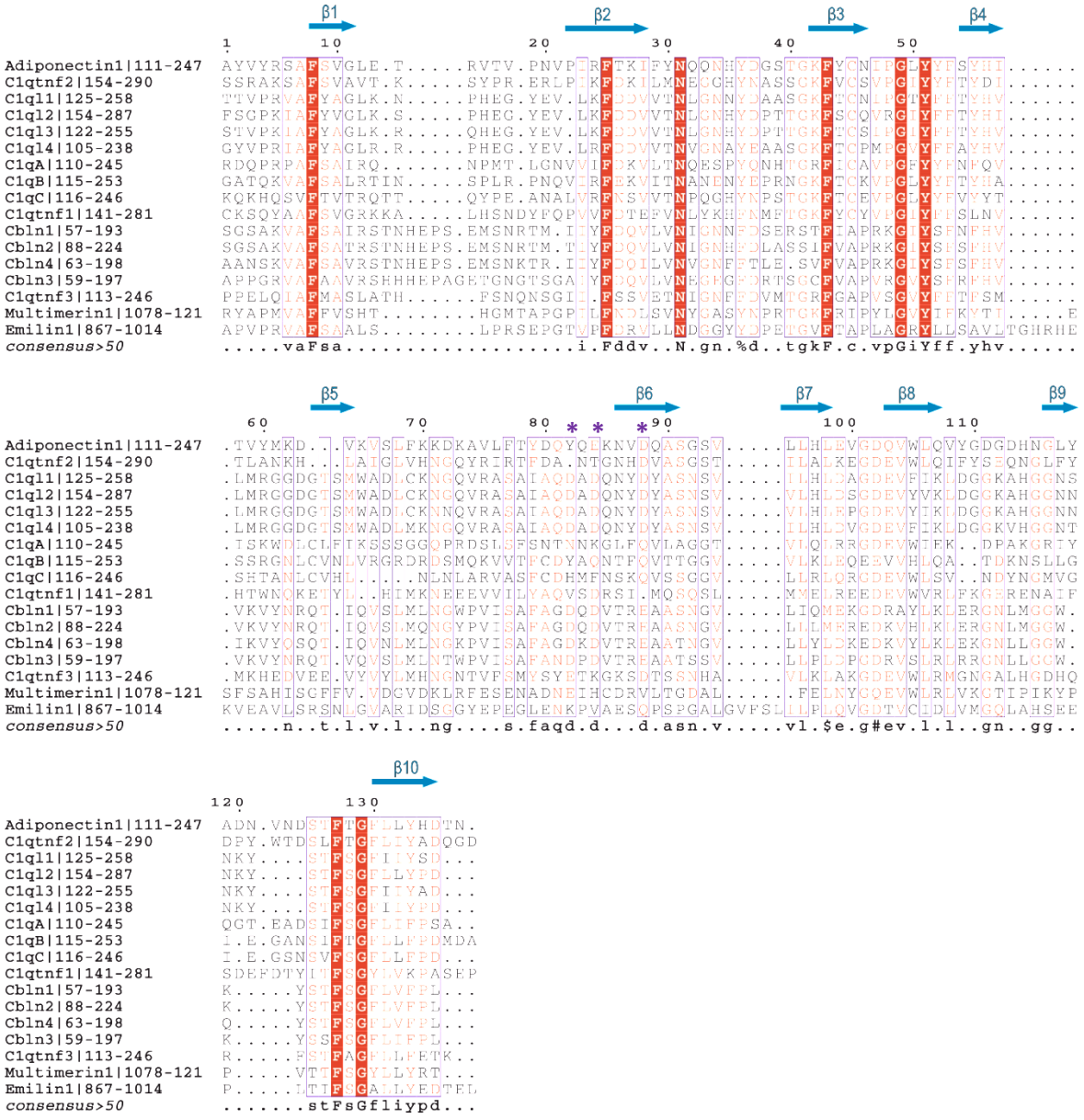


Figure 6.3: Multiple sequence alignment of gC1q domains from representative members of the mouse C1q family. The uniprot accession codes of the proteins used are: Adiponectin (Q60994),Multimerin-1 (B2RPV6), Emilin-1 (Q99K41), Cerebellin-1 (Q9R171), Cerebellin-2 (Q8BGU2), Cerebellin-3 (Q9JHG0), Cerebellin-4 (Q8BME9), Complement C1q chain A (P98086), Complement C1q chain B (P14106), Complement C1q chain C (Q02105), C1q tumor necrosis factor related protein-1 (Q9QXP7), C1q tumor necrosis factor related protein-2 (Q9D8U4), C1q tumor necrosis factor related protein-3 (Q9ES30), C1q-like 1 (O88992), C1q-like 2 (Q8CFR0), C1q-like 3 (Q9ESN4) and C1q-like 4 (Q4ZJM9). Secondary structure elements appear in blue. Residues important for C1ql metal ion coordination are indicated with purple asterisks. The alignment was generated with MultAlign online interface of a hierarchical clustering algorithm (Corpet F., 1988) and edited with ESPript interface (Gouet P., *et al.*, 2003).

The variability of the N-terminal region of the C1q family members contributes to a diversification on the modes of multimerisation of the primary trimeric unit (Yuzaki M., 2008, Mayne R. and Brewton RG., 1993, Doliana R., *et al.*, 2000, Bao D., *et al.*, 2005, Pajvani UB., *et al.*, 2003), and in certain cases the mode of oligomerisation has been associated with certain functional effects (Pajvani UB., *et al.*, 2003). C1q family members can form heteromeric trimers (as in the case of C1q and Cerebellins), homomeric trimers (as in the case of Adiponection, Multimerins, Collagen VIIIαs) or trimers of unknown composition (Such as the C1q-like proteins) (reviewed in Yuzaki M., 2008). The full complement C1q (460kDa) is arranged in a bouquet-like structure of six collagenous stems with a total of 18 polypeptide chains (Ricklin D., *et al.*, 2010).

A number of crystal structures for gC1q domains of the C1q family have been determined to date, namely the mouse ACRP30 (Shapiro L. and Scherer PE., 1998), the human collagen X (Bogin O., *et al.*, 2002), the mouse Collagen VIIIα1 (Kvansakul M., *et al.*, 2003), the human complement C1q heterotrimer (Gaboriaud C., et al., 2003), the human adiponectin (Min X., et al., 2012) and the human C1q and tumor necrosis factor-related protein-5 (Tu X. and Palczewski K., 2012). The gC1q domain universally adopts a 10-stranded β-sandwich fold in two antiparallel planes and an overall jelly-roll topology (Figure 6.4). The highly conserved residues across the family (Figure 6.3) are part of hydrophobic patches that hold the gC1q trimer intact (Gaboriaud C., et al., 2003). There is evidence, in some of the structures mentioned above, of a calcium binding site at the tip of the trimers, which is postulated to enable calcium ions to further stabilise the trimer (Kishore U., *et al.*, 2004, Ghai R., *et al.*, 2007). The role of calcium ions bound on complement C1q has been demonstrated to be critical in ligand recognition and the

initiation of the cascade, as shown by functional mutagenesis (Roumenina LT., et al., 2005).

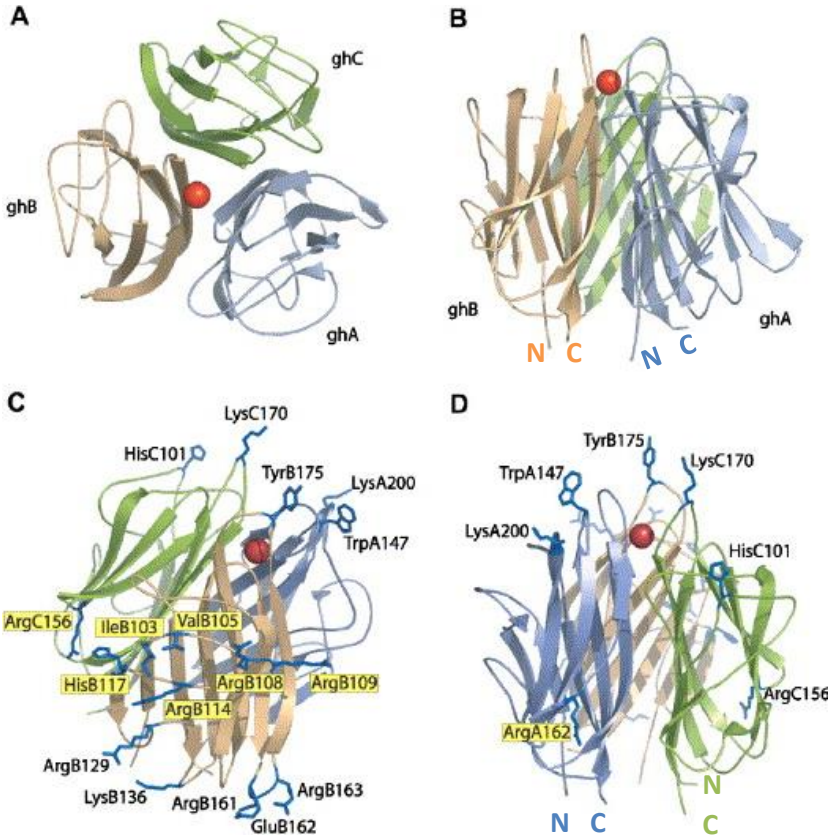


Figure 6.4: The gC1q domain. Two different views of the compact, spherical heterotrimeric gC1q domain are shown (ghA blue, ghB brown, ghC green): top view (A), side view (B). The red sphere indicates the calcium ion located at the apex of the domain. Residues considered important for the C1q–ligand interactions are explicitly labeled (C, D). (Image and caption adopted from Ghai R., *et al.*, 2007).

The first structural elucidation of a gC1q domain showed the striking structural homology with the C-terminal domain of tumor necrosis factor, structures of which were already known (Jones EY., *et al.*, 1989, Eck MJ. and Sprang SR., 1989), providing a basis for functional connections and modes of interactions with ligands, in the light of their apparent evolutionary links (Shapiro L. and Scherer PE., 1998).

C1q has a diverse range of ligands, which interact with its gC1q domain and include: IgG, IgM, SAP, pentraxins, decorin, HTLV-I gp21 virion protein, HIV1 gp41, the Moloney virus

p15E, β-amyloid peptide, cardiolipin, Omp bacterial proteins, heparin, fibrinogen, defensins and others (reviewed in Kishore U., *et al.*, 2004).

6.2.3 An overview of C1q-like proteins

The C1q-like subfamily is one of the functionally most unexplored areas of the C1q family. While its members have a similar domain organisation with the C1q group of the C1q phylogenetic tree (Figures 6.2, 6.5), they must have evolved differently from the rest of the C1q/TNF superfamily. This is further supported from the fact that gC1q domains of C1q-like proteins and Cerebellins are the only ones to be encoded from multiple exons, in contrast with the rest of the family (Yuzaki M., 2008).

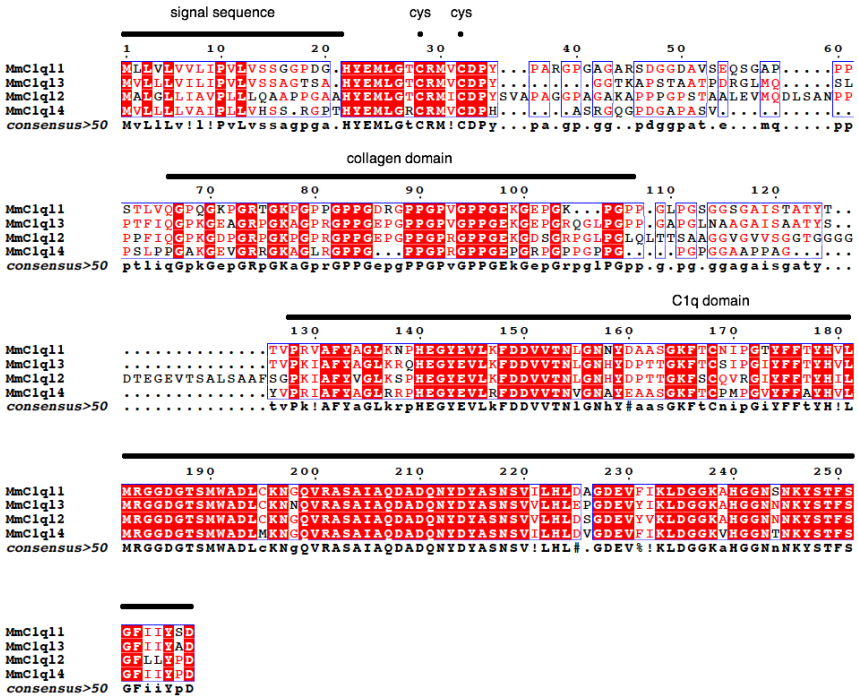


Figure 6.5: Multiple sequence alignment of mouse C1q-like family members, C1q-like 1 (O88992), C1q-like 2 (Q8CFR0), C1q-like 3 (Q9ESN4) and C1q-like 4 (Q4ZJM9). Domain organisation information is provided above the sequences. The alignment was generated with MultAlign online interface of a hierarchical clustering algorithm (Corpet F., 1988) and edited with ESPript interface (Gouet P., *et al.*, 2003).

The first of the c1q-like subfamily members to be discovered, C1ql1, was initially cloned

and identified as a senescence-related genomic product (Berube NG., *et al.*, 1999). As cerebellins, c1q-like proteins are predominantly expressed in the central nervous system (Iijima T., *et al.*, 2010).

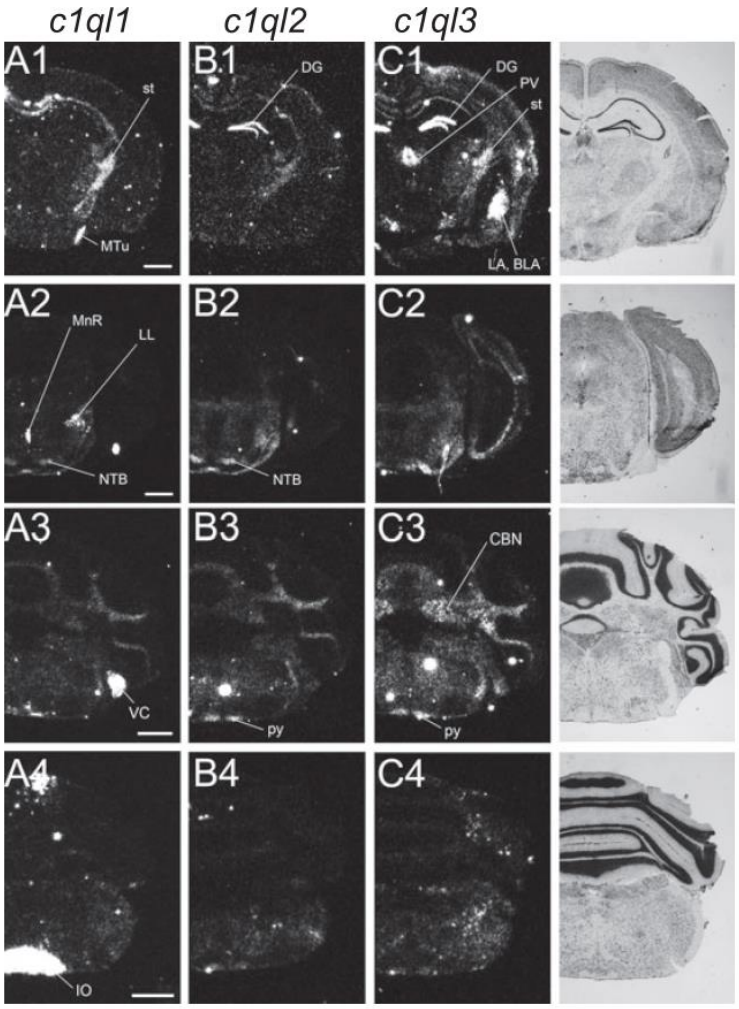


Figure 6.6: Detailed expression profiles of the C1ql1–C1ql4 mRNAs in adult mouse brain. Coronal sections were hybridized with ^{33}P-labeled oligonucleotide probes for the C1ql1 (A), C1ql2 (B) and C1ql3 (C) mRNAs. Methyl green pyronine-stained histology is shown at the far right. BLA, basolateral amygdalar nucleus; CBN, cerebellar nuclei; DG, dentate gyrus of the hippocampus; IO, inferior olivary complex; LA, lateral amygdalar nucleus; LL, lateral lemniscus; MnR, median raphe; MTu, medial tuberal nucleus; NTB, nucleus of the trapezoid body; PV, paraventricular thalamic nucleus; py, pyramidal tract; st, stria terminalis; VC, ventral cochlear nucleus. Scale bar, 1 mm. (Image and caption adopted from Iijima T., *et al.*, 2010).

Quantitative mRNA and *in situ* hybridisation analysis revealed a spatial distinction for C1ql1, C1ql2 and C1ql3, among various areas in the adult mouse (Iijima T., *et al.*, 2010) (Figure 6.6). C1ql1 and C1ql3 expression is appearing during as early as E10 and E12, while C1ql2 appears in later embryonic stages (Iijima T., *et al.*, 2010) (Figure 6.7). A preliminary biochemical characterisation revealed that C1q-like proteins form both homo- and heterotrimers, with detected multimerisation into hexamer and higher order multimers (Iijima T., *et al.*, 2010).

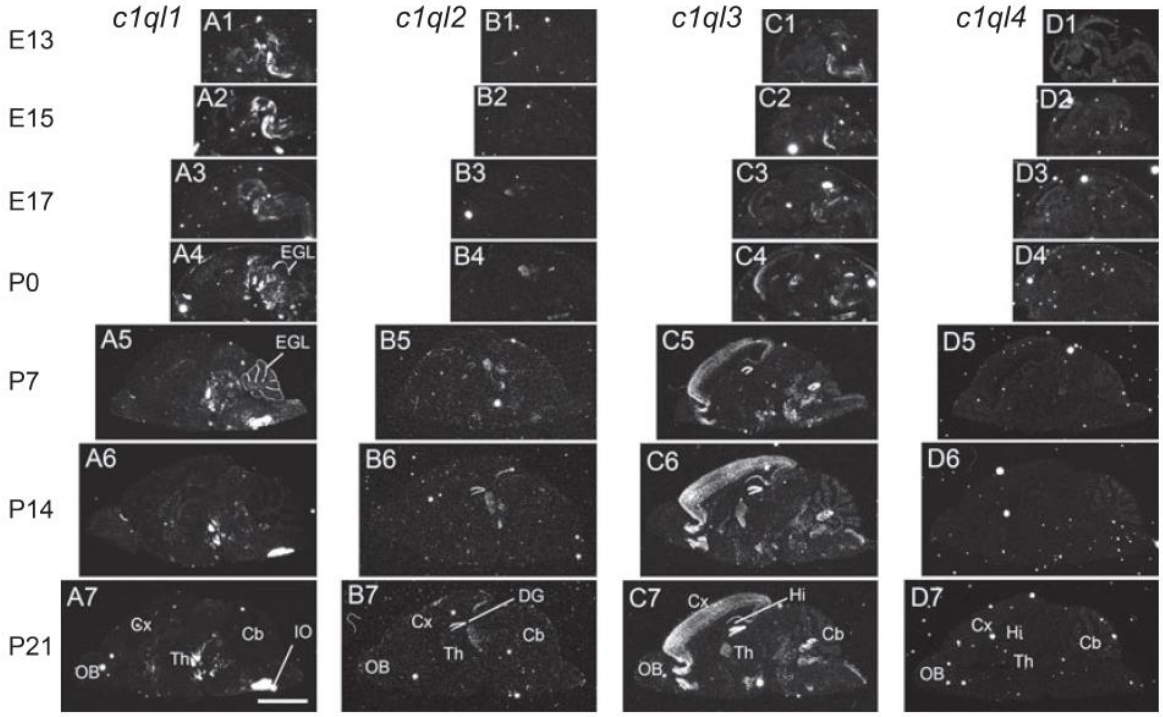


Figure 6.7: Developmental changes in the expression patterns of the C1ql1 (A), C1ql2 (B), C1ql3 (C) and C1ql4 (D) mRNAs from E13 to P21. Note that the spatial expression patterns of the C1ql2 and C1ql3 mRNAs were largely preserved throughout development. Also note that the C1ql1 mRNA was transiently detected at high levels in the cerebellar external granule layer (EGL) at P0 and P7. Cb, cerebellum; Cx, cerebral cortex; DG, dentate gyrus of hippocampus; Hi, hippocampus; IO, inferior olivary complex; OB, olfactory bulb; Th, thalamus. Scale bar, 3 mm. (Image and caption adopted from Iijima T., *et al.*, 2010).

6.2.4 In search of C1q-like synaptic partners: The case of BAI proteins

The adhesion subfamily of G-protein-coupled receptors (GPCRs), represent the second largest class of receptors sharing the classical seven-transmembrane-spanning domain (7TM), counting 150 distinct homologues conserved from invertebrates to human (Yona S., et al., 2008). The signature characteristic of the adhesion subfamily is a relatively elongated extracellular N-terminal region, which can have multiple types of domains able for diverse protein-protein interactions (Langenhan T., *et al.*, 2013) (Figure 6.8). The N-terminal ectodomains are connected via an autoproteolytic GPCR proteolysis site (GPS) to the 7TM region (Krasnoperov V., *et al.*, 2002).

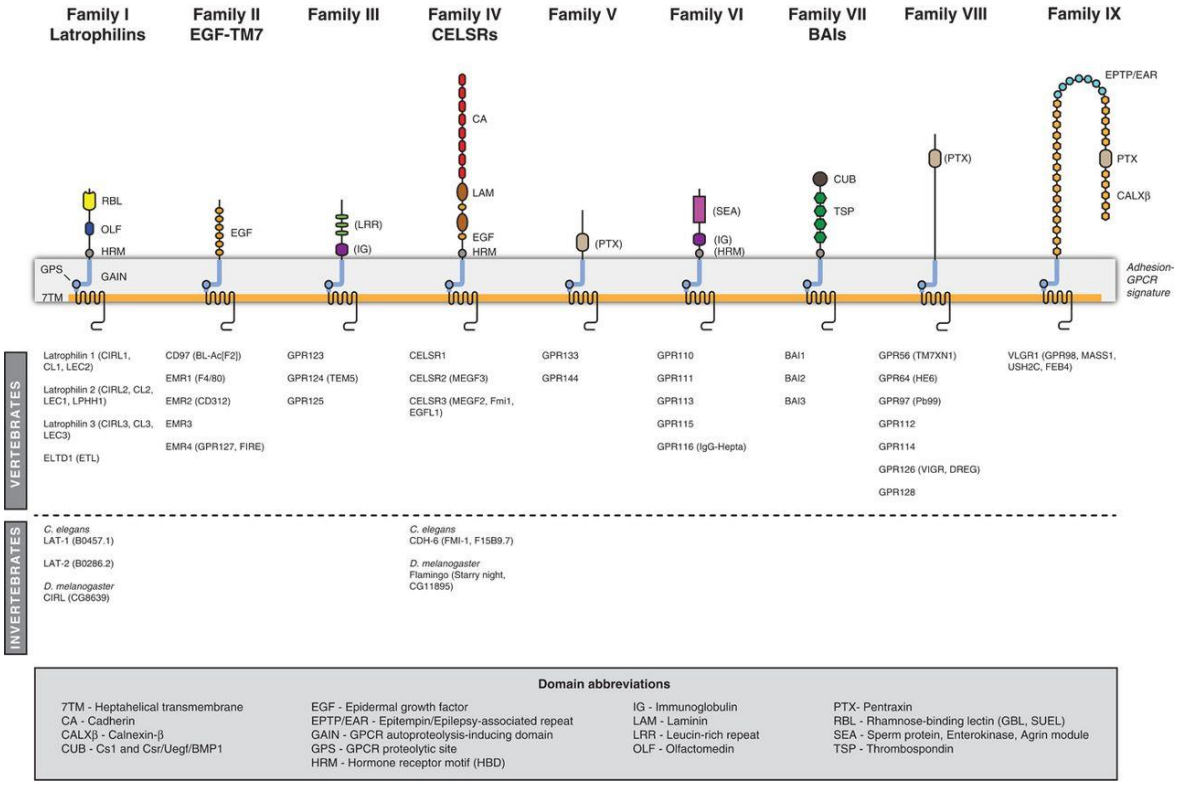


Figure 6.8: The Adhesion-GPCR class. Adhesion-GPCRs can be subdivided into nine distinct families with 33 homologs in mammalian genomes. Each family is specified by a unique combination of extracellular folds within the N-terminal fragment (bracketed domains are not present in every homolog of the family) and strong sequence similarity at the level of the 7TM domain. All families share a GPS and 7TM domain (Adhesion-GPCR signature). Families I and IV are present in invertebrate species, whereas all families can be found in vertebrates. Synonymous names are given in brackets (Image and caption adopted from Langenhan T., *et al.*, 2013)

An autoproteolytic treatment is facilitated at the GPS universally across the family, upon which the ectodomain remains non-covalently attached to the 7TM (Arac D., *et al.*, 2012). While it has not been demonstrated whether adhesion GPCRs function can be regulated by ligand binding as the rest GPCRs, it has been shown for Gpr126 that it can promote intracellular signalling events in zebrafish mutagenesis analyses (Monk KR., *et al.*, 2009).

There are three genes encoding for Brain-specific angiogenesis inhibitor (BAI) proteins, BAI1, BAI2 and BAI3, and their extracellular regions contain a CUB domain, a disordered region,a number of thrombospondin type I repeat domains, a hormone-binding region and the GPS (Nishimori H., *et al.*, 1997, Shiratsuchi T., et al., 1997). BAI proteins are highly expressed in the brain, but there are detectable levels in other regions as well (Haitina T., *et al.*, 2008, Koh JT., *et al.*, 2001, Kee HJ., *et al.*, 2002). BAI1 has been implicated in the regulation of vascular homeostasis and the prevention of tumorigenesis (Kaur B., et al., 2005). BAI3 has been recently demonstrated to regulate dendritic arborisation growth and branching in cultured cerebellar neurons, by inducing RhoGTPase signalling and causing a re-organisation of the actin cytoskeleton (Lanoue V., *et al.*, 2013). BAI3 appears to be expressed in most areas of the cerebal cortex and the hippocampus (as BAI1 and BAI2), but showed distinct patterns of neonatal expression than the other two BAI products, namely BAI3 expression peaked earlier in development (Kee HJ., et al., 2004). Genetic linkage analyses in schizophrenia revealed single-nucleotide polymorphisms (SNPs) in BAI3 (DeRosse P., *et al.*, 2008), contributing to a recent model for the disease aetiology, as primarily a neurodevelopmental disorder (Rapoport JL., *et al.*, 2005). Intriguingly, it was recently reported that C1ql proteins were identified by affinity chromatography to be BAI3 ligands (Bolliger MF., *et al.*, 2011). It was also demonstrated

that C1ql proteins can promote a decrease in synapse numbers in primary hippocampal cultures, and that this observation could be inhibited by the C1ql-binding fragment of BAI3 (Bolliger MF., *et al.*, 2011). Meanwhile, in single knock-out mouse models of C1ql2 and C1ql3, as well as in C1ql2/3 double knock-outs, the punctate ionotropic glutamate receptor (iGluR) K2/3 immunoreactivity in the CA3 region of the hippocampus is significantly reduced (Yuzaki M., unpublished data). What is more, recombinant C1ql2/C1ql3 have not been able to induce clustering of kainate iGluRs in hippocampal cultures (Yuzaki M., unpublished data). Given that neuropilin and tolloid-like (NETO) proteins, which are CUB-domain containing, have been demonstrated to be auxiliary subunits in the kainate iGluR function (Copits BA. and Swanson GT., 2012), it would be very interesting to investigate whether a synaptic assembly between C1q-like/BAI3/iGluR-kainate proteins, targets glutamatergic function in specialised areas of the brain.

6.3 Aims

The aim of this project is to assess by structural and biophysical means the proposed interactions between C1q-like molecules and their postulated synaptic ligands, BAI3 and GluK2. In addition C1q-like proteins will be tested for binding to Neurexin-1β isoforms.

Structural work will be functionally validated in animal studies, in collaboration with Prof. Michisuke Yuzaki (Keio University, Japan). Thus I am to contribute to the understanding of the role this family plays in synapse function and integrity.

6.4 Expression and Purification of C1ql, BAI3, iGluK2 proteins

6.4.1 Expression of C1ql, BAI3, iGluK2 proteins

A range of constructs targeting various regions on the extracellular region of *Mus musculus* BAI3 receptor, on members of the *Mus musculus* C1ql family C1ql1, C1ql2, C1ql3 and the amino-terminal domain of *Rattus norvegicus* ionotropic glutamate receptor GluK2 were designed, as described in section 2.1 and domain boundaries are listed in Figure 6.9 and Appendix B. The N-glycosylation pattern for all constructs is provided in Figure 6.9, as it was predicted from NetNGlyc 1.0 server (Gupta R. and Brunak S., 2002). All constructs were expressed in HEK293 cells, at high levels, as shown in Table 6.1.

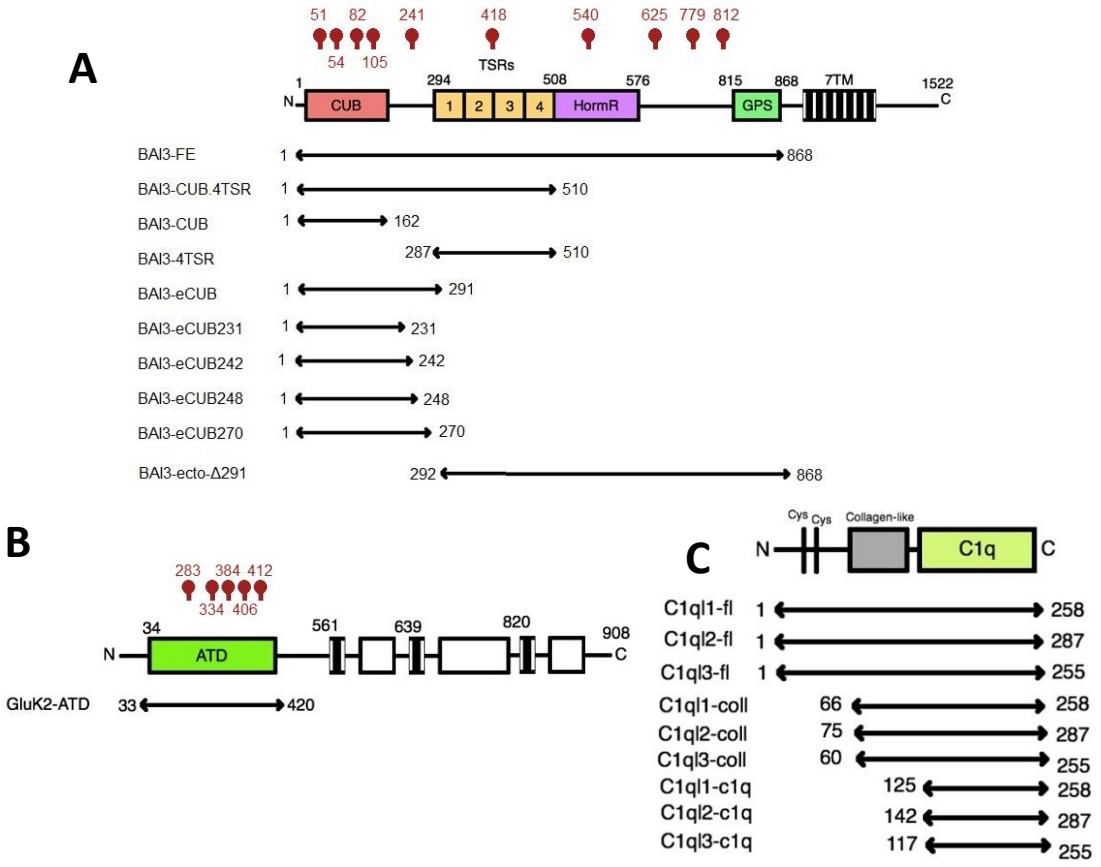


Figure 6.9: Schematic domain representation and boundaries for protein constructs used within the experimental context of this chapter for *Mm*Bai3 **(A)**, *Rn*GluK2 **(B)** and *Mm*C1ql family **(C)**. N-linked glycosylation sites are depicted as brown blobs. Domain boundaries were adopted from SMART database (Schultz J., *et al.*, 1998).

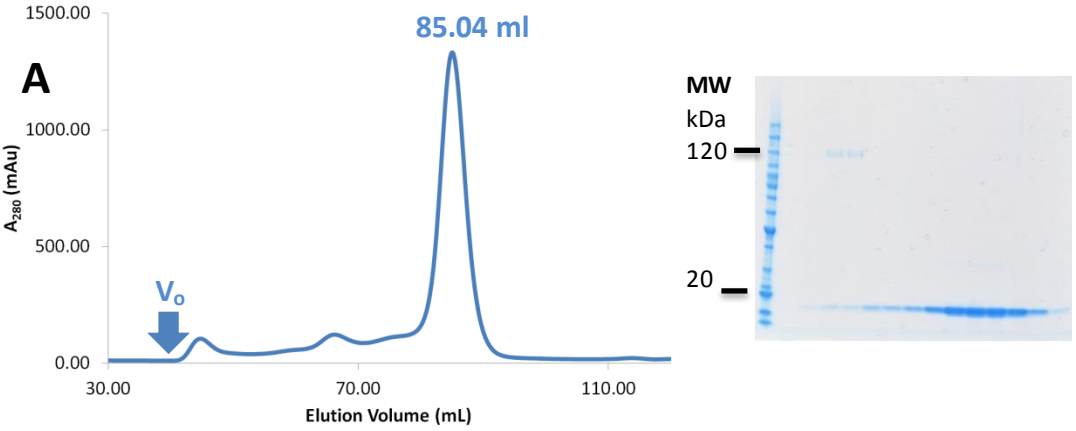
	Cell volume	Yield
***Mm*BAI3-CUB.4TSR**	~ 1.5 L	1.94 mg
***Mm*BAI3-4TSR**	~ 3 L	3.3 mg
***Mm*BAI3-eCUB**	~ 3 L	5.48 mg
***Mm*BAI3-eCUB242**	~ 3 L	2.7 mg
***Mm*BAI3-ecto-Δ291**	~ 1.5 L	1.28 mg
***Mm*C1ql1-c1q**	~ 3 L	4.1 mg
***Mm*C1ql3-c1q**	~ 3 L	4.7 mg
***Rn*GluK2-ATD**	~ 1.5 L	3 mg
***Hs*Neurexin1β**	~ 1 L	12.53 mg
***Hs*Neurexin1β-(+SS4)**	~ 1 L	9.38 mg

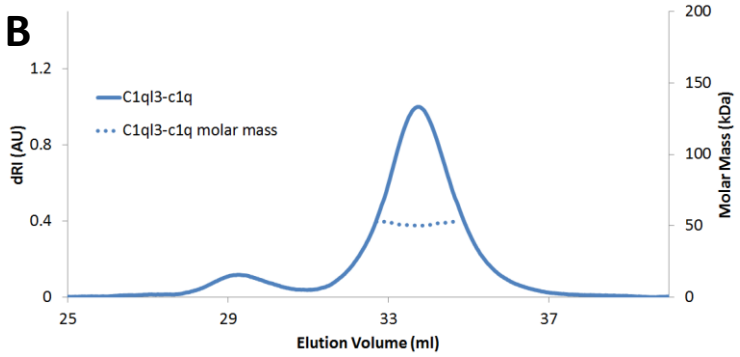
Table 6.1: Expression levels of BAI3, C1ql and GluK2 proteins. Yields stated correspond to final amounts at the end of the purification process.

*Hs*Neurexin1β and *Hs*Neurexin1β-(+SS4) constructs were kindly provided by Dr. Jordan Clay (Division of Structural biology, University of Oxford), and sequence information is provided in Appendix B.

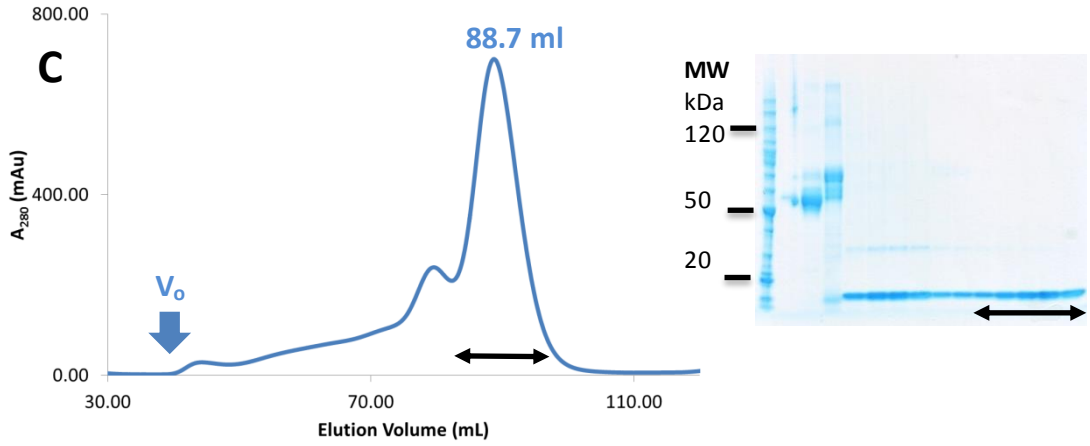
6.4.2 Purification of individual C1ql, BAI3, iGluK2 proteins

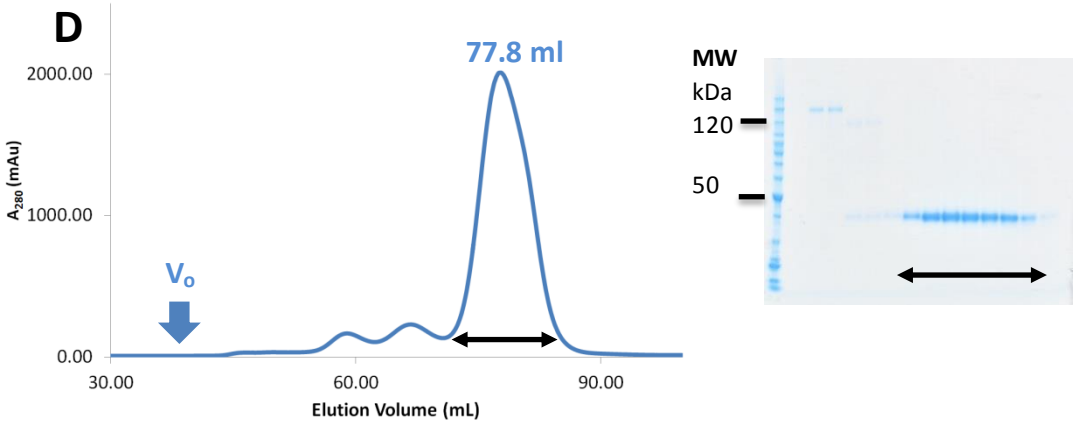
Ni-affinity purification of *Mm*C1ql1-c1q (~15.9 kDa), *Mm*C1ql3-c1q (~16.7 kDa), *Mm*BAI3-CUB.4TSR (~59.2 kDa), *Mm*BAI3-4TSR (~26 kDa), *Mm*BAI3-eCUB (~31.5 kDa), *Mm*BAI3-eCUB242 (~29.5 kDa), *Mm*BAI3-ecto-Δ291 (~66.8 kDa), *Rn*GluK2-ATD (~45.1 kDa), *Hs*Neurexin1β (~20.9 kDa) and *Hs*Neurexin1β-(+SS4) (~24.4 kDa) was performed as described in section 2.2.4.2. High imidazole elution fractions were subsequently gel purified, as described in section 2.2.4.4 (Figure 6.10). MALLS analysis, performed as described in section 2.8, of C1ql3-c1q indicated that it adopts a trimeric form in solution (Figure 6.10.B).

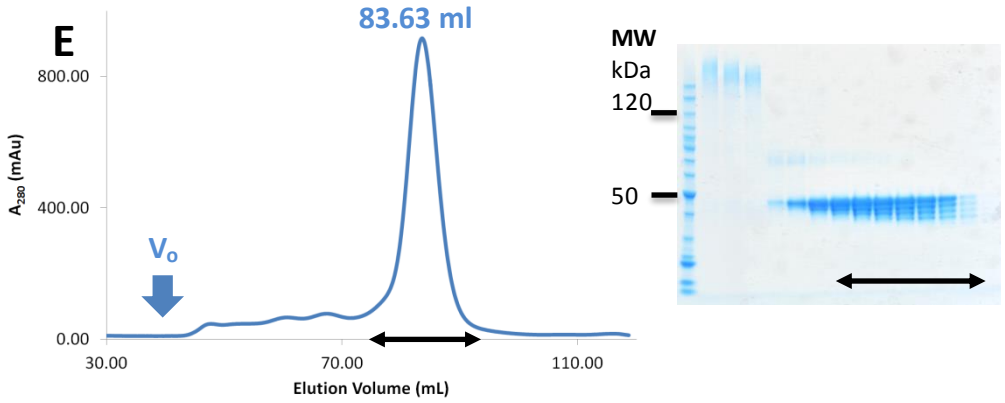


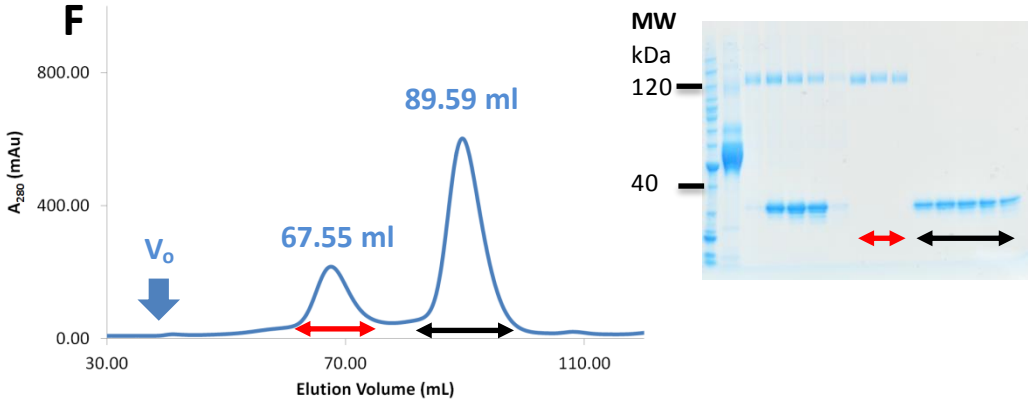


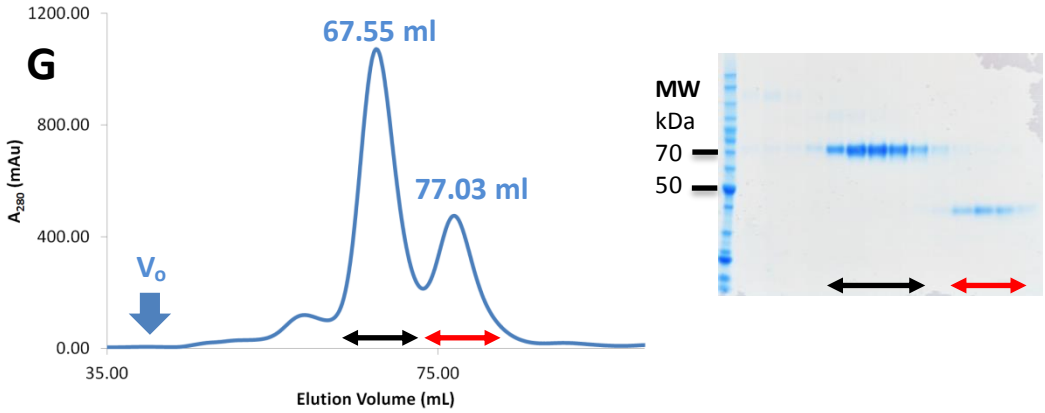
Measured Molar Mass (kDa)	Molecular Weight of a Single Subunit (kDa)	Measured Molar Mass/Single Subunit Molecular Weight	Oligomeric State of Sample
50.1	16.7	3	Trimer

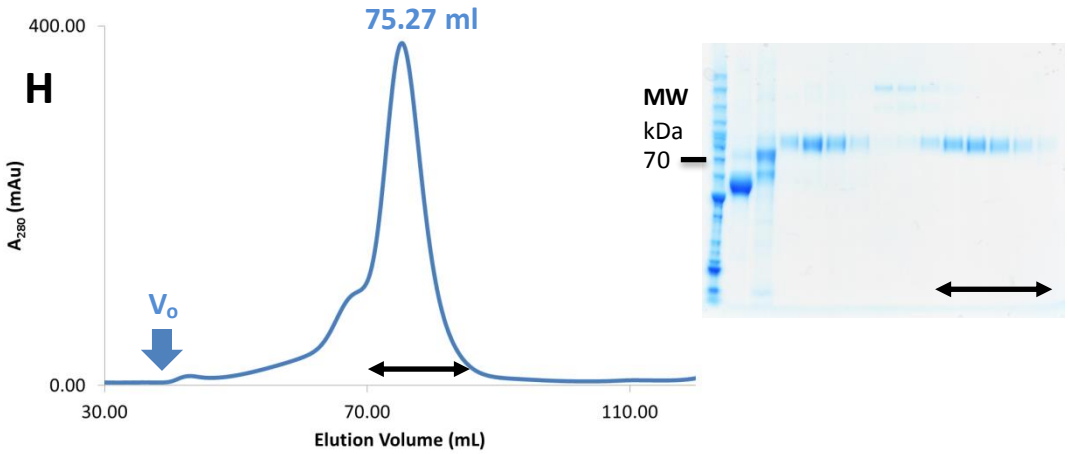





E
83.63 ml
800.00
400.00
0.00
A280 (mAu)
Vo
30.00
70.00
110.00
Elution Volume (mL)
MW
kDa
120
50


F
89.59 ml
67.55 ml
800.00
400.00
0.00
A280 (mAu)
Vo
30.00
70.00
110.00
Elution Volume (mL)
MW
kDa
120
40


G
67.55 ml
77.03 ml
1200.00
800.00
400.00
0.00
A280 (mAu)
Vo
35.00
75.00
Elution Volume (mL)
MW
kDa
70
50


H
75.27 ml
400.00
0.00
A280 (mAu)
Vo
30.00
70.00
110.00
Elution Volume (mL)
MW
kDa
70

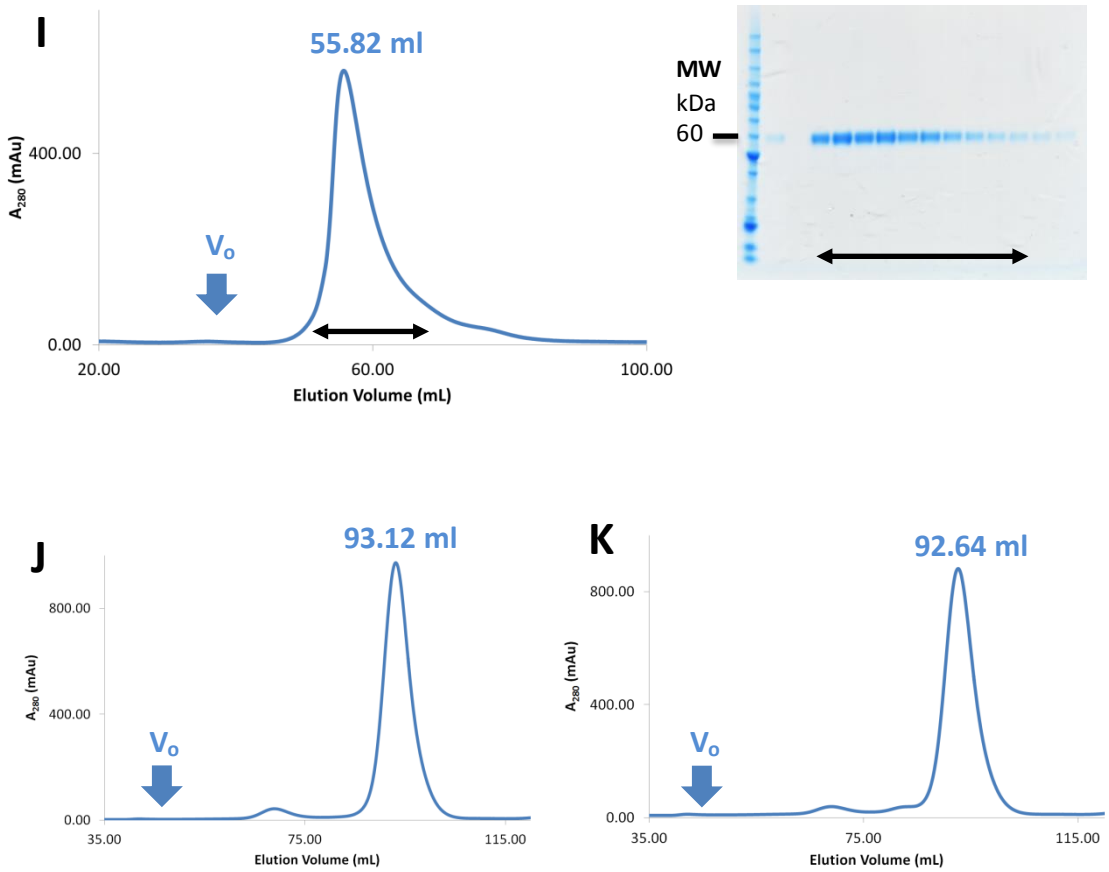


Figure 6.10: Gel filtration profiles of C1ql, BAI3 and iGluK2 protein constructs, accompanied by SDS-PAGE and MALLS, where appropriate. Black arrows correspond to peaks for proteins of interest. **(A)** S200 elution profile of C1ql3-c1q and SDS-PAGE. **(B)** MALLS analysis of C1ql3-c1q, indicating that it is trimeric in solution. **(C)** S200 elution profile of C1ql1-c1q and SDS-PAGE. **(D)** S200 elution profile of BAI3-4TSR and SDS-PAGE. **(E)** S200 elution profile of BAI3-eCUB and SDS-PAGE. **(F)** S200 elution profile of BAI3-eCUB242 and SDS-PAGE. Red arrows correspond to unidentified contaminant. **(G)** S200 elution profile of BAI3-CUB.4TSR and SDS-PAGE (Red arrows correspond to potential proteolytic cleavage product). **(H)** S200 elution profile of BAI3-ecto-Δ291 and SDS-PAGE. **(I)** S200 elution profile of GluK2-ATD and SDS-PAGE. **(J)** S200 elution profile of Neurexin1β. **(K)** S200 elution profile of Neurexin1β-(+SS4).

6.5 Structure determination of C1ql1 and C1ql3 c1q domains

C1ql3-c1q was concentrated to 5.37 mg/ml and was used for nanolitre-scale crystallization trials, as described in section 2.3.1. Three-dimensional crystals were grown approximately within 3 days after setup (Figure 6.11.A), which diffracted up to 1.42 Å resolution (Figure 6.11.B). A 360^{o} diffraction data set was collected with 0.2^{o} oscillation step on a Pilatus-2M detector on Diamond-I04-1 beamline (Diamond Light Source, Oxfordshire, UK). Data collection statistics are described in Table 6.2. The crystal structure of the Cerebellin1-C1q, determined by Dr. Jordan Clay in the Dr. Aricescu laboratory, was used as a search model for molecular replacement using Phaser (McCoy AJ.,et al., 2005), yielding a solution with a translation score of 34.8, a LLG of 611 and a single monomer in the asymmetric unit (Figure 6.12). The solvent content of the crystal was 30.71 according to the Matthews Coefficient (Matthews BW., 1968), while the trimer can be observed being reconstituted by the crystallographic symmetry operations (H3 spacegroup). Iterative rounds of manual model building in Coot (Emsley P. and Cowtan K., 2004), followed by refinement using Refmac (Mushudov GN., *et al.*, 1997) or Phenix (Adams PD., *et al.*, 2010) were performed. Refinement statistics are also available in Table 6.2.

C1ql3-c1q crystallised in a different condition and space group, $P2_12_12_1$, while pursuing the co-crystallisation with a potential protein-protein interaction partner, as described in section 6.8. The crystals were grown approximately within a month after setup (Figure 6.11.C) and diffracted up to 1.72 Å resolution (Figure 6.11.D). A 360^{o} diffraction data set was collected with 0.2^{o} oscillation step on a Pilatus-6M detector on Diamond-I02 beamline (Diamond Light Source, Oxfordshire, UK). Data collection statistics are available

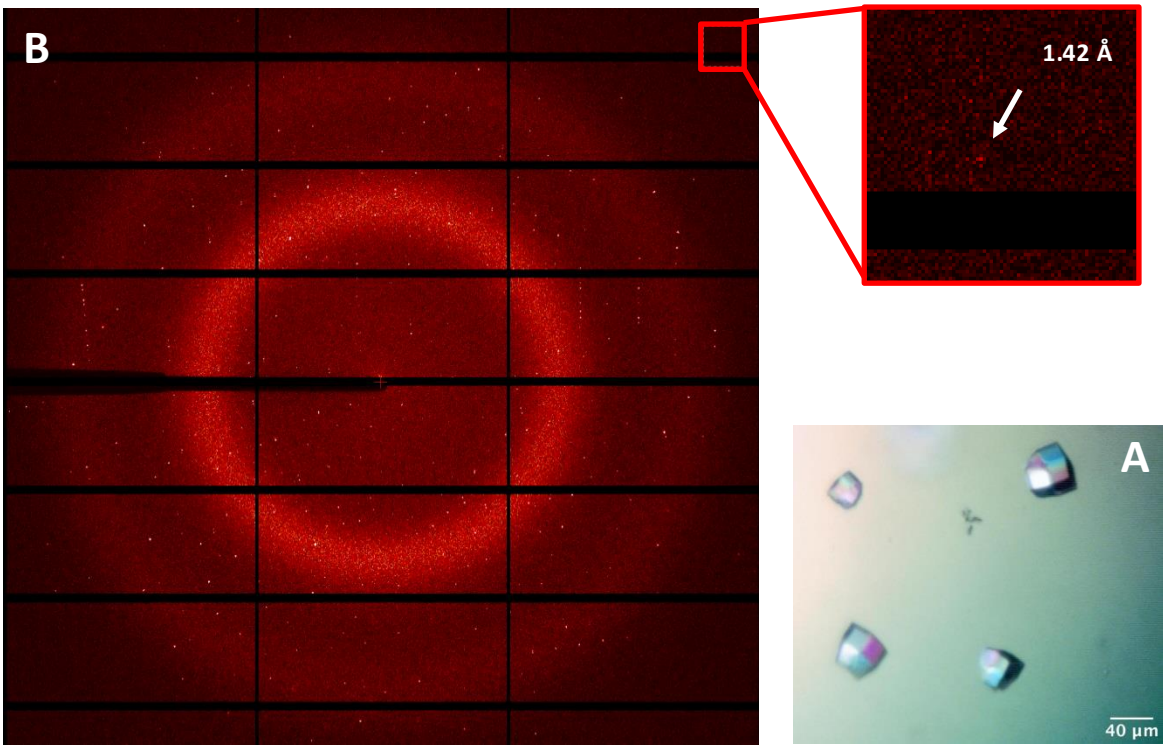
in Table 6.2. The C1ql3-c1q$_{H3}$ structure described above was used as a search model for molecular replacement using Phaser (McCoy AJ.,et al., 2005), yielding a solution with a translation score of 44.4, a LLG of 6834 and a trimer in the asymmetric unit (Figure 6.13).

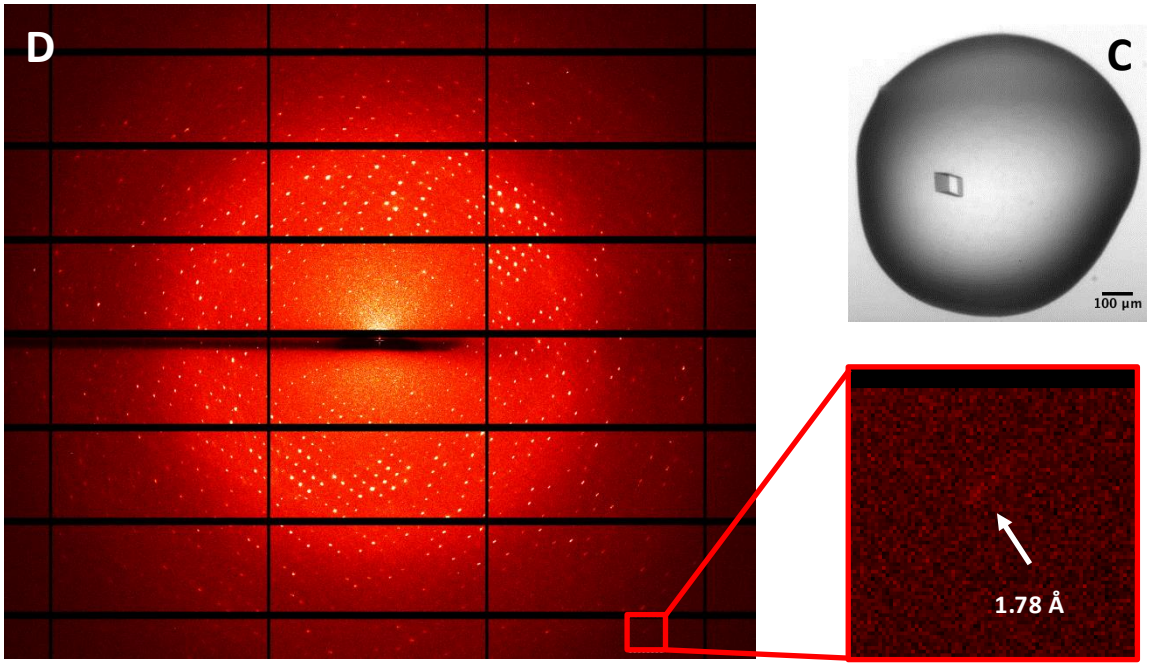
Data Collection Statistics			
Protein	C1ql1-c1q	C1ql3-c1q	C1ql3-c1q *(in presence of GluK2-ATD)*
Beamline	Diamond-I04	Diamond-I04-1	Diamond-I02
Resolution (Å)	34.04-1.49 (1.53-1.49)	44.01 - 1.42 (1.46-1.42)	45.00-1.72 (1.77-1.72)
Spacegroup	H3	H3	$P2_12_12_1$
Cell dimensions a, b, c (Å) α, β, γ (^{o})	 68.08, 68.08, 65.92 90.00, 90.00, 120.00	 68.50, 68.50, 65.64 90.00, 90.00, 120.00	 54.30, 80.43, 87.52 90.00, 90.00, 90.00
Wavelength (Å)	0.97625	0.91730	0.97949
Unique reflections	18641 (1414)	19355 (758)	41154 (3011)
Completeness (%)	100.0 (100.0)	89.2 (46.7)	100 (99.9)
R_{merge} (%)	6.1 (62.6)	6.7 (47)	4.2 (66.8)
I/σI	19.1 (3)	13.9 (2.4)	22.1 (2.7)
Redundancy	7.6 (7.6)	6.0 (3.7)	6.4 (6.5)
Refinement Statistics			
Resolution range (Å)	34.04-1.49 (1.53-1.49)	44.01 - 1.42 (1.46-1.42)	45.00-1.72 (1.77-1.72)
Number of reflections	18641 (2548)	18391 (722)	41092 (2570)
R_{work} (%)	13.81 (18.17)	11.62 (21.10)	16.24 (22.84)
R_{free} (%)	16.32 (21.72)	16.76 (30.3)	18.67 (27.19)
No. of all atoms	1112	1148	3328
-macromolecules	1017	1054	3326
-ligands	7	11	2
-water molecules	88	83	196
R.M.S.D. bonds (Å)	0.006	0.021	0.007
R.M.S.D. angles (^{o})	1.14	2.18	1.118
Average B factor (Å^2)	18.80	15.80	32.40
-macromolecules	17.70	14.60	31.80
-ligands	19.80	29.00	50.90
-solvent	32.30	30.10	42.40
Ramachandran plot (% residues)			
Favoured	95.45	95.16	97.46
Additionally allowed	4.58	4.84	2.54
Disallowed	0	0	0

Table 6.2: Crystallographic statistics for C1ql crystal structures. Numbers in brackets refer to the high resolution shell.

The solvent content of the crystal was 42.11 according to the Matthews Coefficient calculation for a trimer in the asymmetric unit (Matthews BW., 1968). Iterative rounds of manual model building in Coot (Emsley P. and Cowtan K., 2004), followed by refinement using Refmac (Mushudov GN., *et al.*, 1997) or Phenix (Adams PD., *et al.*, 2010) were performed. Tight non-crystallographic symmetry restraints that were implemented during most of the refinement process, were released towards the final stages. Refinement statistics are also available in Table 6.2.

C1ql1-c1q was concentrated to 5.46 mg/ml and was used for nanolitre-scale crystallization trials, as described in section 2.3.1. Three-dimensional crystals were grown approximately within 24 hours after setup (Figure 6.11.E), which diffracted up to 1.49 Å resolution (Figure 6.11.F). A 360^{o} diffraction data set was collected with 0.2^{o} oscillation step on a Pilatus-6M-F detector on Diamond-I04 beamline (Diamond Light Source, Oxfordshire, UK). Data collection statistics are available in Table 6.2 The rhombohedral crystal form of C1ql3-c1q structure described above was used as a search model for molecular replacement using Phaser (McCoy AJ.,et al., 2005), yielding a solution with a translation score of 90.1, a LLG of 4870 and a and a single monomer in the asymmetric unit (Figure 6.14). The solvent content of the crystal was 37.28 according to the Matthews Coefficient (Matthews BW., 1968), while the trimer can be observed being reconstituted by the crystallographic symmetry operations (negated for H3 spacegroup). Iterative rounds of manual model building in Coot (Emsley P. and Cowtan K., 2004), followed by refinement using Refmac (Mushudov GN., *et al.*, 1997) or Phenix (Adams PD., *et al.*, 2010) were performed. Refinement statistics are also available in Table 6.2.


B
1.42 Å
A
40 µm


D
C
100 µm
1.78 Å

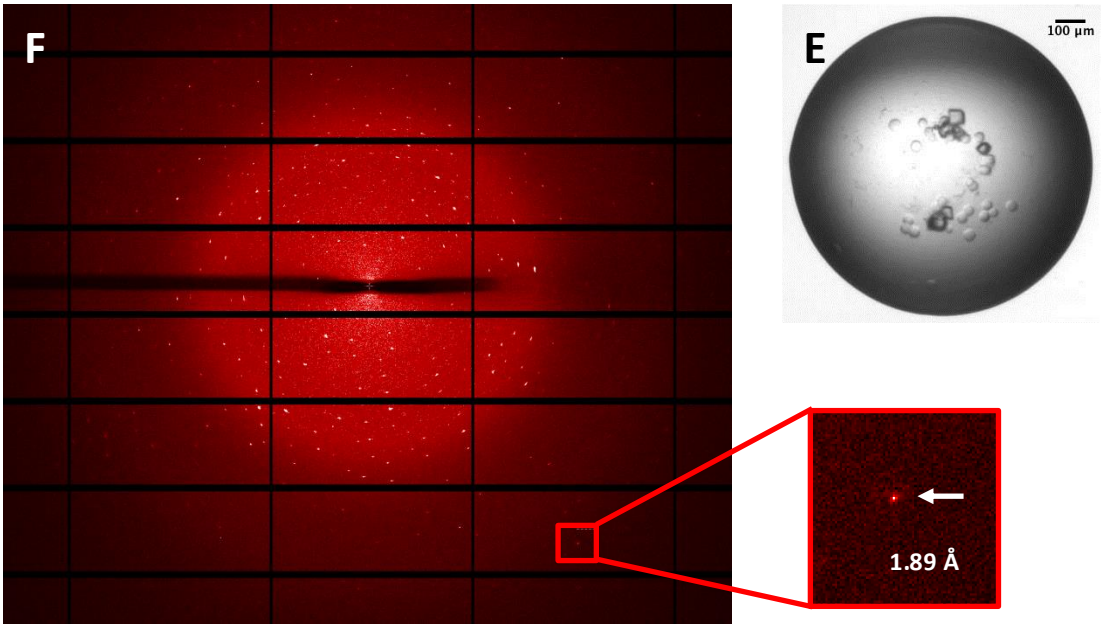


Figure 6.11: Diffraction of C1ql crystals. **(A)** Representative C1ql3-c1q crystals grown in 0.02 M Nickel(II) chloride hexahydrate, 0.02 M Magnesium chloride hexahydrate, 0.02 M Cadmium chloride hydrate, 0.1 M Sodium acetate trihydrate pH 4.5, 24% w/v polyethylene glycol monomethyl ether 2000. **(B)** Diffraction data up to ~1.42 Å were collected from crystals in panel A. **(C)** Representative C1ql3-c1q crystals grown in 0.1 M Citrate pH 5, 2.4 M Ammonium Sulfate, in presence of GluK2-ATD. **(D)** Diffraction data up to ~1.72 Å were collected from crystals in panel C. **(E)** Representative C1ql1-c1q crystals grown in 0.02 M Nickel(II) chloride hexahydrate, 0.02 M Magnesium chloride hexahydrate, 0.02 M Cadmium chloride hydrate, 0.1 M Sodium acetate trihydrate pH 4.5, 24% w/v polyethylene glycol monomethyl ether 2000. **(F)** Diffraction data up to ~1.48 Å were collected from crystals in panel A.

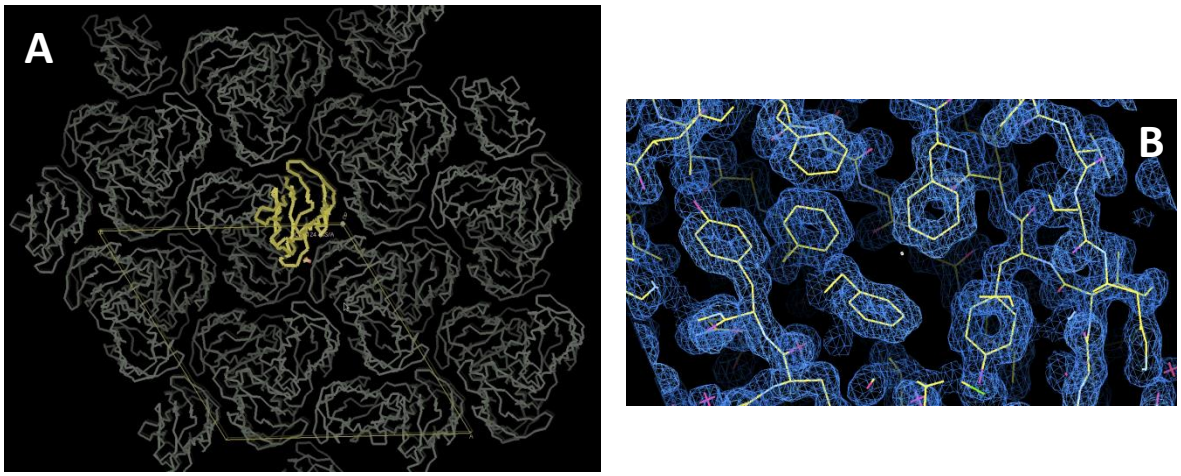


Figure 6.12: Crystal packing and final electron density maps of C1ql3- c1q (rhombohedral crystal form) structure refinement. **(A)** Packing of C1ql3- c1q molecules in the crystal. One monomer comprises the asymmetric unit (yellow). **(B)** Electron density maps of C1ql3- c1q (rhombohedral crystal form) at the end of the refinement. $2F_c$-$2F_o$ maps (blue) and F_o-F_c maps (green and red) are contoured at 1 and 3 σ respectively.

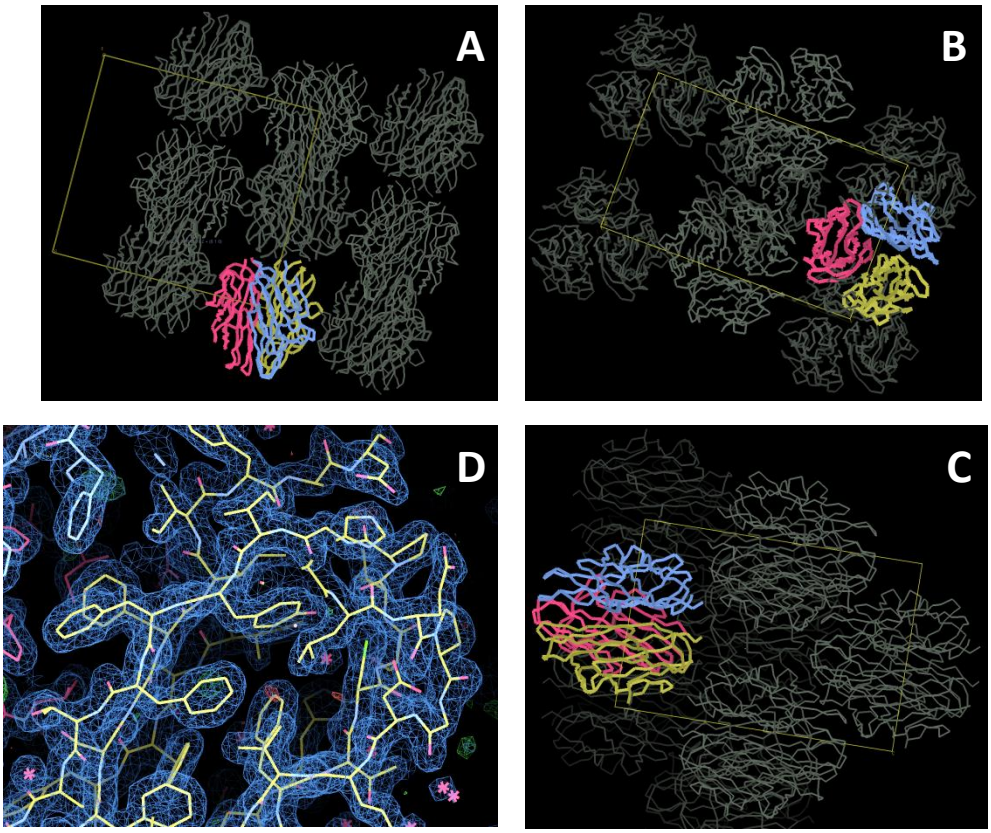


Figure 6.13: Crystal packing and final electron density maps of C1ql3- c1q (orthorombic crystal form) structure refinement. **(A)** Packing of C1ql3- c1q molecules in the crystal. The asymmetric unit is comprised of three monomers depicted inmagent, yellow and blue. **(B)** 90o horizontal rotation of panel A. **(C)** 90o vertical rotation of panel B. **(D)** Electron density maps of C1ql3- c1q (orthorombic crystal form) at the end of the refinement. $2F_c$-$2F_o$ maps (blue) and F_o-F_c maps (green and red) are contoured at 1 and 3 σ respectively.

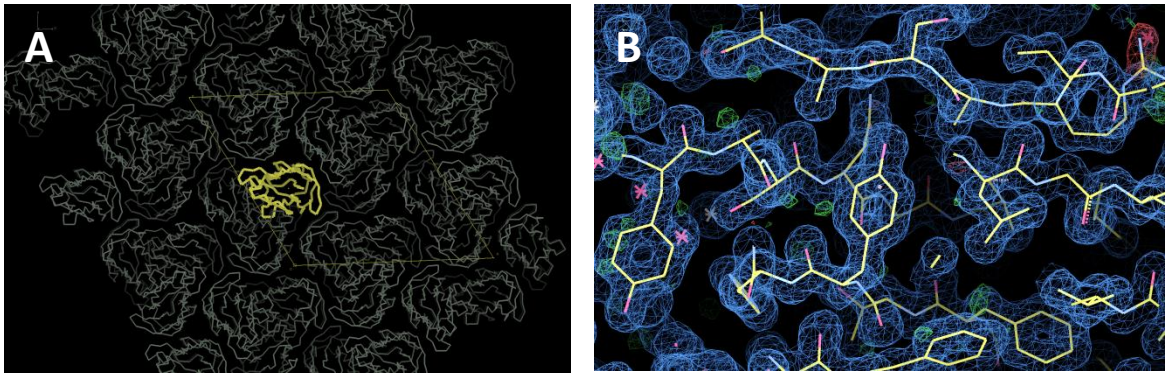


Figure 6.14: Crystal packing and final electron density maps of C1ql1- c1q structure refinement. **(A)** Packing of C1ql1- c1q molecules in the crystal. The asymmetric unit is comprised of one monomer (yellow). **(B)** Electron density maps of C1ql1- c1q at the end of the refinement. $2F_c$-$2F_o$ maps (blue) and F_o-F_c maps (green and red) are contoured at 1 and 3 σ respectively.

The C1q domains of C1ql1 (Figure 6.15.A) and C1ql3 (Figure 6.15.B) are compact trimer of three identical β-sandwiches formed by two antiparallel β-sheets and bear the classic topology of a jelly-roll motif.

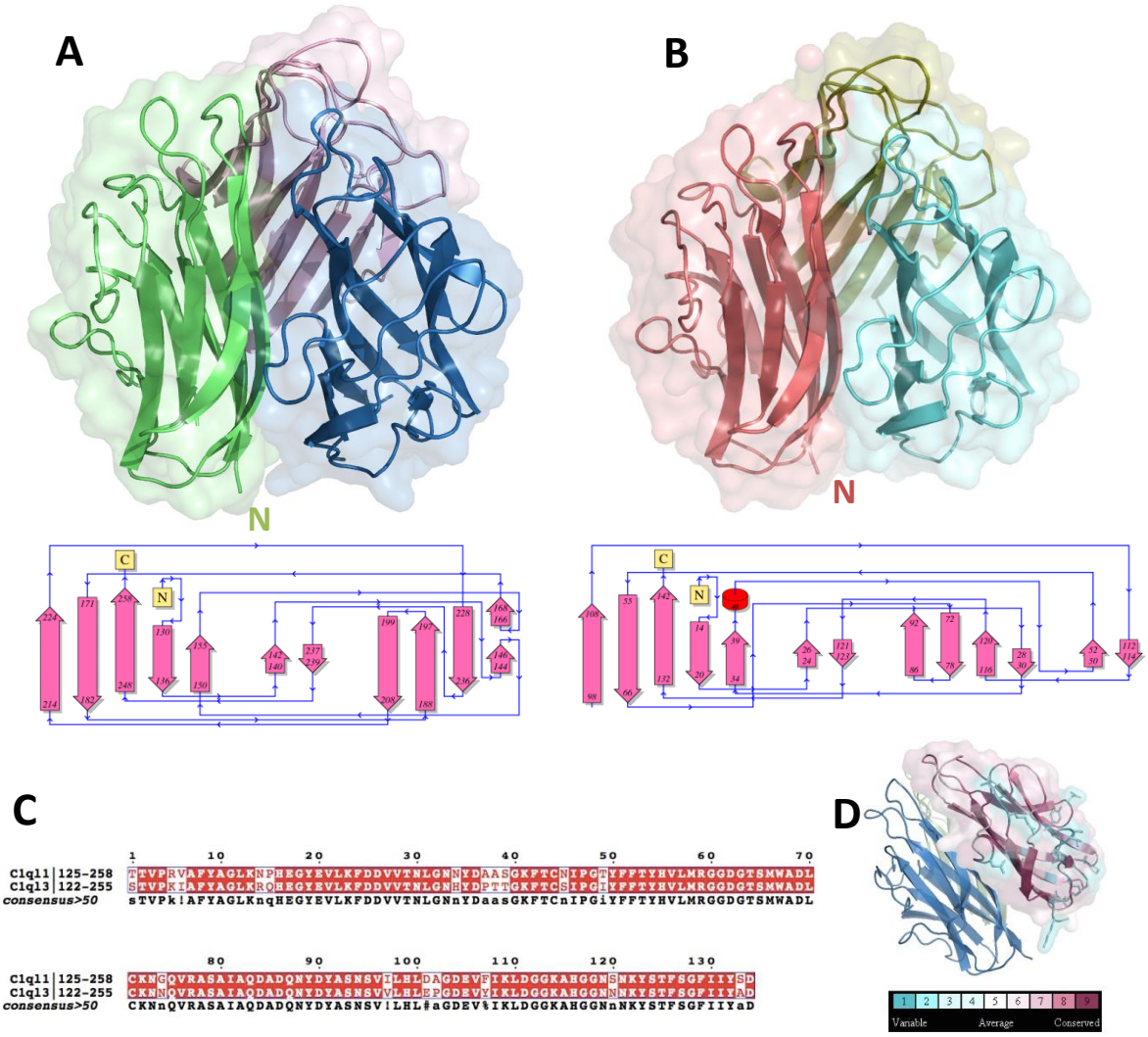
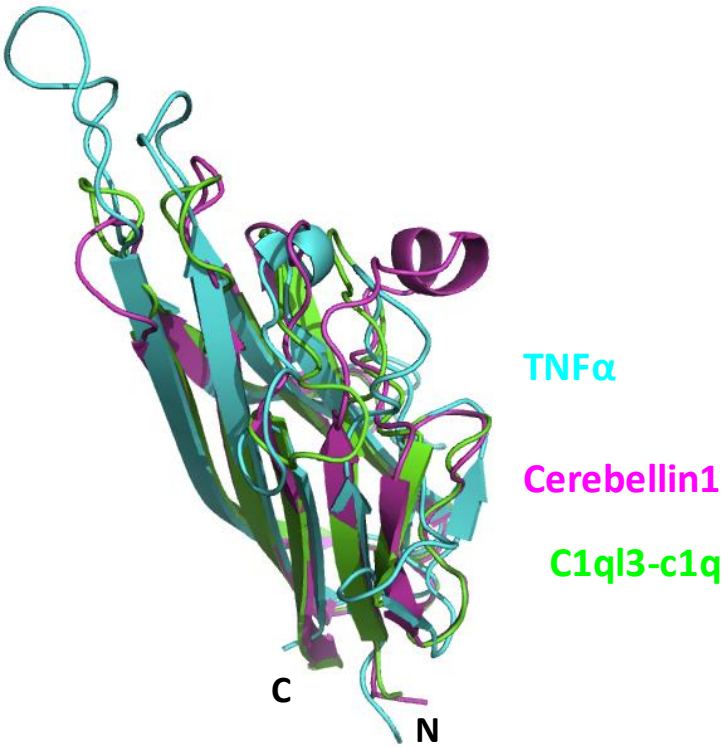


Figure 6.15: C1ql1-c1q and C1ql3-c1q crystal structures. **(A)** Homotrimeric C1ql1-c1q crystal structure in cartoon and transparent surface representation, coloured by each monomer chain (lime, skyblue and purple). The topology diagram is depicted below the model. **(B)** Homotrimeric C1ql3-c1q crystal structure in cartoon and transparent surface representation, coloured by each monomer chain (salmon, cyan and deep olive). The topology diagram is depicted below the model. **(C)** Alignment of sequences for C1ql1 and C1ql3 proteins that appear in the structures. C1ql3-c1q differs from C1ql1-c1q in 17 residues, located primarily on the external side of the trimer, as shown on panel D. **(D)** C1ql3-c1q structure in cartoon and transparent surface representation. The alignment of panel C was used to highlight the variable residues on one of the monomers of the trimer using the ConSURF server (Celniker G., *et al.*, 2013).

C1q domains of C1ql proteins appear to be more compact when compared to other C1q superfamily members (Figure 6.16). Most of the flexible regions appear shorter than the ones of TNFα, while C1ql also lack the distinctive helix on the side of the Cerebellin trimer (Figure 6.16).




```
                    1         10        20        30        40        50        60        70
MmTNFa|80-235       LRSSSQNSSDKPVAHVVANHQVEEQLEWLSQRANALLANGMDLKDNQLVVPADGLYLVYSQVLFKGQGCP
MmCbln1|59-193      .SAKVAFSAIRSTNHEPSEMSNRTM.IIYFDQVLVNIGNNFDSERSTFIAPRKGIYSFNFHVV.KV....
MmC1ql3|117-255     .SAATYSTVPKIAFYAGLKRQHEGYEVLKFDDVVTNLGNHYDPTTGKFTCSIPGIYFFTYHVLMRG....
consensus>50        .sa....s..k...h...n.q.e...i..f#qv..nlgN.fD.....fv.p..GiY.f.fhVl.kg....

                              80        90        100       110       120       130       140
MmTNFa|80-235       DYVLLTHTVSRFAISYQEKVNLLSAVKSPCPKDTPEGAELKPWYEPIYLGGVFQLEKGDQLSAEVNLPKY
MmCbln1|59-193      ..............YNRQTIQVSLMLNGWPVISAFAGDQDVTREAASNGVLIQMEKGDRAYLKLERGNL
MmC1ql3|117-255     ..............GDGTSMWADLCKNNQVRASAIAQDADQNYDYASNSVVLHLEPGDEVYIKLDGGKA
consensus>50        ..............y#.....sl.kn..p..sa.a.#.d..y#.asngvv.q$EkGDq.y.kl#.gk.

                    150
MmTNFa|80-235       LDFAESGQVYFGVIAL..
MmCbln1|59-193      MGGW..KYSTFSGFLVFPL
MmC1ql3|117-255     HGGNNNKYSTFSGFIIYAD
consensus>50        lgg.e.kystFsgf.vf..
```

Figure 6.16: Comparison of C1ql-c1q structure with other related proteins. *Mm*Cerebellin1 (magenta, unpublished data Aricescu lab) and MmTNFα (cyan, PDB: 2TNF, Baeyens KJ., *et al.*, 1999) are superposed on C1ql3-c1q (green) structure. An alignment below the superimposition highlights the low sequence identity of the family members.

Interestingly, in our C1ql3-c1q rhombohedral crystal form, a series of cadmium ions are coordinated by three conserved aspartates (D205, D207 and D211) at the interface of the three subunits (Figure 6.17) (Figure 6.3), while this is not the case for the C1ql3-c1q orthorhombic crystal form which was grown in a different crystallization condition (Figure 6.18) (Table 2.3).

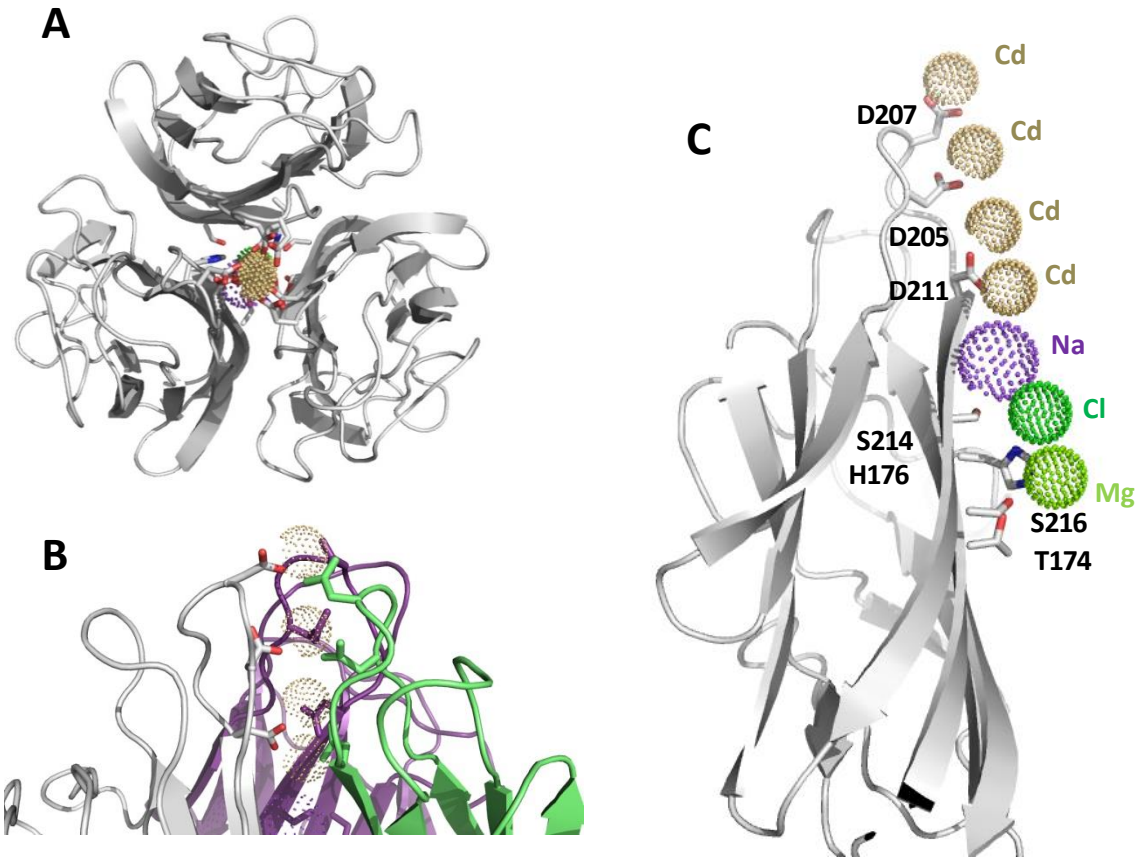


Figure 6.17: Metals bound on C1ql3-c1q **rhombohedral** crystal form. **(A)** Top view of a cartoon representation of C1ql3-c1q structure. A set of metals appears to be located on the 3-fold symmetry axis. **(B)** Side view of a cartoon representation of C1ql3-c1q structure, highlighting the coordination of metals by residues of all three monomers (colored in grey, green and purple). **(C)** Four cadmium ions (wheat), a sodium (purple), a chloride (dark green) and a magnesium ion (light green) are coordinated by sidechains of D207, D205, D211, S214, H176, S216 and T174.

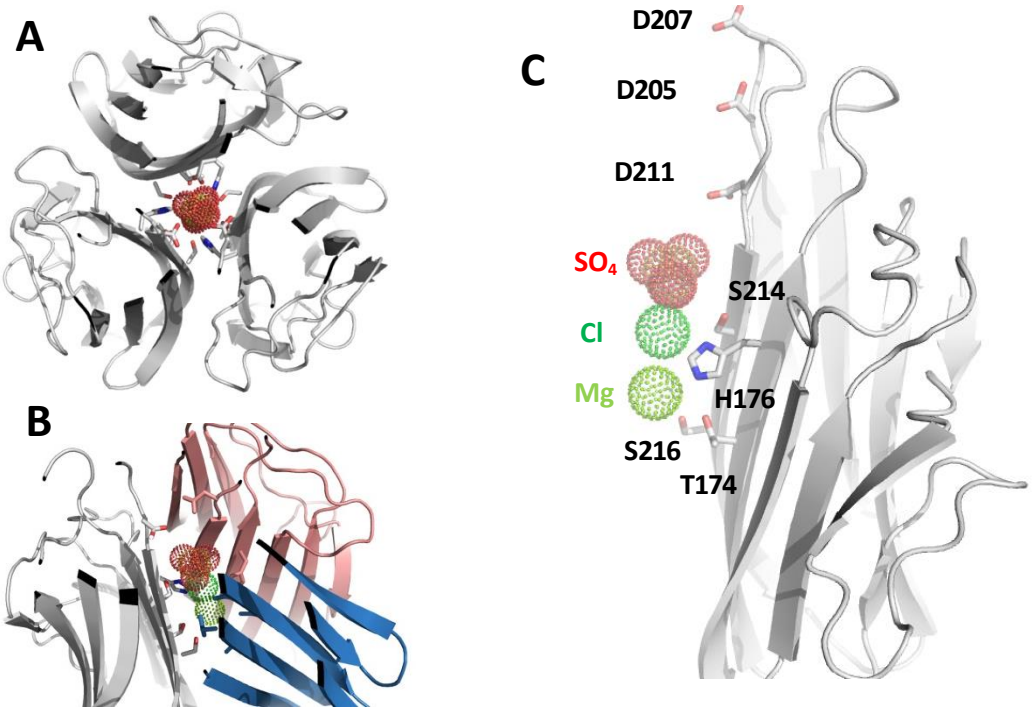


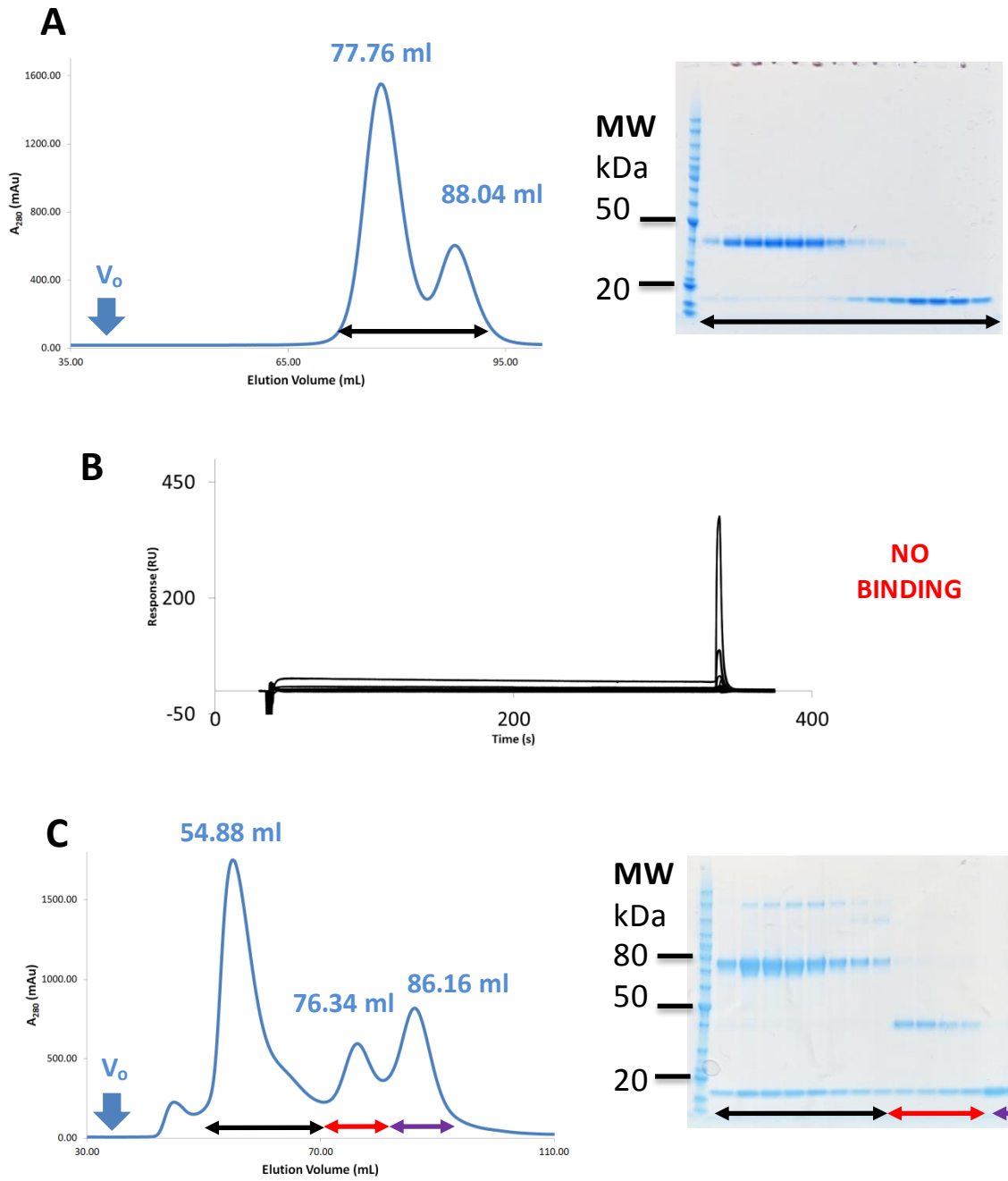
Figure 6.18: Metals bound on C1ql3-c1q **orthorhombic** crystal form. **(A)** Top view of a cartoon representation of C1ql3-c1q structure. **(B)** Side view of a cartoon representation of C1ql3-c1q structure, highlighting the coordination of metals by residues of all three monomers (colored in grey, green and purple). **(C)** A sulphate ion (red), a chloride (dark green) and a magnesium ion (light green) are coordinated by sidechains of S214, H176, S216 and T174.

6.6 Molecular dissection of C1ql/BAI-3 interaction

6.6.1 Mapping C1ql3/BAI3 interaction with deletion constructs

Constructs described in section 6.4.1 (and Appendix B) were used to map the interaction between BAI3 receptor and C1ql proteins. The essential units for the interaction has been reported reported to be the C1q domain of C1qls and the four thrombospondin domain region on the ectodomain of BAI3 (BAI-4TSR, Figure 6.9) (Bollinger MF., *et al.*, 2011). However, we were unable to reproduce this finding after *in vitro* reconstitution with a molar ratio of 1:1.5 (BAI3-4TSR:C1ql3-c1q) (Figure 6.19.A), in presence of 2 mM $CaCl_2$ and 2 mM $MgCl_2$. Surface plasmon resonance (SPR) provided additional confirmation for the

lack of interaction (Figure 6.19.B). On the contrary, we could reproduce binding between more extended ectodomain regions (BAI3-FE, BAI3-CUB.4TSR) to C1ql-c1q, as indicated from SPR (Figure 6.19.D.E) and gel filtration of co-expressed proteins (BAI3-CUB.4TSR/C1ql3-c1q) (Figure 6.19.C).



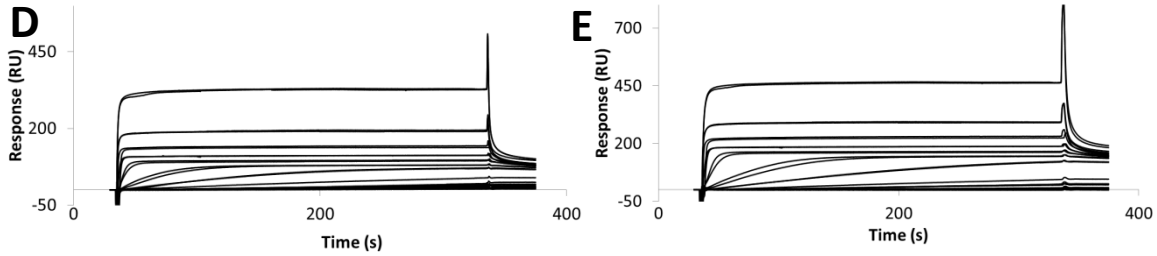
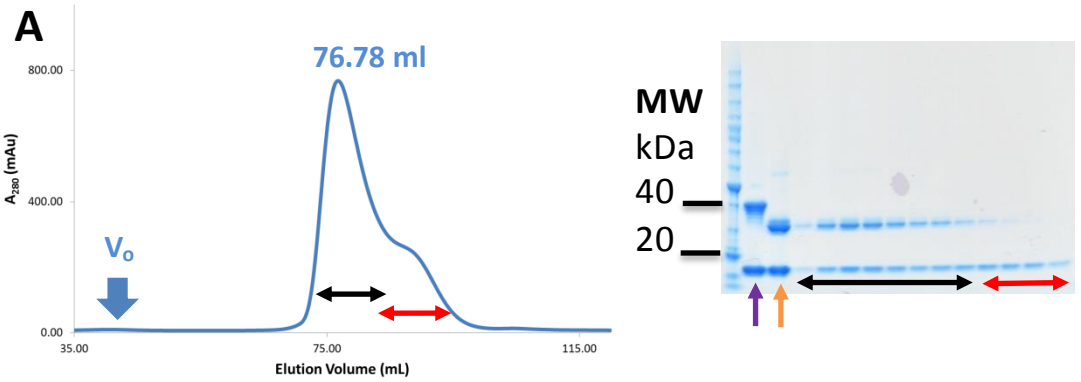
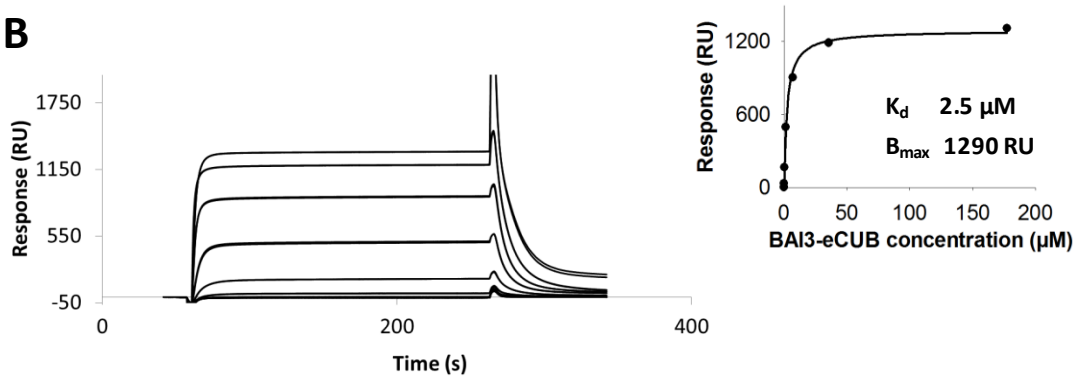
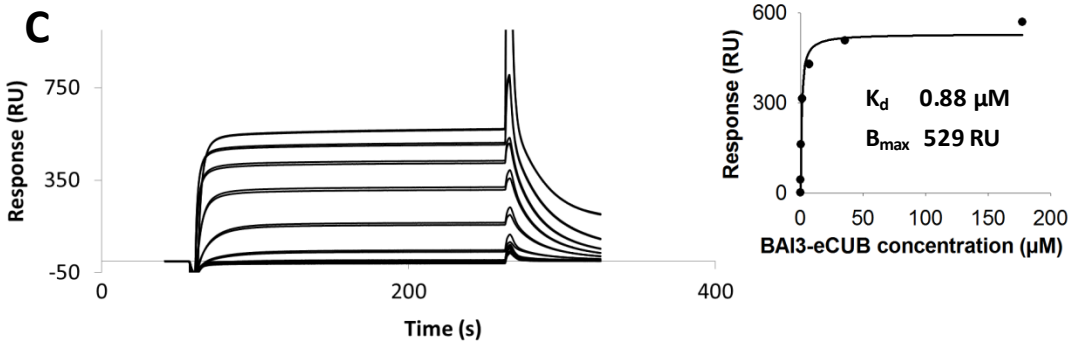


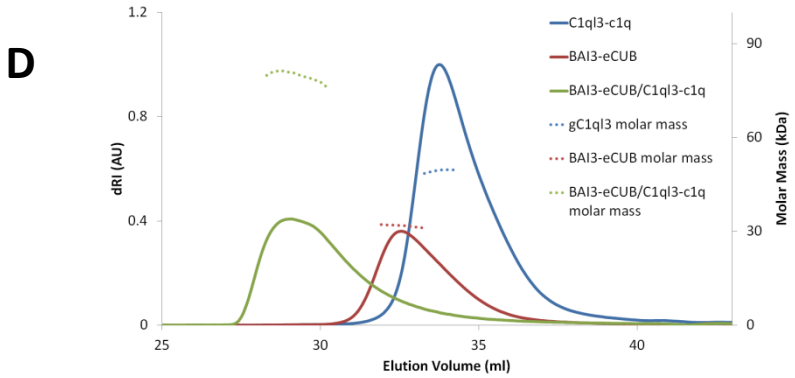
Figure 6.19: C1ql3-c1q binding to BAI3 ectodomain deletion constructs, in an effort to reproduce previous reports (Bollinger MF., *et al.*, 2011). **(A)** S200 elution profile of *in vitro* reconstituted (1:1.5) BAI3-4TSR:C1ql3-c1q mix and SDS-PAGE. **(B)** Serial five-fold dilution series of C1ql3-c1q was tested for binding on BAI3-4TSR. Top C1ql3-c1q concentration tested was 125 µM. **(C)** S200 elution profile of co-expressed BAI3-CUB.4TSR:C1ql3-c1q and SDS-PAGE. Three peaks are highlighted and correspond to C1ql3-c1q-apo (purple arrows), a potential BAI3-CUB.4TSR proteolytic cleavage product (red arrows) (see Figure 6.2.G) and the BAI3-CUB.4TSR/C1ql30c1q complex (black arrows). **(D)** Serial five-fold dilution series of C1ql3-c1q was tested for binding on BAI3-FE. Top C1ql3-c1q concentration tested was 125 µM. **(E)** Serial five-fold dilution series of C1ql3-c1q was tested for binding on BAI3-CUB.4TSR. Top C1ql3-c1q concentration tested was 125 µM.

We questioned whether the BAI3 extracellular region (Uniprot Q80ZF8, residues 1-291, termed as BAI3-eCUB in section 6.4.1) located N-terminaly of the four thrombospondin domain region was the minimal unit responsible for C1ql binding. We were able to prove that the complex is formed after *in vitro* reconstitution with a molar ratio of 1:1.5 (BAI3-eCUB:C1ql3-c1q) (Figure 6.20.A). Additional confirmation for a low µM affinity interaction was provided by SPR, for both C1ql1-c1q and C1ql3-c1q (Figure 6.20.B,C). Interestingly, MALLS analysis revealed that the stoichiometry of the complex is 1 BAI3-eCUB monomer to a trimer of C1ql3-c1qs (Figure 6.20.D).









Sample	Measured Molar Mass (kDa)	Molecular Weight of a Single Subunit (kDa)	Measured Molar Mass/Single Subunit Molecular Weight	Oligomeric State of Sample
C1ql3-c1q	49.6	16.7	2.9	Trimer
BAI3-eCUB	31.9	35.1	0.9	Monomer
BAI3-eCUB/ C1ql3-c1q complex	80.9	-	-	1 C1ql3-c1q trimer + 1 BAI3-eCUB monomer

Figure 6.20: C1ql binding to BAI3-eCUB. **(A)** S200 elution profile of *in vitro* reconstituted (1:1.5) of BAI3-eCUB:C1ql3-c1q complex, after deglycosylation, and SDS-PAGE. Black arrows highlight the complex peak, while red arrows highlight a small excess of unbound C1ql3-c1q. The efficiency of deglycosylation reaction is also depicted: purple arrow indicates the complex sample before the reaction, while orange arrow indicates the complex after the reaction. **(B)** SPR curves showing binding of BAI3eCUB to C1ql3-c1ql. Serial five-fold dilution series of BAI3-eCUB was tested for binding. Top BAI3-eCUB concentration tested was 177.3 µM. **(C)** SPR curves showing binding of BAI3eCUB to C1ql1-c1ql. Serial five-fold dilution series of BAI3-eCUB was tested for binding. Top BAI3-eCUB concentration tested was 177.3 µM. **(D)** Overlaid MALLS analyses of BAI3-eCUB (red), C1ql3-c1q (blue) and BAI3-eCUB+C1ql3-c1q (green), indicating that the complex stoichiometry is 1:3 (BAI3-eCUB:C1ql3-c1q).

Given the high percentage of lysines (7.9%) in BAI3-eCUB amino acid sequence, reductive methylation of surface exposed lysine residues for the reconstituted complex was pursued but led to the disruption of the complex, as shown by gel filtration (Figure 6.21). So, surface-exposed lysines must form a positively charged cavity on BAI3-eCUB structure, which appears to be relevant for complex formation with C1qls.

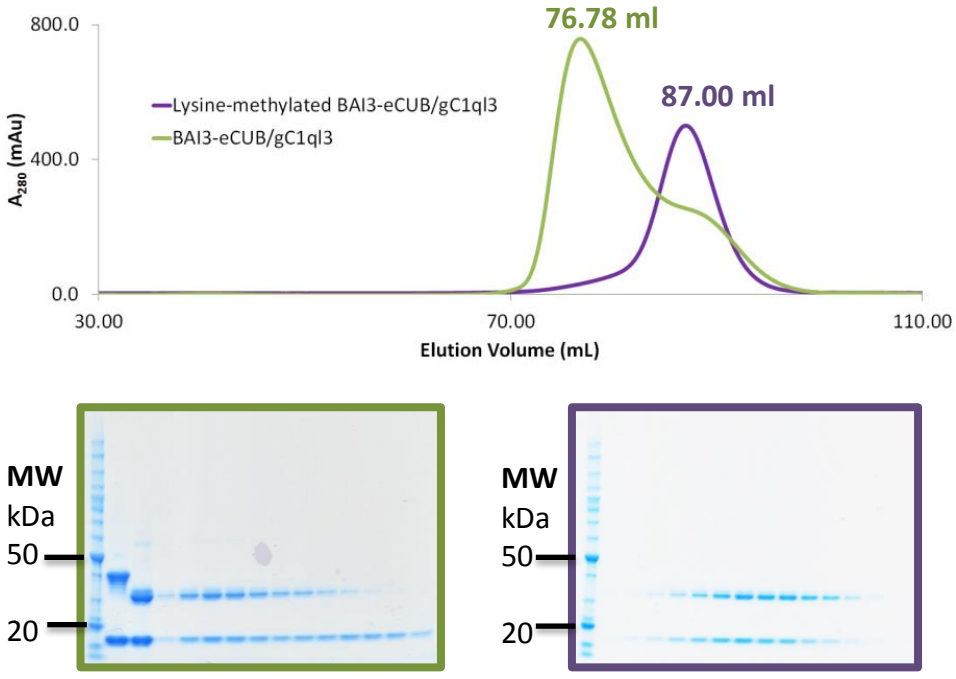


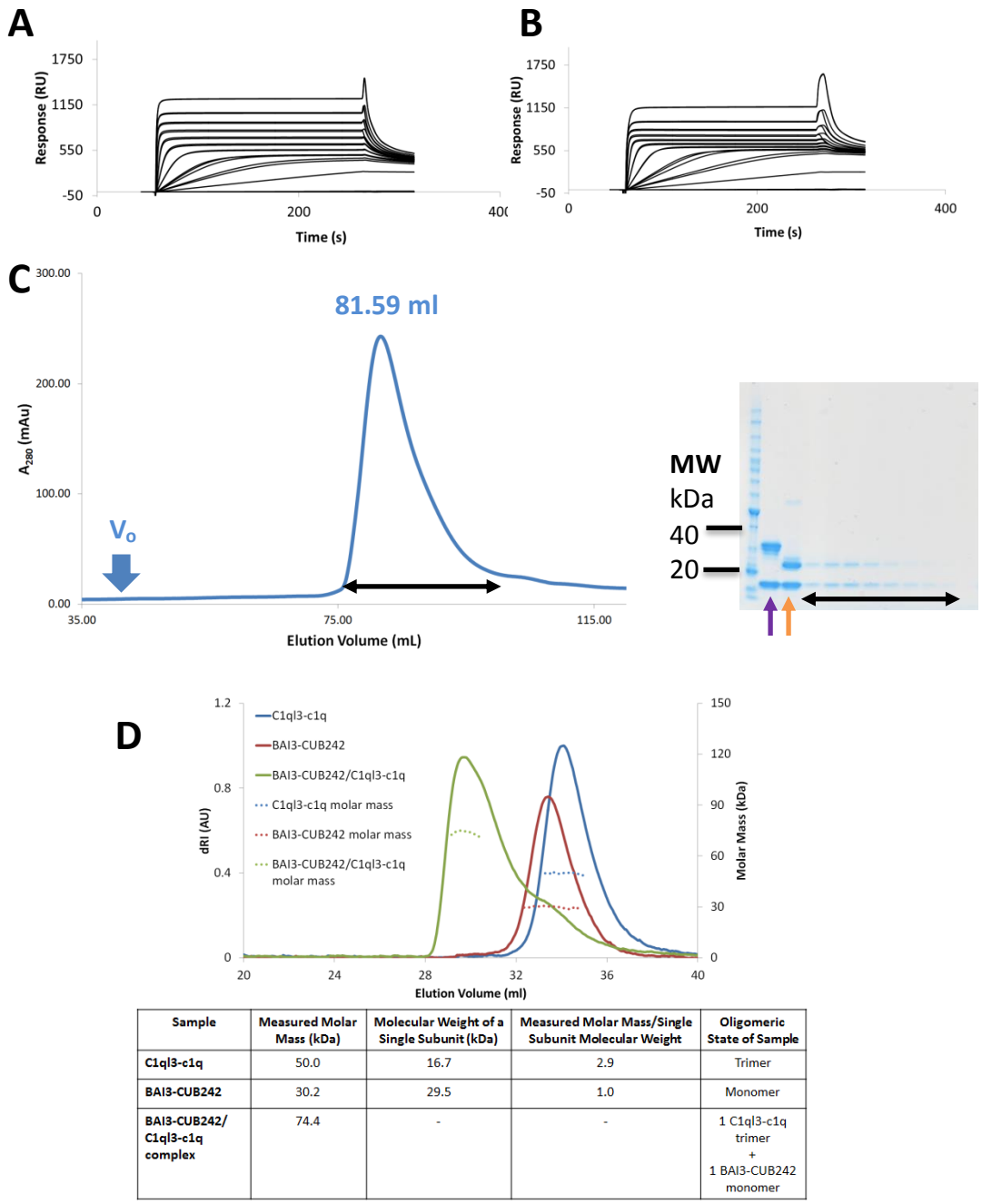
Figure 6.21: Effect of lysine-methylation on BAI3-eCUB/C1ql3-c1q complex. Overlay of S200 elution profiles of methylated (purple) and unmethylated (green) *in vitro* reconstituted (1:1.5) of BAI3-eCUB:C1ql3-c1q complex, after deglycosylation, and corresponding SDS-PAGEs.

Extensive co-crystallisation screening trials of BAI3-eCUB/C1ql3-c1q failed to yield crystals of the complex, as discussed in section 6.6. A disorder prediction analysis (RONN server, University of Oxford, Yang ZR., *et al.*, 2005), indicated that the region between 241 and 291 may be disordered (Figure 6.22). We then questioned the importance of this potentially disordered region for BAI3 ability to bind C1qls. A set of deletion constructs targeting this region was generated, as described in section 6.4.1 (Figure 6.9.A).



Figure 6.22: Disorder prediction analysis of the N-terminal region of the BAI3 ectodomain (RONN server, University of Oxford, Yang ZR., *et al.*, 2005). Region 242-291 is predicted to be disordered (as indicated by the star below the sequence). Vertical lines at positions 231, 242, 248, 270 and 291 represent the deletion constructs generated to target the contribution of region to C1ql binding.

SPR analysis showed that the shorter constructs, BAI3-eCUB231 and BAI3-eCUB242, were still able to bind C1ql3-c1q (Figure 6.23.A and B), while gel filtration of *in vitro* reconstituted (1:1.5) BAI3-eCUB242/C1ql3-c1q, after deglycosylation, showed that the complex is formed (Figure 6.23.C). MALLS analysis revealed that the stoichiometry of the complex is 1 BAI3-eCUB242 monomer to a trimer of C1ql3-c1qs (Figure 6.23.D), reproducing with the finding described above for BAI3-eCUB.



Sample	Measured Molar Mass (kDa)	Molecular Weight of a Single Subunit (kDa)	Measured Molar Mass/Single Subunit Molecular Weight	Oligomeric State of Sample
C1ql3-c1q	50.0	16.7	2.9	Trimer
BAI3-CUB242	30.2	29.5	1.0	Monomer
BAI3-CUB242/ C1ql3-c1q complex	74.4	-	-	1 C1ql3-c1q trimer + 1 BAI3-CUB242 monomer

Figure 6.23: C1ql3 binding to BAI3-eCUB242. **(A)** SPR curves showing binding of BAI3eCUB231 to C1ql3-c1ql. Serial five-fold dilution series of C1ql3-c1q was tested for binding. Top C1ql3-c1q concentration tested was 103.47 µM. **(B)** SPR curves showing binding of BAI3eCUB242 to C1ql3-c1ql. Serial five-fold dilution series of C1ql3-c1q was tested for binding. Top C1ql3-c1q concentration tested was 103.47 µM. **(C)** S200 elution profile of *in vitro* reconstituted (1:1.5) of BAI3-eCUB242:C1ql3-c1q complex, after deglycosylation, and SDS-PAGE. Black arrows highlight the complex peak. The efficiency of deglycosylation reaction is also depicted: purple arrow indicates the complex sample before the reaction, while orange arrow indicates the complex after the reaction. **(D)** Overlaid MALLS analyses of BAI3-eCUB242 (red), C1ql3-c1q (blue) and BAI3-eCUB+C1ql3-c1q (green), indicating that the complex stoichiometry is 1:3 (BAI3-eCUB242:C1ql3-c1q).

Studies have been extended to evaluate how tight the full length C1ql1 can bind BAI3 receptor. Within this context, C1ql1-FL appears to bind BAI3-eCUB tighter in SPR (Figure 6.24), than C1ql1-c1q (Figure 6.20.C).

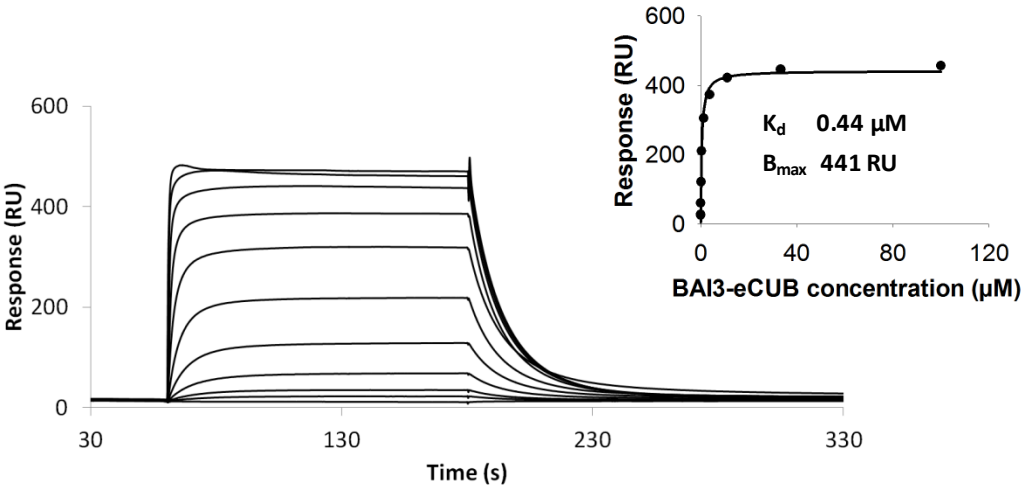


Figure 6.24: SPR curves showing binding of BAI3eCUB to C1ql1-FL. Serial three-fold dilution series of BAI3-eCUB was tested for binding. Top BAI3-eCUB concentration tested was 100 µM.

BAI3ectoΔ291 construct (see section 6.4.1) was used to confirm that the N-terminal region (1-291) of BAI3 receptor is the minimal binding unit for C1ql. SPR analysis indicated that there may be some low micro-molar affinity interaction between BAI3ectoΔ291 and both C1ql1-FL (Figure 6.25.A) and C1ql1-c1q (Figure 6.25.B), supporting previous findings from pull-down experiments (Figure 4.C, Bollinger MF., *et al.*, 2011).

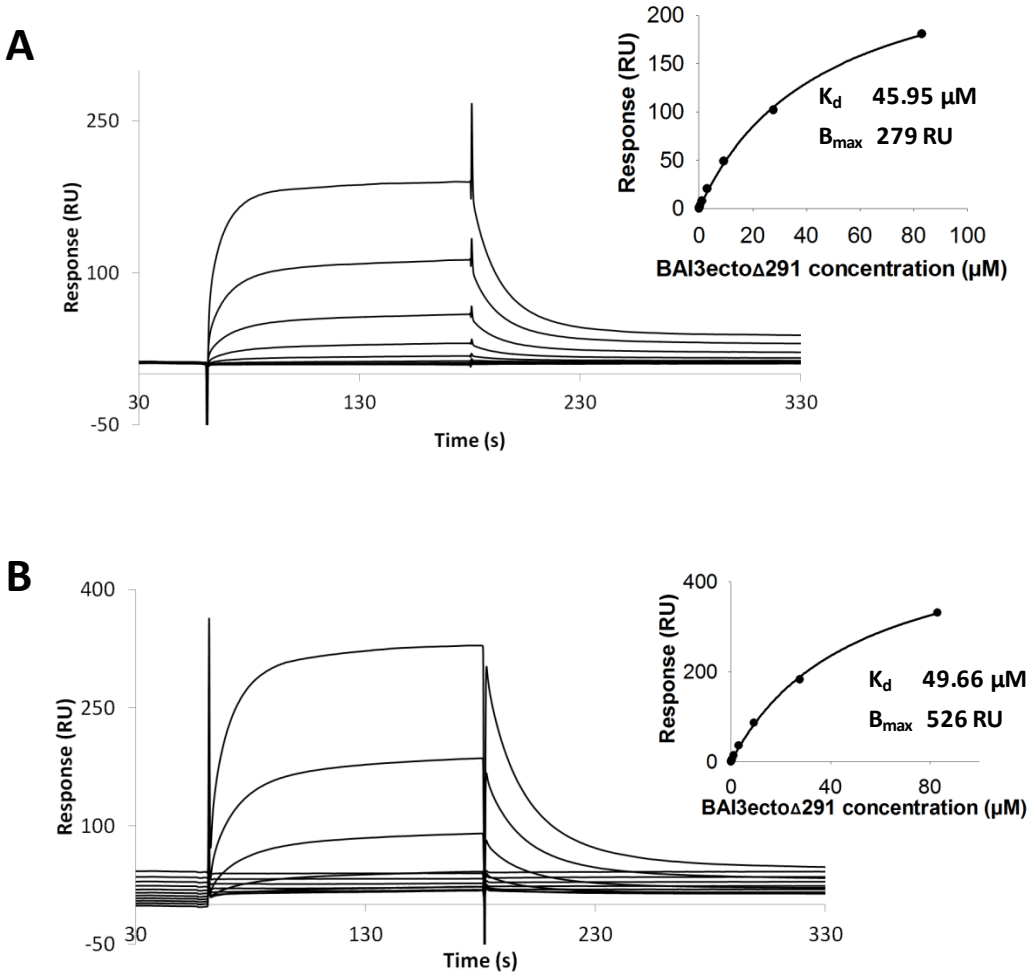


Figure 6.25: SPR curves showing binding of BAI3ectoΔ291 to C1ql proteins. **(A)** Serial three-fold dilution series of BAI3ectoΔ291 was tested for binding immobilised C1ql1-FL. Top BAI3ectoΔ291 concentration tested was 83 μM. **(B)** Serial three-fold dilution series of BAI3ectoΔ291 was tested for binding immobilised C1ql1-c1q. Top BAI3ectoΔ291 concentration tested was 83 μM.

6.6.2 Structure-based mutagenesis of C1ql proteins and effect on BAI-3 binding

A set of C1ql1 mutants were designed, based on the structure described in section 6.3, in order to further characterise the mode of binding of BAI3 receptor to C1ql1. Areas of the C1q domain, known to participate in protein-protein interaction in other C1q family members were targeted. Namely, Cerebellin has been demonstrated to participate in trans-synaptic interactions with the 'tip' of the C1q trimer (Dr. Jordan Clay, University of Oxford), while the side faces of the trimer have been shown to participate in TNF/TNF-receptor interactions (Banner DW., et al., 1993).

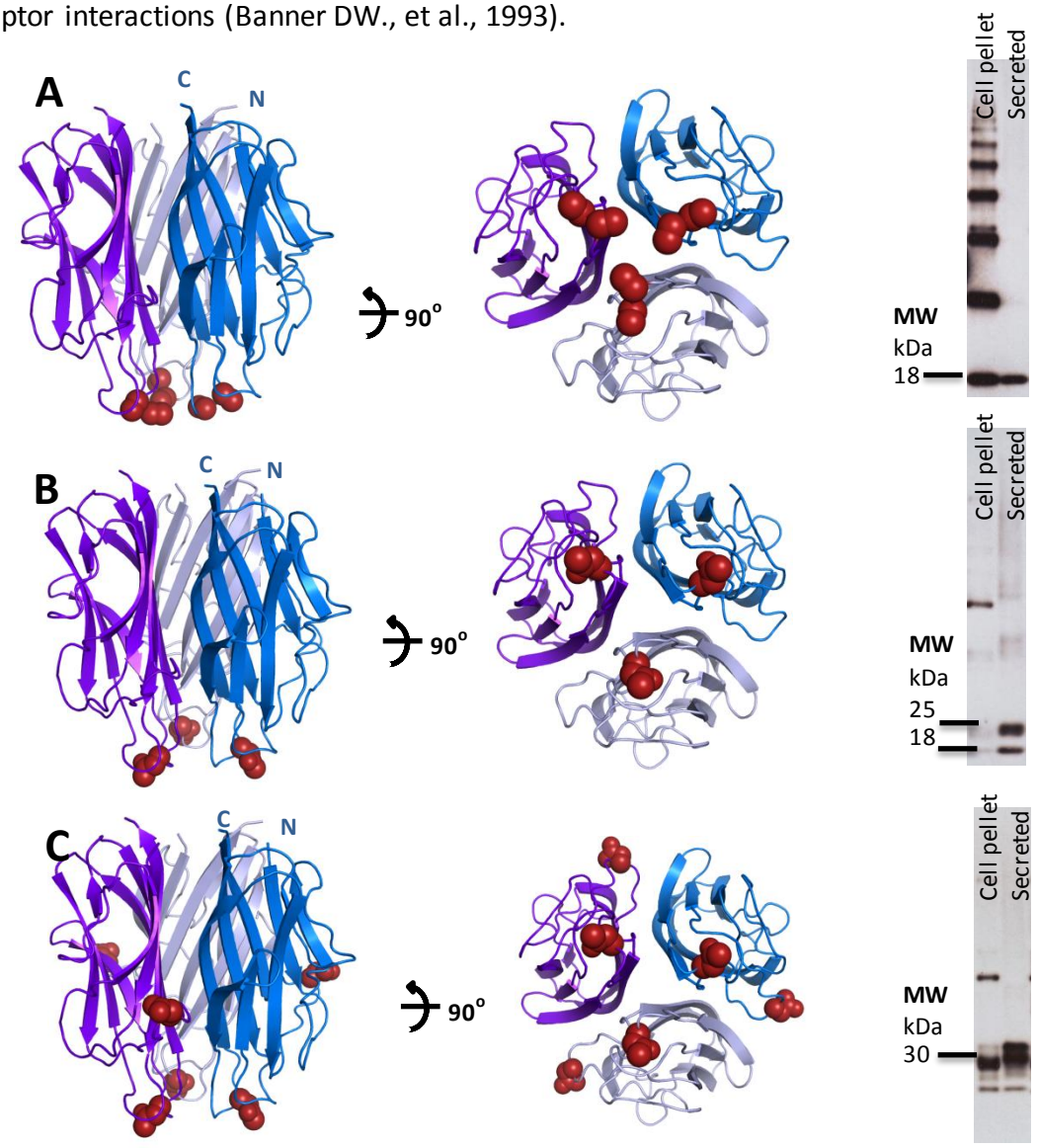


Figure 6.26: Structure-based mutations designed for C1ql1. **(A)** Cartoon representation of C1ql1-c1q structure, with the positions of D210A, Q211A mutations highlighted in red spacefill. Top and side views of the trimer are depicted, coloured by monomer chain (blue, purple and grey). Anti-His western blot with aliquots of expressed (in HEK293 pellets) and secreted mutant is also shown on the right. **(B)** Cartoon representation of C1ql1-c1q structure, with the positions of Q211N, N212S, Y213T mutations highlighted in red spacefill. Top and side views of the trimer are depicted, coloured by monomer chain (blue, purple and grey). Anti-His western blot with aliquots of expressed (in HEK293 pellets) and secreted mutant is also shown on the right. **(C)** Cartoon representation of C1ql1-c1q structure, with the positions of Q211N, N212S, Y213T, S244N, K246S mutations highlighted in red spacefill. Top and side views of the trimer are depicted, coloured by monomer chain (blue, purple and grey). Anti-His western blot with aliquots of expressed (in HEK293 pellets) and secreted mutant is also shown on the right.

Three mutants were generated for C1ql1, as shown in Figure 6.26: C1ql1-c1q-(D210A, Q211A) named as 'C1ql1-Ala' mutant, C1ql1-c1q-(Q211N, N212S, Y213T) named as 'C1ql1-single-sweet' mutant and C1ql1-c1q-(Q211N, N212S, Y213T, S244N, K246S) named as 'C1ql1-double-sweet' mutant. In C1ql1-c1q-(D210A, Q211A) (Figure 6.26.A), the 'tip' of the trimer is targeted with alanine substitutions of polar residues. In C1ql1-c1q-(Q211N, N212S, Y213T) (Figure 6.26.B), a N-linked glycosylation site is introduced on the 'tip' of the trimer, while in C1ql1-c1q-(Q211N, N212S, Y213T, S244N, K246S) (Figure 6.26.C) a second N-linked glycosylation site is also introduced on the side face of the trimer. SPR analysis showed that the introduction of a single glycosylation site impaired BAI3-eCUB binding, while the introduction of both glycosylation sites completely abolished binding to BAI3-eCUB (Figure 6.27), when compared to the wild type. The C1ql1-Ala mutant exhibited a lower affinity interaction than the wild type, although the response levels recorded were higher than the wild type (Figure 6.27). This possibly suggests that these Ala mutations somehow locally destabilised the protein surface increasing non-specific binding.

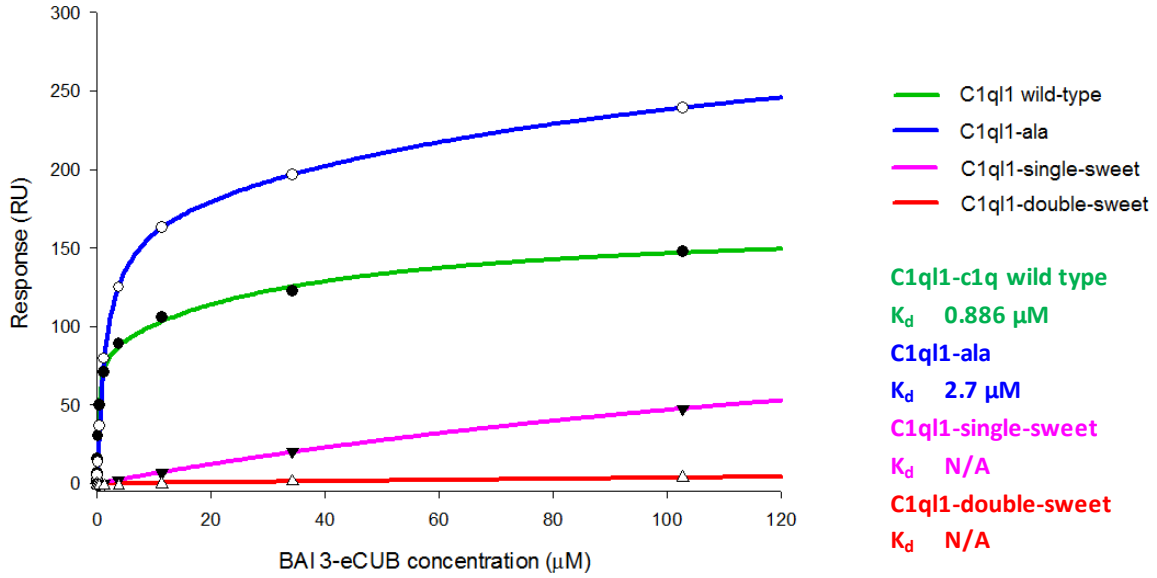


Figure 6.27: SPR analysis of interaction between BAI3eCUB and structure-based C1ql1-c1q mutant proteins, C1ql1-ala (blue), C1ql1-single-sweet (pink), C1ql1-double-sweet (red). C1ql1-c1q binding curve is depicted in green. Serial three-fold dilution series of BAI3eCUB were tested for binding immobilised C1ql1-c1q constructs. Top BAI3eCUB concentration tested was 102.77 µM.

When Q211N, N212S, Y213T, S244N, K246S mutations were introduced to the full length C1ql1, BAI3-eCUB as well as BAI3ectoΔ291 binding events were abolished as well (Figure 6.28.A.B).

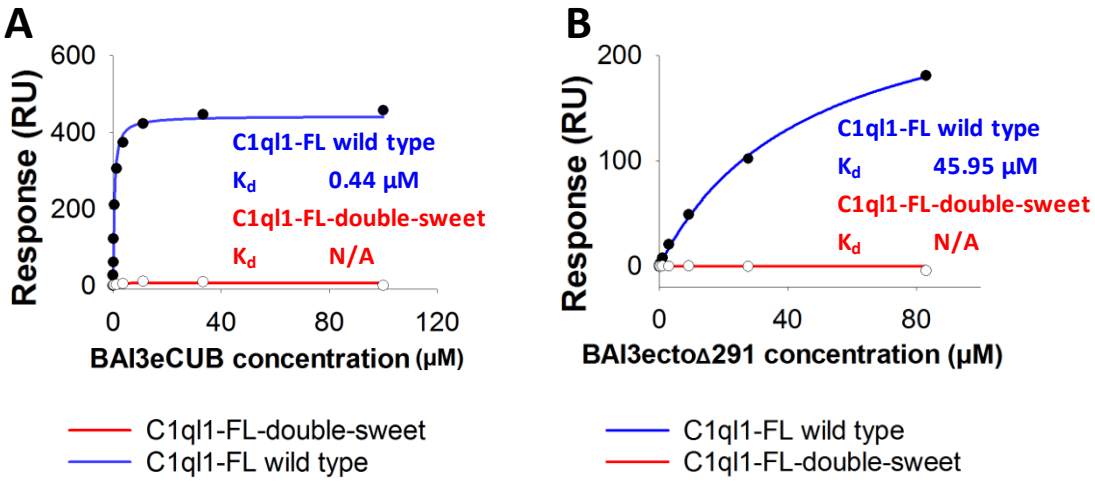


Figure 6.28: SPR analysis of interaction between BAI3 proteins and structure-based C1ql1-FL. Serial three-fold dilution series of BAI3 proteins were tested for binding immobilised C1ql1 constructs. **(A)** Binding of BAI3eCUB to C1ql1-FL wild type (blue) and C1ql1-FL-double-sweet (red) mutant. Top BAI3eCUB concentration tested was 100 µM. **(B)** Binding of BAI3ectoΔ291 to C1ql1-FL wild type (blue) and C1ql1-FL-double-sweet (red) mutant. Top BAI3eCUB concentration tested was 83 µM.

An additional C1ql1 mutant was generated to evaluate the contribution of the base of the C1q domain on BAI3 binding. In C1ql1-c1q-(T121N), a N-linked glycosylation site was introduced to the disordered N-terminal region upstream of the start of the C1q domain, as shown in Figure 6.29.

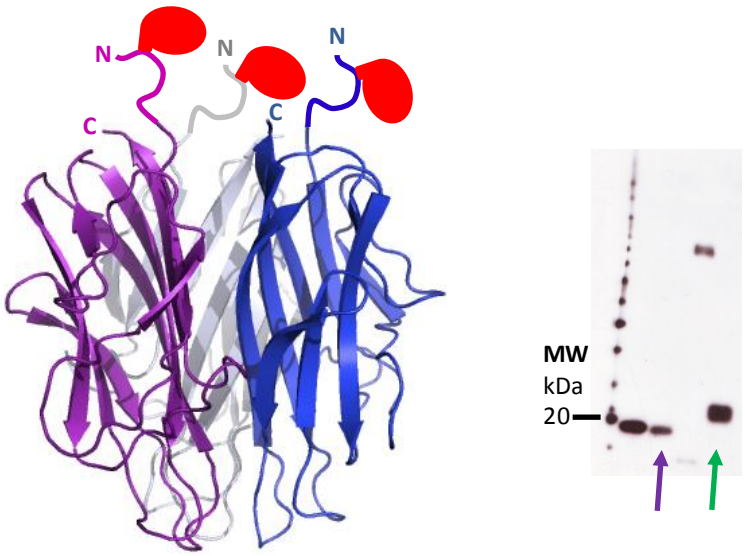


Figure 6.29: Structure-based mutation targeting the base of C1ql1 trimer. Cartoon representation of side view of C1ql1-c1q structure, coloured by monomer chain (blue, purple and grey), with the positions of T121N mutations highlighted with red blobs. Anti-HRP western blot is provided on the right, with secreted and biotinilated C1ql1-c1q-(T121N) (green arrow) and C1ql1-c1q-wild-type (purple arrow).

SPR analysis showed that the introduction of a glycosylation site close to the N-terminus had minimal effect on BAI3-eCUB binding when compared to the wild type (Figure 6.30), suggesting that this area of the C1ql1 protein is not participating in BAI3 receptor interactions.

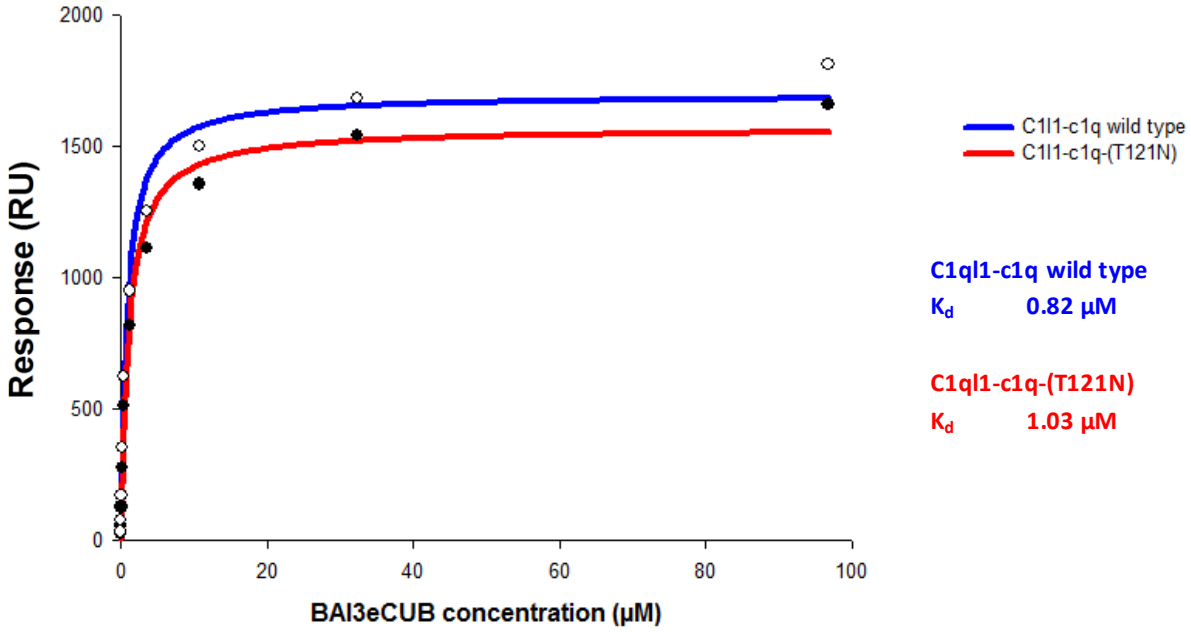


Figure 6.30: SPR analysis of BAI3eCUB interaction with structure-based C1ql1-c1q-(T121N) mutant protein (red), in comparison with C1ql1-c1q wild type (blue). Serial three-fold dilution series of BAI3eCUB were tested for binding to immobilised C1ql1-c1q constructs. Top BAI3eCUB concentration tested was 96.82 µM.

6.7 Molecular dissection of C1ql/iGluK2 interaction

Constructs described in section 6.4.1 (and Appendix B) were used to map the interaction between GluK2-ATD and C1ql proteins. SPR showed that the ATD of the ionotropic glutamate receptor K2 (of the kainate subfamily) can bind the C1q domains of both C1ql1 and C1ql3 (Figure 6.31 A and B). In addition, GluK2-ATD appeared to bind approximately 10-fold stronger the full length C1ql1 (Figure 6.31.C), in comparison with C1ql1-c1q. The C1ql1-FL-double-sweet mutant abolished binding of C1ql1 to GluK2-ATD (Figure 6.31.D).

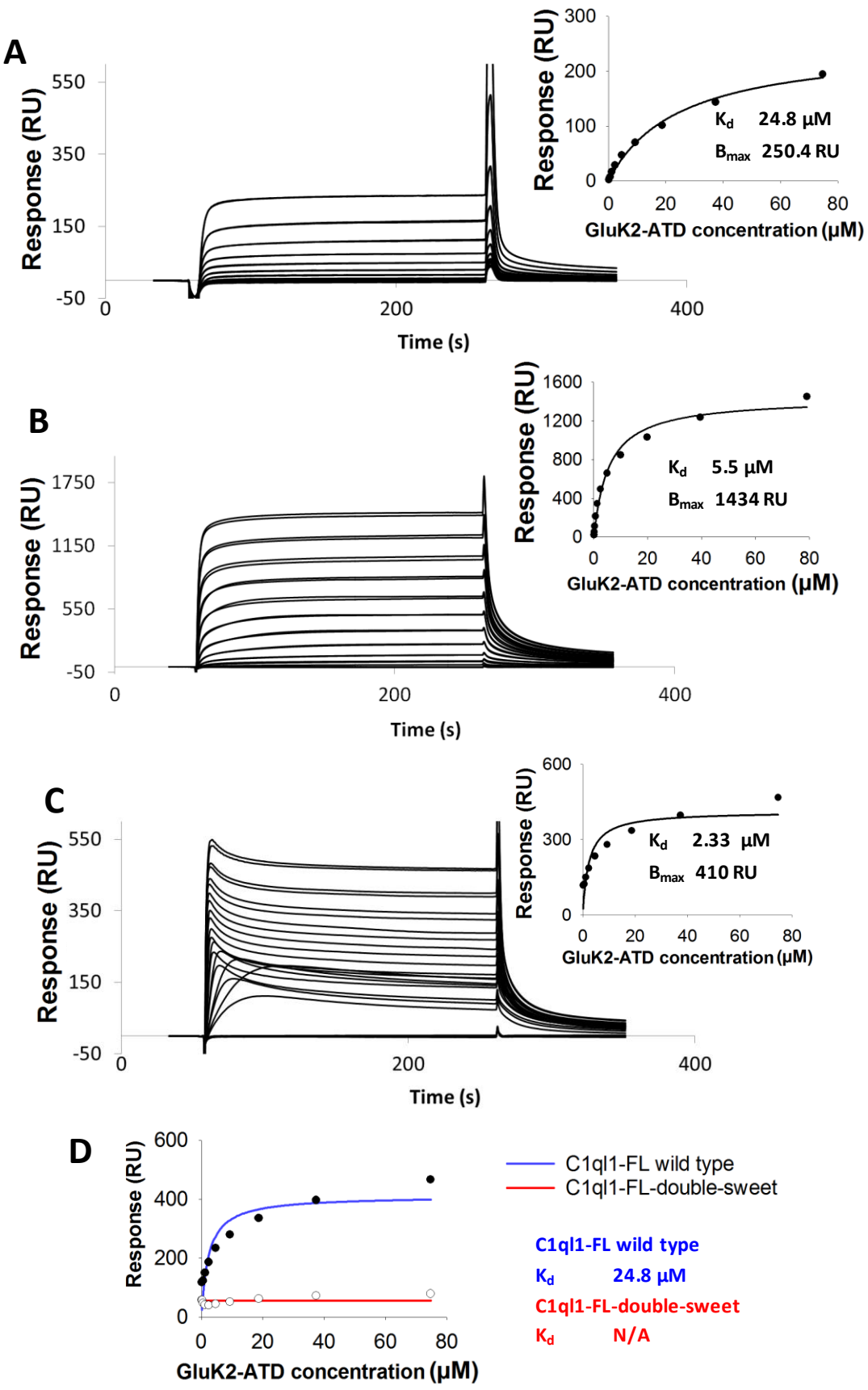
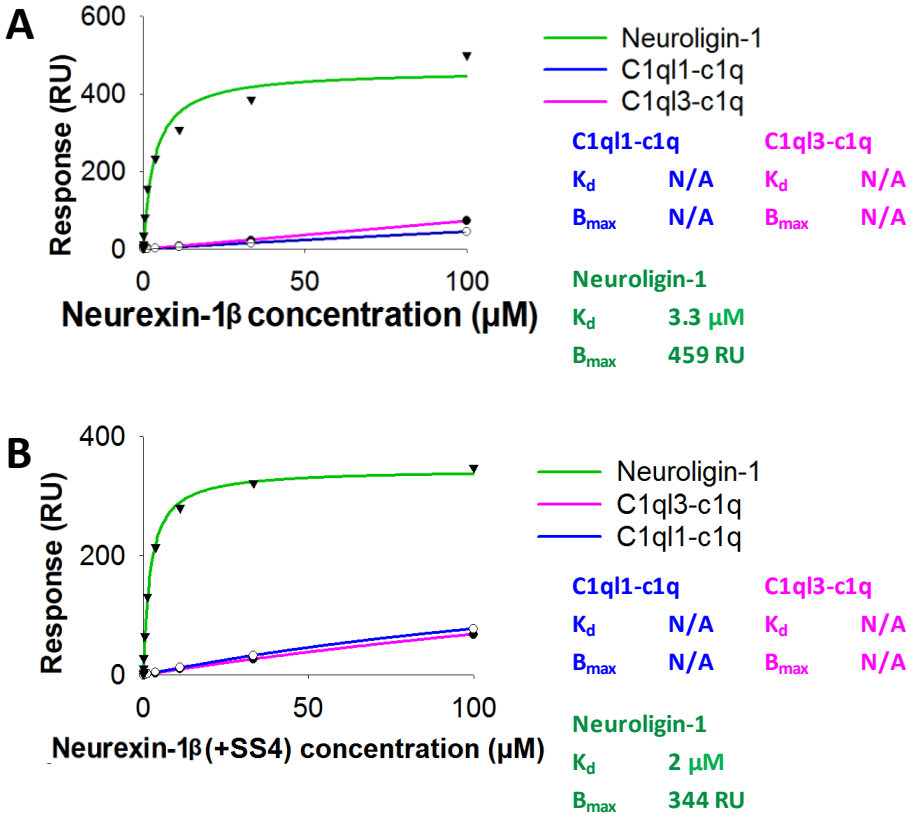

A
Response (RU)
550
350
150
-50
0
200
400
Time (s)
Response (RU)
300
200
100
0
0
20
40
60
80
GluK2-ATD concentration (µM)
Kd 24.8 µM
Bmax 250.4 RU
B
Response (RU)
1750
1150
550
-50
0
200
400
Time (s)
Response (RU)
1600
1200
800
400
0
0
20
40
60
80
GluK2-ATD concentration (µM)
Kd 5.5 µM
Bmax 1434 RU
C
Response (RU)
550
350
150
-50
0
200
400
Time (s)
Response (RU)
600
300
0
0
20
40
60
80
GluK2-ATD concentration (µM)
Kd 2.33 µM
Bmax 410 RU
D
Response (RU)
600
400
200
0
0
20
40
60
80
GluK2-ATD concentration (µM)
C1ql1-FL wild type
C1ql1-FL-double-sweet
C1ql1-FL wild type
Kd 24.8 µM
C1ql1-FL-double-sweet
Kd N/A

Figure 6.31: Molecular dissection of C1ql1/iGluK2 interaction, by SPR. **(A)** Serial two-fold dilution series of GluK2-ATD was tested for binding immobilised C1ql1-c1q. Top GluK2-ATD concentration tested was 74.66 µM. **(B)** Serial two-fold dilution series of GluK2-ATD was tested for binding immobilised C1ql3-c1q. Top GluK2-ATD concentration tested was 79.1 µM. **(C)** Serial two-fold dilution series of GluK2-ATD was tested for binding immobilised C1ql1-FL. Top GluK2-ATD concentration tested was 74.66 µM. **(D)** Analysis of GluK2-ATD interaction with structure-based C1ql1-FL-double-sweet mutant protein (red), in comparison with C1ql1-FL wild type (blue). Serial two-fold dilution series of GluK2-ATD were tested for binding to immobilised C1ql1 constructs. Top GluK2-ATD concentration tested was 74.66 µM.

6.8 Molecular dissection of C1ql/βNeurexin1 interaction

Constructs described in section 6.4.1 (and Appendix B) were used to test whether there is any interaction between βNeurexin1 and C1ql proteins. SPR showed that both versions of Neurexin1β, with and without splice form S4, cannot bind the C1q domains of both C1ql1 and C1ql3 (Figure 6.32 A and B). In addition, either Neurexin1β proteins appeared unable to bind the full length C1ql1 (Figure 6.32.C.D).



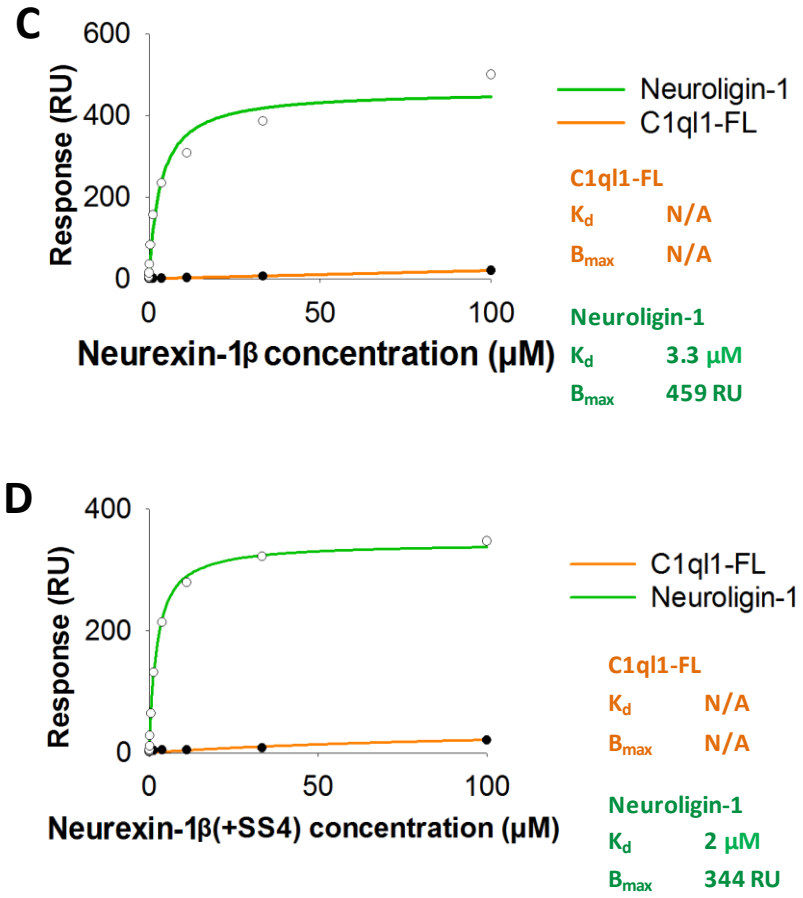


Figure 6.32: Molecular dissection of C1ql1/ βNeurexin1 interaction, by SPR. **(A)** Analysis of βNeurexin1 interaction with C1ql1-c1q (blue) and C1ql3-c1q (magenta), in comparison with control measurement of neuroligin-1 (green). Serial two-fold dilution series of GluK2-ATD were tested for binding to immobilised C1ql1/Neuroligin constructs. Top GluK2-ATD concentration tested was 100 μM. **(B)** Analysis of βNeurexin1 (+ splice form S4) interaction with C1ql1-c1q (blue) and C1ql3-c1q (magenta), in comparison with control measurement of neuroligin-1 (green). Serial two-fold dilution series of GluK2-ATD were tested for binding to immobilised C1ql1/Neuroligin constructs. Top GluK2-ATD concentration tested was 100 μM. **(C)** Analysis of βNeurexin1 interaction with C1ql1-FL (orange), in comparison with control measurement of neuroligin-1 (green). Serial two-fold dilution series of GluK2-ATD were tested for binding to immobilised C1ql1/Neuroligin constructs. Top GluK2-ATD concentration tested was 100 μM. **(D)** Analysis of βNeurexin1 (+ splice form S4) interaction with C1ql1-FL (orange), in comparison with control measurement of neuroligin-1 (green). Serial two-fold dilution series of GluK2-ATD were tested for binding to immobilised C1ql1/Neuroligin constructs. Top GluK2-ATD concentration tested was 100 μM.

6.9 Attempts to crystallise C1ql/BAI3 and C1ql/GluK2 complexes

Complexes between C1ql-c1q and partner proteins, as documented in sections 6.6 and 6.7, were subjected to extensive nanolitre-scale crystallization trials, as described in section 2.3.1, at 20^{o} and 4^{o}C. Gel filtration elution peaks corresponding to BAI3-eCUB/C1ql3-c1q (Figure 6.12.A), BAI3-eCUB242/C1ql3-c1q (Figure 6.15.C) were pooled and concentrated to 2-10 mg/ml prior to crystallisation. Gel purified BAI3-eCUB and C1ql1-c1q, for which SPR analysis indicated a direct interaction (Figure 6.12.C), were mixed with a 1:1.5 molar ratio and concentrated to 2-10 mg/ml prior to crystallisation. Similarly gel purified GluK2-ATD and C1ql3-c1q were mixed with a 1:1.5 molar ratio and concentrated to 2-10 mg/ml prior to crystallisation. Crystals obtained from such screens were so far found to contain only C1ql molecules, as in the case of the orthorhombic crystal form of C1ql3-c1q, described in section 6.5.

6.10 Conclusions and future perspectives

The C1q-like synaptic interactome remains little understood, let alone the specific functional outcomes it may have on neuronal adhesion or/and function. Recently, BAI3 has been indicated as a direct partner of C1q-like proteins, in a manner that affects synapse density in the hippocampus (Bolliger MF., *et al.*, 2011). The results presented in this chapter reinforce the finding that there is a tight interaction between BAI3/C1qls, decipher the minimal domains involved and provide initial biochemical evidence on the stoichiometry and mode of the interaction. While these studies have been largely assisted by the structural elucidation of C1q-like globular head domains presented in this

chapter, a crystal structure of the complex would be more descriptive in terms of the exact residues involved in the interface. In addition, C1q-like globular head domains have been demonstrated to bind inotropic Glutamate receptor amino-terminal domains of the kainite subfamily, within this chapter. It seems though that this interaction may not be mediated by β-neurexin, which according to SPR data presented here does not bind C1q-like proteins, in a way similar to the *trans*-synaptic interaction hub of Cerebellin/iGluD/β-neurexin (Uemura T., *et al.*, 2010). Limited-proteolysis of complexes between C1qls and BAI3-eCUB will be pursued, in order to trim the C-terminal region of BAI3-eCUB that is predicted to be disordered (Figure 6.22), and therefore increase the co-crystallisation potential. In addition, work is currently planned to engineer the μM affinity interactions between BAI3/C1ql and iGluK/C1ql in a yeast surface display system (Chao G., *et al.*, 2006, Weiskopf K., *et al.*, 2013, Ring AM., *et al.*, 2013), in order to generate interaction partners with enhanced affinities and increase the chances of co-crystallisation. Such engineering outcomes will also be useful in testing the functional effects of these interactions in cellular and behavioural settings studies by our collaborators.

Chapter 7

List of references

1. Unified nomenclature for Eph family receptors and their ligands, the ephrins. Eph Nomenclature Committee. Cell 90, 403-404 (1997).

2. Adams, P.D. et al. PHENIX: a comprehensive Python-based system for macromolecular structure solution. Acta Cryst (2010). D66, 213-221 [doi:10.1107/S0907444909052925], 1-9 (2010).

3. Aicher, B., Lerch, M.M., Müller, T., Schilling, J. & Ullrich, A. Cellular redistribution of protein tyrosine phosphatases LAR and PTPsigma by inducible proteolytic processing. The Journal of Cell Biology 138, 681-696 (1997).

4. Alete, D.E., Weeks, M.E., Hovanession, A.G., Hawadle, M. & Stoker, A.W. Cell surface nucleolin on developing muscle is a potential ligand for the axonal receptor protein tyrosine phosphatase-σ. FEBS Journal 273, 4668-4681 (2006).

5. Alexandrov, A.I., Mileni, M., Chien, E.Y.T., Hanson, M.A. & Stevens, R.C. Microscale Fluorescent Thermal Stability Assay for Membrane Proteins. Structure 16, 351-359 (2008).

6. Allen, N.J. et al. Astrocyte glypicans 4 and 6 promote formation of excitatory synapses via GluA1 AMPA receptors. Nature 486, 410-414 (2012).

7. Almo, S.C. et al. Structural genomics of protein phosphatases. Journal of Structural and Functional Genomics 8, 121-140 (2007).

8. Alonso, A. et al. Protein Tyrosine Phosphatases in the Human Genome. Cell 117, 699-711 (2004).

9. Alonso, G. et al. Immunocytochemical localization of the sigma(1) receptor in the adult rat central nervous system. Neuroscience 97, 155-170 (2000).

10. Anders, L. et al. Furin-, ADAM 10-, and gamma-secretase-mediated cleavage of a receptor tyrosine phosphatase and regulation of beta-catenin's transcriptional activity. Molecular and Cellular Biology 26, 3917-3934 (2006).

11. Andersen, J.N. et al. Structural and Evolutionary Relationships among Protein Tyrosine Phosphatase Domains. Molecular and Cellular Biology 21, 7117-7136 (2001).

12. Araç, D. et al. A novel evolutionarily conserved domain of cell-adhesion GPCRs mediates autoproteolysis. The EMBO Journal 31, 1364-1378 (2012).

13. Aricescu, A.R., Lu, W. & Jones, E.Y. A time- and cost-efficient system for high-level protein production in mammalian cells. Acta Crystallographica Section D Biological Crystallography 62, 1243-1250 (2006).

14. Aricescu, A.R., McKinnell, I.W., Halfter, W. & Stoker, A.W. Heparan Sulfate Proteoglycans Are Ligands for Receptor Protein Tyrosine Phosphatase Molecular and Cellular Biology 22, 1881-1892 (2002).

15. Aricescu, A.R. et al. Structure of a Tyrosine Phosphatase Adhesive Interaction Reveals a Spacer-Clamp Mechanism. Science 317, 1217-1220 (2007).

16. Arvanitis, D. & Davy, A. Eph/ephrin signaling: networks. Genes & Development 22, 416-429 (2008).

17. Ashida, S. et al. Molecular features of the transition from prostatic intraepithelial neoplasia (PIN) to prostate cancer: genome-wide gene-expression profiles of prostate cancers and PINs. Cancer research 64, 5963-5972 (2004).

18. Ashkenazy, H., Erez, E., Martz, E., Pupko, T. & Ben-Tal, N. ConSurf 2010: calculating evolutionary conservation in sequence and structure of proteins and nucleic acids. Nucleic Acids Research 38, W529-W533 (2010).

19. Aydar, E., Palmer, C.P., Klyachko, V.A. & Jackson, M.B. The sigma receptor as a ligand-regulated auxiliary potassium channel subunit. Neuron 34, 399-410 (2002).

20. Baeyens, K.J., De Bondt, H.L., Raeymaekers, A., Fiers, W. & De Ranter, C.J. The structure of mouse tumour-necrosis factor at 1.4 A resolution: towards modulation of its selectivity and trimerization. Acta Cryst D 55, 772-778 (1999).

21. Baker, N.A., Sept, D., Joseph, S., Holst, M.J. & McCammon, J.A. Electrostatics of nanosystems: application to microtubules and the ribosome. Proceedings of the National Academy of Sciences of the United States of America 98, 10037-10041 (2001).

22. Bandtlow, C.E. & Zimmermann, D.R. Proteoglycans in the developing brain: new conceptual insights for old proteins. Physiological reviews 80, 1267-1290 (2000).

23. Banner, D.W. et al. Crystal structure of the soluble human 55 kd TNF receptor-human TNF beta complex: implications for TNF receptor activation. Cell 73, 431-445 (1993).

24. Bao, D., Pang, Z. & Morgan, J.I. The structure and proteolytic processing of Cbln1 complexes. Journal of Neurochemistry 95, 618-629 (2005).

25. Barde, Y.A. Trophic factors and neuronal survival. Neuron 2, 1525-1534 (1989).

26. Barde, Y.A., Edgar, D. & Thoenen, H. Purification of a new neurotrophic factor from mammalian brain. The EMBO Journal 1, 549-553 (1982).

27. Barford, D., Flint, A.J. & Tonks, N.K. Crystal structure of human protein tyrosine phosphatase 1B. Science 263, 1397-1404 (1994).

28. Barr, A.J. et al. Large-scale structural analysis of the classical human protein tyrosine phosphatome. Cell 136, 352-363 (2009).

29. Bartley, T.D. et al. B61 is a ligand for the ECK receptor protein-tyrosine kinase. Nature 368, 558-560 (1994).

30. Battye, T.G.G., Kontogiannis, L., Johnson, O., Powell, H.R. & Leslie, A.G.W. iMOSFLM: a new graphical interface for diffraction-image processing with MOSFLM. Acta Cryst (2011). D67, 271-281 [doi:10.1107/S0907444910048675], 1-11 (2011).

31. Bayés, A. et al. Characterization of the proteome, diseases and evolution of the human postsynaptic density. Nature Neuroscience 14, 19-21 (2011).

32. Beltran, P.J. & Bixby, J.L. Receptor protein tyrosine phosphatases as mediators of cellular adhesion. Frontiers in bioscience : a journal and virtual library 8, d87-99 (2003).

33. Benke, T.A., Lüthi, A., Isaac, J.T. & Collingridge, G.L. Modulation of AMPA receptor unitary conductance by synaptic activity. Nature 393, 793-797 (1998).

34. Benoit, M.E. et al. C1q-induced LRP1B and GPR6 proteins expressed early in Alzheimer disease mouse models, are essential for the C1q-mediated protection against amyloid-β neurotoxicity. Journal of Biological Chemistry 288, 654-665 (2013).

35. Benoit, M.E. & Tenner, A.J. Complement protein C1q-mediated neuroprotection is correlated with regulation of neuronal gene and microRNA expression. The Journal of neuroscience : the official journal of the Society for Neuroscience 31, 3459-3469 (2011).

36. Benson, M.D. et al. Ephrin-B3 is a myelin-based inhibitor of neurite outgrowth. Proceedings of the National Academy of Sciences of the United States of America 102, 10694-10699 (2005).

37. Bernfield, M. et al. Functions of cell surface heparan sulfate proteoglycans. Annual review of biochemistry 68, 729-777 (1999).

38. Bérubé, N.G., Swanson, X.H., Bertram, M.J. & Kittle, J.D. Cloning and characterization of CRF, a novel C1q-related factor, expressed in areas of the brain involved in motor function. Molecular brain … (1999).

39. Bliss, T.V. & Collingridge, G.L. A synaptic model of memory: long-term potentiation in the hippocampus. Nature 361, 31-39 (1993).

40. Bliss, T.V. & Gardner-Medwin, A.R. Long-lasting potentiation of synaptic transmission in the dentate area of the unanaestetized rabbit following stimulation of the perforant path. The Journal of Physiology 232, 357-374 (1973).

41. Bliss, T.V. & Lomo, T. Long-lasting potentiation of synaptic transmission in the dentate area of the anaesthetized rabbit following stimulation of the perforant path. The Journal of Physiology 232, 331-356 (1973).

42. Bogin, O. et al. Insight into Schmid metaphyseal chondrodysplasia from the crystal structure of the collagen X NC1 domain trimer. Structure/Folding and Design 10, 165-173 (2002).

43. Bolliger, M.F., Martinelli, D.C. & Sudhof, T.C. The cell-adhesion G protein-coupled receptor BAI3 is a high-affinity receptor for C1q-like proteins. Proceedings of the National Academy of Sciences 108, 2534-2539 (2011).

44. Boulter, J. et al. Molecular cloning and functional expression of glutamate receptor subunit genes. Science 249, 1033-1037 (1990).

45. Bourgin, C., Murai, K.K., Richter, M. & Pasquale, E.B. The EphA4 receptor regulates dendritic spine remodeling by affecting beta1-integrin signaling pathways. The Journal of Cell Biology 178, 1295-1307 (2007).

46. Bowden, T.A. et al. Structural Plasticity of Eph Receptor A4 Facilitates Cross-Class Ephrin Signaling. Structure/Folding and Design 17, 1386-1397 (2009).

47. Brantley-Sieders, D.M. Clinical relevance of Ephs and ephrins in cancer: lessons from breast, colorectal, and lung cancer profiling. Seminars in Cell & Developmental Biology 23, 102-108 (2012).

48. Bricogne, G., Blanc, E., Brandl, M., Flensburg, C. & Keller, P. BUSTER v. 2.11. 2. Cambridge: Global Phasing … (2011).

49. Brittis, P.A., Canning, D.R. & Silver, J. Chondroitin sulfate as a regulator of neuronal patterning in the retina. Science 255, 733-736 (1992).

50. Bronner-Fraser, M. & Lallier, T. A monoclonal antibody against a laminin-heparan sulfate proteoglycan complex perturbs cranial neural crest migration in vivo. The Journal of Cell Biology 106, 1321-1329 (1988).

51. Brönnimann, C. et al. Continuous sample rotation data collection for protein crystallography with the PILATUS detector. Nuclear Instruments and Methods in Physics Research Section A: Accelerators, Spectrometers, Detectors and Associated Equipment 510, 24-28 (2003).

52. Brose, K. et al. Slit proteins bind Robo receptors and have an evolutionarily conserved role in repulsive axon guidance. Cell 96, 795-806 (1999).

53. Budreck, E.C. et al. Neuroligin-1 controls synaptic abundance of NMDA-type glutamate receptors through extracellular coupling. Proceedings of the National Academy of Sciences 110, 725-730 (2013).

54. Bukalo, O., Schachner, M. & Dityatev, A. Modification of extracellular matrix by enzymatic removal of chondroitin sulfate and by lack of tenascin-R differentially affects several forms of synaptic plasticity in the hippocampus. Neuroscience 104, 359-369 (2001).

55. Burridge, K., Sastry, S.K. & Sallee, J.L. Regulation of cell adhesion by protein-tyrosine phosphatases. I. Cell-matrix adhesion. The Journal of biological chemistry 281, 15593-15596 (2006).

56. Butte, M.J., Hwang, P.K., Mobley, W.C. & Fletterick, R.J. Crystal structure of neurotrophin-3 homodimer shows distinct regions are used to bind its receptors. Biochemistry 37, 16846-16852 (1998).

57. Cajal, S.R.y. A quelle epoque apparaissent les expansions des cellule nerveuses de la moelle epinere du poulet. Anat. Anzerger. 5, 609-613 (1890).

58. Cajal, S.R.y. Histology of the nervous system of man and vertebrates. Oxford Univ Press (1995).

59. Carland, T.M. & Gerwick, L. The C1q domain containing proteins: Where do they come from and what do they do? Developmental and comparative immunology 34, 785-790 (2010).

60. Carroll, R.C., Beattie, E.C., von Zastrow, M. & Malenka, R.C. Role of ampa receptor endocytosis in synaptic plasticity. Nature Reviews Neuroscience 2, 315-324 (2001).

61. Celniker, G. et al. ConSurf: Using Evolutionary Data to Raise Testable Hypotheses about Protein Function. Israel Journal of Chemistry 53, 199-206 (2013).

62. Chan, S.S. et al. UNC-40, a C. elegans homolog of DCC (Deleted in Colorectal Cancer), is required in motile cells responding to UNC-6 netrin cues. Cell 87, 187-195 (1996).

63. Chang, V.T. et al. Glycoprotein Structural Genomics: Solving the Glycosylation Problem. Structure 15, 267-273 (2007).

64. Chao, G. et al. Isolating and engineering human antibodies using yeast surface display. Nature Protocols 1, 755-768 (2006).

65. Chao, M.V. & Hempstead, B.L. p75 and Trk: A two-receptor system. Trends in Neurosciences (1995).

66. Charron, F., Stein, E., Jeong, J., McMahon, A.P. & Tessier-Lavigne, M. The morphogen sonic hedgehog is an axonal chemoattractant that collaborates with netrin-1 in midline axon guidance. Cell 113, 11-23 (2003).

67. Chen, Y., Hajipour, A.R., Sievert, M.K., Arbabian, M. & Ruoho, A.E. Characterization of the Cocaine Binding Site on the Sigma-1 Receptor †. Biochemistry 46, 3532-3542 (2007).

68. Chilton, J.K. Molecular mechanisms of axon guidance. Developmental Biology 292, 13-24 (2006).

69. Chrencik, J.E. et al. Structural and biophysical characterization of the EphB4*ephrinB2 protein-protein interaction and receptor specificity. The Journal of biological chemistry 281, 28185-28192 (2006).

70. Chun, E. et al. Fusion partner toolchest for the stabilization and crystallization of G protein-coupled receptors. Structure 20, 967-976 (2012).

71. Clare, R., King, V.G., Wirenfeldt, M. & Vinters, H.V. Synapse loss in dementias. Journal of neuroscience research 88, 2083-2090 (2010).

72. Clayton, A. et al. Crystal Structure of the GluR2 Amino-Terminal Domain Provides Insights into the Architecture and Assembly of Ionotropic Glutamate Receptors. Journal of molecular biology 392, 1125-1132 (2009).

73. Cline, H. Synaptogenesis: a balancing act between excitation and inhibition. Current biology : CB 15, R203-5 (2005).

74. Cohen, S. & Greenberg, M.E. Communication Between the Synapse and the Nucleus in Neuronal Development, Plasticity, and Disease. Annual review of cell and developmental biology 24, 183-209 (2008).

75. Coles, C.H. et al. Proteoglycan-specific molecular switch for RPTPσ clustering and neuronal extension. Science 332, 484-488 (2011).

76. Collaborative Computational Project, N. The CCP4 suite: programs for protein crystallography. Acta Cryst (1994). D50, 760-763 [doi:10.1107/S0907444994003112], 1-4 (1994).

77. Collingridge, G.L., Kehl, S.J. & McLennan, H. Excitatory amino acids in synaptic transmission in the Schaffer collateral-commissural pathway of the rat hippocampus. The Journal of Physiology 334, 33-46 (1983).

78. Copits, B.A. & Swanson, G.T. Dancing partners at the synapse: auxiliary subunits that shape kainate receptor function. 1-12 (2012).

79. Corpet, F. Multiple sequence alignment with hierarchical clustering. Nucleic Acids Research 16, 10881-10890 (1988).

80. Csordás, G. et al. Structural and functional features and significance of the physical linkage between ER and mitochondria. The Journal of Cell Biology 174, 915-921 (2006).

81. Cunningham, B.C. et al. Dimerization of the extracellular domain of the human growth hormone receptor by a single hormone molecule. Science 254, 821-825 (1991).

82. Daar, I.O. Non-SH2/PDZ reverse signaling by ephrins. Seminars in Cell & Developmental Biology 23, 65-74 (2012).

83. Dalva, M.B., McClelland, A.C. & Kayser, M.S. Cell adhesion molecules: signalling functions at the synapse. Nature Reviews Neuroscience 8, 206-220 (2007).

84. Dalva, M.B. et al. EphB receptors interact with NMDA receptors and regulate excitatory synapse formation. Cell 103, 945-956 (2000).

85. Daniel, E. et al. xtalPiMS: A PiMS-based web application for the management and monitoring of crystallization trials. JOURNAL OF STRUCTURAL BIOLOGY 175, 230-235 (2011).

86. Davis, I.W. et al. MolProbity: all-atom contacts and structure validation for proteins and nucleic acids. Nucleic Acids Research 35, W375-W383 (2007).

87. Davis, S. et al. Ligands for EPH-related receptor tyrosine kinases that require membrane attachment or clustering for activity. Science 266, 816-819 (1994).

88. de Vivo, L. et al. Extracellular matrix inhibits structural and functional plasticity of dendritic spines in the adult visual cortex. Nature Communications 4, 1484-10 (2013).

89. de Wit, J. et al. Unbiased Discovery of Glypican as a Receptor for LRRTM4 in Regulating Excitatory Synapse Development. Neuron 79, 696-711 (2013).

90. de Wit, J. & Verhaagen, J. Proteoglycans as modulators of axon guidance cue function. Advances in experimental medicine and biology 600, 73-89 (2007).

91. Debant, A. et al. The multidomain protein Trio binds the LAR transmembrane tyrosine phosphatase, contains a protein kinase domain, and has separate rac-specific and rho-specific guanine nucleotide exchange factor domains. Proceedings of the National Academy of Sciences of the United States of America 93, 5466-5471 (1996).

92. Dechant, G. & Barde, Y.-A. The neurotrophin receptor p75(NTR): novel functions and implications for diseases of the nervous system. Nature Neuroscience 5, 1131-1136 (2002).

93. Denu, J.M. & Dixon, J.E. A catalytic mechanism for the dual-specific phosphatases. Proceedings of the National Academy of Sciences of the United States of America 92, 5910-5914 (1995).

94. Denu, J.M. & Dixon, J.E. Protein tyrosine phosphatases: mechanisms of catalysis and regulation. Current Opinion in Chemical Biology 2, 633-641 (1998).

95. Denu, J.M., Lohse, D.L., Vijayalakshmi, J., Saper, M.A. & Dixon, J.E. Visualization of intermediate and transition-state structures in protein-tyrosine phosphatase catalysis. Proceedings of the National Academy of Sciences of the United States of America 93, 2493-2498 (1996).

96. DeRosse, P. et al. The Genetics of Symptom-Based Phenotypes: Toward a Molecular Classification of Schizophrenia. Schizophrenia … (2008).

97. Dickson, B.J. Molecular Mechanisms of Axon Guidance. Science 298, 1959-1964 (2002).

98. Dingledine, R., Borges, K., Bowie, D. & Traynelis, S.F. The glutamate receptor ion channels. Pharmacological Reviews 51, 7-61 (1999).

99. Doliana, R., Bot, S., Bonaldo, P. & Colombatti, A. EMI, a novel cysteine-rich domain of EMILINs and other extracellular proteins, interacts with the gC1q domains and participates in multimerization. FEBS letters 484, 164-168 (2000).

100. Dravis, C. et al. Bidirectional signaling mediated by ephrin-B2 and EphB2 controls urorectal development. Developmental Biology 271, 272-290 (2004).

101. Dreyfus, C.F. Effects of nerve growth factor on cholinergic brain neurons. Trends in Pharmacological Sciences 10, 145-149 (1989).

102. Dudek, S.M. & Bear, M.F. Homosynaptic long-term depression in area CA1 of hippocampus and effects of N-methyl-D-aspartate receptor blockade. Proceedings of the National Academy of Sciences of the United States of America 89, 4363-4367 (1992).

103. Dunah, A.W. et al. LAR receptor protein tyrosine phosphatases in the development and maintenance of excitatory synapses. Nature Neuroscience (2005).

104. Easty, D.J. et al. Loss of expression of receptor tyrosine kinase family genes PTK7 and SEK in metastatic melanoma. International journal of cancer. Journal international du cancer 71, 1061-1065 (1997).

105. Eck, M.J. & Sprang, S.R. The structure of tumor necrosis factor-alpha at 2.6 A resolution. Implications for receptor binding. The Journal of biological chemistry 264, 17595-17605 (1989).

106. Egan, M.F. et al. The BDNF val66met polymorphism affects activity-dependent secretion of BDNF and human memory and hippocampal function. Cell 112, 257-269 (2003).

107. Egea, J. & Klein, R. Bidirectional Eph–ephrin signaling during axon guidance. Trends in Cell Biology 17, 230-238 (2007).

108. Egea, J. et al. Regulation of EphA4 Kinase Activity Is Required for a Subset of Axon Guidance Decisions Suggesting a Key Role for Receptor Clustering in Eph Function. Neuron 47, 515-528 (2005).

109. Elbein, A.D., Tropea, J.E., Mitchell, M. & Kaushal, G.P. Kifunensine, a potent inhibitor of the glycoprotein processing mannosidase I. The Journal of biological chemistry 265, 15599-15605 (1990).

110. Elchebly, M. et al. Neuroendocrine dysplasia in mice lacking protein tyrosine phosphatase &sgr. Nature Genetics 21, 330-333 (1999).

111. Emsley, P. & Cowtan, K. Coot: model-building tools for molecular graphics. Acta Cryst (2004). D60, 2126-2132 [doi:10.1107/S0907444904019158], 1-7 (2004).

112. Engle, E.C. Human Genetic Disorders of Axon Guidance. Cold Spring Harbor Perspectives in Biology 2, 784-784 (2010).

113. Ensslen-Craig, S.E. & Brady-Kalnay, S.M. Receptor protein tyrosine phosphatases regulate neural development and axon guidance. Developmental Biology 275, 12-22 (2004).

114. Espanel, X. et al. Pulling strings below the surface: hormone receptor signaling through inhibition of protein tyrosine phosphatases. Endocrine 15, 19-28 (2001).

115. Fabre, P.J., Shimogori, T. & Charron, F. Segregation of ipsilateral retinal ganglion cell axons at the optic chiasm requires the Shh receptor Boc. The Journal of neuroscience : the official journal of the Society for Neuroscience 30, 266-275 (2010).

116. Faux, C. et al. PTPσ binds and dephosphorylates neurotrophin receptors and can suppress NGF-dependent neurite outgrowth from sensory neurons. Biochimica et Biophysica Acta (BBA) - Molecular Cell Research 1773, 1689-1700 (2007).

117. Finger, S. Origins of Neuroscience: A History of Explorations Into Brain Function, 48 (Oxford University Press, 2001).

118. Fischer, E.H. Protein Phosphorylation and cellular regulation, II. Nobel Lect, 95-113 (1992).

119. Fisher, J.L. & Mott, D.D. Modulation of homomeric and heteromeric kainate receptors by the auxiliary subunit Neto1. The Journal of Physiology 591, 4711-4724 (2013).

120. Flanagan, J.G. & Vanderhaeghen, P. THE EPHRINS AND EPH RECEPTORS IN NEURAL DEVELOPMENT. Annual Review of Neuroscience 21, 309-345 (1998).

121. Fox, A.N. & Zinn, K. The heparan sulfate proteoglycan syndecan is an in vivo ligand for the Drosophila LAR receptor tyrosine phosphatase. Current biology : CB 15, 1701-1711 (2005).

122. Frangioni, J.V., Beahm, P.H., Shifrin, V., Jost, C.A. & Neel, B.G. The nontransmembrane tyrosine phosphatase PTP-1B localizes to the endoplasmic reticulum via its 35 amino acid C-terminal sequence. Cell 68, 545-560 (1992).

123. French, S. & Wilson, K. On the treatment of negative intensity observations. Acta Crystallographica Section A: Crystal Physics, Diffraction, Theoretical and General Crystallography 34, 517-525 (1978).

124. Fry, E.J., Chagnon, M.J., López-Vales, R., Tremblay, M.L. & David, S. Corticospinal tract regeneration after spinal cord injury in receptor protein tyrosine phosphatase sigma deficient mice. Glia 58, 423-433 (2010).

125. Fujisawa, H. Discovery of semaphorin receptors, neuropilin and plexin, and their functions in neural development. Journal of Neurobiology 59, 24-33 (2004).

126. Gaboriaud, C. The Crystal Structure of the Globular Head of Complement Protein C1q Provides a Basis for Its Versatile Recognition Properties. Journal of Biological Chemistry 278, 46974-46982 (2003).

127. Gale, N.W. et al. Eph receptors and ligands comprise two major specificity subclasses and are reciprocally compartmentalized during embryogenesis. Neuron 17, 9-19 (1996).

128. Garman, E.F. Radiation damage in macromolecular crystallography: what is it and why should we care? Acta Cryst (2010). D66, 339-351 [doi:10.1107/S0907444910008656], 1-13 (2010).

129. Gerlai, R. Eph receptors and neural plasticity. Nature Reviews Neuroscience 2, 205-209 (2001).

130. Ghai, R. et al. C1q and its growing family. Immunobiology 212, 253-266 (2007).

131. Ginty, D.D. & Segal, R.A. Retrograde neurotrophin signaling: Trk-ing along the axon. Current Opinion in Neurobiology 12, 268-274 (2002).

132. Goldshmit, Y., Galea, M.P., Wise, G., Bartlett, P.F. & Turnley, A.M. Axonal regeneration and lack of astrocytic gliosis in EphA4-deficient mice. The Journal of neuroscience : the official journal of the Society for Neuroscience 24, 10064-10073 (2004).

133. Gouet, P. ESPript/ENDscript: extracting and rendering sequence and 3D information from atomic structures of proteins. Nucleic Acids Research 31, 3320-3323 (2003).

134. Grant, S.G.N. Synaptopathies: diseases of the synaptome. Current Opinion in Neurobiology 22, 522-529 (2012).

135. Gray, E.G. Axo-somatic and axo-dendritic synapses of the cerebral cortex. Journal of Anatomy (1959).

136. Grimes, M.L., Beattie, E. & Mobley, W.C. A signaling organelle containing the nerve growth factor-activated receptor tyrosine kinase, TrkA. Proceedings of the National Academy of Sciences of the United States of America 94, 9909-9914 (1997).

137. Grimes, M.L. et al. Endocytosis of activated TrkA: evidence that nerve growth factor induces formation of signaling endosomes. The Journal of neuroscience : the official journal of the Society for Neuroscience 16, 7950-7964 (1996).

138. Groves, J.T. & Kuriyan, J. Molecular mechanisms in signal transduction at the membrane. Nature Structural & Molecular Biology 17, 659-665 (2010).

139. Grueninger Leitch, F., D'Arcy, A., D'Arcy, B. & Chène, C. Deglycosylation of proteins for crystallization using recombinant fusion protein glycosidases. Protein Science 5, 2617-2622 (1996).

140. Grunwald, I.C. et al. Kinase-independent requirement of EphB2 receptors in hippocampal synaptic plasticity. Neuron 32, 1027-1040 (2001).

141. Guitart, X., Codony, X. & Monroy, X. Sigma receptors: biology and therapeutic potential. Psychopharmacology 174(2004).

142. Gupta, R. & Brunak, S. Prediction of glycosylation across the human proteome and the correlation to protein function. 7, 310-322 (2002).

143. Haapasalo, A. et al. Presenilin/gamma-secretase-mediated cleavage regulates association of leukocyte-common antigen-related (LAR) receptor tyrosine phosphatase with beta-catenin. The Journal of biological chemistry 282, 9063-9072 (2007).

144. Haitina, T. et al. Expression profile of the entire family of Adhesion G protein-coupled receptors in mouse and rat. BMC neuroscience 9, 43 (2008).

145. Halloran, M.C. & Wolman, M.A. Repulsion or adhesion: receptors make the call. Current Opinion in Cell Biology (2006).

146. Hamburger, V. & Levi-Montalcini, R. Proliferation, differentiation and degeneration in the spinal ganglia of the chick embryo under normal and experimental conditions. Journal of Experimental Zoology 111, 457-501 (1949).

147. Hanner, M. et al. Purification, molecular cloning, and expression of the mammalian sigma1-binding site. Proceedings of the National Academy of Sciences of the United States of America 93, 8072-8077 (1996).

148. Hanner, M. et al. Phenylalkylamine Ca2+ antagonist binding protein. Molecular cloning, tissue distribution, and heterologous expression. The Journal of biological chemistry 270, 7551-7557 (1995).

149. Hansen, M.J., Dallal, G.E. & Flanagan, J.G. Retinal axon response to ephrin-as shows a graded, concentration-dependent transition from growth promotion to inhibition. Neuron 42, 717-730 (2004).

150. Harris, K.M., Cruce, W.L., Greenough, W.T. & Teyler, T.J. A Golgi impregnation technique for thin brain slices maintained in vitro. Journal of neuroscience methods 2, 363-371 (1980).

151. Harris, K.M. & Weinberg, R.J. Ultrastructure of Synapses in the Mammalian Brain. Cold Spring Harbor Perspectives in Biology 4, a005587-a005587 (2012).

152. Hattori, M., Osterfield, M. & Flanagan, J.G. Regulated cleavage of a contact-mediated axon repellent. Science 289, 1360-1365 (2000).

153. Hayashi, T. Sigma-1 receptors at galactosylceramide-enriched lipid microdomains regulate oligodendrocyte differentiation. Proceedings of the National Academy of Sciences 101, 14949-14954 (2004).

154. Hayashi, T., Maurice, T. & Su, T.P. Ca(2+) signaling via sigma(1)-receptors: novel regulatory mechanism affecting intracellular Ca(2+) concentration. The Journal of pharmacology and experimental therapeutics 293, 788-798 (2000).

155. Hayashi, T. & Su, T.-P. Intracellular dynamics of σ-1 receptors (σ1 binding sites) in NG108-15 cells. Journal of Pharmacology and Experimental Therapeutics 306, 726-733 (2003).

156. Hayashi, T. & Su, T.-P. Sigma-1 receptor ligands: potential in the treatment of neuropsychiatric disorders. CNS drugs 18, 269-284 (2004).

157. Hayashi, T. & Su, T.-P. Sigma-1 Receptor Chaperones at the ER- Mitochondrion Interface Regulate Ca2+ Signaling and Cell Survival. Cell 131, 596-610 (2007).

158. Hayashi, T. & Su, T.P. Regulating ankyrin dynamics: Roles of sigma-1 receptors. Proceedings of the National Academy of Sciences of the United States of America 98, 491-496 (2001).

159. He, X.-L. & Garcia, K.C. Structure of nerve growth factor complexed with the shared neurotrophin receptor p75. Science 304, 870-875 (2004).

160. Hebb, D.O. The Organization of Behavior, 378 (Psychology Press, 2002).

161. Heldin, C.H. Dimerization of cell surface receptors in signal transduction. Cell 80, 213-223 (1995).

162. Herbst, R. & Burden, S.J. The juxtamembrane region of MuSK has a critical role in agrin-mediated signaling. The EMBO Journal 19, 67-77 (2000).

163. Himanen, J.-P. et al. Repelling class discrimination: ephrin-A5 binds to and activates EphB2 receptor signaling. Nature Neuroscience 7, 501-509 (2004).

164. Himanen, J.-P., Saha, N. & Nikolov, D.B. Cell–cell signaling via Eph receptors and ephrins. Current Opinion in Cell Biology 19, 534-542 (2007).

165. Himanen, J.P. Ectodomain structures of Eph receptors. Seminars in Cell & Developmental Biology 23, 35-42 (2012).

166. Himanen, J.P. et al. Ligand recognition by A-class Eph receptors: crystal structures of the EphA2 ligand-binding domain and the EphA2/ephrin-A1 complex. EMBO reports 10, 722-728 (2009).

167. Himanen, J.P. et al. Crystal structure of an Eph receptor-ephrin complex. Nature 414, 933-938 (2001).

168. Himanen, J.P. et al. Architecture of Eph receptor clusters. Proceedings of the National Academy of Sciences 107, 10860-10865 (2010).

169. Hirai, H., Maru, Y., Hagiwara, K., Nishida, J. & Takaku, F. A novel putative tyrosine kinase receptor encoded by the eph gene. Science 238, 1717-1720 (1987).

170. Ho, V.M., Lee, J.-A. & Martin, K.C. The cell biology of synaptic plasticity. Science 334, 623-628 (2011).

171. Hollmann, M., O'Shea-Greenfield, A., Rogers, S.W. & Heinemann, S. Cloning by functional expression of a member of the glutamate receptor family. Nature 342, 643-648 (1989).

172. Holmberg, J., Clarke, D.L. & Frisen, J. Regulation of repulsion versus adhesion by different splice forms of an Eph receptor. Nature 408, 203-206 (2000).

173. Honoré, T., Lauridsen, J. & Krogsgaard-Larsen, P. The binding of [3H]AMPA, a structural analogue of glutamic acid, to rat brain membranes. Journal of Neurochemistry 38, 173-178 (1982).

174. Howe, C.L., Valletta, J.S., Rusnak, A.S. & Mobley, W.C. NGF signaling from clathrin-coated vesicles: evidence that signaling endosomes serve as a platform for the Ras-MAPK pathway. Neuron 32, 801-814 (2001).

175. Huang, E.J. & Reichardt, L.F. Trk receptors: roles in neuronal signal transduction. Annual review of biochemistry 72, 609-642 (2003).

176. Hunter, T. Protein kinases and phosphatases: the yin and yang of protein phosphorylation and signaling. Cell 80, 225-236 (1995).

177. Hunter, T. & Sefton, B.M. Transforming gene product of Rous sarcoma virus phosphorylates tyrosine. Proceedings of the National Academy of Sciences of the United States of America 77, 1311-1315 (1980).

178. Hussain, S.A. et al. A Molecular Mechanism for the Heparan Sulfate Dependence of Slit-Robo Signaling. Journal of Biological Chemistry 281, 39693-39698 (2006).

179. Huynh-Do, U. Surface densities of ephrin-B1 determine EphB1-coupled activation of cell attachment through alpha vbeta 3 and alpha 5beta 1 integrins. The EMBO Journal 18, 2165-2173 (1999).

180. Ibarra-Sánchez, M.J. et al. The T-cell protein tyrosine phosphatase. Seminars in immunology 12, 379-386 (2000).

181. Iiizumi, M. et al. EphA4 receptor, overexpressed in pancreatic ductal adenocarcinoma, promotes cancer cell growth. Cancer Science 97, 1211-1216 (2006).

182. Iijima, T., Miura, E., Watanabe, M. & Yuzaki, M. Distinct expression of C1q-like family mRNAs in mouse brain and biochemical characterization of their encoded proteins. European Journal of Neuroscience 31, 1606-1615 (2010).

183. Indo, Y. Molecular basis of congenital insensitivity to pain with anhidrosis (CIPA): mutations and polymorphisms in TRKA (NTRK1) gene encoding the receptor tyrosine kinase for nerve growth factor. Human mutation 18, 462-471 (2001).

184. Ishii, N., Wadsworth, W.G., Stern, B.D., Culotti, J.G. & Hedgecock, E.M. UNC-6, a laminin-related protein, guides cell and pioneer axon migrations in C. elegans. Neuron 9, 873-881 (1992).

185. Ito, M. Long-term depression. Annual Review of Neuroscience 12, 85-102 (1989).

186. Ito, M. The molecular organization of cerebellar long-term depression. Nature Reviews Neuroscience 3, 896-902 (2002).

187. Ivins, J.K., Litwack, E.D., Kumbasar, A., Stipp, C.S. & Lander, A.D. Cerebroglycan, a Developmentally Regulated Cell-Surface Heparan Sulfate Proteoglycan, Is Expressed on Developing Axons and Growth Cones. Developmental Biology 184, 320-332 (1997).

188. Janes, P.W. et al. Eph receptor function is modulated by heterooligomerization of A and B type Eph receptors. The Journal of Cell Biology 195, 1033-1045 (2011).

189. Janes, P.W. et al. Adam Meets Eph: An ADAM Substrate Recognition Module Acts as a Molecular Switch for Ephrin Cleavage In trans. Cell 123, 291-304 (2005).

190. Janes, P.W. et al. Cytoplasmic Relaxation of Active Eph Controls Ephrin Shedding by ADAM10. PLoS Biology 7, e1000215 (2009).

191. Janssen, B.J.C. et al. Neuropilins lock secreted semaphorins onto plexins in a ternary signaling complex. Nature Structural & Molecular Biology 19, 1293-1299 (2012).

192. Janssen, B.J.C. et al. Structural basis of semaphorin-plexin signalling. Nature 467, 1118-1122 (2010).

193. Jiang, G., den Hertog, J. & Hunter, T. Receptor-like protein tyrosine phosphatase alpha homodimerizes on the cell surface. Molecular and Cellular Biology 20, 5917-5929 (2000).

194. Jiang, G. et al. Dimerization inhibits the activity of receptor-like protein-tyrosine phosphatase-alpha. Nature 401, 606-610 (1999).

195. Jiang, Y.P. et al. Cloning and characterization of R-PTP-kappa, a new member of the receptor protein tyrosine phosphatase family with a proteolytically cleaved cellular adhesion molecule-like extracellular region. Molecular and Cellular Biology 13, 2942-2951 (1993).

196. Johnson, D., Lanahan, A., Buck, C.R., Sehgal, A. & Morgan, C. Expression and structure of the human NGF receptor. Cell (1986).

197. Johnson, K.G. & Holt, C.E. Expression of CRYP-alpha, LAR, PTP-delta, and PTP-rho in the developing Xenopus visual system. Mechanisms of development 92, 291-294 (2000).

198. Johnson, K.G. et al. The HSPGs Syndecan and Dallylike Bind the Receptor Phosphatase LAR and Exert Distinct Effects on Synaptic Development. Neuron 49, 517-531 (2006).

199. Johnson, K.G. & Van Vactor, D. Receptor protein tyrosine phosphatases in nervous system development. Physiological reviews 83, 1-24 (2002).

200. Jones, E.Y., Stuart, D.I. & Walker, N.P. Structure of tumour necrosis factor. Nature 338, 225-228 (1989).

201. Kantardjieff, K.A. & Rupp, B. Matthews coefficient probabilities: Improved estimates for unit cell contents of proteins, DNA, and protein-nucleic acid complex crystals. Protein Science 12, 1865-1871 (2003).

202. Kaplan, D.R., Hempstead, B.L., Martin-Zanca, D., Chao, M.V. & Parada, L.F. The trk proto-oncogene product: a signal transducing receptor for nerve growth factor. Science 252, 554-558 (1991).

203. Kaplan, D.R. & Miller, F.D. Neurotrophin signal transduction in the nervous system. Current Opinion in Neurobiology 10, 381-391 (2000).

204. Kaplan, R. et al. Cloning of three human tyrosine phosphatases reveals a multigene family of receptor-linked protein-tyrosine-phosphatases expressed in brain. Proceedings of the National Academy of Sciences of the United States of America 87, 7000-7004 (1990).

205. Kasai, H., Fukuda, M. & Watanabe, S. Structural dynamics of dendritic spines in memory and cognition. Trends in … (2010).

206. Katz, L.C. & Shatz, C.J. Synaptic activity and the construction of cortical circuits. Science 274, 1133-1138 (1996).

207. Kaur, B., Brat, D.J., Devi, N.S. & Van Meir, E.G. Vasculostatin, a proteolytic fragment of brain angiogenesis inhibitor 1, is an antiangiogenic and antitumorigenic factor. Oncogene 24, 3632-3642 (2005).

208. Kawate, T. & Gouaux, E. Fluorescence-Detection Size-Exclusion Chromatography for Precrystallization Screening of Integral Membrane Proteins. Structure 14, 673-681 (2006).

209. Kee, H.J. et al. Expression of brain-specific angiogenesis inhibitor 3 (BAI3) in normal brain and implications for BAI3 in ischemia-induced brain angiogenesis and malignant glioma. FEBS letters 569, 307-316 (2004).

210. Kee, H.J. et al. Expression of brain-specific angiogenesis inhibitor 2 (BAI2) in normal and ischemic brain: involvement of BAI2 in the ischemia-induced brain angiogenesis. Journal of cerebral blood flow and metabolism : official journal of the International Society of Cerebral Blood Flow and Metabolism 22, 1054-1067 (2002).

211. Keino-Masu, K. et al. Deleted in Colorectal Cancer (DCC) encodes a netrin receptor. Cell 87, 175-185 (1996).

212. Keleman, K. & Dickson, B.J. Short- and long-range repulsion by the Drosophila Unc5 netrin receptor. Neuron 32, 605-617 (2001).

213. Kidd, T., Bland, K.S. & Goodman, C.S. Slit is the midline repellent for the robo receptor in Drosophila. Cell 96, 785-794 (1999).

214. Kinnunen, A. et al. N-syndecan and HB-GAM (heparin-binding growth-associated molecule) associate with early axonal tracts in the rat brain. The European journal of neuroscience 10, 635-648 (1998).

215. Kinnunen, A. et al. Heparan sulphate and HB-GAM (heparin-binding rowth-associated molecule) in the development of the thalamocortical pathway of rat brain. European Journal of Neuroscience 11, 491-502 (1999).

216. Kirkwood, A., Dudek, S.M., Gold, J.T., Aizenman, C.D. & Bear, M.F. Common forms of synaptic plasticity in the hippocampus and neocortex in vitro. Science 260, 1518-1521 (1993).

217. Kishore, U. et al. Structural and functional anatomy of the globular domain of complement protein C1q. Immunology letters 95, 113-128 (2004).

218. Klassen, M.P. & Shen, K. Wnt signaling positions neuromuscular connectivity by inhibiting synapse formation in C. elegans. Cell 130, 704-716 (2007).

219. Klein, R. Eph/ephrin signaling in morphogenesis, neural development and plasticity. Current Opinion in Cell Biology 16, 580-589 (2004).

220. Klein, R. Axon guidance: opposing EPHects in the growth cone. Cell 121, 4-6 (2005).

221. Klein, R. Bidirectional modulation of synaptic functions by Eph/ephrin signaling. Nature Neuroscience 12, 15-20 (2008).

222. Klein, R. Eph/ephrin signalling during development. Development 139, 4105-4109 (2012).

223. Klein, R., Jing, S.Q., Nanduri, V., O'Rourke, E. & Barbacid, M. The trk proto-oncogene encodes a receptor for nerve growth factor. Cell 65, 189-197 (1991).

224. Kleywegt, G.J. & Jones, T.A. Detecting folding motifs and similarities in protein structures. Methods in enzymology 277, 525-545 (1997).

225. Koh, J.T. et al. Characterization of mouse brain-specific angiogenesis inhibitor 1 (BAI1) and phytanoyl-CoA alpha-hydroxylase-associated protein 1, a novel BAI1-binding protein. Brain research. Molecular brain research 87, 223-237 (2001).

226. Kolkman, M.J.M. et al. Mice lacking leukocyte common antigen-related (LAR) protein tyrosine phosphatase domains demonstrate spatial learning impairment in the two-trial water maze and hyperactivity in multiple behavioural tests. Behavioural Brain Research 154, 171-182 (2004).

227. Kolodkin, A.L. et al. Fasciclin IV: sequence, expression, and function during growth cone guidance in the grasshopper embryo. Neuron 9, 831-845 (1992).

228. Kolodkin, A.L. & Tessier-Lavigne, M. Mechanisms and Molecules of Neuronal Wiring: A Primer. Cold Spring Harbor Perspectives in Biology 3, a001727-a001727 (2011).

229. Kolodziej, P.A. et al. frazzled encodes a Drosophila member of the DCC immunoglobulin subfamily and is required for CNS and motor axon guidance. Cell 87, 197-204 (1996).

230. Konstantinova, I. et al. EphA-Ephrin-A-mediated beta cell communication regulates insulin secretion from pancreatic islets. Cell 129, 359-370 (2007).

231. Kourrich, S., Su, T.-P., Fujimoto, M. & Bonci, A. The sigma-1 receptor: roles in neuronal plasticity and disease. Trends in Neurosciences 35, 762-771 (2012).

232. Krasnoperov, V. et al. Protein-tyrosine phosphatase-sigma is a novel member of the functional family of alpha-latrotoxin receptors. The Journal of biological chemistry 277, 35887-35895 (2002).

233. Krasnoperov, V. et al. Post-translational proteolytic processing of the calcium-independent receptor of alpha-latrotoxin (CIRL), a natural chimera of the cell adhesion protein and the G protein-coupled receptor. Role of the G protein-coupled receptor proteolysis site (GPS) motif. The Journal of biological chemistry 277, 46518-46526 (2002).

234. Krebs, E.G. Protein phosphorylation and cellular regulation, I. Nobel Lect, 1-18 (1992).

235. Krueger, N.X. et al. The transmembrane tyrosine phosphatase DLAR controls motor axon guidance in Drosophila. Cell 84, 611-622 (1996).

236. Kullander, K. & Klein, R. Mechanisms and functions of eph and ephrin signalling. Nature Reviews Molecular Cell Biology 3, 475-486 (2002).

237. Kumar, K.N., Tilakaratne, N., Johnson, P.S., Allen, A.E. & Michaelis, E.K. Cloning of cDNA for the glutamate-binding subunit of an NMDA receptor complex. Nature 354, 70-73 (1991).

238. Kvansakul, M., Bogin, O., Hohenester, E. & Yayon, A. Crystal structure of the collagen alpha1(VIII) NC1 trimer. Matrix biology : journal of the International Society for Matrix Biology 22, 145-152 (2003).

239. Kwok, J.C.F., Carulli, D. & Fawcett, J.W. In vitro modeling of perineuronal nets: hyaluronan synthase and link protein are necessary for their formation and integrity. Journal of Neurochemistry 114, 1447-1459 (2010).

240. Kwon, S.K., Woo, J., Kim, S.Y., Kim, H. & Kim, E. Trans-synaptic Adhesions between Netrin-G Ligand-3 (NGL-3) and Receptor Tyrosine Phosphatases LAR, Protein-tyrosine Phosphatase (PTP), and PTP via Specific Domains Regulate Excitatory Synapse Formation. Journal of Biological Chemistry 285, 13966-13978 (2010).

241. Lackmann, M. et al. Distinct subdomains of the EphA3 receptor mediate ligand binding and receptor dimerization. The Journal of biological chemistry 273, 20228-20237 (1998).

242. Lancaster, E., Martinez-Hernandez, E. & Dalmau, J. Encephalitis and antibodies to synaptic and neuronal cell surface proteins. Neurology 77, 179-189 (2011).

243. Landolt, R.M., Vaughan, L., Winterhalter, K.H. & Zimmermann, D.R. Versican is selectively expressed in embryonic tissues that act as barriers to neural crest cell migration and axon outgrowth. Development 121, 2303-2312 (1995).

244. Langenhan, T., Aust, G. & Hamann, J. Sticky signaling--adhesion class G protein-coupled receptors take the stage. Science Signaling 6, re3 (2013).

245. Lanoue, V. et al. The adhesion-GPCR BAI3, a gene linked to psychiatric disorders, regulates dendrite morphogenesis in neurons. Molecular Psychiatry 18, 943-950 (2013).

246. Lee, H.-K. et al. Phosphorylation of the AMPA receptor GluR1 subunit is required for synaptic plasticity and retention of spatial memory. Cell 112, 631-643 (2003).

247. Lee, J.-S. & Chien, C.-B. When sugars guide axons: insights from heparan sulphate proteoglycan mutants. Nature Reviews Genetics 5, 923-935 (2004).

248. Lee, R., Kermani, P., Teng, K.K. & Hempstead, B.L. Regulation of cell survival by secreted proneurotrophins. Science 294, 1945-1948 (2001).

249. Lee, S. et al. Dimerization of protein tyrosine phosphatase sigma governs both ligand binding and isoform specificity. Molecular and Cellular Biology 27, 1795-1808 (2007).

250. Leibrock, J. et al. Molecular cloning and expression of brain-derived neurotrophic factor. Nature 341, 149-152 (1989).

251. Lemmon, M.A. & Schlessinger, J. Regulation of signal transduction and signal diversity by receptor oligomerization. Trends in Biochemical Sciences 19, 459-463 (1994).

252. Leslie, A.G.W. & Powell, H.R. Processing diffraction data with mosflm. Vol. 245 41-51 (Springer Netherlands, Dordrecht, 2007).

253. Li, H.S. et al. Vertebrate slit, a secreted ligand for the transmembrane protein roundabout, is a repellent for olfactory bulb axons. Cell 96, 807-818 (1999).

254. Li, S., Depetris, R.S., Barford, D., Chernoff, J. & Hubbard, S.R. Crystal structure of a complex between protein tyrosine phosphatase 1B and the insulin receptor tyrosine kinase. Structure/Folding and Design 13, 1643-1651 (2005).

255. Li, Z. et al. Caspase-3 activation via mitochondria is required for long-term depression and AMPA receptor internalization. Cell 141, 859-871 (2010).

256. Lin, Y.-L., Lei, Y.-T., Hong, C.-J. & Hsueh, Y.-P. Syndecan-2 induces filopodia and dendritic spine formation via the neurofibromin-PKA-Ena/VASP pathway. The Journal of Cell Biology 177, 829-841 (2007).

257. Lisman, J. A mechanism for the Hebb and the anti-Hebb processes underlying learning and memory. Proceedings of the National Academy of Sciences of the United States of America 86, 9574-9578 (1989).

258. Liu, Y. et al. Ryk-mediated Wnt repulsion regulates posterior-directed growth of corticospinal tract. Nature Neuroscience 8, 1151-1159 (2005).

259. Lomeli, H. et al. The rat delta-1 and delta-2 subunits extend the excitatory amino acid receptor family. FEBS letters 315, 318-322 (1993).

260. Lowery, L.A. & Van Vactor, D. The trip of the tip: understanding the growth cone machinery. Nature Reviews Molecular Cell Biology 10, 332-343 (2009).

261. Lu, B. & Gottschalk, W. Modulation of hippocampal synaptic transmission and plasticity by neurotrophins. Progress in brain research 128, 231-241 (2000).

262. Lučić, V., Yang, T., Schweikert, G., Förster, F. & Baumeister, W. Morphological characterization of molecular complexes present in the synaptic cleft. Structure/Folding and Design 13, 423-434 (2005).

263. Luo, Y., Raible, D. & Raper, J.A. Collapsin: a protein in brain that induces the collapse and paralysis of neuronal growth cones. Cell 75, 217-227 (1993).

264. Lüscher, C. & Malenka, R.C. NMDA receptor-dependent long-term potentiation and long-term depression (LTP/LTD). Cold Spring Harbor Perspectives in Biology 4(2012).

265. Ly, A. et al. DSCAM is a netrin receptor that collaborates with DCC in mediating turning responses to netrin-1. Cell 133, 1241-1254 (2008).

266. Lyuksyutova, A.I. et al. Anterior-posterior guidance of commissural axons by Wnt-frizzled signaling. Science 302, 1984-1988 (2003).

267. Ma, L. & Tessier-Lavigne, M. Dual branch-promoting and branch-repelling actions of Slit/Robo signaling on peripheral and central branches of developing sensory axons. The Journal of neuroscience : the official journal of the Society for Neuroscience 27, 6843-6851 (2007).

268. Malenka, R.C. & Bear, M.F. LTP and LTD: an embarrassment of riches. Neuron 44, 5-21 (2004).

269. Malenka, R.C. & Nicoll, R.A. Long-term potentiation--a decade of progress? Science 285, 1870-1874 (1999).

270. Marquardt, T. et al. Coexpressed EphA receptors and ephrin-A ligands mediate opposing actions on growth cone navigation from distinct membrane domains. Cell 121, 127-139 (2005).

271. Marston, D.J., Dickinson, S. & Nobes, C.D. Rac-dependent trans-endocytosis of ephrinBs regulates Eph-ephrin contact repulsion. Nature cell biology 5, 879-888 (2003).

272. Matsuda, K. et al. Cbln1 Is a Ligand for an Orphan Glutamate Receptor 2, a Bidirectional Synapse Organizer. Science 328, 363-368 (2010).

273. Matthews, B.W. Solvent content of protein crystals. Journal of molecular biology 33, 491-497 (1968).

274. Maurice, T., Roman, F.J. & Privat, A. Modulation by neurosteroids of the in vivo (+)-[3H]SKF-10,047 binding to sigma 1 receptors in the mouse forebrain. Journal of neuroscience research 46, 734-743 (1996).

275. Maurice, T. & Su, T.-P. The pharmacology of sigma-1 receptors. Pharmacology and Therapeutics 124, 195-206 (2009).

276. Mauro, L.J. & Dixon, J.E. 'Zip codes' direct intracellular protein tyrosine phosphatases to the correct cellular 'address'. Trends in Biochemical Sciences 19, 151-155 (1994).

277. Mayne, R. & Brewton, R.G. New members of the collagen superfamily. Current Opinion in Cell Biology 5, 883-890 (1993).

278. Mayo, C.J. et al. Benefits of automated crystallization plate tracking, imaging, and analysis. Structure/Folding and Design 13, 175-182 (2005).

279. McCann, D.J. & Su, T.P. Solubilization and characterization of haloperidol-sensitive (+)-[3H]SKF-10,047 binding sites (sigma sites) from rat liver membranes. Journal of Pharmacology and Experimental Therapeutics (1991).

280. McCoy, A.J., Grosse-Kunstleve, R.W., Storoni, L.C. & Read, R.J. Likelihood-enhanced fast translation functions. Acta Crystallographica Section D Biological Crystallography 61, 458-464 (2005).

281. McDonald, N.Q. et al. New protein fold revealed by a 2.3-A resolution crystal structure of nerve growth factor. Nature 354, 411-414 (1991).

282. McLaughlin, T., Hindges, R., Yates, P.A. & O'Leary, D.D.M. Bifunctional action of ephrin-B1 as a repellent and attractant to control bidirectional branch extension in dorsal-ventral retinotopic mapping. Development 130, 2407-2418 (2003).

283. McLean, J., Batt, J., Doering, L.C., Rotin, D. & Bain, J.R. Enhanced rate of nerve regeneration and directional errors after sciatic nerve injury in receptor protein tyrosine

phosphatase sigma knock-out mice. The Journal of neuroscience : the official journal of the Society for Neuroscience 22, 5481-5491 (2002).

284. Mei, J. & Pasternak, G.W. Molecular cloning and pharmacological characterization of the rat sigma1 receptor. Biochemical Pharmacology 62, 349-355 (2001).

285. Min, X. et al. Crystal structure of a single-chain trimer of human adiponectin globular domain. FEBS letters 586, 912-917 (2012).

286. Moebius, F.F., Reiter, R.J., Hanner, M. & Glossmann, H. High affinity of sigma 1-binding sites for sterol isomerization inhibitors: evidence for a pharmacological relationship with the yeast sterol C8-C7 isomerase. British Journal of Pharmacology 121, 1-6 (1997).

287. Monk, K.R. et al. A G Protein-Coupled Receptor Is Essential for Schwann Cells to Initiate Myelination. Science 325, 1402-1405 (2009).

288. Morin-Surun, M.P., Collin, T., Denavit-Saubié, M., Baulieu, E.E. & Monnet, F.P. Intracellular sigma1 receptor modulates phospholipase C and protein kinase C activities in the brainstem. Proc Natl Acad Sci USA 96, 8196-8199 (1999).

289. Morlot, C. et al. Structural insights into the Slit-Robo complex. Proceedings of the National Academy of Sciences of the United States of America 104, 14923-14928 (2007).

290. Muise, A.M. et al. Protein-tyrosine phosphatase sigma is associated with ulcerative colitis. Current biology : CB 17, 1212-1218 (2007).

291. Mulkey, R.M., Endo, S., Shenolikar, S. & Malenka, R.C. Involvement of a calcineurin/inhibitor-1 phosphatase cascade in hippocampal long-term depression. Nature 369, 486-488 (1994).

292. Mulkey, R.M., Herron, C.E. & Malenka, R.C. An essential role for protein phosphatases in hippocampal long-term depression. Science 261, 1051-1055 (1993).

293. Mulkey, R.M. & Malenka, R.C. Mechanisms underlying induction of homosynaptic long-term depression in area CA1 of the hippocampus. Neuron 9, 967-975 (1992).

294. Murai, K.K., Nguyen, L.N., Irie, F., Yamaguchi, Y. & Pasquale, E.B. Control of hippocampal dendritic spine morphology through ephrin-A3/EphA4 signaling. Nature Neuroscience 6, 153-160 (2002).

295. Murshudov, G.N., Vagin, A.A. & Dodson, E.J. Refinement of Macromolecular Structures by the Maximum-Likelihood Method. Acta Cryst (1997). D53, 240-255 [doi:10.1107/S0907444996012255], 1-16 (1997).

296. Mus-Veteau, I. Heterologous Expression of Membrane Proteins, 1-271 (Humana Press, 2009).

297. Naito, A.T. et al. Complement C1q Activates Canonical Wnt Signaling and Promotes Aging-Related Phenotypes. Cell 149, 1298-1313 (2012).

298. Nam, H.-J., Poy, F., Saito, H. & Frederick, C.A. Structural basis for the function and regulation of the receptor protein tyrosine phosphatase CD45. The Journal of experimental medicine 201, 441-452 (2005).

299. Nam, H.J., Poy, F., Krueger, N.X., Saito, H. & Frederick, C.A. Crystal structure of the tandem phosphatase domains of RPTP LAR. Cell 97, 449-457 (1999).

300. Navarro, G. et al. Direct involvement of sigma-1 receptors in the dopamine D1 receptor-mediated effects of cocaine. Proceedings of the National Academy of Sciences 107, 18676-18681 (2010).

301. Neel, B.G., Gu, H. & Pao, L. The 'Shp'ing news: SH2 domain-containing tyrosine phosphatases in cell signaling. Trends in Biochemical Sciences 28, 284-293 (2003).

302. Nguyen, E.C., McCracken, K.A., Liu, Y., Pouw, B. & Matsumoto, R.R. Involvement of sigma (sigma) receptors in the acute actions of methamphetamine: receptor binding and behavioral studies. Neuropharmacology 49, 638-645 (2005).

303. Nievergall, E., Lackmann, M. & Janes, P.W. Eph-dependent cell-cell adhesion and segregation in development and cancer. Cellular and Molecular Life Sciences 69, 1813-1842 (2012).

304. Nishimori, H. et al. A novel brain-specific p53-target gene, BAI1, containing thrombospondin type 1 repeats inhibits experimental angiogenesis. Oncogene 15, 2145-2150 (1997).

305. Nitkin, R.M. et al. Identification of agrin, a synaptic organizing protein from Torpedo electric organ. The Journal of Cell Biology 105, 2471-2478 (1987).

306. Noren, N.K. & Pasquale, E.B. Eph receptor-ephrin bidirectional signals that target Ras and Rho proteins. Cellular signalling 16, 655-666 (2004).

307. O'Brien, R.J. et al. Synaptic clustering of AMPA receptors by the extracellular immediate-early gene product Narp. Neuron 23, 309-323 (1999).

308. O'Grady, P., Thai, T.C. & Saito, H. The laminin-nidogen complex is a ligand for a specific splice isoform of the transmembrane protein tyrosine phosphatase LAR. The Journal of Cell Biology 141, 1675-1684 (1998).

309. Oakley, R.A., Lasky, C.J., Erickson, C.A. & Tosney, K.W. Glycoconjugates mark a transient barrier to neural crest migration in the chicken embryo. Development 120, 103-114 (1994).

310. Oakley, R.A. & Tosney, K.W. Peanut agglutinin and chondroitin-6-sulfate are molecular markers for tissues that act as barriers to axon advance in the avian embryo. Developmental Biology 147, 187-206 (1991).

311. Okada, A. et al. Boc is a receptor for sonic hedgehog in the guidance of commissural axons. Nature 444, 369-373 (2006).

312. Ortega-Roldan, J.L., Ossa, F. & Schnell, J.R. Characterization of the Human Sigma-1 Receptor Chaperone Domain Structure and Binding Immunoglobulin Protein (BiP) Interactions. Journal of Biological Chemistry 288, 21448-21457 (2013).

313. Ostman, A. & Böhmer, F.D. Regulation of receptor tyrosine kinase signaling by protein tyrosine phosphatases. Trends in Cell Biology 11, 258-266 (2001).

314. Packard, M., Koo, E.S., Gorczyca, M. & Sharpe, J. The Drosophila Wnt, Wingless, Provides an Essential Signal for Pre- and Postsynaptic Differentiation. Cell (2002).

315. Pajvani, U.B. et al. Complex distribution, not absolute amount of adiponectin, correlates with thiazolidinedione-mediated improvement in insulin sensitivity. The Journal of biological chemistry 279, 12152-12162 (2004).

316. Pal, A. et al. The sigma-1 receptor protects against cellular oxidative stress and activates antioxidant response elements. European journal of pharmacology 682, 12-20 (2012).

317. Palmer, C.P., Mahen, R., Schnell, E., Djamgoz, M.B.A. & Aydar, E. Sigma-1 receptors bind cholesterol and remodel lipid rafts in breast cancer cell lines. Cancer research 67, 11166-11175 (2007).

318. Pannifer, A.D., Flint, A.J., Tonks, N.K. & Barford, D. Visualization of the cysteinyl-phosphate intermediate of a protein-tyrosine phosphatase by x-ray crystallography. The Journal of biological chemistry 273, 10454-10462 (1998).

319. Pasquale, E.B. Developmental Cell Biology: Eph receptor signalling casts a wide net on cell behaviour. Nature Reviews Molecular Cell Biology 6, 462-475 (2005).

320. Pasquale, E.B. Eph-Ephrin Bidirectional Signaling in Physiology and Disease. Cell 133, 38-52 (2008).

321. Pasquale, E.B. Eph receptors and ephrins in cancer: bidirectional signalling and beyond. 1-16 (2010).

322. Paul, S. & Lombroso, P.J. Receptor and nonreceptor protein tyrosine phosphatases in the nervous system. Cellular and Molecular Life Sciences 60, 2465-2482 (2003).

323. Penzes, P., Cahill, M.E., Jones, K.A., VanLeeuwen, J.-E. & Woolfrey, K.M. Dendritic spine pathology in neuropsychiatric disorders. Nature Neuroscience 14, 285-293 (2011).

324. Petersen, T.N., Brunak, S., von Heijne, G. & Nielsen, H. SignalP 4.0: discriminating signal peptides from transmembrane regions. Nature Methods 8, 785-786 (2011).

325. Phillips, W.C. et al. Multiple CCD detector for macromolecular X-ray crystallography. Journal of applied crystallography 33, 243-251 (2000).

326. Pincus, D. et al. BiP binding to the ER-stress sensor Ire1 tunes the homeostatic behavior of the unfolded protein response. PLoS Biology 8, e1000415 (2010).

327. Pizzorusso, T. et al. Reactivation of ocular dominance plasticity in the adult visual cortex. Science 298, 1248-1251 (2002).

328. Prévost, N. et al. Eph kinases and ephrins support thrombus growth and stability by regulating integrin outside-in signaling in platelets. Proceedings of the National Academy of Sciences of the United States of America 102, 9820-9825 (2005).

329. Puius, Y.A. et al. Identification of a second aryl phosphate-binding site in protein-tyrosine phosphatase 1B: a paradigm for inhibitor design. Proceedings of the National Academy of Sciences of the United States of America 94, 13420-13425 (1997).

330. Pulido, R., Krueger, N.X., Serra-Pagès, C., Saito, H. & Streuli, M. Molecular characterization of the human transmembrane protein-tyrosine phosphatase delta. Evidence for tissue-specific expression of alternative human transmembrane protein-tyrosine phosphatase delta isoforms. The Journal of biological chemistry 270, 6722-6728 (1995).

331. Qin, H. et al. Structural Characterization of the EphA4-Ephrin-B2 Complex Reveals New Features Enabling Eph-Ephrin Binding Promiscuity. Journal of Biological Chemistry 285, 644-654 (2009).

332. Qin, H., Shi, J., Noberini, R., Pasquale, E.B. & Song, J. Crystal structure and NMR binding reveal that two small molecule antagonists target the high affinity ephrin-binding channel of the EphA4 receptor. The Journal of biological chemistry 283, 29473-29484 (2008).

333. Rapoport, J.L., Addington, A.M., Frangou, S. & Psych, M.R.C. The neurodevelopmental model of schizophrenia: update 2005. Molecular Psychiatry 10, 434-449 (2005).

334. Raulo, E., Chernousov, M.A., Carey, D.J., Nolo, R. & Rauvala, H. Isolation of a neuronal cell surface receptor of heparin binding growth-associated molecule (HB-GAM). Identification as N-syndecan (syndecan-3). The Journal of biological chemistry 269, 12999-13004 (1994).

335. Reeves, P.J., Callewaert, N., Contreras, R. & Khorana, H.G. Structure and function in rhodopsin: high-level expression of rhodopsin with restricted and homogeneous N-glycosylation by a tetracycline-inducible N-acetylglucosaminyltransferase I-negative HEK293S stable mammalian cell line. Proceedings of the National Academy of Sciences of the United States of America 99, 13419-13424 (2002).

336. Reichardt, L.F. Neurotrophin-regulated signalling pathways. Philosophical transactions of the Royal Society of London. Series B, Biological sciences 361, 1545-1564 (2006).

337. Reist, N.E., Magill, C. & McMahan, U.J. Agrin-like molecules at synaptic sites in normal, denervated, and damaged skeletal muscles. The Journal of Cell Biology 105, 2457-2469 (1987).

338. Rhee, S.G. Cell signaling. H2O2, a necessary evil for cell signaling. Science 312, 1882-1883 (2006).

339. Richter, M., Murai, K.K., Bourgin, C., Pak, D.T. & Pasquale, E.B. The EphA4 receptor regulates neuronal morphology through SPAR-mediated inactivation of Rap GTPases. The Journal of neuroscience : the official journal of the Society for Neuroscience 27, 14205-14215 (2007).

340. Ricklin, D., Hajishengallis, G., Yang, K. & Lambris, J.D. Complement: a key system for immune surveillance and homeostasis. Nature immunology 11, 785-797 (2010).

341. Ring, A.M. et al. Adrenaline-activated structure of β2-adrenoceptor stabilized by an engineered nanobody. Nature, 1-7 (2013).

342. Ring, C., Hassell, J. & Halfter, W. Expression pattern of collagen IX and potential role in the segmentation of the peripheral nervous system. Developmental Biology 180, 41-53 (1996).

343. Robbe, D., Kopf, M., Remaury, A., Bockaert, J. & Manzoni, O.J. Endogenous cannabinoids mediate long-term synaptic depression in the nucleus accumbens. Proceedings of the National Academy of Sciences of the United States of America 99, 8384-8388 (2002).

344. Robinson, R.C., Radziejewski, C., Stuart, D.I. & Jones, E.Y. Structure of the brain-derived neurotrophic factor/neurotrophin 3 heterodimer. Biochemistry 34, 4139-4146 (1995).

345. Rogers, S.W. et al. Autoantibodies to glutamate receptor GluR3 in Rasmussen's encephalitis. Science 265, 648-651 (1994).

346. Rossmann, M.G. & Blow, D.M. The detection of sub-units within the crystallographic asymmetric unit. Acta Cryst (1962). Q15, 24-31 [doi:10.1107/S0365110X62000067], 1-8 (1962).

347. Roumenina, L.T. et al. Role of Ca2+ in the electrostatic stability and the functional activity of the globular domain of human C1q. Biochemistry 44, 14097-14109 (2005).

348. Rupp, B. Biomolecular Crystallography, 809 (Garland Pub, 2010).

349. Saglietti, L. et al. Extracellular interactions between GluR2 and N-cadherin in spine regulation. Neuron 54, 461-477 (2007).

350. Saiki, R. et al. Primer-directed enzymatic amplification of DNA with a thermostable DNA polymerase. Science 239, 487-491 (1988).

351. Sajnani-Perez, G., Chilton, J.K., Aricescu, A.R., Haj, F. & Stoker, A.W. Isoform-specific binding of the tyrosine phosphatase PTPsigma to a ligand in developing muscle. Molecular and Cellular Neuroscience 22, 37-48 (2003).

352. Salaita, K. et al. Restriction of Receptor Movement Alters Cellular Response: Physical Force Sensing by EphA2. Science 327, 1380-1385 (2010).

353. Sallee, J.L. Regulation of Cell Adhesion by Protein-tyrosine Phosphatases: II. CELL-CELL ADHESION. Journal of Biological Chemistry 281, 16189-16192 (2006).

354. Salmeen, A. et al. Redox regulation of protein tyrosine phosphatase 1B involves a sulphenyl-amide intermediate. Nature 423, 769-773 (2003).

355. Salmeen, A., Andersen, J.N., Myers, M.P., Tonks, N.K. & Barford, D. Molecular Basis for the Dephosphorylation of the Activation Segment of the Insulin Receptor by Protein Tyrosine Phosphatase 1B. Molecular Cell 6, 1401-1412 (2000).

356. Salmeen, A. & Barford, D. Functions and mechanisms of redox regulation of cysteine-based phosphatases. Antioxidants & redox signaling 7, 560-577 (2005).

357. Sánchez-Camacho, C. & Bovolenta, P. Autonomous and non-autonomous Shh signalling mediate the in vivo growth and guidance of mouse retinal ganglion cell axons. Development 135, 3531-3541 (2008).

358. Sankarshanan, M., Ma, Z., Iype, T. & Lorenz, U. Identification of a novel lipid raft-targeting motif in Src homology 2-containing phosphatase 1. Journal of immunology (Baltimore, Md. : 1950) 179, 483-490 (2007).

359. Sap, J., D'Eustachio, P., Givol, D. & Schlessinger, J. Cloning and expression of a widely expressed receptor tyrosine phosphatase. Proceedings of the National Academy of Sciences of the United States of America 87, 6112-6116 (1990).

360. Schaapveld, R.Q. et al. Impaired mammary gland development and function in mice lacking LAR receptor-like tyrosine phosphatase activity. Developmental Biology 188, 134-146 (1997).

361. Schindler, C., Levy, D.E. & Decker, T. JAK-STAT signaling: from interferons to cytokines. The Journal of biological chemistry 282, 20059-20063 (2007).

362. Schlessinger, J. Signal transduction by allosteric receptor oligomerization. Trends in Biochemical Sciences 13, 443-447 (1988).

363. Schormair, B. et al. PTPRD (protein tyrosine phosphatase receptor type delta) is associated with restless legs syndrome. Nature Genetics 40, 946-948 (2008).

364. Schultz, J., Milpetz, F., Bork, P. & Ponting, C.P. SMART, a simple modular architecture research tool: identification of signaling domains. Proceedings of the National Academy of Sciences of the United States of America 95, 5857-5864 (1998).

365. Segal, R.A. & Greenberg, M.E. Intracellular signaling pathways activated by neurotrophic factors. Annual Review of Neuroscience 19, 463-489 (1996).

366. Seiradake, E., Harlos, K., Sutton, G., Aricescu, A.R. & Jones, E.Y. An extracellular steric seeding mechanism for Eph-ephrin signaling platform assembly. Nature Structural & Molecular Biology 17, 398-402 (2010).

367. Seiradake, E. et al. Structurally encoded intraclass differences in EphA clusters drive distinct cell responses. Nature Structural & Molecular Biology 20, 958-964 (2013).

368. Selkoe, D.J. Alzheimer's disease is a synaptic failure. Science 298, 789-791 (2002).

369. Serafini, T. et al. Netrin-1 is required for commissural axon guidance in the developing vertebrate nervous system. Cell 87, 1001-1014 (1996).

370. Serafini, T. et al. The netrins define a family of axon outgrowth-promoting proteins homologous to C. elegans UNC-6. Cell 78, 409-424 (1994).

371. Serra-Pagès, C. et al. The LAR transmembrane protein tyrosine phosphatase and a coiled-coil LAR-interacting protein co-localize at focal adhesions. The EMBO Journal 14, 2827-2838 (1995).

372. Serra-Pagès, C., Medley, Q.G., Tang, M., Hart, A. & Streuli, M. Liprins, a family of LAR transmembrane protein-tyrosine phosphatase-interacting proteins. The Journal of biological chemistry 273, 15611-15620 (1998).

373. Seth, P. et al. Expression pattern of the type 1 sigma receptor in the brain and identity of critical anionic amino acid residues in the ligand-binding domain of the receptor. Biochimica et biophysica acta 1540, 59-67 (2001).

374. Shapiro, L. & Scherer, P.E. The crystal structure of a complement-1q family protein suggests an evolutionary link to tumor necrosis factor. Current biology : CB 8, 335-338 (1998).

375. Sharkey, J., Glen, K.A., Wolfe, S. & Kuhar, M.J. Cocaine binding at sigma receptors. European journal of pharmacology 149, 171-174 (1988).

376. Shen, K. & Cowan, C.W. Guidance molecules in synapse formation and plasticity. Cold Spring Harbor Perspectives in Biology 2, a001842 (2010).

377. Shen, K. & Scheiffele, P. Genetics and cell biology of building specific synaptic connectivity. Annual Review of Neuroscience 33, 473-507 (2010).

378. Shen, Y. et al. PTP Is a Receptor for Chondroitin Sulfate Proteoglycan, an Inhibitor of Neural Regeneration. Science 326, 592-596 (2009).

379. Sheng, M., Sabatini, B. & Südhof, T.C. The Synapse, 397 (2012).

380. Shepherd, J.D. & Huganir, R.L. The cell biology of synaptic plasticity: AMPA receptor trafficking. Annual review of cell and developmental biology 23, 613-643 (2007).

381. Shin, D.S. et al. Superoxide Dismutase from the Eukaryotic Thermophile Alvinella pompejana: Structures, Stability, Mechanism, and Insights into Amyotrophic Lateral Sclerosis. Journal of molecular biology 385, 1534-1555 (2009).

382. Shioda, N. et al. Expression of a truncated form of the endoplasmic reticulum chaperone protein, σ1 receptor, promotes mitochondrial energy depletion and apoptosis. Journal of Biological Chemistry 287, 23318-23331 (2012).

383. Shiratsuchi, T., Nishimori, H., Ichise, H., Nakamura, Y. & Tokino, T. Cloning and characterization of BAI2 and BAI3, novel genes homologous to brain-specific angiogenesis inhibitor 1 (BAM). Cytogenetic and Genome Research 79, 103-108 (1997).

384. Sia, G.-M. et al. Interaction of the N-terminal domain of the AMPA receptor GluR4 subunit with the neuronal pentraxin NP1 mediates GluR4 synaptic recruitment. Neuron 55, 87-102 (2007).

385. Siddiqui, T.J. et al. An LRRTM4-HSPG Complex Mediates Excitatory Synapse Development on Dentate Gyrus Granule Cells. Neuron 79, 680-695 (2013).

386. Silver, J. & Miller, J.H. Regeneration beyond the glial scar. Nature Reviews Neuroscience 5, 146-156 (2004).

387. Simon, J.R., Contrera, J.F. & Kuhar, M.J. Binding of [3H] kainic acid, and analogue of Lglutamate, to brain membranes. Journal of Neurochemistry 26, 141-147 (1976).

388. Simons, K. & Ikonen, E. Functional rafts in cell membranes. Nature 387, 569-572 (1997).

389. Simons, K. & Toomre, D. Lipid rafts and signal transduction. Nature Reviews Molecular Cell Biology 1, 31-39 (2000).

390. Singla, N. et al. Crystal structure of the ligand-binding domain of the promiscuous EphA4 receptor reveals two distinct conformations. Biochemical and Biophysical Research Communications 399, 555-559 (2010).

391. Siu, R., Fladd, C. & Rotin, D. N-cadherin is an in vivo substrate for protein tyrosine phosphatase sigma (PTPsigma) and participates in PTPsigma-mediated inhibition of axon growth. Molecular and Cellular Biology 27, 208-219 (2007).

392. Small, D.H. et al. A heparin-binding domain in the amyloid protein precursor of Alzheimer's disease is involved in the regulation of neurite outgrowth. The Journal of neuroscience : the official journal of the Society for Neuroscience 14, 2117-2127 (1994).

393. Smith, F.M. Dissecting the EphA3/Ephrin-A5 Interactions Using a Novel Functional Mutagenesis Screen. Journal of Biological Chemistry 279, 9522-9531 (2004).

394. Sobolevsky, A.I., Rosconi, M.P. & Gouaux, E. X-ray structure, symmetry and mechanism of an AMPA-subtype glutamate receptor. Nature 462, 745-756 (2009).

395. Soding, J., Biegert, A. & Lupas, A.N. The HHpred interactive server for protein homology detection and structure prediction. Nucleic Acids Research 33, W244-W248 (2005).

396. Song, Y.S. & Kim, E. Presynaptic Proteoglycans: Sweet Organizers of Synapse Development. Neuron 79, 609-611 (2013).

397. Sperry, R.W. Chemoaffinity in the orderly growth of nerve fiber patterns and connections. Proceedings of the National Academy of Sciences of the United States of America 50, 703-710 (1963).

398. Stein, E. et al. Eph receptors discriminate specific ligand oligomers to determine alternative signaling complexes, attachment, and assembly responses. Genes & Development 12, 667-678 (1998).

399. Stephan, A.H. et al. A Dramatic Increase of C1q Protein in the CNS during Normal Aging. The Journal of neuroscience : the official journal of the Society for Neuroscience 33, 13460-13474 (2013).

400. Stevens, B. et al. The Classical Complement Cascade Mediates CNS Synapse Elimination. Cell 131, 1164-1178 (2007).

401. Stoker, A.W. Isoforms of a novel cell adhesion molecule-like protein tyrosine phosphatase are implicated in neural development. Mechanisms of development 46, 201-217 (1994).

402. Stoker, A.W. Receptor tyrosine phosphatases in axon growth and guidance. Current Opinion in Neurobiology 11, 95-102 (2001).

403. Stoker, A.W. Protein tyrosine phosphatases and signalling. Journal of Endocrinology 185, 19-33 (2005).

404. Stoker, A.W., Gehrig, B., Haj, F. & Bay, B.H. Axonal localisation of the CAM-like tyrosine phosphatase CRYP alpha: a signalling molecule of embryonic growth cones. Development 121, 1833-1844 (1995).

405. Streuli, M. et al. Expression of the receptor-linked protein tyrosine phosphatase LAR: proteolytic cleavage and shedding of the CAM-like extracellular region. The EMBO Journal 11, 897-907 (1992).

406. Su, T.-P., Hayashi, T., Maurice, T., Buch, S. & Ruoho, A.E. The sigma-1 receptor chaperone as an inter-organelle signaling modulator. Trends in Pharmacological Sciences, 1-10 (2010).

407. Su, T.P., Hayashi, T. & Vaupel, D.B. When the Endogenous Hallucinogenic Trace Amine N,N-Dimethyltryptamine Meets the Sigma-1 Receptor. Science Signaling 2, pe12-pe12 (2009).

408. Su, T.P., London, E.D. & Jaffe, J.H. Steroid binding at sigma receptors suggests a link between endocrine, nervous, and immune systems. Science 240, 219-221 (1988).

409. Südhof, T.C. Neuroligins and neurexins link synaptic function to cognitive disease. Nature 455, 903-911 (2008).

410. Sumioka, A. Auxiliary subunits provide new insights into regulation of AMPA receptor trafficking. Journal of Biochemistry 153, 331-337 (2013).

411. Sun, H. & Tonks, N.K. The coordinated action of protein tyrosine phosphatases and kinases in cell signaling. Trends in Biochemical Sciences 19, 480-485 (1994).

412. Tabiti, K. et al. Novel alternative splicing predicts a secreted extracellular isoform of the human receptor-like protein tyrosine phosphatase LAR. Gene 175, 7-13 (1996).

413. Takahashi, H. et al. Postsynaptic TrkC and Presynaptic PTPσ Function as a Bidirectional Excitatory Synaptic Organizing Complex. Neuron 69, 287-303 (2011).

414. Takahashi, H. et al. Selective control of inhibitory synapse development by Slitrk3-PTPδ trans-synaptic interaction. Nature Neuroscience 15, 389-98- S1-2 (2012).

415. Takasu, M.A. Modulation of NMDA Receptor- Dependent Calcium Influx and Gene Expression Through EphB Receptors. Science 295, 491-495 (2002).

416. Takeda, A., Matsuda, A., Paul, R.M.J. & Yaseen, N.R. CD45-associated protein inhibits CD45 dimerization and up-regulates its protein tyrosine phosphatase activity. Blood 103, 3440-3447 (2004).

417. ten Hoeve, J. et al. Identification of a nuclear Stat1 protein tyrosine phosphatase. Molecular and Cellular Biology 22, 5662-5668 (2002).

418. Thanos, C.D. Oligomeric Structure of the Human EphB2 Receptor SAM Domain. Science 283, 833-836 (1999).

419. Thoenen, H. Neurotrophins and neuronal plasticity. Science 270, 593-598 (1995).

420. Thoenen, H. & Barde, Y.A. Physiology of nerve growth factor. Physiological reviews (1980).

421. Toni, N., Buchs, P.A., Nikonenko, I., Bron, C.R. & Muller, D. LTP promotes formation of multiple spine synapses between a single axon terminal and a dendrite. Nature 402, 421-425 (1999).

422. Tonks, N.K. PTP1B: from the sidelines to the front lines! FEBS letters 546, 140-148 (2003).

423. Tonks, N.K. Redox redux: revisiting PTPs and the control of cell signaling. Cell 121, 667-670 (2005).

424. Tonks, N.K. Protein tyrosine phosphatases: from genes, to function, to disease. Nature Reviews Molecular Cell Biology 7, 833-846 (2006).

425. Tonks, N.K., Diltz, C.D. & Fischer, E.H. Characterization of the major protein-tyrosine-phosphatases of human placenta. The Journal of biological chemistry 263, 6731-6737 (1988).

426. Tonks, N.K., Diltz, C.D. & Fischer, E.H. Purification of the major protein-tyrosine-phosphatases of human placenta. The Journal of biological chemistry 263, 6722-6730 (1988).

427. Tran, T.S., Kolodkin, A.L. & Bharadwaj, R. Semaphorin regulation of cellular morphology. Annual review of cell and developmental biology 23, 263-292 (2007).

428. Traynelis, S.F. et al. Glutamate Receptor Ion Channels: Structure, Regulation, and Function. Pharmacological Reviews 62, 405-496 (2010).

429. Trousse, F., Martí, E., Gruss, P., Torres, M. & Bovolenta, P. Control of retinal ganglion cell axon growth: a new role for Sonic hedgehog. Development 128, 3927-3936 (2001).

430. Tu, X. & Palczewski, K. Crystal structure of the globular domain of C1QTNF5: Implications for late-onset retinal macular degeneration. JOURNAL OF STRUCTURAL BIOLOGY 180, 439-446 (2012).

431. Uemura, T. et al. Trans-synaptic interaction of GluRdelta2 and Neurexin through Cbln1 mediates synapse formation in the cerebellum. Cell 141, 1068-1079 (2010).

432. Uetani, N. et al. Impaired learning with enhanced hippocampal long-term potentiation in PTPdelta-deficient mice. The EMBO Journal 19, 2775-2785 (2000).

433. Um, J.W. & Ko, J. LAR-RPTPs: synaptic adhesion molecules that shape synapse development. Trends in Cell Biology 23, 465-475 (2013).

434. Ushiro, H. & Cohen, S. Identification of phosphotyrosine as a product of epidermal growth factor-activated protein kinase in A-431 cell membranes. The Journal of biological chemistry 255, 8363-8365 (1980).

435. van Montfort, R.L.M., Congreve, M., Tisi, D., Carr, R. & Jhoti, H. Oxidation state of the active-site cysteine in protein tyrosine phosphatase 1B. Nature 423, 773-777 (2003).

436. Van Vactor, D., Wall, D.P. & Johnson, K.G. Heparan sulfate proteoglycans and the emergence of neuronal connectivity. Current Opinion in Neurobiology 16, 40-51 (2006).

437. Vance, J.E. Phospholipid synthesis in a membrane fraction associated with mitochondria. The Journal of biological chemistry 265, 7248-7256 (1990).

438. Veerhuis, R., Nielsen, H.M. & Tenner, A.J. Complement in the brain. Molecular Immunology 48, 1592-1603 (2011).

439. Vicario-Abejón, C., Owens, D., McKay, R. & Segal, M. Role of neurotrophins in central synapse formation and stabilization. Nature Reviews Neuroscience 3, 965-974 (2002).

440. Vincent, A., Bien, C.G., Irani, S.R. & Waters, P. Autoantibodies associated with diseases of the CNS: new developments and future challenges. Lancet neurology 10, 759-772 (2011).

441. Wadsworth, W.G., Bhatt, H. & Hedgecock, E.M. Neuroglia and pioneer neurons express UNC-6 to provide global and local netrin cues for guiding migrations in C. elegans. Neuron 16, 35-46 (1996).

442. Walicke, P.A. Interactions between basic fibroblast growth factor (FGF) and glycosoaminoglycans in promoting neurite outgrowth. Experimental Neurology 102, 144-148 (1988).

443. Wallace, M.J. et al. Neuronal defects and posterior pituitary hypoplasia in mice lacking the receptor tyrosine phosphatase PTPsigma. Nature Genetics 21, 334-338 (1999).

444. Walter, L. & Hajnoczky, G. Mitochondria and endoplasmic reticulum: the lethal interorganelle cross-talk. Journal of bioenergetics and biomembranes 37, 191-206 (2005).

445. Walter, T.S. et al. A procedure for setting up high-throughput nanolitre crystallization experiments. Crystallization workflow for initial screening, automated storage, imaging and optimization. Acta Cryst (2005). D61, 651-657 [doi:10.1107/S0907444905007808], 1-7 (2005).

446. Walter, T.S. et al. Lysine Methylation as a Routine Rescue Strategy for Protein Crystallization. Structure 14, 1617-1622 (2006).

447. Wang, J. & Bixby, J.L. Receptor tyrosine phosphatase-delta is a homophilic, neurite-promoting cell adhesion molecular for CNS neurons. Molecular and Cellular Neuroscience 14, 370-384 (1999).

448. Wehrman, T. et al. Structural and mechanistic insights into nerve growth factor interactions with the TrkA and p75 receptors. Neuron 53, 25-38 (2007).

449. Weiskopf, K. et al. Engineered SIRPα variants as immunotherapeutic adjuvants to anticancer antibodies. Science 341, 88-91 (2013).

450. Weiss, A. & Schlessinger, J. Switching signals on or off by receptor dimerization. Cell 94, 277-280 (1998).

451. Weissman, A.D., Su, T.P., Hedreen, J.C. & London, E.D. Sigma receptors in post-mortem human brains. The Journal of pharmacology and experimental therapeutics 247, 29-33 (1988).

452. Wiesmann, C., Ultsch, M.H., Bass, S.H. & de Vos, A.M. Crystal structure of nerve growth factor in complex with the ligand-binding domain of the TrkA receptor. Nature 401, 184-188 (1999).

453. Wilkinson, D.G. Multiple roles of EPH receptors and ephrins in neural development. Nature Reviews Neuroscience 2, 155-164 (2001).

454. Williamson, T.G., Nurcombe, V., Beyreuther, K., Masters, C.L. & Small, D.H. Affinity purification of proteoglycans that bind to the amyloid protein precursor of Alzheimer's disease. Journal of Neurochemistry 65, 2201-2208 (1995).

455. Wimmer-Kleikamp, S.H. Recruitment of Eph receptors into signaling clusters does not require ephrin contact. The Journal of Cell Biology 164, 661-666 (2004).

456. Winter, G. xia2: an expert system for macromolecular crystallography data reduction. J. Appl. Cryst (2010). 43, 186-190 [doi:10.1107/S0021889809045701], 1-5 (2009).

457. Woo, J., Kwon, S.-K. & Kim, E. The NGL family of leucine-rich repeat-containing synaptic adhesion molecules. Molecular and Cellular Neuroscience 42, 1-10 (2009).

458. Wyszynski, M. et al. Interaction between GRIP and liprin-alpha/SYD2 is required for AMPA receptor targeting. Neuron 34, 39-52 (2002).

459. Xu, N.-J. & Henkemeyer, M. Ephrin reverse signaling in axon guidance and synaptogenesis. Seminars in Cell & Developmental Biology 23, 58-64 (2012).

460. Yamaguchi, Y. & Pasquale, E.B. Eph receptors in the adult brain. Current Opinion in Neurobiology 14, 288-296 (2004).

461. Yamamoto, H. et al. Amino acid residues in the transmembrane domain of the type 1 sigma receptor critical for ligand binding. FEBS letters 445, 19-22 (1999).

462. Yan, D. & Tomita, S. Defined criteria for auxiliary subunits of glutamate receptors. The Journal of Physiology, no-no (2011).

463. Yan, H. et al. A novel receptor tyrosine phosphatase-sigma that is highly expressed in the nervous system. The Journal of biological chemistry 268, 24880-24886 (1993).

464. Yang, T. et al. Leukocyte antigen-related protein tyrosine phosphatase receptor: a small ectodomain isoform functions as a homophilic ligand and promotes neurite outgrowth. The

Journal of neuroscience : the official journal of the Society for Neuroscience 23, 3353-3363 (2003).

465. Yang, T., Yin, W., Derevyanny, V.D., Moore, L.A. & Longo, F.M. Identification of an ectodomain within the LAR protein tyrosine phosphatase receptor that binds homophilically and activates signalling pathways promoting neurite outgrowth. The European journal of neuroscience 22, 2159-2170 (2005).

466. Yang, Z.R., Thomson, R., McNeil, P. & Esnouf, R.M. RONN: the bio-basis function neural network technique applied to the detection of natively disordered regions in proteins. Bioinformatics 21, 3369-3376 (2005).

467. Yao, V.J. et al. Targeting pancreatic islets with phage display assisted by laser pressure catapult microdissection. The American journal of pathology 166, 625-636 (2005).

468. Yazdani, U. & Terman, J.R. The semaphorins. Genome biology 7, 211 (2006).

469. Yeo, G.S.H. et al. A de novo mutation affecting human TrkB associated with severe obesity and developmental delay. Nature Neuroscience 7, 1187-1189 (2004).

470. Yeo, T.T. et al. Deficient LAR expression decreases basal forebrain cholinergic neuronal size and hippocampal cholinergic innervation. Journal of neuroscience research 47, 348-360 (1997).

471. Yim, Y.S. et al. Slitrks control excitatory and inhibitory synapse formation with LAR receptor protein tyrosine phosphatases. Proceedings of the National Academy of Sciences 110, 4057-4062 (2013).

472. Yona, S., Lin, H.-H., Siu, W.O., Gordon, S. & Stacey, M. Adhesion-GPCRs: emerging roles for novel receptors. Trends in Biochemical Sciences 33, 491-500 (2008).

473. Yoshikawa, S., McKinnon, R.D., Kokel, M. & Thomas, J.B. Wnt-mediated axon guidance via the Drosophila Derailed receptor. Nature 422, 583-588 (2003).

474. Yudushkin, I.A. et al. Live-cell imaging of enzyme-substrate interaction reveals spatial regulation of PTP1B. Science 315, 115-119 (2007).

475. Yuzaki, M. Cbln and C1q family proteins: new transneuronal cytokines. Cellular and Molecular Life Sciences 65, 1698-1705 (2008).

476. Zhang, J.S. & Longo, F.M. LAR tyrosine phosphatase receptor: alternative splicing is preferential to the nervous system, coordinated with cell growth and generates novel isoforms containing extensive CAG repeats. The Journal of Cell Biology 128, 415-431 (1995).

477. Zhang, X., Gureasko, J., Shen, K., Cole, P.A. & Kuriyan, J. An allosteric mechanism for activation of the kinase domain of epidermal growth factor receptor. Cell 125, 1137-1149 (2006).

478. Zhang, Z.-Y., Wang, Y. & Dixon, J.E. Dissecting the catalytic mechanism of protein-tyrosine phosphatases. Proceedings of the National Academy of Sciences of the United States of America 91, 1624-1627 (1994).

479. Zhao, C. et al. Bidirectional ephrinB2-EphB4 signaling controls bone homeostasis. Cell metabolism 4, 111-121 (2006).

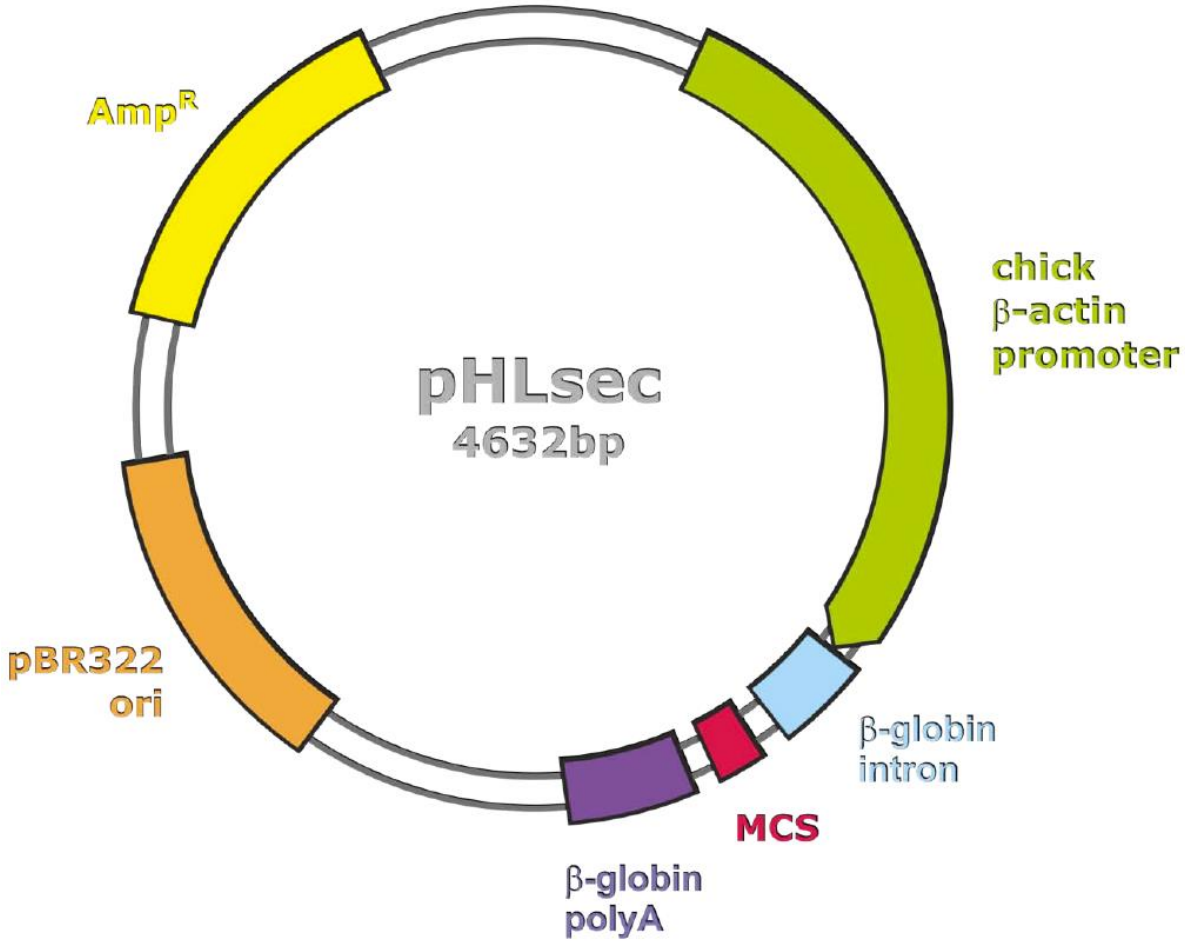
480. Zhou, R. The Eph family receptors and ligands. Pharmacology and Therapeutics 77, 151-181 (1998).

481. Zhou, Y., Gunput, R.-A.F. & Pasterkamp, R.J. Semaphorin signaling: progress made and promises ahead. Trends in Biochemical Sciences 33, 161-170 (2008).

482. Zimmer, M., Palmer, A., Köhler, J. & Klein, R. EphB-ephrinB bi-directional endocytosis terminates adhesion allowing contact mediated repulsion. Nature cell biology 5, 869-878 (2003).

483. Zuber, B., Nikonenko, I., Klauser, P., Muller, D. & Dubochet, J. The mammalian central nervous synaptic cleft contains a high density of periodically organized complexes. Proceedings of the National Academy of Sciences of the United States of America 102, 19192-19197 (2005).

Appendix A -
Expression Vectors



Key features of pHLSec vector backbone. Figure provided by Dr. Radu Aricescu. Multiple Cloning sites for pHLSec and subsequent vector variations used are provided below, and are based on Aricescu, A. R., Lu, W. & Jones, E. Y. A time- and cost-efficient system for high-level protein production in mammalian cells. *Acta Crystallogr D Biol Crystallogr* **62,** 1243–1250 (2006).

Multiple Cloning Sites (MCS) for different vector variations

pHLSec:

EcoRI-HindIII-Kozak-Secretion signal sequence-AgeI-*insert*-KpnI-6xHis-STOPcodon-STOPcodon-STOPcodon-XhoI

GAATTCAAGCTTGCCACCATGGGGATCCTTCCCAGCCCTGGGATGCCTGCGCTGCTCTCCCTCGTG
AGCCTTCTCTCCGTGCTGCTGATGGGTTGCGTAGCTGAA**ACCGGT***insert*ggtaccAAGCACCAC
CATCACCATCACTAATGATCActcgag

pHLAvitag3:

EcoRI-HindIII-Kozak-Secretion signal sequence-AgeI-*insert*-KpnI-GGS linker-**BirA recognition site**-6xHis-STOPcodon-STOPcodon-STOPcodon-XhoI

GAATTCAAGCTTGCCACCATGGGGATCCTTCCCAGCCCTGGGATGCCTGCGCTGCTCTCCCTCGTG
AGCCTTCTCTCCGTGCTGCTGATGGGTTGCGTAGCTGAA**ACCGGT***insert*ggtaccGGAGGTTCC
GGTGGTTCC**GGTCTGAATGATATCTTTGAAGCTCAGAAGATTGAATGGCATGAA**GGACGTACCAAG
CACCACCATCACCATCAC**TAATGATCA**ctcgag

pHLSec-mVenus:

EcoRI-HindIII-Kozak-Secretion signal sequence-AgeI-*insert*-KpnI-**3C protease recognition site**-**monoVenus**-8xHis-STOPcodon-STOPcodon-STOPcodon-XhoI

GAATTCAAGCTTGCCACCATGGGGATCCTTCCCAGCCCTGGGATGCCTGCGCTGCTCTCCCTCGTG
AGCCTTCTCTCCGTGCTGCTGATGGGTTGCGTAGCTGAA**ACCGGT***insert*ggtacc**CTGGAGGTG**
CTGTTCCAGGGCCCCGGAATGGTGAGCAAGGGCGAGGAGCTGTTCACCGGGGTGGTGCCCATCCTG
GTCGAGCTGGACGGCGACGTAAACGGCCACAAGTTCAGCGTGTCCGGCGAGGGCGAGGGCGATGCC
ACCTACGGCAAGCTGACCCTGAAGCTGATCTGCACCACCGGCAAGCTGCCCGTGCCCTGGCCCACC
CTCGTGACCACCCTGGGCTACGGCCTGCAGTGCTTCGCCCGCTACCCCGACCACATGAAGCAGCAC
GACTTCTTCAAGTCCGCCATGCCCGAAGGCTACGTCCAGGAGCGCACCATCTTCTTCAAGGACGAC
GGCAACTACAAGACCCGCGCCGAGGTGAAGTTCGAGGGCGACACCCTGGTGAACCGCATCGAGCTG
AAGGGCATCGACTTCAAGGAGGACGGCAACATCCTGGGGCACAAGCTGGAGTACAACTACAACAGC
CACAACGTCTATATCACCGCCGACAAGCAGAAGAACGGCATCAAGGCCAACTTCAAGATCCGCCAC
AACATCGAGGACGGCGGCGTGCAGCTCGCCGACCACTACCAGCAGAACACCCCCATCGGCGACGGC
CCCGTGCTGCTGCCCGACAACCACTACCTGAGCTACCAGTCCAAGCTGAGCAAAGACCCCAACGAG
AAGCGCGATCACATGGTCCTGCTGGAGTTCGTGACCGCCGCCGGGATCACTCTCGGCATGGACGAG
CTGTACAAGCACCACCATCACCATCACCATCAT**TAATGA**ctcgag

pHLSec-1D4:

EcoRI-HindIII-Kozak-Secretion signal sequence-AgeI-*insert*-KpnI-ID4 Ab recognition site-STOPcodon-STOPcodon-XhoI

GAATTCAAGCTTGCCACCATGGGGATCCTTCCCAGCCCTGGGATGCCTGCGCTGCTCTCCCTCGTG
AGCCTTCTCTCCGTGCTGCTGATGGGTTGCGTAGCTGAA**ACCGGT***insert*ggtaccGAGACCAGCC
AGGTGGCCCCTGCA**TAATGA**ctcgag

pHLSec-1D4-Avitag3:

EcoRI-HindIII-Kozak-Secretion signal sequence-**AgeI**-*insert*-KpnI-GGS linker-**BirA recognition site**-ID4 Ab recognition site-STOPcodon-STOPcodon-XhoI

GAATTCAAGCTTGCCACCATGGGGATCCTTCCCAGCCCTGGGATGCCTGCGCTGCTCTCCCTCGTG AGCCTTCTCTCCGTGCTGCTGATGGGTTGCGTAGCTGAA**ACCGGT***insert*ggtaccGGAGGTTCC GGTGGTTCC**GGTCTGAATGATATCTTTGAAGCTCAGAAGATTGAATGGCATGAA**GGACGTACCAAG GAGACCAGCCAGGTGGCCCCTGCATAATGActcgag

pHLSec-SBP-1D4:

EcoRI-HindIII-Kozak-Secretion signal sequence-SBP-linker-TEV recognition site-**AgeI**-*insert*-KpnI-ID4 Ab recognition site-STOPcodon-STOPcodon-XhoI

GAATTCAAGCTTGCCACCATGGGGATCCTTCCCAGCCCTGGGATGCCTGCGCTGCTCTCCCTCGTG AGCCTTCTCTCCGTGCTGCTGATGGGTTGCGTAGCTGAGATGGACGAGAAAACCACCGGCTGGAGA GGAGGCCACGTCGTCGAAGGACTGGCCGGCGAGCTGGAACAGCTGCGGGCCAGACTGGAACACCAC CCCCAGGGCCAGAGAGAGCCCGACTACGACATCCCCACCACCGAGAACCTGTATTTTCAGGGC**ACC GGT***insert*ggtaccGAGACCAGCCAGGTGGCCCCTGCATAATGActcgag

Appendix B - Constructs

Construct Name	Uniprot Accession Number of Parent Protein and Construct Amino Acid Boundaries	Primers (5' -> 3')	Cloning Strategy	Destination Vector
Human EphA4	P54764: 20-547	Clone provided by Dr. Elena Seriadake		pHLsec
Human EphrinA5	P52803: 27-166	Clone provided by Dr. Elena Seriadake		pHLsec
Human Sigma-1 receptor::pHL-1D4	Q99720: 1-223	Fwd: taatgaattcGCCACCATGCAGT GGGCCGTGGGCC Rev: cgcggtaccAGGGTCCTGGCCAA AGAGGTAGGT	PCR product digested with EcoRI and KpnI. Destination vector digested with EcoRI and KpnI.	pHLSec-1D4
Human Sigma-1 receptor::pHL-SBP-1D4	Q99720: 1-223	Fwd: taatgaattcGCCACCATGCAGT GGGCCGTGGGCC Rev: cgcggtaccAGGGTCCTGGCCAA AGAGGTAGGT	PCR product digested with EcoRI and KpnI. Destination vector digested with EcoRI and KpnI.	pHLSec-SBP-1D4
Human Sigma-1 receptor::pHL-mVenus	Q99720: 1-223	Fwd: taatgaattcGCCACCATGCAGT GGGCCGTGGGCC Rev: cgcggtaccAGGGTCCTGGCCAA AGAGGTAGGT	PCR product digested with EcoRI and KpnI. Destination vector digested with EcoRI and KpnI.	pHLSec-mVenus
Chicken RPTPσ-(Ig1-Ig2-Ig3)	Genbank NM_205407.1: 30-334	Clone provided by Dr. Charlotte Coles		pHLSec, pHLAvitag3

Human RPTPσ-(Ig1-Ig2-Ig3)	Q13332: 30-334	Clone provided by Dr. Charlotte Coles		pHLSec, pHLAvitag3
Human RPTPσ-(dFN3)	Q13332: 30-614	Clone provided by Dr. Charlotte Coles		pHLAvitag3
Human RPTPσ-(ecto)	Q13332: 30-1117	Clone provided by Dr. Charlotte Coles		pHLSec, pHLAvitag3
Human RPTPσ-(full-length)	Q13332: 30-1948	Fwd1: cgcaccggtTACCCCTACGACGTGCCCGACTACGCCGGGTCCGAAGAGCCCCCCAGGTTTATCAAAGAAC Rev1: cgcggtaccGGGAGCTTTGGGGAGAGATTTCACCGT Fwd2: cgcggtaccCCCATGGTGACTGAGAACACAGCCA Rev2: tgtcgtcgacTCATTAGGTTGCATAGTGGTCAAAGCTTCCGAG	Joining PCR was carried out in two PCR stages. First stage involved individual fragment amplification with Fwd1/Rev1 and Fwd2/Rev2. Joining PCR took place with primers Fwd1/Rev2. Joining PCR product digested with AgeI and XhoI. Destination vector digested with AgeI and SalI.	pHLSec

Human RPTPσ-(Ig1-Ig2-Ig3-R96A, R99A)	Q13332: 30-334 with R96A, R99A substitutions	Clone provided by Dr. Charlotte Coles		pHLSec, pHLAvitag3
Human RPTPσ-(full-length-R96A, R99A)	Q13332: 30-1948 with R96A, R99A substitutions	Fwd: cgcaccggtTACCCCTACGACGTGCC CGACTACGCCGGGTCCGAAGAGCC CCCCAGGTTTATCAAAGAAC Rev: cgcggtaccGGGAGCTTTGGGGAGA GATTTCACCGT	PCR with Fwd/Rev with human RPTPσ-(Ig1-Ig2-Ig3-R96A, R99A) as a template. PCR product digested with AgeI and KpnI. Destination vector containing Human RPTPσ-(full-length) clone digested with AgeI and SalI.	pHlSec
Human RPTPσ-(Ig1-Ig2-Ig3-Y223S)	Q13332: 30-334 with Y223S substitution	Clone provided by Dr. Charlotte Coles		pHLSec, pHLAvitag3
Human RPTPσ-(full-length-Y223S)	Q13332: 30-1948 with Y223S substitution	Fwd: cgcaccggtTACCCCTACGACGTGCC CGACTACGCCGGGTCCGAAGAGCC CCCCAGGTTTATCAAAGAAC Rev: cgcggtaccGGGAGCTTTGGGGAGA GATTTCACCGT	PCR with Fwd/Rev with human RPTPσ-(Ig1-Ig2-Ig3-Y223S) as a template. PCR product digested with AgeI and KpnI. Destination vector containing Human RPTPσ-(full-length) clone digested with AgeI and SalI.	pHLSec
Human RPTPσ-(Ig1-Ig2-Ig3-R241A, R242A)	Q13332: 30-334 with R241A, R242A substitutions	Clone provided by Dr. Charlotte Coles		pHLSec, pHLAvitag3
Human RPTPσ-(full-length-R241A, R242A)	Q13332: 30-1948 with R241A, R242A substitutions	Fwd: cgcaccggtTACCCCTACGACGTGCC CGACTACGCCGGGTCCGAAGAGCC CCCCAGGTTTATCAAAGAAC Rev: cgcggtaccGGGAGCTTTGGGGAGA GATTTCACCGT	PCR with Fwd/Rev with human RPTPσ-(Ig1-Ig2-Ig3-R241A, R242A) as a template. PCR product digested with AgeI and KpnI. Destination vector containing Human RPTPσ-(full-length) clone digested with AgeI and SalI.	pHLSec

Human RPTPσ-(Ig1-Ig2-Ig3-K68A, K69A, K71A, K72A)	Q13332: 30-334 with K68A, K69A, K71A, K72A substitutions	Clone provided by Dr. Charlotte Coles		pHLSec, pHLAvitag3
Human RPTPσ-(full-length-K68A, K69A, K71A, K72A)	Q13332: 30-1948 with K68A, K69A, K71A, K72A substitutions	Fwd: cgcaccggtTACCCCTACGACGTGCCCGACTACGCCGGGTCCGAAGAGCCCCCCAGGTTTATCAAAGAAC Rev: cgcggtaccGGGAGCTTTGGGGAGAGATTTCACCGT	PCR with Fwd/Rev with human RPTPσ-(Ig1-Ig2-Ig3-K68A, K69A, K71A, K72A) as a template. PCR product digested with AgeI and KpnI. Destination vector containing Human RPTPσ-(full-length) clone digested with AgeI and SalI.	pHLSec
Chicken TrkC-(LRR-Ig1)	Q91044: 31-302	Clone provided by Dr. Charlotte Coles		pHLAvitag3
Mouse TrkC-(LRR-Ig1)	Q6VNS1: 31-302	Clone provided by Dr. Charlotte Coles		pHLSec, pHLAvitag3
Mouse TrkC-(LRR-Ig1-D224A, D226A)	Q6VNS1: 31-302 with D224A, D226A substitutions	Clone provided by Dr. Charlotte Coles		pHLSec, pHLAvitag3
Mouse TrkC-(LRR-Ig1-N68Q, N72Q)	Q6VNS1: 31-302 with N68Q, N72Q substitutions	Clone provided by Dr. Charlotte Coles		pHLSec, pHLAvitag3
Mouse C1ql3-c1q	Q9ESN4: 117-255	Fwd: cgcaccggtAGTGCAGCCACCTATAGCACGGTG REV: gcggtaccGTCAGCATAAATAATAAATCCAGAGAATGTGCTGTA	PCR product digested with AgeI and KpnI. Destination vector digested with AgeI and KpnI.	pHLSec, pHLAvitag3

Mouse C1ql1-c1q	O88992: 125-258	Fwd: cgcaccggtACCAC**A**GTGCCACG**A**GT GGC**A**TTC Rev: gcggtaccATCCGAGTAGATGATGA AGCCAGAGAAAG	PCR product digested with AgeI and KpnI. Destination vector digested with AgeI and KpnI.	pHLSec, pHLAvitag3
Mouse C1ql1-c1q-(D210A, Q211A)	O88992: 129-258 with D210A, Q211A substitutions	Fwd1: cgcaccggtCGAGTGGCATTCTACGC TGGCCTCAAG Rev1: AGTCGTAGTTTGCTGCTGCATCCTG GGCAATTGCACTTGCTCGTACCTG G Fwd2: CCAGGATGCA**GCAGCA**AACTACGA CTATGCCAGCAACAGCGTGATCCT GC Rev2: gcggtaccATCCGAGTAGATGATGA AGCCAGAGAAAG	Joining PCR was carried out in two PCR stages. First stage involved individual fragment amplification with Fwd1/Rev1 and Fwd2/Rev2. Joining PCR took place with primers Fwd1/Rev2. Joining PCR product digested with AgeI and kpnI. Destination vector digested with AgeI and KpnI.	pHLAvitag3
Mouse C1ql1-c1q-(Q211N, N212S, Y213T)	O88992: 129-258 with Q211N, N212S, Y213T substitutions	Fwd1: cgcaccggtCGAGTGGCATTCTACGC TGGCCTCAAG Rev1: GGCATAGTCAGTTGAGTTGTCTGC ATCCTGTGCAATTGCACTTGCTCGC A Fwd2: GGATGCAGACAACTCAACTGACTA TGCCAGCAACAGCGTGATCCTGCA TC Rev2: gcggtaccATCCGAGTAGATGATGA AGCCAGAGAAAG	Joining PCR was carried out in two PCR stages. First stage involved individual fragment amplification with Fwd1/Rev1 and Fwd2/Rev2. Joining PCR took place with primers Fwd1/Rev2. Joining PCR product digested with AgeI and kpnI. Destination vector digested with AgeI and KpnI.	pHLAvitag3

Mouse C1ql1-c1q-(Q211N, N212S, Y213T, S244N, K246S)	O88992: 129-258 with Q211N, N212S, Y213T, S244N, K246S substitutions	Fwd1: cgcaccggtCGAGTGGCATTCTACGCTGGCCTCAAG Rev1: AGTGCTGTATGAGTTGTTGTTGCCCCCGTGTGCTTTGCCTCCATCCAGCT Fwd2: GGGGGCAACAACAACTCATACAGCACTTTCTCTGGCTTCATCATCTACTC Rev2: gcggtaccATCCGAGTAGATGATGAAGCCAGAGAAAG	Joining PCR was carried out in two PCR stages. First stage involved individual fragment amplification with Fwd1/Rev1 and Fwd2/Rev2. Joining PCR took place with primers Fwd1/Rev2. Joining PCR product digested with AgeI and kpnI. Destination vector digested with AgeI and KpnI.	pHLAvitag3
Mouse C1ql1-c1q-(T121N)	O88992: 120-258 with T121N substitutions	Fwd: cgcaccggtAGCAACGCCACCTATACCACGGTG Rev: gcggtaccATCCGAGTAGATGATGAAGCCAGAGAAAG	PCR product digested with AgeI and KpnI. Destination vector digested with AgeI and KpnI.	pHLAvitag3
Mouse C1ql1-full-length	O88992: 1-258	Fwd: cgcgaattcGCCACCATGCTGCTCGTGCTGGTGGTGCT Rev: gcggtaccATCCGAGTAGATGATGAAGCCAGAGAAAG	PCR product digested with EcoRI and KpnI. Destination vector digested with EcoRI and KpnI.	pHL-1D4-Avitag3

Mouse C1ql1-full-length-(Q211N, N212S, Y213T, S244N, K246S)	O88992: 1-258 with Q211N, N212S, Y213T, S244N, K246S substitutions	Fwd: cgcgaattcGCCACCATGCTGCTCGTGCTGGTGGTGCT Rev1: AGTGCTGTATGAGTTGTTGTTGCCCCCGTGTGCTTTGCCTCCATCCAGCT Fwd2: GGGGGCAACAACAACTCATACAGCACTTTCTCTGGCTTCATCATCTACTC Rev2: gcggtaccATCCGAGTAGATGATGAAGCCAGAGAAAG	Joining PCR was carried out in two PCR stages. First stage involved individual fragment amplification with Fwd1/Rev1 and Fwd2/Rev2. Joining PCR took place with primers Fwd1/Rev2. Joining PCR product digested with AgeI and kpnI. Destination vector digested with AgeI and KpnI.	pHLAvitag3
Mouse BAI3-FE	O80ZF8: 1-868	Fwd: cgcgaattcGCCACCATGAAGGCTGTTCGTAACCTGCTGATTTATATAT Rev: gcggtaccTTCTCTAGGTTGCTGAGCCAAAATGGCG	PCR product digested with EcoRI and KpnI. Destination vector digested with EcoRI and KpnI.	pHLSec, pHLAvitag3
Mouse BAI3-CUB.4TSR	O80ZF8: 1-510	Fwd: cgcgaattcGCCACCATGAAGGCTGTTCGTAACCTGCTGATTTATATAT Rev: gcggtaccAGGTGCTGGGCACCGCTGCT	PCR product digested with EcoRI and KpnI. Destination vector digested with EcoRI and KpnI.	pHLSec, pHLAvitag3
Mouse BAI3-CUB	O80ZF8: 1-162	Fwd: cgcgaattcGCCACCATGAAGGCTGTTCGTAACCTGCTGATTTATATAT Rev: gcggtaccGCTCACCTTGTTCAGTACCAAAAACTCAAAAAAAG	PCR product digested with EcoRI and KpnI. Destination vector digested with EcoRI and KpnI.	pHLSec, pHLAvitag3

Mouse BAI3-4TSR	O80ZF8: 287-510	Fwd: cgcaccggtGCACAAACTGGTGAATCTGGTGTGGAA Rev: gcgggtaccAGGTGCTGGGCACCGCTGCT	PCR product digested with AgeI and KpnI. Destination vector digested with AgeI and KpnI.	pHLSec, pHLAvitag3
Mouse BAI3-eCUB	O80ZF8: 1-291	Fwd: cgcgaattcGCCACCATGAAGGCTGTTCGTAACCTGCTGATTTATATAT Rev: gcgggtaccTTCACCAGTTTGTGCCATAAATTTAGCAGCATC	PCR product digested with EcoRI and KpnI. Destination vector digested with EcoRI and KpnI.	pHLSec, pHLAvitag3
Mouse BAI3-eCUB231	O80ZF8: 1-231	Fwd: cgcgaattcGCCACCATGAAGGCTGTTCGTAACCTGCTGATTTATATAT Rev: gcgggtaccAGTCAGGCAACCCTCTGTCTGCTC	PCR product digested with EcoRI and KpnI. Destination vector digested with EcoRI and KpnI.	pHLSec, pHLAvitag3
Mouse BAI3-eCUB242	O80ZF8: 1-242	Fwd: cgcgaattcGCCACCATGAAGGCTGTTCGTAACCTGCTGATTTATATAT Rev: gcgggtaccCAGATTGCAGACTTGAGTAGTTTGCAGC	PCR product digested with EcoRI and KpnI. Destination vector digested with EcoRI and KpnI.	pHLSec, pHLAvitag3
Mouse BAI3-eCUB248	O80ZF8: 1-248	Fwd: cgcgaattcGCCACCATGAAGGCTGTTCGTAACCTGCTGATTTATATAT Rev: gcgggtaccTCTCTTGGCCTCCCTGGTCAGATTG	PCR product digested with EcoRI and KpnI. Destination vector digested with EcoRI and KpnI.	pHLSec, pHLAvitag3

Mouse BAI3-eCUB270	O80ZF8: 1-270	Fwd: cgcgaattcGCCACCATGAAGGCTGTTCGTAACCTGCTGATTTATATAT Rev: gcggtaccGACAGATCGAGGTCGCTGACTTTTAATTG	PCR product digested with EcoRI and KpnI. Destination vector digested with EcoRI and KpnI.	pHLSec, pHLAvitag3
Mouse BAI3-ecto-Δ291	O80ZF8: 292-868	Fwd: cgcaccggtGACTACAAGGACGACGACGACAAGGAATCTGGTGTGGAAGAGTGGTCCCA Rev: gcggtaccTTCTCTAGGTTGCTGAGCCAAAATGGCG	PCR product digested with AgeI and KpnI. Destination vector digested with AgeI and KpnI.	pHLSec, pHLAvitag3
Mouse BAI3-full-length	O80ZF8: 1-1522	Fwd: cgcgaattcGCCACCATGAAGGCTGTTCGTAACCTGCTGATTTATATAT Rev: cgccgtacgTTACTAAACTTCTGTTTGAAAGTCACCCTCTTGCACA	PCR product digested with EcoRI and BsiWI. Destination vector digested with EcoRI and Acc65I.	pHLSec
Mouse BAI3-full-length-Δ151	O80ZF8: 152-1522	Fwd: cgcaccggtGACTACAAGGACGACGACGACAAGTCTTTTTTTGAGTTTTTGGTATTGAACAAGGTCAGC Rev: cgccgtacgTTACTAAACTTCTGTTTGAAAGTCACCCTCTTGCACA	PCR product digested with AgeI and BsiWI. Destination vector digested with AgeI and Acc65I.	pHLSec
Mouse BAI3-full-length-Δ291	O80ZF8: 292-1522	Fwd: cgcaccggtGACTACAAGGACGACGACGACAAGGAATCTGGTGTGGAAGAGTGGTCCCA Rev: cgccgtacgTTACTAAACTTCTGTTTGAAAGTCACCCTCTTGCACA	PCR product digested with AgeI and BsiWI. Destination vector digested with AgeI and Acc65I.	pHLSec

Rat GluK2-ATD	P42260: 33-420	Fwd: cgcaccggtACACATGTGTTAAGATT CGGTGGTATATTTGAATATG Rev: gcgggtaccCTTTCCTTTCTGACTTTCT GTCATATTCAGGC	PCR product digested with AgeI and KpnI. Destination vector digested with AgeI and KpnI.	pHLSec, pHLAvitag3

Appendix C -
List of Formulae

Formula C1:

$$I_{\mathrm{hkl}} = |F_{\mathrm{hkl}}|^2$$

where $F_{\mathrm{hkl}} = \sum_j f_{\mathrm{j}} \exp(2\pi i(hx_{\mathrm{j}} + ky_{\mathrm{j}} + lz_{\mathrm{j}}))exp(-B_{\mathrm{j}} sin^2\vartheta/\lambda^2)$

and f_j is the atomic scattering factor.

Formula C2:

$$R(\kappa, \varphi, \psi) = \int_{r_{\mathrm{min}}}^{r_{\mathrm{max}}} P_{\mathrm{obs}}(u) P_{\mathrm{model}}(\kappa, \varphi, \psi, u)\, du$$

where $P_{\mathrm{obs}}(u)$ and $P_{\mathrm{model}}(\kappa, \varphi, \psi, u)$ are the observed and model Patterson functions:

$$P(u) = \sum_{hkl} |F_{\mathrm{hkl}}|^2 \exp(-2\pi i(hx + ky + lz))$$

u represents a point (x,y,z) in 3D space for the Patterson function
κ, φ,ψ are the rotation angles of the model solution
r_{max} is the maximum intramolecular vector in the Patterson function
r_{min} is the minimum limit set to exclude the large origin peak in the Patterson function

Formula C3:

$$C(t) = \frac{\sum(|F_{\mathrm{obs}}|^2 - \overline{|F_{\mathrm{obs}}|^2})(|F_{\mathrm{calc}}(\mathrm{t})|^2 - \overline{|F_{\mathrm{calc}}(\mathrm{t})|^2})}{\sqrt{\sum(|F_{\mathrm{obs}}|^2 - \overline{|F_{\mathrm{obs}}|^2})\sum(|F_{\mathrm{calc}}(\mathrm{t})|^2 - \overline{|F_{\mathrm{calc}}(\mathrm{t})|^2})}}$$

The correlation coefficient C(t) can be used to evaluate translation search solutions, as a measure of agreement between observed and calculated squared structure factor amplitudes. It is calculated for each trial solution t in the translation search.

Formula C4:

$$\mathrm{R_{work}} = \frac{\sum_{hkl} \big| |F_{\mathrm{obs}}| - k|F_{\mathrm{calc}}| \big|}{\sum_{hkl} |F_{\mathrm{obs}}|}$$

where $|F_{\mathrm{obs}}|$ are the experimentally observed structure factor amplitudes
and $|F_{\mathrm{calc}}|$ are the structure factor amplitudes calculated from the model.

Formula C5:

$$\mathrm{R_{free}} = \frac{\sum_{test\ set\ hkl}\left||F_{\mathrm{obs}}| - k|F_{\mathrm{calc}}|\right|}{\sum_{test\ set\ hkl}|F_{\mathrm{obs}}|}$$

calculated as R_{work} but only with 5% of data that have been excluded from the refinement.

Formula C6:

$$\mathrm{Bound} = \frac{[\mathrm{C^A}]\mathrm{B_{max}}}{[\mathrm{C^A}] + K_{\mathrm{d}}}$$

where $[\mathrm{C^A}]$ is the analyte concentration
$\mathrm{B_{max}}$ is the maximum amount of bound analyte (in response units)
K_{d} is the equilibrium dissociation constant

Formula C7:

$$f'(x) = \frac{d(f(x))}{dx}$$

Appendix D - Abbreviations

Abbreviations

1D4	Anti-rhodopsin antibody epitope
2 % Media	DMEM supplemented with NEAA, L-glutamine and 2 % FBS
10 % Media	DMEM supplemented with NEAA, L-glutamine and 10 % FBS
AGE	Agarose Gel Electrophoresis
AMPA	α-amino-3-hydroxy-5-methyl-4-isoxazole-propionic acid
ASDs	Autism Spectrum Disorders
ASU	Asymmetric Unit
ATD	Amino-Terminal Domain
BAI	Brain Angiogenesis Inhibitor
BDNF	Brain-derived Neurotrophic Factor
BirA	Biotin ligase
Bmax	Maximum Amount Of Analyte Bound
b-OG	N-octyl-b-d-glucoside
C1ql	C1q-like
C8E4	Tetraethylene glycol monooctyl ether
C10E5	Pentaethylene glycol monodecyl ether
CaMKII	Calcium/Calmodulin-Dependent Protein Kinase II
cDNA	Complementary DNA
CF	Climbing Fibre Neuron
CHS	Cholesteryl Hemisuccinate
CIPA	Congenital Insensitivity to Pain with Anhydrosis
CNS	Central Nervous System
CPM	N-[4-(7-diethylamino-4-methyl-3coumarinyl)phenyl]maleimide
CREB	cAMP Response Element-Binding
CSPG	Chondroitin sulfate proteoglycans
CTD	C-terminal domain
D1R	Dopamine-1 receptor
DCC	Deleted in Colorectal Cancer
DDM	n-Dodecyl-ß-maltoside
DM	N-decyl-b-d-maltoside
DNMG	Decyl Maltose Neopentyl Glycol
DMEM	Dulbecco's Modified Eagle's Medium
DMT	N,N-dimethyltryptamine
DNA	Deoxyribonucleic Acid
DNAse	Deoxyribonuclease
dNTPs	Deoxyribonucleotide Triphosphate
DSCAM	Down Syndrome Cell Adhesion Molecule
EGF-like	Epidermal Growth-Factor-Like Domain
EM	Electron Microscopy
EndoF1	Endoglycosidase F1
Eph	Erytrhopoetin producing hepatoma

EPSC	Excitatory Post-Synaptic Current
ESRF	European Synchrotron Radiation Facility
ER	Endoplasmic Reticulum
FCS	Fetal Calf Serum
FN	Fibronectin
FSEC	Fluorescence Size Exclusion Chromatography
GNTI$^-$	N-acetylglucosaminyltransferase I deficient
Glc	Glucose
GlcNAc	N-acetyl-glucosamine
GPCR	G Protein-Coupled Receptors
GPI	Glycosylphosphatidylinositol
HEK293T	Human Embryonic Kidney 293 Cells Expressing SV40 Type T Antigen
HEK293S	Human Embryonic Kidney 293 Cells, GnT I Deficient
HEPES	*N*-[2-Hydroxyethyl]piperazine-*N'*-[2-ethanesulphonic acid]
HPLC	High Pressure Liquid Chromatography
HS	Heparan Sulfate
HSPG	Heparan sulfate proteoglycans
iGluRs	Ionotropic Glutamate Receptors
iGluK	Ionotropic Glutamate Receptors of the kainite subfamily
IMAC	Immobilised Metal Ion Affinity Chromatography
IP_3R	Ionositol Trisphosphate Receptor
K_d	Equilibrium Binding Constant
KO	Knock-Out
LBC	Ligand Binding Core
LBD	Ligand binding domain
LLG	Log-Likelihood Gain
LNS	LamininA/Neurexin/Sex Hormone-Binding Globulin Domain
LTD	Long-Term Synaptic Depression
LTP	Long-Term Synaptic Potentiation
MALLS	Multi-Angle Light Scattering
MAM	Mitochondria Associated Membranes
MAPK	Mitogen-activated protein kinase
mGluR1	Metabotropic Glutamate Receptor 1
MPBS	Marvel Milk powder containing PBS
NARP	Neuronal Activity Regulated Pentraxin
NDSB	Non-Detergent SulfoBetaine
NEAA	Non-Essential Amino-Acids
NGF	Nerve Growth Factor
NMDA	*N*-methyl-d-aspartate
NP1	Neuronal Pentraxin 1
NT-3	Neurotrophin-3
NT-4	Neurotrophin-4
Oligo	Oligonucleotide
PBS	Phosphate Buffered Saline Solution
PC	Purkinje Cell
PCR	Polymerase Chain Reaction
PDB	Protein Data Bank

PEI	Polyethylenimine
PF	Parallel Fibre Neuron
PF-PC	Parallel Fibre-Purkinje Cell Synapse
PI3	Phosphatidylinositol-3
PI3 Kinase	Phosphatidylinositol-3-Kinase
PKA	cAMP-Dependent Protein Kinase
PKC	Protein Kinase C
PLC	Phospholipase C
PP1	Protein phosphatase 1
PSD	Post-Synaptic Density
RBD	Receptor binding domain
RMSD	Root Mean Square Deviation
RNAse	Ribonuclease
RPTP	Receptor protein tyrosine phosphatase
RTK	Receptor Tyrosine Kinases
S1R	Sigma-1 receptor
SAM	Sterile-α motif domain
SDS	Sodium Dodecyl Sulphate
SDS-PAGE	Sodium Dodecyl Sulphate Polyacrylamide Gel Electrophoresis
SEC	Size Exclusion Chromatography
SFM	DMEM Supplemented with NEAA and L-glutamine
Shh	Sonic Hedgehog
SOC	Super Optimal Medium With Catabolite Repression
SPR	Surface Plasmon Resonance
SS4	Splice Site Four Of β-Neurexin1
STRUBI	Division of Structural Biology, University of Oxford
TEV	Tobacoo Etch Virus protease
TGF-β	Transforming Growth Factor-β
TMD	Transmembrane domain
TNF	Tumour Necrosis Factor
TPBS	0.1 % Tween 20 containing PBS
Trk	Tropomyosin Receptor Kinase
UPR	Unfolded Protein Response
v/v	Volume By Volume
w/v	Weight By Volume

Appendix E - Publication

nature structural & molecular biology

Structurally encoded intraclass differences in EphA clusters drive distinct cell responses

Elena Seiradake[1], Andreas Schaupp[2], Daniel del Toro Ruiz[2], Rainer Kaufmann[1,3], Nikolaos Mitakidis[1], Karl Harlos[1], A Radu Aricescu[1], Rüdiger Klein[2] & E Yvonne Jones[1]

Functional outcomes of ephrin binding to Eph receptors (Ephs) range from cell repulsion to adhesion. Here we used cell collapse and stripe assays, showing contrasting effects of human ephrinA5 binding to EphA2 and EphA4. Despite equivalent ligand binding affinities, EphA4 triggered greater cell collapse, whereas EphA2-expressing cells adhered better to ephrinA5-coated surfaces. Chimeric receptors showed that the ectodomain is a major determinant of cell response. We report crystal structures of EphA4 ectodomain alone and in complexes with ephrinB3 and ephrinA5. These revealed closed clusters with a dimeric or circular arrangement in the crystal lattice, contrasting with extended arrays previously observed for EphA2 ectodomain. Localization microscopy showed that ligand-stimulated EphA4 induces smaller clusters than does EphA2. Mutant Ephs link these characteristics to interactions observed in the crystal lattices, suggesting a mechanism by which distinctive ectodomain surfaces determine clustering, and thereby signaling, properties.

© 2013 Nature America, Inc. All rights reserved.

The 14 erythropoietin-producing hepatocellular receptors (Ephs) comprise the largest family of receptor tyrosine kinases in humans. Eph receptor signaling can exert localized effects on cytoskeletal dynamics, thereby directing repulsive or migratory responses. Family members are expressed in many tissues during morphogenesis and have essential roles in cell-cell communication to guide cell positioning, segregation and migration in tissue homeostasis as well as in development[1–3]. Conversely, Ephs are widely expressed in cancer cells and in tumor blood vessels; they are implicated in tumor progression and metastatic spread, with examples of both increased and decreased levels of expression linked to malignancy[4–6].

Eph receptors bind protein ligands, the Eph receptor–interacting proteins (ephrins), presented on the surface of an opposing cell (that is, a *trans* mode of ligand-receptor binding requiring direct cell-cell contact). All eight members of the human ephrin family are membrane tethered, either by a glycosylphosphatidylinositol anchor in the ephrinA proteins or by a transmembrane helix and short cytoplasmic region in the ephrinB proteins. The Eph family is also subdivided into two classes—EphAs and EphBs—groupings that are in part determined by sequence similarity but that also reflect the general preference of EphA receptors to bind ephrinA ligands and EphB receptors to bind ephrinB ligands[7]. Within classes, ephrin-Eph binding is relatively promiscuous, although measurements of binding affinities reveal some potential for selectivity in the intraclass ligand-receptor pairings[8–10].

All Eph receptors share a conserved domain composition[1] (**Fig. 1a**). The ectodomain comprises an N-terminal ligand-binding domain (LBD), a cysteine-rich region, which can be divided into a sushi domain and an epidermal growth factor–like domain (EGF), and two fibronectin type III domains (FN1 and FN2). A single transmembrane helix connects to the intracellular tyrosine kinase domain and a sterile-alpha-motif (SAM) domain that can carry a C-terminal PDZ-binding motif. Likewise, the ephrins are characterized by the conserved architecture of an N-terminal receptor-binding domain (RBD). The ephrin RBD conforms to a 'Greek key' β-barrel fold of eight β-strands (designated A–K), and the Eph LBD consists of a β-sandwich 'jelly roll' fold of 12 β-strands (A–M). Structural studies of complexes between the Eph LBD and the ephrin RBD have revealed a conserved 1:1 interaction interface generic to all ligand-receptor combinations[10]. This high-affinity binding mode is, in essence, insertion of a single long loop from the ephrin RBD (loop G–H) into a substantial cavity on the surface of the Eph LBD. The detailed architecture of this RBD-LBD interface determines the specificity and binding affinity of ephrin-Eph interactions[10]. However, the 1:1 ligand-receptor binding mode does not, in isolation, provide a molecular mechanism for Eph receptor kinase autophosphorylation and signaling. Eph signaling requires receptor clustering[11].

The first crystal structure for an Eph–ephrin complex, namely EphB2 LBD in complex with ephrinB2 RBD, highlighted a tetrameric arrangement involving a second low-affinity Eph-ephrin interaction surface. The region of the Eph LBD contributing to this interaction was designated the HI loop[12]. Functional data[13] provided support for the biological significance of the tetrameric arrangement; however, crystallographic studies for a series of other Eph LBD–ephrin RBD complexes only revealed interfaces mediating the 1:1 high-affinity binding mode[10]. Subsequent structural and functional studies on

[1]Division of Structural Biology, Wellcome Trust Centre for Human Genetics, University of Oxford, Oxford, UK. [2]Max Planck Institute of Neurobiology, Martinsried, Germany. [3]Department of Biochemistry, University of Oxford, Oxford, UK. Correspondence should be addressed to E.Y.J. (yvonne@strubi.ox.ac.uk) or R.K. (rklein@neuro.mpg.de).

Received 10 January; accepted 8 May; published online 30 June 2013; doi:10.1038/nsmb.2617

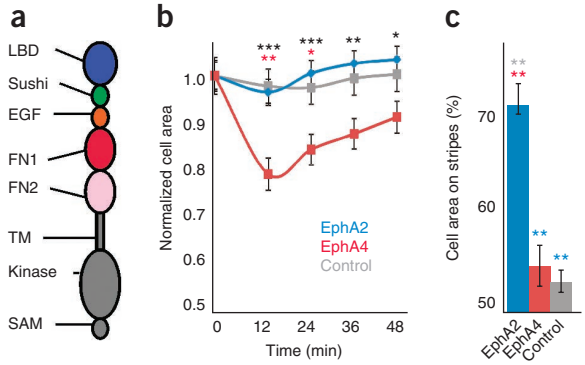


Figure 1 Stimulation of EphA2 and EphA4 triggers different cell responses. (**a**) Schematic overview showing Eph domain composition. Ligand-binding domain (LBD), sushi, epidermal growth factor like (EGF), fibronectin type III (FN1 and FN2), transmembrane helix (TM), tyrosine kinase and sterile-alpha motif (SAM) are shown. Domains are colored separately for the ectodomain. (**b**) Rounding responses of nontransfected control and Eph-transfected HeLa cells upon ephrinA5-Fc stimulation. Average adherent-cell surface areas are normalized to the values at time 0 (before receptor stimulation). Statistical significance determined by one-way ANOVA and Tukey's *post hoc* test is shown with red asterisks (control, EphA4) and black asterisks (EphA2, EphA4). Error bars, s.e.m. $*P < 0.05$; $**P < 0.01$; $***P < 0.001$ for three independent biological experiments; $n > 80$. (**c**) HeLa cell stripe assay. Adhesion of Eph-transfected cells to ephrinA5-Fc coated surfaces is shown. (50% corresponds to random distribution; >50% reflects adhesion.) Statistical significance calculated with one-way ANOVA and Tukey's *post hoc* test is shown with red asterisks (to EphA4), blue asterisks (to EphA2) and gray asterisks (to control). Error bars, s.e.m. $**P < 0.01$ for duplicate measurements from three independent biological experiments.

the full EphA2 ectodomain identified two in-*cis* Eph-Eph dimerization surfaces, which are equally essential for EphA2 clustering at cell-cell contacts[14,15]. These are a polar region on the LBD that includes the HI loop plus adjacent surfaces and a hydrophobic region on the sushi domain. Together, these interactions promote the assembly of extended EphA2 arrays that can form in the presence or absence of ephrin[14,15].

The functionality of the ephrin-Eph system is complex. Depending on receptor and ligand availability, as well as cell-specific factors, Eph signaling mediates responses ranging from cell repulsion to adhesion. This variation in cellular response complicates dissection of fundamental molecular mechanisms in ephrin-Eph signaling. Eph ectodomain binding to the RBD of class A or B ephrin ligands on neighboring cells classically triggers cell-cell repulsion through activation of the Eph intracellular kinase domain[1]. In the nervous system, repulsive EphA4-ephrin interaction is required for the formation of precise neuronal connections in the brain[16,17] and spinal cord[18] and for motor and sensory innervation of peripheral targets[19,20]. Although EphA2 protein is found in axons[21], its overall expression in the brain is low[22]. It is expressed in many other tissues[22] including the eye lens, where EphA2-ephrinA5 interaction is implicated in the adhesive packing of fiber cells through cross-talk with cadherin and catenin protein families[23]. EphA2 is also associated with invasive cell behavior and is upregulated in many cancers, in which it increases cancer malignancy and poor clinical prognosis[4].

EphA2 binds only class A ephrins, whereas EphA4 is unusually promiscuous, binding ephrinAs and Bs[7,8,24]. Both Ephs bind ephrinA5. To investigate the potential role of Eph receptor clustering characteristics in cellular response, we carried out a comparative structural and functional analysis of the EphA2-ephrinA5 and EphA4-ephrinA5 systems.

RESULTS

Eph-dependent differences in cellular response to ephrinA5

Although many factors can contribute to the functional outcome of Eph activation, we asked whether Eph receptors themselves possess intrinsically distinct properties that generate different cell responses. Cell rounding assays are widely used model systems for repulsive signaling and have been used to study Eph signaling upon stimulation with preclustered ephrins[25]. Cytoskeleton collapse, cell rounding and de-adherence result from Eph kinase activation. Because ligand binding affinity and kinetics could contribute to functional outcome, we first sought to control for this factor. To do so, we investigated the relative binding affinities of ephrinA5 to EphA2 and EphA4 in surface plasmon resonance assays. We found that ephrinA5 binds with similar affinity to EphA2 and EphA4 (data not shown), consistent with previous reports based on enzyme-linked immunosorbent assays[9]. We engineered constructs in which full-length, transmembrane mouse EphA4 and human EphA2 receptors were fused to a fluorescent protein tag (mVenus) and expressed them in HeLa or COS7 cells (Online Methods). Transiently transfected cells expressed EphA2 and EphA4 at comparable levels after ~20 h (**Supplementary Fig. 1**). We found that EphA4-transfected cells, as compared to that of EphA2-transfected cells, undergo significantly stronger rounding in response to preclustered ephrinA5-Fc (**Fig. 1b**, **Supplementary Fig. 2** and **Supplementary Movies 1** and **2**). We did not detect endogenous EphA2 or EphA4 in our HeLa cell cultures (**Fig. 1b** and **Supplementary Fig. 1**), a result consistent with the low level of collapse observed with untransfected control cells. Conversely, in a stripe assay, we found that EphA2-transfected HeLa cells adhere strongly to ephrinA5-Fc–coated stripes, whereas EphA4-transfected cells distribute more randomly between control and ephrinA5-Fc–coated stripes (**Fig. 1c**). What determines these Eph-specific signaling responses?

EphA4 ligand-free and ligand-bound crystal structures

To dissect the molecular properties that distinguish the EphA4 ectodomain ($EphA4_{ecto}$) from the EphA2 ectodomain ($EphA2_{ecto}$), we solved four crystal structures for the complete $EphA4_{ecto}$, in its ligand-free form (to 3.65-Å resolution), in complex with ephrinB3 RBD (one crystal, 4.65 Å) or with ephrinA5 RBD (two crystals: lysine-methylated, 4.0 Å and native, 4.95 Å). Data statistics and the highest-resolution shells using the $CC_{1/2}$ criteria[26] or data quality of $I/\sigma I > 2$ are provided in **Table 1**. We expressed human $EphA4_{ecto}$ and ephrin RBD proteins in HEK293S GnTI$^-$ cells, crystallized them and phased the structures by molecular replacement (Online Methods and **Supplementary Note**). The unusually high solvent content of the crystals (76–88%) in conjunction with solvent flattening methods produced good-quality electron density maps despite the generally low resolution of the diffraction data sets (**Table 1** and **Supplementary Fig. 3**). We maintained strong stereochemical restraints for refinement of the ligand-free $EphA4_{ecto}$ structure and the lysine-methylated $EphA4_{ecto}$ ephrinA5 RBD complex. For the native $EphA4_{ecto}$–ephrinA5 RBD and $EphA4_{ecto}$–ephrinB3 RBD complexes, we limited refinement to rigid body and translation-libration-screw motion (TLS) of the individual domains; stereochemical outlier residues present in high-resolution molecular replacement models were not altered for these two lowest-resolution structures. All four crystal structures have greater than 95% of residues in the favored regions of the Ramachandran plot (and 0.0–0.4% in disallowed regions), as assessed by MolProbity[27].

© 2013 Nature America, Inc. All rights reserved.

Table 1 Data collection and refinement statistics

	EphA4 ectodomain	EphA4 ectodomain + ephrinA5 (methylated)	EphA4 ectodomain + ephrinA5 (not methylated)	EphA4 ectodomain + ephrinB3
Data collection				
Space group	$P3_221$	$H32$	$H32$	$P4_332$
Cell dimensions				
a, *b*, *c* (Å)	166.88, 166.88, 192.07	256.95, 256.95, 252.51	202.88, 202.88, 326.51	300.53, 300.53, 300.53
Resolution (Å)[a]	83–3.65 (3.7–3.65)	70–4.0 (4.05–4.00)	48–4.95 (5.00–4.95)	106–4.65 (4.7–4.65)
R_{meas} (%)[a,b]	19.2 (545)	41.0 (586)	74.3 (558)	26.2 (367)
$CC_{1/2}$[b]	100 (17.7)	99.7 (15.9)	95.8 (22.0)	99.9 (16.1)
$I / \sigma I$[a]	14.17 (0.48)	7.74 (0.59)	3.32 (0.32)	7.7 (0.50)
Highest-resolution shell				
with $I / \sigma I$ >2 (Å)	4.2–4.1	4.55–4.45	7.0–6.9	5.8–5.7
Completeness (%)[a]	99.9 (100)	99.9 (100)	99.7 (98.5)	99.9 (99.9)
Redundancy[a]	20.0 (20.1)	11.3 (11.3)	9.4 (7.6)	10.8 (6.9)
Refinement				
Resolution (Å)[a]	48.2–3.65 (3.76–3.65)	70–4.0 (4.15–4.0)	48–4.95 (5.08–4.95)	106–4.65 (4.84–4.65)
No. reflections[a]	34,842 (2,951)	27,150 (2,680)	11,147 (744)	25,492 (2,802)
R_{work} / R_{free}	0.349 / 0.386	0.313 / 0.321	0.396 / 0.414	0.328 / 0.342
No. atoms (all protein)	6,344	5,087	5,087	10,126
B factors (average)	125.0	188.0	243.0	221.2
r.m.s. deviations				
Bond lengths (Å)	0.007	0.007	0.007	0.010
Bond angles (°)	0.85	0.87	0.87	1.01

[a]Values in parentheses are for highest-resolution shell. [b]Criteria for data cutoff were from ref. 26.

The domain arrangement within $EphA4_{ecto}$ is similar to that of $EphA2_{ecto}$ (refs. 14,15), with sequential LBD, sushi, EGF, FN1 and FN2 domains resulting in an oblong molecule with an ~90° kink at the FN1-FN2 linkage (**Fig. 2a**). Unlike $EphA2_{ecto}$ (refs. 14,15), EphA4 shows conservation of the FN1–FN2 linker conformation and of the relative orientation of the FN1 and FN2 domains in all four crystal structures, a result suggesting rigidity (**Supplementary Fig. 4**). The amino acid sequences of EphA2 and EphA4 in the FN1–FN2 linker region are not conserved and include a potential N-linked glycosylation site in EphA2 but not EphA4. Also, the EphA4 FN2 domain packs closely against the FN1 domain by using loop residues 518–520 (Ala-Ala-Gly). Two of these residues are replaced by bulkier and more hydrophilic amino acids for the corresponding residues 512–514 in EphA2 (Gln-Glu-Gly). Taken together, these differences may underlie the reduction in interdomain rigidity for this region in EphA2 relative to EphA4. The functional consequences of these differences in rigidity are unclear, but given the proximity of FN2 to the plasma membrane they may affect receptor-membrane interactions and orientation at the cell surface.

All reported structures of $EphA2_{ecto}$ revealed continuous array-like arrangements within the crystal lattice, compatible with EphA2 clustering in *cis* on the cell membrane[14,15] (**Supplementary Fig. 5**). Here we show that $EphA4_{ecto}$ does not form extended EphA2-like arrays in the crystal but does form defined units. The $EphA4_{ecto}$ units compatible with in-*cis* interaction in the context of a cell surface are composed of two, three or six copies of EphA4 in a dimeric or circular arrangement (**Fig. 2b**). These structural data suggest that the mode of clustering observed in EphA2 cannot be extrapolated to all Eph-family members.

Superposition of the $EphA4_{ecto}$ structure (ligand free or bound to ephrin) on $EphA2_{ecto}$ as arranged in its characteristic arrays does not lead to obvious clashes. We conclude that surface properties, rather than differences in the overall shape, determine the mode of Eph ectodomain clustering. $EphA2_{ecto}$ arrays form through Eph-Eph interactions mediated by two specific surface patches, one centered on the

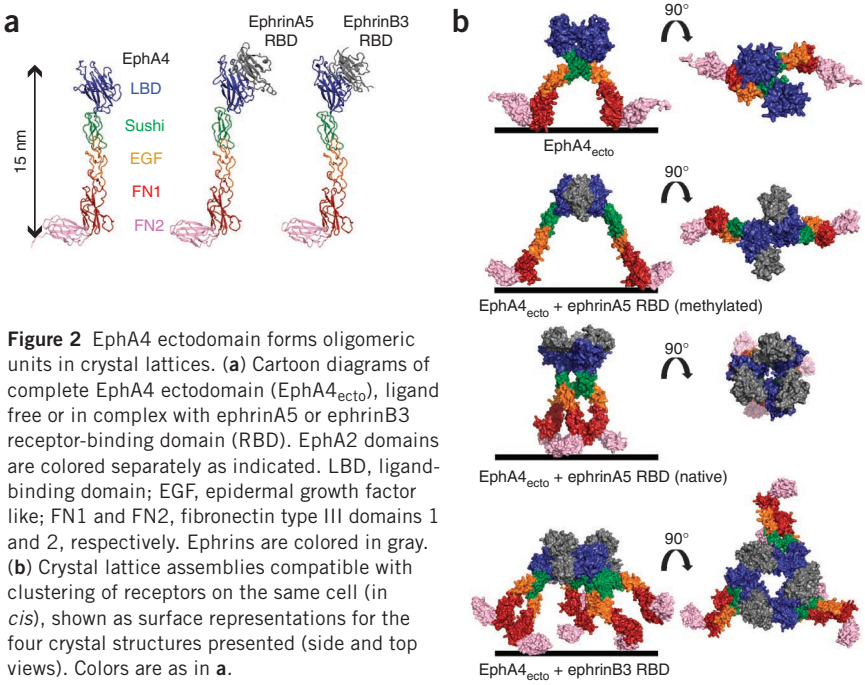


Figure 2 EphA4 ectodomain forms oligomeric units in crystal lattices. (**a**) Cartoon diagrams of complete EphA4 ectodomain ($EphA4_{ecto}$), ligand free or in complex with ephrinA5 or ephrinB3 receptor-binding domain (RBD). EphA2 domains are colored separately as indicated. LBD, ligand-binding domain; EGF, epidermal growth factor like; FN1 and FN2, fibronectin type III domains 1 and 2, respectively. Ephrins are colored in gray. (**b**) Crystal lattice assemblies compatible with clustering of receptors on the same cell (in *cis*), shown as surface representations for the four crystal structures presented (side and top views). Colors are as in **a**.

© 2013 Nature America, Inc. All rights reserved.

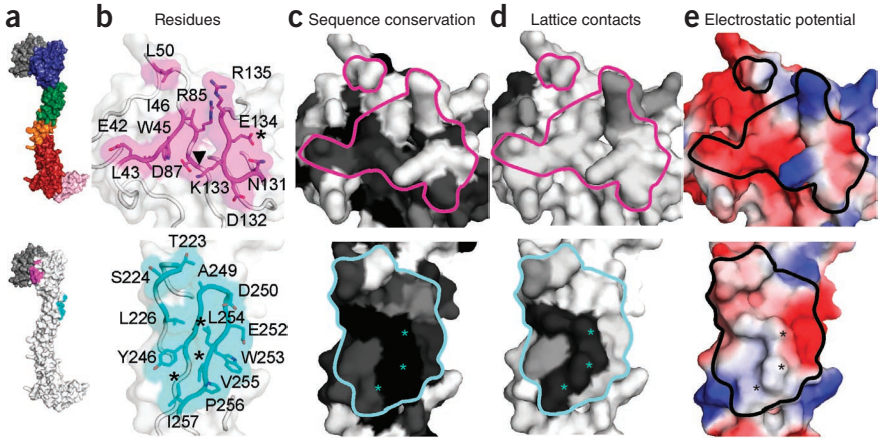


Figure 3 Properties of the EphA4 HI-loop area and sushi dimerization region. (**a**) Surface of $EphA4_{ecto}$ in complex with ephrinB3 RBD, shown in two color schemes. Top, domains are colored separately, as in **Figure 2**. Bottom, colors are: white, EphA4; gray, ephrinB3; magenta, HI loop and adjacent regions implicated in clustering for EphA2 (ref. 14); cyan, sushi dimerization surface. (**b**–**e**) Zoomed-in view of the EphA4 HI-loop region (magenta) and sushi dimerization surfaces (cyan). In **b**, Residues are shown as sticks. Arrowhead marks Lys133. Asterisks mark Glu134 (equivalent to Gly131 in EphA2, which is mutated to tyrosine in $EphA2^{HI}$) and the surface residues Leu254, Val255 and Ile257 on the sushi domain (mutated to aspartate in $EphA4^{su}$, $EphA2^{su}$ and $EphA2^{nb\text{-}su}$). In **c**, colors are according to sequence conservation among human EphAs, ranging from black (highly conserved) to white (not conserved). The HI-loop area and sushi dimerization surface are encircled. In **d**, colors are according to the frequency of residues mediating lattice contacts in the four crystal structures presented, ranging from black (involved in all lattices) to white (not involved in any lattices). In **e**, colors are according to electrostatic potential, calculated for vacuum. Blue, positive charge; red, negative charge; white, neutral; units in PyMoL adjusted to ± 63.

© 2013 Nature America, Inc. All rights reserved.

HI loop of the LBD and one on the sushi domain[14,15] (**Supplementary Figs. 5** and **6**). The structures reported here show that the EphA4 sushi domain can also mediate Eph-Eph interaction by using the equivalent surface patch, often through dimerization as found in $EphA2_{ecto}$ structures[14,15]. In contrast, the less-conserved HI-loop region on the LBD mediates no EphA4-EphA4 contacts in three of the four $EphA4_{ecto}$ structures presented (**Fig. 3** and **Supplementary Figs. 6** and **7**). It provides Eph-Eph contacts only in the crystal structure derived from lysine-methylated $EphA4_{ecto}$–ephrinA5 RBD complex (**Supplementary Fig. 8**), but as the EphA4 HI loop contains a lysine (**Fig. 3b**), it may have non-native properties in this sample. Taken together, the data show that, of the two EphA2 surfaces required to build up $EphA2_{ecto}$ arrays, only one, henceforth termed the sushi dimerization surface, is functionally conserved in EphA4 as an Eph-Eph interaction surface. The structural results further suggest that one such interaction surface is not sufficient to support the formation of EphA2-like arrays. Might Eph response to ligand be modulated by the structurally encoded clustering properties of the receptors' ectodomains?

Eph ectodomain clustering characteristics and function

To test whether differences in the clustering properties of the EphA2 and EphA4 ectodomains have a functional role in the cell, we first produced chimeras of the full-length, mVenus-tagged transmembrane receptors in which the ectodomains of EphA2 and EphA4 were switched (**Fig. 4a**). Expression levels in HeLa cells were similar for mutant and wild-type receptors (**Supplementary Fig. 1**). Indeed, the cell rounding assays showed that the EphA4 ectodomain produced more collapse than did the EphA2 ectodomain (**Fig. 4b**), indicating that the Eph ectodomain is the major determinant defining the response. However, switching the ectodomains of EphA2 and EphA4 did not fully switch the receptor functionality, thus suggesting that the identity of the transmembrane helix and/or the cytoplasmic region also contribute to the cell response, possibly through distinct steric or protein-interaction properties in these regions. Next we sought to test whether the ectodomain-dependent functional differences relate to their clustering properties.

To directly characterize the clustering properties of fluorescently tagged EphA2 and EphA4 in COS7 cells, we used time-lapse and localization microscopy techniques in living and fixed cells, respectively. Our COS7 cells expressed no EphA4 and moderate levels of endogenous EphA2 (**Supplementary Fig. 1**). We found that in live-cell imaging, EphA2 clusters formed at the cell surface within minutes after the addition of preclustered ephrinA5-Fc, initially with increased abundance of clusters at the cell periphery (**Fig. 4c** and **Supplementary Fig. 9**). At 15–30 min after stimulation, EphA2 was found in large endocytic vesicles, and the cell membrane was essentially cleared of the receptor (**Supplementary Fig. 9** and data not shown). In contrast, EphA4 formed relatively small clusters and vesicles at the cell surface under the same conditions (**Fig. 4c** and **Supplementary Fig. 9**).

To gain quantitative information on the Eph clusters, we analyzed fixed cells, implementing one of the recently developed methods of super-resolution fluorescence microscopy. Spectral position determination microscopy (SPDM)[28] is a form of localization microscopy (also termed direct stochastic optical reconstruction microscopy or dSTORM[29]) applicable for standard fluorophores such as mVenus. An intense laser excitation of the sample shifts all the fluorophores into a long-lived dark state. The stochastic recovery of individual molecules to the relatively short-lived fluorescent state then separates their signals over time (and with sequential image acquisition also provides separation in space), thus allowing the positions of single molecules to be determined with high accuracy. We collected data sets of individual molecular positions of mVenus-tagged wild-type and chimeric Ephs in paraformaldehyde-fixed samples of COS7 cells (nonstimulated or 10 min after addition of preclustered ephrinA5-Fc). We chose cells showing similar Eph expression levels and analyzed the distribution of distances between receptor positions. To detect deviations from a spatially homogeneous distribution (that is, clustering) we used Ripley's L function[30], which essentially shows the normalized distribution of distances between the single-molecule positions (Online Methods). A random distribution will approximately follow the horizontal zero axis with constant dispersion only if the data follow a homogeneous Poisson process. Signals above zero therefore reflect both the amount of clustering (y values) and cluster diameter (x values). Further analysis of the receptor clusters was performed with a method[31] based on a threshold of local molecule density to identify and characterize individual clusters in the data sets (Online Methods). The chimeric Eph receptors

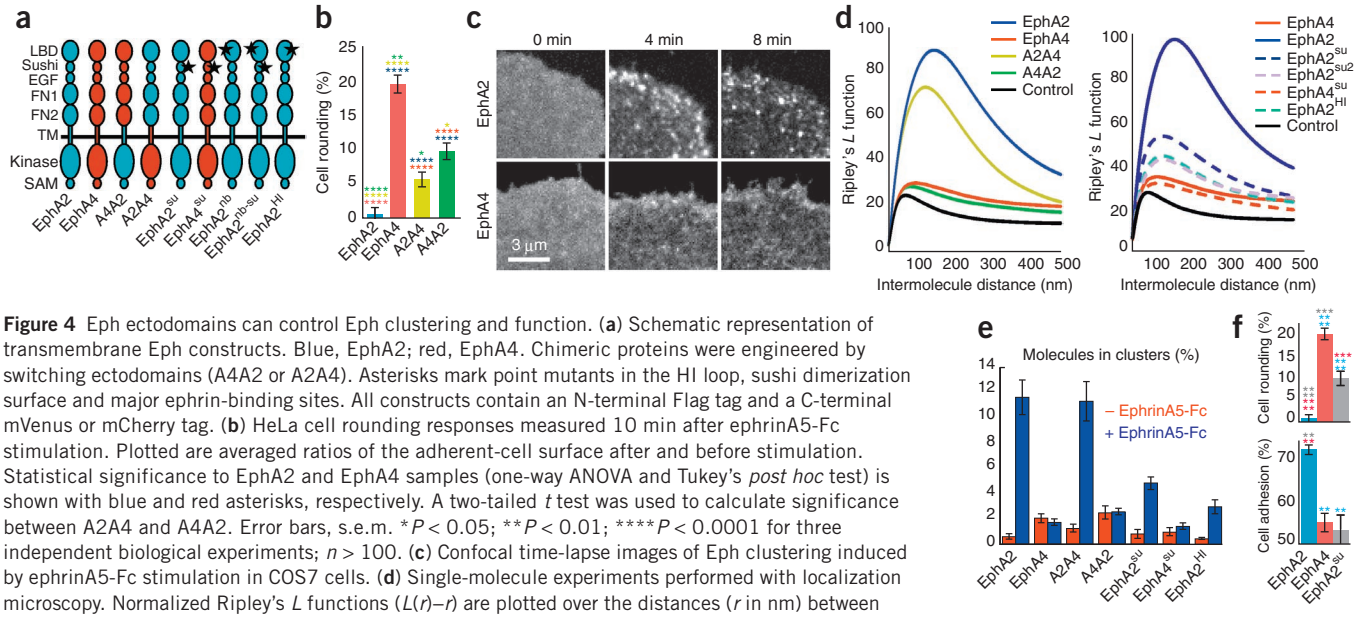


Figure 4 Eph ectodomains can control Eph clustering and function. (**a**) Schematic representation of transmembrane Eph constructs. Blue, EphA2; red, EphA4. Chimeric proteins were engineered by switching ectodomains (A4A2 or A2A4). Asterisks mark point mutants in the HI loop, sushi dimerization surface and major ephrin-binding sites. All constructs contain an N-terminal Flag tag and a C-terminal mVenus or mCherry tag. (**b**) HeLa cell rounding responses measured 10 min after ephrinA5-Fc stimulation. Plotted are averaged ratios of the adherent-cell surface after and before stimulation. Statistical significance to EphA2 and EphA4 samples (one-way ANOVA and Tukey's *post hoc* test) is shown with blue and red asterisks, respectively. A two-tailed *t* test was used to calculate significance between A2A4 and A4A2. Error bars, s.e.m. $*P < 0.05$; $**P < 0.01$; $****P < 0.0001$ for three independent biological experiments; $n > 100$. (**c**) Confocal time-lapse images of Eph clustering induced by ephrinA5-Fc stimulation in COS7 cells. (**d**) Single-molecule experiments performed with localization microscopy. Normalized Ripley's *L* functions ($L(r)–r$) are plotted over the distances (r in nm) between the molecules. Increased $L(r) - r$ at particular distances reflect the amount of clustering and the cluster sizes. (**e**) Further quantification of data presented in **d**. The percentage of detected molecules present in clusters is shown. Clusters were defined as molecules having at least 20 neighboring molecules within a radius of 50 nm (**Supplementary Fig. 10**). (**f**) Cell rounding in response to preclustered ephrinA5-Fc and cell adhesion to ephrinA5-Fc containing stripes in transfected HeLa cells. Cyan, EphA2; pink, EphA4; gray, EphA2^{su}. Statistical significance was determined by one-way ANOVA and Tukey's *post hoc* test. Error bars, s.e.m. $**P < 0.01$; $***P < 0.001$; $****P < 0.0001$.

© 2013 Nature America, Inc. All rights reserved.

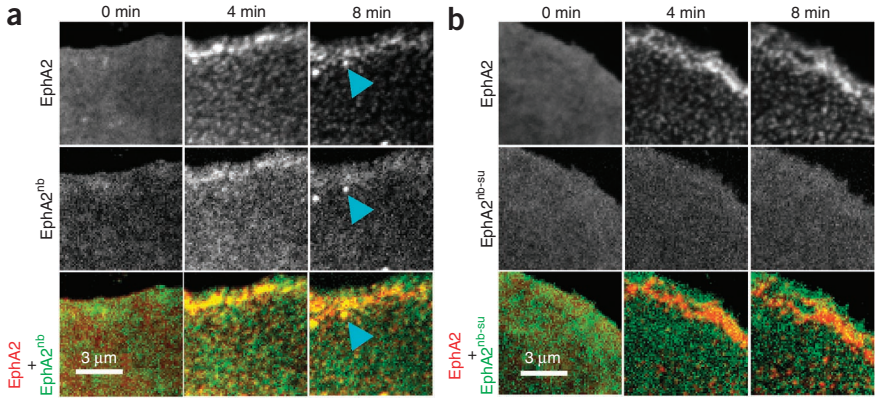
revealed that the ectodomain strongly drives the clustering properties (**Fig. 4d**,**e** and **Supplementary Figs. 9** and **10**). Notably, small clusters for EphA4 correlated with small units found in the EphA4$_{ecto}$ crystals, whereas larger clusters correlated with the extended arrays described for EphA2$_{ecto}$.

The molecular determinants of clustering

To identify whether the molecular determinants responsible for the differing functional effects were those mediating Eph-Eph interactions in the lattice assemblies of the crystal structures, we designed a panel of mutant Eph-mVenus–tagged constructs. EphA2^{su} and EphA4^{su} each contain the multiple mutations L254D V255D I257D in the sushi dimerization surface. To target the EphA2 HI loop that mediates Eph-Eph contacts specifically in EphA2$_{ecto}$ crystal structures, we used the G131Y mutant EphA2^{HI}.

In localization microscopy, we found that mutations in the HI loop (construct EphA2^{HI}) or in the sushi dimerization surface (construct EphA2^{su}) reduced EphA2 clustering to a level closer to that of EphA4 (**Fig. 4d**,**e**). To further validate this result, we introduced a second EphA2 sushi mutant, EphA2^{su2}, containing an N-type glycosylation site in the sushi dimerization surface (H246N A248S). The bulky sugar in this region of EphA2^{su2} reduced clustering of the receptor even further as compared to that for EphA2^{su} (**Fig. 4d**). EphA2^{su} had EphA4-like characteristics also in cell rounding and stripe assays (**Fig. 4f**). Thus, targeting the array-forming abilities of EphA2 can convert its function. The equivalent mutant EphA4^{su} also showed reduced clustering compared to that of wild type EphA4 (**Fig. 4d**). However, the overall clustering response of wild-type EphA4 was low, and this further reduction was not significant.

In sequence comparisons between Ephs, the sushi dimerization surface is highly conserved, and this suggests that this surface may mediate a conserved (Eph-Eph) interaction mode across all family members, with the possible exception of EphB4 (**Supplementary Fig. 11**). In contrast, sequence variation in the HI loop is high. Nevertheless, Gly131, which we show here is important in EphA2 clustering, is conserved in all EphAs except EphA4 (**Supplementary Fig. 11**). It remains to be seen whether the other EphA receptors have EphA2- or EphA4-like clustering characteristics.



Ligand-independent recruitment to clusters

Previously reported fluorescence microscopy data for EphA3 (ref. 32) suggested that ephrin-independent Eph-Eph association can increase the size of clusters. To test whether

Figure 5 Non-ligand-bound EphA2 clustering depends on Eph-Eph ectodomain interactions. (**a**) Live COS7 cell time-lapse experiment showing coclustering of the non-ephrin-binding mutant EphA2^{nb}-mVenus with EphA2-mCherry. Blue arrowheads indicate a coclustering event. (**b**) As in **a**, but with a non-ephrin-binding mutant EphA2^{nb-su}-mVenus with mutations in the sushi dimerization surface.

the strong EphA2 clustering response observed in COS7 cells involves Eph-Eph association independently of ephrin binding, we coexpressed EphA2 (mCherry tagged) and the non-ephrin-binding mutant EphA2^{nb} (mVenus tagged). EphA2^{nb} contains mutation A190N L192S to sterically hinder high-affinity ephrin binding through creation of an N-linked glycosylation site. We found, using live-cell imaging, that EphA2^{nb} is recruited into clusters of stimulated wild-type EphA2 (**Fig. 5a**). When expressed on its own, EphA2^{nb} did not cluster in response to ephrinA5-Fc addition (data not shown). To find out whether the recruitment of EphA2^{nb} into EphA2 clusters depended on the array-forming Eph-Eph interaction surfaces, we coexpressed EphA2 with the non-ephrin-binding mutant EphA2$^{nb\text{-}su}$, which combined the mutations in the sushi dimerization surface (L254D V255D I257D) and in the ephrin-binding site (A190N L192S). In agreement with the crystallographic results, EphA2$^{nb\text{-}su}$ was not recruited into wild-type EphA2 clusters (**Fig. 5b**). **Supplementary Movies 3–10** show time-lapse experiments of Eph clustering experiments.

DISCUSSION

The different members of the Eph receptor family are responsible for a myriad of often opposing functions including cell-cell adhesion and repulsion[1,4]. EphA4 is best known for its role as a classical guidance receptor in the neuronal system, in which it controls cell dynamics and motility mostly through repulsive signaling[16–19]. EphA2 has been extensively studied for its function in controlling cell adhesion, motility and invasiveness in a variety of tissues, especially in many cancers[4]. Most previous efforts to dissect the different functionalities of Ephs have focused either on the ephrin binding specificities[1,33] or the intracellular interactions with downstream signaling proteins[1,34]. A recent study suggested that EphA2 clustering propensities can affect function, although the underlying mechanisms remained unclear[35]. We are now able to address this issue by structural comparison of Eph ectodomain assemblies. We found that Ephs within the same class, EphA2 and EphA4, have distinct ectodomain properties that can determine differential clustering, albeit with the caveat that a simple switch of ectodomains does not entirely switch the receptor functionality. These results demonstrate that, together with the functional contributions of the intracellular domains, the distinctive extracellular-clustering characteristics can modulate signaling responses of the full-length receptor. The HI loop and its adjacent regions on the LBD contain some of these receptor-specific features. Early structural studies using EphB2 LBD and ephrinB2 RBD implicated this region (then termed the 'specificity loop') in secondary Eph-ephrin interactions that give rise to circular Eph–ephrin heterotetramers[12]. The functional importance of Eph surfaces mediating heterotetramerization were further confirmed in a mutagenesis study[13]. More recently, we and others presented structural data for complete EphA2 ectodomains and found that for these, the EphA2 HI loop is part of a large homotypic Eph-Eph interaction surface contributing to EphA2 array formation in *cis*. These results led to a new array-based model for Eph clustering[14,15]. The data reported here reveal that there is no single generic arrangement for Eph cluster formation but rather that the different modes of interaction involving the HI-loop region reflect a diverse functional repertoire. The sushi dimerization surface is the only surface showing a conserved (Eph-Eph) interaction mode. In the absence of additional Eph- or ephrin-mediated interactions, this surface can give rise only to dimeric but not multimeric arrangements. It is therefore necessary but not sufficient for array-like clustering.

Our results suggest a model in which different Eph ectodomain interaction properties are capable of dramatic modulation of signaling outputs to provide an additional level of control. This model allows for structural fine-tuning of functional output in cells coexpressing different Eph receptors, given the receptors' abilities to form hetero-oligomeric clusters[36,37], presumably through the conserved sushi dimerization surface. The Ephs may thus exemplify a new mechanism whereby a relatively small number of distinct receptors can control the vast number of diverse signaling processes associated with the complexity we find in higher organisms.

EphA2 is notorious for its oncogenic effects in many cancers[4,5,35]. These effects have been, at least in part, linked to Eph kinase–independent clustering properties[38] as well as more generally to the level of the receptor-ligand clustering and activation[6]. In the results reported here, we demonstrated that, by targeting surfaces involved in EphA2 clustering, we can convert EphA2 activity to resemble repulsion-mediating EphA4. The correlation of EphA2 clustering ability with breast cancer cell malignancy[35] renders this mechanism for altering cellular response therapeutically relevant. Classically, efforts in targeting Eph functions in cancers have aimed at the kinase and ligand binding functions of the receptor or at regulating the overall expression levels[4]. Our results highlight the potential of a new approach in which Eph receptor function can be controlled by modulation of its clustering properties.

METHODS

Methods and any associated references are available in the online version of the paper.

Accession codes. Coordinates and structural factors have been deposited in the Protein Data Bank, under the following accession codes: EphA4 ectodomain, 4BK4; EphA4 ectodomain in complex with ephrinA5, methylated sample, 4BK5; EphA4 ectodomain in complex with ephrinA5 4BKA; and EphA4 ectodomain in complex with ephrinB3, 4BKF.

Note: Supplementary information is available in the online version of the paper.

ACKNOWLEDGMENTS

We thank Y. Zhao and W. Lu for protein expression and M. Jones and T.S. Walter for technical support. We are grateful to T. Gaitanos for help with confocal microscopy data acquisition, I. Davis and I.M. Dobbie for discussion and assistance at the single-molecule–localization facility in the Micron Advanced Bioimaging Unit, J. Erl and M. Ponserre for assistance with cell-based assays, K.J. Morris for providing access to MetaMorph software and R.M. Esnouf for aiding in protein structure analysis. We thank the staff of the Diamond Light Source for assistance with diffraction data collection and K. Diederichs for help with data integration. This research was funded by a Cancer Research United Kingdom grant to E.Y.J. (grant A10979). Localization microscopy facilities in the Micron Advanced Bioimaging Unit were funded by the Wellcome Trust (grant 091911). E.S. was funded by an Intra-European Fellowship (Marie Curie); D.d.T.R. was funded by an European Molecular Biology Organization long-term fellowship; N.M. is supported by a Wellcome Trust D.Phil. studentship; and A.R.A. was supported as a United Kingdom Medical Research Council Career Development Award Fellow. Partial funding was provided by the Deutsche Forschungsgemeinschaft (SFB870) to R. Klein and Wellcome Trust grant 090532/Z/09/Z supporting the Wellcome Trust Centre for Human Genetics.

AUTHOR CONTRIBUTIONS

E.S. performed protein crystallization, structure analysis, cell rounding assays and Eph clustering experiments. A.S. contributed to time-lapse imaging experiments. D.d.T.R. performed stripe assays. R. Kaufman conducted localization microscopy data acquisition and analysis. N.M. contributed to protein crystallization. K.H. performed Eph crystal mounting for data collection. A.R.A., R. Klein and E.Y.J. contributed to discussion at all stages of the project. All authors contributed to writing of the manuscript.

COMPETING FINANCIAL INTERESTS

The authors declare no competing financial interests.

Reprints and permissions information is available online at http://www.nature.com/reprints/index.html.

© 2013 Nature America, Inc. All rights reserved.

npg

1. Klein, R. Eph/ephrin signalling during development. *Development* **139**, 4105–4109 (2012).
2. Batlle, E. & Wilkinson, D.G. Molecular mechanisms of cell segregation and boundary formation in development and tumorigenesis. *Cold Spring Harb. Perspect. Biol.* **4**, 211–226 (2012).
3. Pitulescu, M.E. & Adams, R.H. Eph/ephrin molecules: a hub for signaling and endocytosis. *Genes Dev.* **24**, 2480–2492 (2010).
4. Pasquale, E.B. Eph receptors and ephrins in cancer: bidirectional signalling and beyond. *Nat. Rev. Cancer* **10**, 165–180 (2010).
5. Brantley–Sieders, D.M. Clinical relevance of Ephs and ephrins in cancer: lessons from breast, colorectal, and lung cancer profiling. *Semin. Cell Dev. Biol.* **23**, 102–108 (2012).
6. Nievergall, E., Lackmann, M. & Janes, P.W. Eph-dependent cell-cell adhesion and segregation in development and cancer. *Cell Mol. Life Sci.* **69**, 1813–1842 (2012).
7. Gale, N.W. *et al.* Eph receptors and ligands comprise two major specificity subclasses and are reciprocally compartmentalized during embryogenesis. *Neuron* **17**, 9–19 (1996).
8. Bowden, T.A. *et al.* Structural plasticity of eph receptor A4 facilitates cross-class ephrin signaling. *Structure* **17**, 1386–1397 (2009).
9. Noberini, R., Rubio de la Torre, E. & Pasquale, E.B. Profiling Eph receptor expression in cells and tissues: a targeted mass spectrometry approach. *Cell Adh. Migr.* **6**, 102–112 (2012).
10. Himanen, J.P. Ectodomain structures of Eph receptors. *Semin. Cell Dev. Biol.* **23**, 35–42 (2012).
11. Janes, P.W., Nievergall, E. & Lackmann, M. Concepts and consequences of Eph receptor clustering. *Semin. Cell Dev. Biol.* **23**, 43–50 (2012).
12. Himanen, J.P. *et al.* Crystal structure of an Eph receptor–ephrin complex. *Nature* **414**, 933–938 (2001).
13. Smith, F.M. *et al.* Dissecting the EphA3/Ephrin-A5 interactions using a novel functional mutagenesis screen. *J. Biol. Chem.* **279**, 9522–9531 (2004).
14. Seiradake, E., Harlos, K., Sutton, G., Aricescu, A.R. & Jones, E.Y. An extracellular steric seeding mechanism for Eph–ephrin signaling platform assembly. *Nat. Struct. Mol. Biol.* **17**, 398–402 (2010).
15. Himanen, J.P. *et al.* Architecture of Eph receptor clusters. *Proc. Natl. Acad. Sci. USA* **107**, 10860–10865 (2010).
16. Egea, J. *et al.* Regulation of EphA 4 kinase activity is required for a subset of axon guidance decisions suggesting a key role for receptor clustering in Eph function. *Neuron* **47**, 515–528 (2005).
17. Dufour, A. *et al.* Area specificity and topography of thalamocortical projections are controlled by ephrin/Eph genes. *Neuron* **39**, 453–465 (2003).
18. Kullander, K. *et al.* Role of EphA4 and EphrinB3 in local neuronal circuits that control walking. *Science* **299**, 1889–1892 (2003).
19. Kao, T.J., Law, C. & Kania, A. Eph and ephrin signaling: lessons learned from spinal motor neurons. *Semin. Cell Dev. Biol.* **23**, 83–91 (2012).
20. Wang, L., Klein, R., Zheng, B. & Marquardt, T. Anatomical coupling of sensory and motor nerve trajectory via axon tracking. *Neuron* **71**, 263–277 (2011).
21. Brittis, P.A., Lu, Q. & Flanagan, J.G. Axonal protein synthesis provides a mechanism for localized regulation at an intermediate target. *Cell* **110**, 223–235 (2002).
22. Hafner, C. *et al.* Differential gene expression of Eph receptors and ephrins in benign human tissues and cancers. *Clin. Chem.* **50**, 490–499 (2004).
23. Cooper, M.A. *et al.* Loss of ephrin-A5 function disrupts lens fiber cell packing and leads to cataract. *Proc. Natl. Acad. Sci. USA* **105**, 16620–16625 (2008).
24. Qin, H. *et al.* Structural characterization of the EphA4–Ephrin-B2 complex reveals new features enabling Eph–ephrin binding promiscuity. *J. Biol. Chem.* **285**, 644–654 (2010).
25. Poliakov, A., Cotrina, M. & Wilkinson, D.G. Diverse roles of eph receptors and ephrins in the regulation of cell migration and tissue assembly. *Dev. Cell* **7**, 465–480 (2004).
26. Karplus, P.A. & Diederichs, K. Linking crystallographic model and data quality. *Science* **336**, 1030–1033 (2012).
27. Davis, I.W. *et al.* MolProbity: all-atom contacts and structure validation for proteins and nucleic acids. *Nucleic Acids Res.* **35**, W375–W383 (2007).
28. Lemmer, P. *et al.* SPDM: light microscopy with single-molecule resolution at the nanoscale. *Appl. Phys. B* **93**, 1–12 (2008).
29. Heilemann, M. *et al.* Subdiffraction-resolution fluorescence imaging with conventional fluorescent probes. *Angew. Chem. Int. Edn Engl.* **47**, 6172–6176 (2008).
30. Ripley, B.D. Modeling spatial patterns. *J. Roy. Stat. Soc. B Met* **39**, 172–212 (1977).
31. Kaufmann, R., Mueller, P., Hildenbrand, G., Hausmann, M. & Cremer, C. Analysis of Her2/neu membrane protein clusters in different types of breast cancer cells using localization microscopy. *J. Microsc.* **242**, 46–54 (2010).
32. Wimmer-Kleikamp, S.H., Janes, P.W., Squire, A., Bastiaens, P.I. & Lackmann, M. Recruitment of Eph receptors into signaling clusters does not require ephrin contact. *J. Cell Biol.* **164**, 661–666 (2004).
33. Triplett, J.W. & Feldheim, D.A. Eph and ephrin signaling in the formation of topographic maps. *Semin. Cell Dev. Biol.* **23**, 7–15 (2012).
34. Astin, J.W. *et al.* Competition amongst Eph receptors regulates contact inhibition of locomotion and invasiveness in prostate cancer cells. *Nat. Cell Biol.* **12**, 1194–1204 (2010).
35. Salaita, K. *et al.* Restriction of receptor movement alters cellular response: physical force sensing by EphA2. *Science* **327**, 1380–1385 (2010).
36. Janes, P.W. *et al.* Eph receptor function is modulated by heterooligomerization of A and B type Eph receptors. *J. Cell Biol.* **195**, 1033–1045 (2011).
37. Freywald, A., Sharfe, N. & Roifman, C.M. The kinase-null EphB6 receptor undergoes transphosphorylation in a complex with EphB1. *J. Biol. Chem.* **277**, 3823–3828 (2002).
38. Miao, H. *et al.* EphA2 mediates ligand-dependent inhibition and ligand-independent promotion of cell migration and invasion via a reciprocal regulatory loop with Akt. *Cancer Cell* **16**, 9–20 (2009).

© 2013 Nature America, Inc. All rights reserved.

ONLINE METHODS

Vectors and cloning. Transmembrane constructs encoding human EphA2 (residues 27–976, UniProt P29317) and mouse EphA4 (residues 28–986, UniProt Q03137) were fused to an N-terminal Flag tag (TGDYKDDDDK). Chimeric construct A2A4 was produced by fusion of EphA2 ectodomain (residues 27–534) to EphA4 transmembrane and intracellular regions (residues 548–986) and an N-terminal Flag tag. Chimeric construct A4A2 was produced by fusion of EphA4 ectodomain (residues 28–547) to EphA2 transmembrane and intracellular regions (residues 535–976) and an N-terminal Flag tag. Point mutants were generated by PCR techniques. All transmembrane Eph constructs were cloned into the AgeI–KpnI cloning site of a modified pHLsec vector[39] encoding an N-terminal secretion signal sequence and a C-terminal mVenus or mCherry tag followed by a polyhistidine tag. Secreted ectodomains of human EphA4 ($EphA4_{ecto}$, residues 20–547, UniProt P54764) and human ephrin RBDs (ephrinA5, residues 27–166, UniProt P52803; ephrinB3, residues 27–169, UniProt Q15768; and ephrinB2, residues 27–167, UniProt P52799) were cloned into the AgeI–KpnI sites of a pHLsec vector[39] encoding an N-terminal secretion signal sequence and a C-terminal polyhistidine tag.

Protein purification and crystallization. We expressed $EphA4_{ecto}$, ephrinA5 RBD and ephrinB3 RBD transiently[39] in GnTI-deficient HEK293S cells[40]. Proteins were purified separately from cell culture medium by Ni-affinity and size-exclusion chromatography. Complexes were formed by mixing either before or after deglycosylation with endoglycosidase F1 (refs. 39,41) and subsequent lysine methylation by established protocols[42] (**Supplementary Note**). All crystals were grown at 20 °C in sitting drops by vapor diffusion[43]. Crystals of ligand-free $EphA4_{ecto}$ were produced by mixture of the concentrated $EphA4_{ecto}$ and ephrinB2 RBD solution (**Supplementary Note**) in a 1:1 ratio (v/v) with crystallization solution 1 (1.8 M ammonium phosphate and 100 mM HEPES, pH 7.4). Crystals of lysine-methylated $EphA4_{ecto}$ in complex with ephrinA5 RBD grew by mixture of concentrated sample 1:1 (v/v) with crystallization solution 2 (8% w/v polyethylene glycol 8000 and 0.1 M Tris-HCl, pH 8.5). Native crystals of $EphA4_{ecto}$ in complex with ephrinA5 RBD grew by mixture of concentrated sample 1:1:1 (v/v/v) with crystallization solution 3 (0.01 M $MgSO_4$, 1.8 M Li_2SO_4 and 0.05 M sodium cacodylate, pH 6) and 4% benzamidine-HCl (Hampton). Native crystals of $EphA4_{ecto}$ in complex with ephrinB3 RBD grew by mixture of concentrated sample 1:1:1 (v/v/v) with crystallization solution 4 (0.08 M magnesium acetate tetrahydrate, 0.05 M cacodylate, pH 6.5, and 15% polyethylene glycol 400) and 0.1 M spermidine (Hampton).

Structure determination. Diffraction data were collected at the Diamond Light Source (beamlines I24, I04 and I04-1) at 100 K. Crystals were flash frozen after brief dipping into reservoir solution supplemented with 15–25% glycerol. Diffraction data were processed with XIA2 (ref. 44), XDS[45], MOSFLM[46] and CCP4 suite[47]. The structure of ligand-free $EphA4_{ecto}$ was solved from subdomains of the previously published $EphA2_{ecto}$ model (PDB 2X10)[14] as inputs for molecular replacement in PHASER[48]. The resultant model was improved with the MR_ROSETTA[49] implementation in PHENIX[50]. Electron-density modification was done with PARROT[51], manual improvement of the model in COOT[52] and final rounds of refinement in autoBUSTER[53], with strong stereochemical restraints and TLS. The resultant model was used to phase the data for lysine-methylated $EphA4_{ecto}$ in complex with ephrinA5 RBD. The structure of ephrinA5 RBD, as found in complex with $EphA2_{ecto}$ (PDB 2X11), was placed manually by superposition. Individual domains were refined with rigid-body refinement in PHASER[50], and minor adjustments were performed by hand in COOT[52]. Electron-density modification was done with PARROT[51]. A final round of refinement was done in autoBUSTER[53], with strong stereochemical restraints and TLS. The resultant model was used to phase the data for native $EphA4_{ecto}$ in complex with ephrinA5 RBD. We used the refinement program in PHENIX[50] and REFMAC5 (ref. 54) for rigid-body and TLS refinement of individual domains. Electron-density modification was done with PARROT[51]. The structure of $EphA4_{ecto}$ in complex with ephrinB3 RBD was solved from the model for ligand-free $EphA4_{ecto}$ and the model for ephrinB3 RBD as found in complex with the Nipah virus G attachment glycoprotein (PDB 3D12)[55]. Rigid-body and TLS refinement were done in PHENIX[56] and BUSTER[53] and electron-density modification in PARROT[51].

HeLa cell collapse assay. HeLa cells were grown in live-cell imaging chambers (Lab-Tek, cat. no. 155380) at 37 °C in Dulbecco's Modified Eagle's Medium (DMEM, 4.5 g/l glucose, + L-glutamine, no pyruvate, Gibco) supplemented with 1× L-glutamine (PAA), 10% fetal calf serum (HyClone) and 1× penicillin and streptomycin (PAA). Cells were transfected with Fugene or X-tremeGene HP DNA transfection reagent (Roche) according to the recommended protocol, with 0.2 µg plasmid DNA per milliliter. After 12–15 h, the medium was changed to imaging medium (DMEM, PAN Biotech GmbH, cat. no. P04–05545) supplemented with 1× L-glutamine, 0.5% fetal calf serum (HyClone) and 1× penicillin and streptomycin (PAA) and the cells incubated at 37 °C for 2–6 h. EphrinA5-Fc (R&D, cat. no. 374-EA) at 0.2 mg ml^{-1} in PBS was mixed with goat anti-human IgG Fcγ (Jackson ImmunoResearch, cat. no. 109-005-098) and imaging medium in a 5:1:28 ratio and incubated for 2 h at room temperature. For stimulation, the ephrinA5-Fc mixture was further diluted with prewarmed imaging medium and added to the cells in a final concentration of 2 µg ephrinA5-Fc and 0.04 µg anti-IgG per ml. Cells were imaged with a Zeiss Axiovert 200M microscope equipped with a temperature-controlled carbon dioxide incubation chamber set to 37 °C, 65% humidity and 5% CO_2. Illumination was provided by an X-Cite lamp (series 120, Lumen Dynamics Group), and images were recorded by a Coolsnap HQ camera (Photometrics). Sequential images were acquired before and every 6 min following preclustered ephrin-Fc addition. MetaMorph imaging software (Molecular Devices) was used to analyze cell collapse responses and to assemble movies.

COS7 stimulation assay. COS7 cells were cultured, transfected and stimulated with ephrinA5-Fc and anti-human IgG as described above for HeLa cells. Cells were imaged with a confocal spinning-disc microscope (Zeiss AXIO Observer Z1) and temperature-controlled incubation chamber (Zeiss) set to 37 °C, before and every 4 min after stimulation at 63× magnification. *Z*-stack slices of 0.5 µm were taken. MetaMorph imaging software was used to pick and project three in-focus *Z*-planes per image and to assemble movies.

Localization microscopy–based analysis. COS7 cells were cultured and transfected with mVenus-tagged Eph constructs as described in previous sections. We prepared paraformaldehyde-fixed samples of nonstimulated COS7 cells and of COS7 cells after 10 min of stimulation with ephrinA5-Fc and anti-IgG. Samples were mounted on regular glass slides with fluorescence mounting medium (Dako). An OMX (optical microscope experimental, V2, API) was modified to enable localization microscopy with conventional fluorescent proteins[28]. The intensity of the 488-nm laser was adjusted to ~14 kW/cm^2 in the object plane to drive the fluorophores into a long-lived dark state; a stochastic recovery of individual molecules to the fluorescent state was recorded by image sequences of 2,000 frames and an integration time of 50 ms per frame. The positions of single molecules were calculated with an estimated mean localization accuracy of <21 nm with a maximum likelihood–based algorithm[57] that we adapted to the OMX hardware configuration. The resulting data sets were sorted according to their mean point densities (number of molecules recorded per square micrometer). To control for the effect of Eph expression level on clustering, only data sets with similar mean point densities (~170/$µm^2$) were selected for further analyses. To analyze the distances between neighboring molecule positions, we used Ripley's *L* function[30], which takes into account distances expected for a homogenous distribution and allows interpretation of the strength of clustering (amplitude) and gives an indication of the size and size variance of clusters (position along the *x* axis, width of the distribution). Receptor clusters were identified and analyzed by a previously described algorithm[31] based on a threshold value of local point density. For the present analysis the value defining what was regarded as a cluster was set to >20 molecule positions within a radius of 50 nm (~2,670 points/$µm^2$).

Stripe assay. EphrinA5-Fc protein (12.5 µg/ml; R&D cat. no. 374-EA) was preclustered (ratio 1:3) with Alexa594-conjugated anti-hFc antibody (Invitrogen, cat. no. A11014) in PBS for 30 min. Clustered ephrinA5-Fc was injected into matrices (90-µm width) placed on 60-mm dishes[58], to result in the first red-fluorescent stripes. After 30-min incubation at 37 °C, dishes were washed with PBS, and matrices were carefully removed. The dishes were further coated with 12.5 µg/ml of Fc (Jackson, cat. no. 009-000-008) protein preclustered with anti-hFc (Jackson, cat. no. 109-005-098; no fluorescent dye) for 30 min at 37 °C. After that, stripes were washed three times with PBS. HeLa cells, transfected with Fugene HD transfection reagent (Roche) according to the manufacturer's instructions, with 0.6 µg per well (six-well format), were cultured for 24 h on the

© 2013 Nature America, Inc. All rights reserved.

stripes (30,000 cells per carpet). Cells were fixed with 4% PFA in PBS for 20 min at RT and washed with PBS. The mVenus tag in the Eph constructs was used to visualize transfected cells. Images of cells and stripes were acquired with an Axioplan epifluorescent microscope (Zeiss) at 10× magnification. Images containing stripes were further separated into two parts (on red or black stripes). The total numbers of Venus+ pixels on red stripes (ephrinA5-Fc) were quantified with ImageJ.

39. Aricescu, A.R., Lu, W. & Jones, E.Y. A time- and cost-efficient system for high-level protein production in mammalian cells. *Acta Crystallogr. D Biol. Crystallogr.* **62**, 1243–1250 (2006).
40. Reeves, P.J., Callewaert, N., Contreras, R. & Khorana, H.G. Structure and function in rhodopsin: high-level expression of rhodopsin with restricted and homogeneous N-glycosylation by a tetracycline-inducible *N*-acetylglucosaminyltransferase I-negative HEK293S stable mammalian cell line. *Proc. Natl. Acad. Sci. USA* **99**, 13419–13424 (2002).
41. Grueninger-Leitch, F., D'Arcy, A., D'Arcy, B. & Chene, C. Deglycosylation of proteins for crystallization using recombinant fusion protein glycosidases. *Protein Sci.* **5**, 2617–2622 (1996).
42. Walter, T.S. *et al.* Lysine methylation as a routine rescue strategy for protein crystallization. *Structure* **14**, 1617–1622 (2006).
43. Walter, T.S. *et al.* A procedure for setting up high-throughput nanolitre crystallization experiments: crystallization workflow for initial screening, automated storage, imaging and optimization. *Acta Crystallogr. D Biol. Crystallogr.* **61**, 651–657 (2005).
44. Winter, G. xia2: an expert system for macromolecular crystallography data reduction. *J. Appl. Crystallogr.* **43**, 186–190 (2010).
45. Kabsch, W. Automatic processing of rotation diffraction data from crystals of initially unknown symmetry and cell constants. *J. Appl. Crystallogr.* **26**, 795–800 (1993).
46. Leslie, A.G. The integration of macromolecular diffraction data. *Acta Crystallogr. D Biol. Crystallogr.* **62**, 48–57 (2006).
47. Collaborative Computational Project 4. The CCP4 suite: programs for protein crystallography. *Acta Crystallogr. D Biol. Crystallogr.* **50**, 760–763 (1994).
48. McCoy, A.J. *et al.* Phaser crystallographic software. *J. Appl. Crystallogr.* **40**, 658–674 (2007).
49. DiMaio, F., Tyka, M.D., Baker, M.L., Chiu, W. & Baker, D. Refinement of protein structures into low-resolution density maps using rosetta. *J. Mol. Biol.* **392**, 181–190 (2009).
50. Zwart, P.H. *et al.* Automated structure solution with the PHENIX suite. *Methods Mol. Biol.* **426**, 419–435 (2008).
51. Zhang, K.Y., Cowtan, K. & Main, P. Combining constraints for electron-density modification. *Methods Enzymol.* **277**, 53–64 (1997).
52. Emsley, P. & Cowtan, K. Coot: model-building tools for molecular graphics. *Acta Crystallogr. D Biol. Crystallogr.* **60**, 2126–2132 (2004).
53. Blanc, E. *et al.* Refinement of severely incomplete structures with maximum likelihood in BUSTER-TNT. *Acta Crystallogr. D Biol. Crystallogr.* **60**, 2210–2221 (2004).
54. Murshudov, G.N., Vagin, A.A. & Dodson, E.J. Refinement of macromolecular structures by the maximum-likelihood method. *Acta Crystallogr. D Biol. Crystallogr.* **53**, 240–255 (1997).
55. Xu, K. *et al.* Host cell recognition by the henipaviruses: crystal structures of the Nipah G attachment glycoprotein and its complex with ephrin-B3. *Proc. Natl. Acad. Sci. USA* **105**, 9953–9958 (2008).
56. Adams, P.D. *et al.* PHENIX: building new software for automated crystallographic structure determination. *Acta Crystallogr. D Biol. Crystallogr.* **58**, 1948–1954 (2002).
57. Gruell, F., Kirchgessner, M., Kaufmann, R., Hausmann, M. & Kebschull, U. Accelerating image analysis for localization microscopy with FPGAs. in *International Conference on Field Programmable Logic and Applications* 1–5 (Institute of Electrical and Electronics Engineers, 2011).
58. Knöll, B., Weinl, C., Nordheim, A. & Bonhoeffer, F. Stripe assay to examine axonal guidance and cell migration. *Nat. Protoc.* **2**, 1216–1224 (2007).

© 2013 Nature America, Inc. All rights reserved.

doi:10.1038/nsmb.2617